Karlsruher Institut für Technologie

IEKP-KA/2014-04

Studien an bestrahlten Siliziumsensoren für den CMS Spurdetektor am HL-LHC

Andreas Nürnberg

Zur Erlangung des akademischen Grades eines
DOKTORS DER NATURWISSENSCHAFTEN
von der Fakultät für Physik des
Karlsruher Institut für Technologie (KIT)

genehmigte

DISSERTATION

von

Dipl.-Phys. Andreas Nürnberg
aus Karlsruhe

Tag der mündlichen Prüfung: 14. 02. 2014

Referent: Prof. Dr. Willem de Boer, Institut für Experimentelle Kernphysik
Korreferent: Prof. Dr. Thomas Müller, Institut für Experimentelle Kernphysik

Karlsruhe Institute of Technology

IEKP-KA/2014-04

STUDIES ON IRRADIATED SILICON SENSORS FOR THE CMS TRACKER AT THE HL-LHC

Andreas Nürnberg

Zur Erlangung des akademischen Grades eines
DOKTORS DER NATURWISSENSCHAFTEN
von der Fakultät für Physik des
Karlsruher Institut für Technologie (KIT)

genehmigte

DISSERTATION

von

Dipl.-Phys. Andreas Nürnberg
aus Karlsruhe

Tag der mündlichen Prüfung: 14. 02. 2014

Referent: Prof. Dr. Willem de Boer, Institut für Experimentelle Kernphysik
Korreferent: Prof. Dr. Thomas Müller, Institut für Experimentelle Kernphysik

Deutsche Zusammenfassung

Der Large Hadron Collider LHC ist der weltweit größte Teilchenbeschleuniger. In einem 27 km langen, ringförmigen Tunnel der Europäischen Organisation für Kernphysik CERN in der Nähe von Genf werden Protonen gegenläufig auf eine Schwerpunktsenergie von $\sqrt{s} = 14\,\text{TeV}$ beschleunigt und an vier Wechselwirkungspunkten frontal zur Kollision gebracht. Aus dem Nachweis der bei der Kollision entstehenden Zerfallsprodukte lässt sich die ursprüngliche Wechselwirkung der Protonen und der an ihr beteiligten Elementarteilchen bestimmen. Die erfolgreiche erste Laufzeit des LHC von 2010 bis Anfang 2013 bei Energien von 7 TeV und 8 TeV hat unter anderem zum Nachweis des Higgs Bosons geführt, dem letzten fehlenden Elementarteilchen im Standardmodell [Cha+12].

Der LHC wird in den kommenden Jahren schrittweise ausgebaut und verbessert, bis er im Jahr 2023 in die Hochluminositätsphase startet. Die Luminosität wird dann um den Faktor fünf über der Luminosität des LHC liegen. Die Verbesserungen am Beschleuniger stellen die Detektoren vor neue Herausforderungen. Durch die erhöhte Luminosität des LHC steigt die Teilchendichte im Detektor stark an. Insbesondere die Spurdetektoren werden wegen ihrer Nähe zum Wechselwirkungspunkt im Inneren des Detektors noch höherer Strahlenbelastung ausgesetzt sein als bisher. Das Sensormaterial wird durch die Wechselwirkung der nachzuweisenden Teilchen mit den Atomen im Kristallgitter geschädigt. Diese Schädigung reduziert die Leistungsfähigeit des Detektors. Neben einer geringeren Signalausbeute steigt die thermische Verlustleistung im Sensor stark an.

Der Spurdetektor des CMS Experiments soll um das Jahr 2022 komplett erneuert werden. Gegenwärtig untersucht die CMS-Tracker-Kollaboration verschiedene Silizium-Grundmaterialien und verschiedene Sensorgeometrien auf ihre Eignung im Spurdetektor, um den erhöhten Anforderungen an Strahlenhärte und Spurdichte gerecht zu werden. Das Institut für Experimentelle Kernphysik des KIT ist an diesen Studien beteiligt. Die vorliegende Arbeit ist im Rahmen dieser Forschungs- und Entwicklungsarbeiten entstanden. Um die höhere Datenrate durch die erhöhte Spurdichte verarbeiten zu können, wird ein neuer binärer Auslesechip entwickelt. Im Gegensatz zur bisherigen analogen Auslese wird die Information über die Signalhöhe der getroffenen Kanäle bereits im Auslesechip verworfen und nur noch eine binäre Trefferinfomation gespeichert. Ein nachträgliches Anpassen der Signalschwellen wie bisher während der Rekonstruktion der Daten ist dadurch nicht mehr möglich. Die Wahl des Schwellwertes hat direkten Einfluss auf die Qualität der aufgezeichneten Daten. Ein sorgfältiges Einstellen des Schwellwerts ist daher besonders wichtig.

Die erhöhte Teilchendichte im Detektor erfordert es, den Spurdetektor in die Trigger-Entscheidung mit einzubeziehen. Um die Datenmenge auf ein handhabbares Maß zu reduzieren,

ist eine Auswahl der interessanten Teilchenspuren mit hohem Transversalimpuls bereits auf der Ebene der Ausleseelektronik direkt im Spurdetektor nötig. Hierfür wird gegenwärtig ein Modulkonzept mit zwei eng übereinander liegenden Sensoren verfolgt. Durch die räumliche Korrelation der Teilchendurchgänge in beiden Sensoren durch die Ausleseelektronik kann auf die Krümmung der Spur im Magnetfeld und damit auf den Teilchenimpuls geschlossen werden. Auf diese Weise werden Spuren von niederenergetischen Teilchen nicht an die Trigger-Logik weitergeleitet.

Für das Funktionieren der binären Ausleseelektronik ist es wichtig, die Eigenschaften der Ladungscluster nach einem Teilchendurchgang durch den Sensor zu kennen. Im Rahmen der vorliegenden Arbeit wurden umfangreiche Studien zur Signalerzeugung in Silizium-Streifensensoren durchgeführt. Neben dem Einfluss von Bestrahlung und anschließendem Ausheilen auf die Sensorparameter wurde ein weiterer Schwerpunkt auf das Verhalten der Sensoren im 3,8 T starken Magnetfeld im CMS-Detektor gelegt. Durch die Lorentzkraft werden die durch Ionisation im Sensormaterial erzeugten Ladungsträger seitlich versetzt, bevor sie von der Ausleseelektronik nachgewiesen werden können. Dieser Versatz führt zu einer verschlechterten Ortsauflösung des Spurdetektors, sofern er nicht bei der Datenprozessierung berücksichtigt und ausgeglichen wird. Um die Abhängigkeit des Versatzes von äußeren Einflüssen wie Bestrahlungsfluenz, angelegter Sperrspannung und Temperatur zu bestimmen, wurden Messungen an über 40 bestrahlten Streifensensoren in einem supraleitenden Magneten am Institut für Technische Physik des KIT bei Feldstärken bis 8 T durchgeführt. Ergänzend wurde der Lorentzwinkel im aktuellen CMS Spurdetektor untersucht, wobei sowohl Ereignisse aus Proton-Proton Kollisionen als auch von kosmischen Teilchen ausgewertet wurden.

Zur genaueren Untersuchung der Eigenschaften bestrahlter Sensoren mit Teilchenspuren wurden Teststrahlmessungen am DESY-Beschleuniger in Hamburg durchgeführt. Hierfür wurden Multi-Geometrie-Sensoren verwendet, die Regionen mit unterschiedlichen Streifengeometrien auf einem Sensor zusammenfassen. Neben den Clustereigenschaften wurde die Ortsauflösung und Effizienz der unterschiedlichen Sensorregionen in Abhängigkeit des Einfallswinkels der Teilchen untersucht. Durch die gute Ortsauflösung des verwendeten Strahlteleskops konnten die Eigenschaften der Sensorregionen mit einer Auflösung untersucht werden, die besser als der Streifenabstand ist. Zur Vorhersage der Leistungsfähigeit der neuen binären Datenerfassung wurden die gewonnenen Messdaten neben der bisher im Spurdetektor verwendeten analogen Signalinterpretation auch mit einem binären Schwellwert verarbeitet. Die Auswirkungen verschiedener Schwellwerte auf die Detektoreffizienz und -auflösung wurden untersucht.

Aus den gewonnenen Daten wurde ein Simulationsmodell entwickelt, das es erlaubt, die Eigenschaften der Ladungscluster nach einem Teilchendurchgang vorherzusagen. Dabei wird die Ladungsträgerdrift im Sensor nachgebildet, wobei der Einfluss des Magnetfeldes sowie der Einfluss von Strahlenschäden berücksichtigt werden. Das Modell wurde umfassend anhand von Messdaten validiert. Neben der Entwicklung des Modells wurden Studien mit Silvaco Atlas durchgeführt, einem kommerziellen Finite-Elemente-Simulationsprogramm.

Abschließend wurde das Simulationsmodell verwendet, um die Funktion der geplanten Triggermodule zu untersuchen. Die räumliche Korrelation der Teilchendurchgänge in zwei dicht benachbarten Sensoren im Magnetfeld wurde in Abhängigkeit der Modulgeometrie untersucht. Es konnte gezeigt werden, dass die gewünschte Unterdrückung von Teilchenspuren

mit niedrigem Transversalimpuls durch das gegenwärtig verfolgte Modulkonzept möglich ist, wobei der Einfluss von Strahlenschäden berücksichtigt wurde.

Im ersten Teil der vorliegenden Arbeit wird der LHC Beschleuniger und die vier großen Detektoren vorgestellt. Der Ausbau des Beschleunigers sowie die Auswirkungen auf die Experimente werden diskutiert, wobei der Schwerpunkt auf den CMS-Spurdetektor gelegt wird. Die Notwendigkeit eines genauen Verständnisses der Signalerzeugung in bestrahlten Siliziumsensoren wird gezeigt. Im zweiten Teil werden die verwendeten Messaufbauten, Methoden und Simulationen vorgestellt. Im dritten Teil werden die erzielten Ergebnisse aus den Lorentzwinkelmessungen, den Teststrahluntersuchungen sowie der Anwendung des Simulationsmodells auf das neue Modulkonzept vorgestellt.

Contents

Part I.

Introduction and basics

1 Introduction

The Large Hadron Collider at the European Organization for Nuclear Research – CERN – is the world's largest particle accelerator. During the successful first run of the LHC from 2010 to 2013, the last remaining particle of the Standard Model of Particle Physics – the Higgs boson – has been discovered [Cha+12].

In the coming years, the LHC will be upgraded and improved. In 2023, the "high luminosity" phase will start. The instantaneous luminosity will be increased by a factor of five compared to the LHC design luminosity. This improvement is a challenge for the detectors. The strip tracker of the CMS Experiment is about to be replaced in 2022 completely for the following reasons

- higher track density,
- track trigger and
- radiation damage.

To cope with the higher track density, the strip length and strip pitch will be reduced and hence more channels have to be read out. To reduce the amount of data that has to be transmitted out of the detector, a new binary readout chip is being developed. In contrast to the currently used analog readout, signal level information is being compared to a threshold already by the readout chip. Only binary hit information is passed out to the data acquisition system. Knowing the properties of the charge clusters on the sensor after a particle hit is crucial for the proper operation of the binary readout. A key aspect has been the understanding of the influence of the 3.8 T strong magnetic field in the CMS Detector on the sensor response. Due to the Lorentz force, charges created by ionizing particles in the sensor are displaced sideways and are drifting under an angle, before being detected by the readout system.

The increased track density is a challenge for the trigger system. One option to handle the higher rate is to include the tracking detector already at the first trigger stage. To reduce the huge amount of data, only the most interesting particle tracks with high transverse momentum have to be selected by the front-end electronics on the detector module. To do so, a combination

of two closely stacked sensors is foreseen. By correlating the particle hit signals of both sensors, the readout electronics can estimate the bending of the track and with that the momentum of the particle in the magnetic field.

The sensors are degraded due to interactions of the particles with the sensor material. Radiation induced damage reduces the performance of the detector. Besides a reduced signal because of an increase of the full depletion voltage of the sensor and increased trapping of charge carriers in the sensor, also the thermal dissipation due to the increased leakage current will increase and the Lorentz angle will change.

To study all these aspects, the CMS Tracker Collaboration started a campaign to evaluate several different silicon base materials and sensor layouts in order to cope with the increasing demands to radiation hardness and track density. The Institut für Experimentelle Kernphysik of KIT is actively involved in this campaign [Hof13][Ebe13][Fre12][Str12]. In the scope of this thesis, studies to all three aspects have been made by irradiating more than 40 silicon sensors with different design parameters (thickness, pitch, p- and n-bulk doping, float zone and magnetic czochralski silicon, p-stop and p-spray isolation between n-strips). All these sensors were characterized in our semi-conductor lab before and after irradiation. In addition, tests in an electron beam and Lorentz angle measurements in a superconducting magnet were performed.

The obtained information from all these measurements was used to develop a simulation model, which is capable to predict the properties of charge clusters after a particle incident to the sensor. Thereby, the Lorentz deflection due to the magnetic field and the influence of radiation damage is taken into account. Both, a commercial software (Silvaco Atlas) and a much faster home-made simulation have been used.

The thesis at hand is divided into thirteen chapters. Chapter 2 introduces the LHC accelerator complex at CERN and the four main detectors. The upgrade of the accelerator and its impact on the experiments will be presented. Chapters 3 and 4 give a brief overview over silicon as a detector material and the influence of radiation induced damage to its performance as a tracking device will be discussed. The campaign to identify a baseline material for the future CMS Tracker is briefly summarized in chapter 5. In the second part, the used equipment and measurement techniques are introduced in chapter 6. In chapter 7, the performed simulations using the newly developed model and the commercial simulation framework are presented. The third part of the thesis is dedicated to the results of the various measurements. The influence of radiation damage to the electrical properties of the investigated test sensors is summarized in chapter 8. The evolution of the leakage current, the full depletion voltage and the charge collection efficiency with irradiation and annealing is discussed. In chapter 9, the performed Lorentz angle measurements on the test sensors and on the CMS Tracker are presented and the results are discussed in detail. The results of both studies are compared to each other and to the simulation models developed in the course of this thesis. Chapter 10 summarizes the test beam measurements on irradiated multi-geometry sensors. The properties of the charge clusters are discussed and compared to simulation predictions. The influence of the binary clustering algorithm on the cluster properties are outlined in chapter 11, before in chapter 12 the new trigger module concept is investigated. Using the simulation model, the working principle of the concept is examined. The operativeness of the concept to reject low momentum particle hits from the trigger logic is demonstrated and the influence of radiation damage on the trigger performance is investigated.

2

LHC and CMS

2.1 Large Hadron Collider

The Large Hadron Collider is the world's largest particle accelerator. In a 27 km long ring, two proton beams are accelerated to an aimed center of mass energy of $\sqrt{s} = 14\,\text{TeV}$ and are collided at four interaction points along the machine. The LHC is operated by CERN, the European Organization for Nuclear Research, near Geneva in Switzerland. Starting its regular operation in 2010 at a center of mass energy of $\sqrt{s} = 7\,\text{TeV}$, the energy could be increased to $\sqrt{s} = 8\,\text{TeV}$ in 2012. In 2015, after the first long shutdown, energies close to the designed one are anticipated. Figure 2.1 gives an overview of the LHC, located between the Lake of Geneva and the Jura mountains.

To investigate the particle fragments originating from the high energetic particle collisions, large particle detectors have been built at the four collision points. ATLAS and CMS are two general purpose detectors, suitable for detecting many different kinds of physics processes, whereas Alice has been optimized for detecting lead-lead collisions and LHCb is designed as a forward spectrometer for the analysis of the decay of b-mesons.

2.2 Compact Muon Solenoid

The Compact Muon Solenoid detector CMS is shown in figure 2.2. Figure 2.2a gives an overview over the whole detector and illustrates the various subdetectors. Figure 2.2b shows a photograph of the detector during the construction phase. Collisions take place at a rate of 40 MHz in the center of the detector. Particles originating from the interaction pass several subdetectors, each measuring different properties of the particle. The silicon tracker reconstructs the tracks of charged particles, measures the momentum via their bending radius in the magnetic field and is used to reconstruct the interaction vertex of the primary particle collision. Per proton-proton bunch crossing, several primary interactions between different protons occur simultaneously. Following the tracker, an electromagnetic and a hadronic calorimeter determine the energy of particles. All three mentioned subdetectors are located in a strong

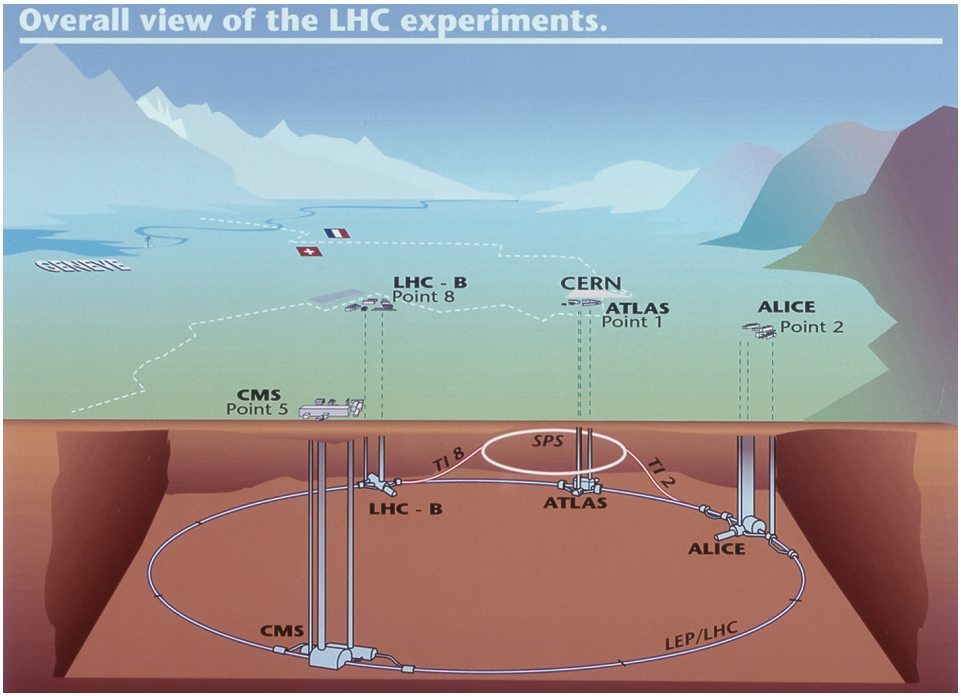

Figure 2.1.: This diagram shows the locations of the four main experiments (ALICE, ATLAS, CMS and LHCb) that take place at the LHC. Located between 50 m and 150 m underground, huge caverns have been excavated to house the giant detectors. The SPS, the final link in the pre-acceleration chain, and its connection tunnels to the LHC are also shown [Acc99].

magnetic field, which bends the tracks of charged particles and by that allows the measurement of the momentum. Outside the superconducting solenoid magnet, muon detectors are interleaved in the iron return yoke of the magnet.

Different particles produce different signatures in the subdetectors, thus allowing particle identification by combining the various contributions. Figure 2.3 shows a transverse slice of the CMS detector and is indicating the signals of muons, electrons, charged and neutral hadrons and photons in the different subdetectors. The silicon tracker reconstructs the path of charged particles emerging the interaction point. The tracks are bend by the magnetic field, the momentum of the particle can be determined from the curvature of the track. The energy of electrons and photons is measured by the electromagnetic calorimeter, where both particle types are slowed to a stop in the transparent lead tungstate crystals of the calorimeter, while the energy of neutrons and charged hadrons is measured in the hadronic calorimeter where the particles are slowed to a stop by the dense materials, producing showers of secondary particles along the way that in turn produce light in thin layers of plastic scintillator material. The amount of light is in both calorimeter types proportional to the energy of the particle. Muons are the only particles that pass also the calorimeters and are detected by the muon chambers outside the solenoid coil.

CMS uses a right-handed coordinate system, with the origin at the nominal interaction point, the x-axis pointing to the centre of the LHC, the y-axis pointing up (perpendicular to the LHC plane), and the z-axis along the anticlockwise-beam direction. The polar angle, θ, is measured from the positive z-axis and the azimuthal angle, ϕ, is measured in the x-y plane. Pseudo-rapidity is $\eta = -\log\tan\frac{\theta}{2}$ [GS12].

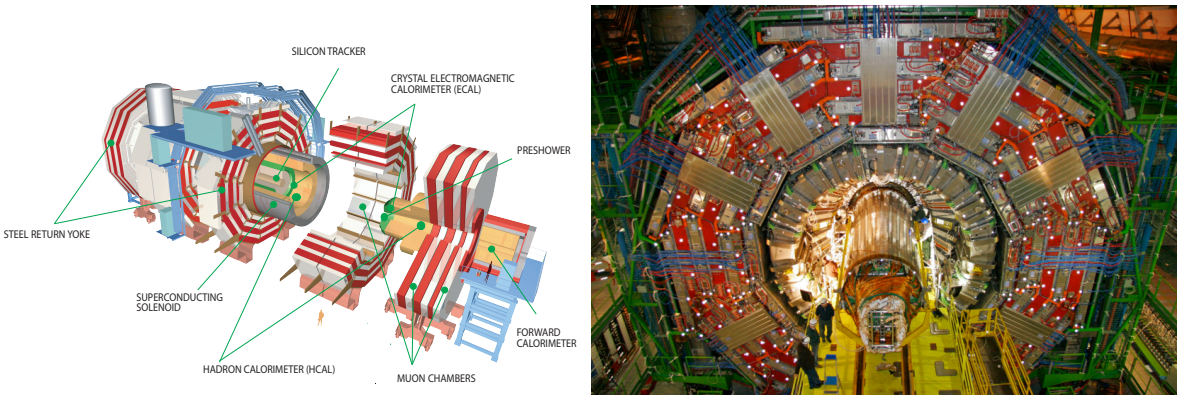

(a) Sketch [BC10]. **(b)** Photo [Hoc07].

Figure 2.2.: Compact Muon Solenoid

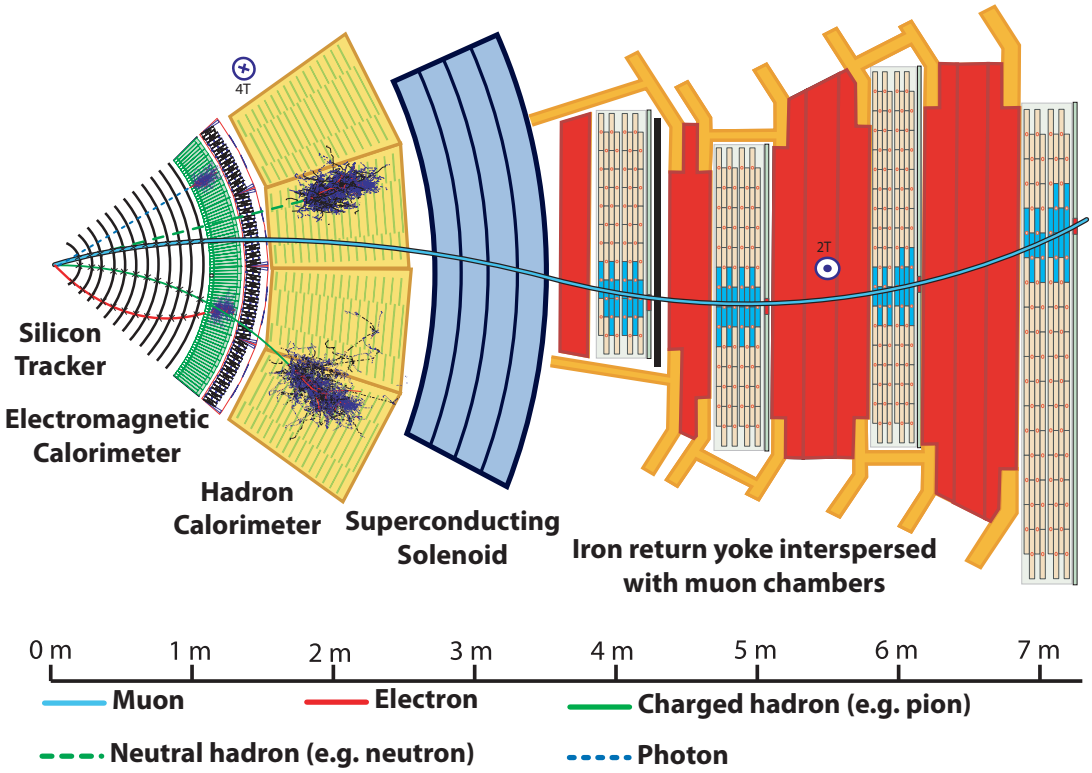

Figure 2.3.: Transverse slice of the CMS detector [Bar11a]

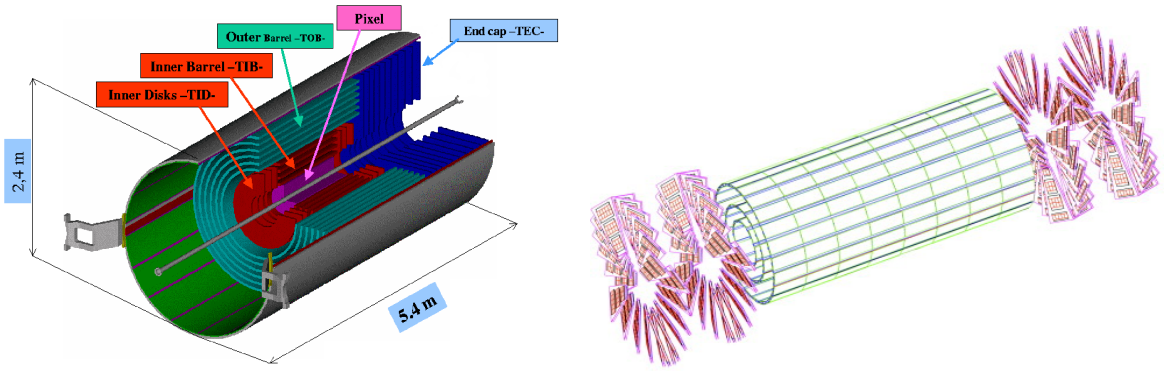

(a) CMS tracker, [Sch03]. **(b)** CMS pixel tracker, [Dom07].

Figure 2.4.: 3d illustration of the CMS tracker and the pixel detector.

2.2.1 Tracker

The silicon tracker is the central part of the CMS detector. It consists of three layers of silicon pixel sensors in the innermost region, followed by ten layers of silicons strip detectors. Charged particles emerging the interaction point are bent in the magnetic field. While passing the silicon sensors of the tracker, the particles generate an ionization signal. By that, each silicon module hit by the particle, either pixel or strip, provides a space point to the particles track and allows its reconstruction.

The silicon sensors of the CMS tracker cover an area of over 200 m^2, which make it the largest all silicon tracker in a high energy physics experiment.

The pixel detector consists of 65 million pixels with a size of 150 µm $\times$ 100 µm, distributed in three barrel layers and two endcap discs per side [Cre03], as shown in figure 2.4b. Due to its pixelated structure, the pixel detector provides 3d space points for particle tracking. Its good spacial resolution in the order of 10 µm [Cre03] allows the reconstruction of secondary vertices created by the decay of relatively long-lived particles, which may travel a short distance before finally decaying. This is especially important in the reconstruction of B mesons.

Following the pixel detector, silicon strip sensors complete the tracker. The strip tracker is subdivided into the Tracker Inner Barrel (TIB), the Tracker Outer Barrel (TOB), the Tracker Inner Discs (TID) and the Tracker Endcaps (TEC), as depicted by figure 2.4a. In total, 15 200 modules with 10 million strips form the strip tracker [CMS]. The strip sensors provide a good spacial resolution perpendicular to the strips. To compensate for the poor resolution along the strips, the two inner layers of TIB and TOB and the corresponding rings in the endcaps are equipped with stereo modules, meaning two modules on top of each other where the sensor of the second module is rotated by 100 mrad. A detailed layout of the strip tracker is shown in figure 2.5. The inner barrel is equipped with 320 µm thick silicon sensors, whereas in the outer barrel 500 µm thick sensors are used. Double sided stereo layers are indicated by double lines, axial only layers by single lines. The strip tracker covers a radial distance from the interaction point of about 20 to 110 cm. Depending on the position in the tracker, the strip pitch is ranging from 122 µm in the inner parts to 183 µm in the outer parts of the outer barrel. The tracker covers the forward region up to a pseudorapidity[1] of $\eta = 2.5$ [Sch03].

[1] $\eta = -\ln\left(\tan\frac{\theta}{2}\right)$

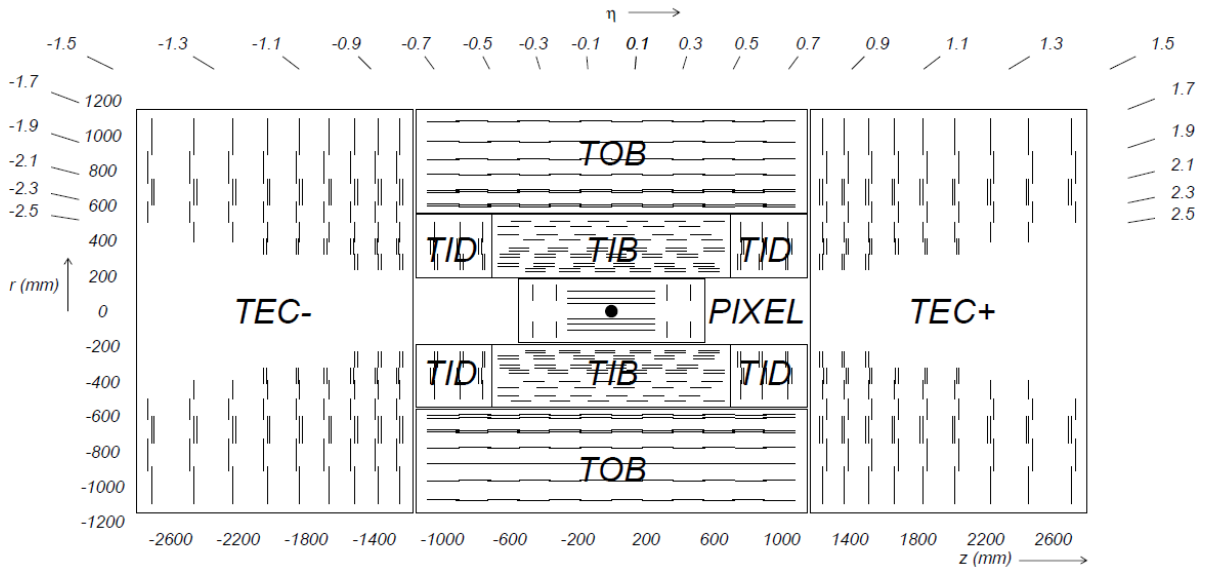

Figure 2.5.: Layout of the silicon strip tracker. A cut through the detector in the rz-plane is shown. The interaction point is located in the center of the detector. The pixel detector is located directly surrounding the interaction point. The strip tracker is divided into TIB, TOB, TID and TEC. The inner barrel is equipped with 320 µm thick silicon sensors, whereas in the outer barrel 500 µm thick sensors are used. Double sided stereo modules are indicated by double lines, single sided modules by single lines. The strip tracker covers a radial distance from the interaction point of about 20 to 110 cm, [CMS08].

Figure 2.6 depicts an event display during a normal run of the LHC at center-of-mass beam energy of $\sqrt{s} = 8\,\text{TeV}$. Twentynine distinct vertices have been reconstructed within a single crossing of the LHC beam [CMS12], demonstrating the good performance of the current tracker.

2.2.2 Solenoid

The magnet is the central device around which the detector is built. It is a superconducting solenoid coil, creating a 3.8 T strong uniform magnetic field, in which the tracker and the calorimeters are embedded. The strong magnetic field bends the tracks of charged particles and together with the good spacial resolution of the tracker ensures a good momentum resolution of high momentum particles. With its 6.3 m cold bore and a length of 12.5 m [CMS08], it is the largest superconducting magnet ever built.

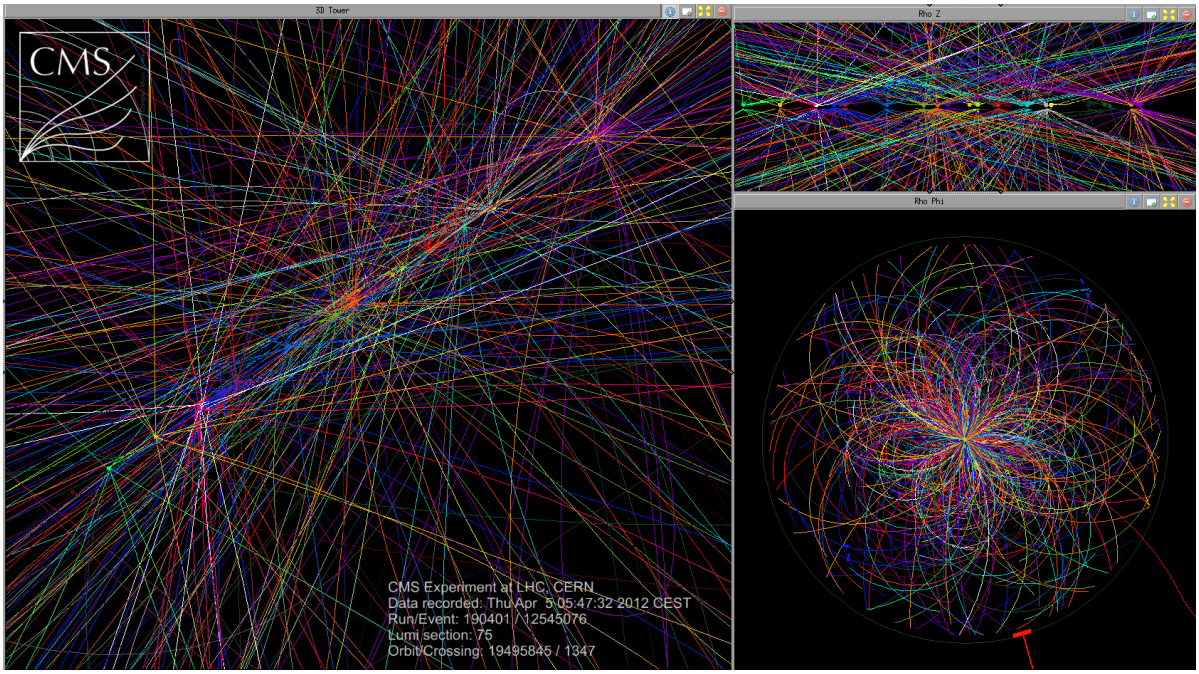

Figure 2.6.: Magnified view of an event display showing that 29 distinct vertices have been reconstructed corresponding to 29 distinct collisions within a single crossing of the LHC beam [CMS12].

2.3 Phase 2 Upgrade

The LHC is planned to be upgraded to allow operation at instantaneous luminosities in the order of $5 \times 10^{34}\,\mathrm{cm}^{-2}\,\mathrm{s}^{-1}$ after 2023 and to reach a total integrated luminosity of up to $3000\,\mathrm{fb}^{-1}$ [HL-LHC]. To be able to cope with the harsh conditions, the CMS Tracker has to be upgraded in terms of radiation tolerance and readout granularity. Therefore, the CMS Tracker collaboration started a campaign to find a suitable silicon base material and sensor geometry. Additionally, the tracker is required to contribute information to the Level-1 trigger, to keep the overall trigger rate at an acceptable level by keeping important events. For both reasons, a replacement of the strip tracker is planned.

2.3.1 Tracker upgrade & contribution to Level-1 trigger

Figure 2.7 illustrates the current baseline layout of the outer part of the new tracker. A quarter of the symmetric layout of the tracker is shown, with the interaction point in the lower left corner. As in the current tracker, a barrel part and an endcap region is foreseen. All modules consist of two silicon sensors in a sandwich configuration. To counteract the high occupancy of the readout channels due to high track densities close to the interaction point at high luminosities, in the inner part up to a radius of 60 cm, the modules are combinations of a pixel and a strip sensor (PS module). In the outer part covering a maximal radial distance of up to 110 cm, the modules consist of two strip sensors (2S module).

Due to the increased luminosity, the trigger rate will increase. Figure 2.8 shows the simulated trigger rate at the different trigger levels as a function of the transverse momentum threshold at the nominal LHC instantaneous luminosity of $1 \times 10^{34}\,\mathrm{cm}^{-2}\,\mathrm{s}^{-1}$. At higher luminosities, the

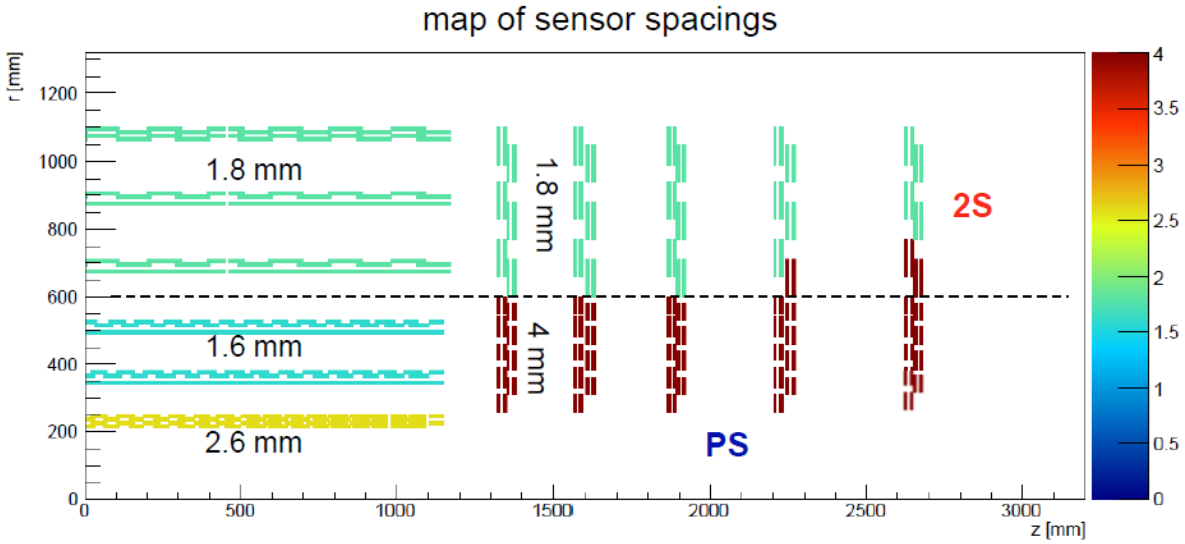

Figure 2.7.: Overview of the current baseline layout of the new outer tracker [Eck14]. As in the current tracker, a barrel part and an endcap region is foreseen. Six barrel layers are approximately at radial distance of 20 cm, 35 cm, 50 cm, 70 cm, 90 cm and 110 cm from the interaction point. The inner three layers are equipped with PS modules, the outer three layers with 2S modules. Five endcap discs per side ensure the tracking in forward direction up to a pseudo-rapidity of $\eta = 2.5$. Sensor spacing ranges from 1.6 to 4 mm.

rate of the Level 1 single muon trigger will exceed 100 kHz and cannot be reduced sufficiently by increasing the transverse momentum threshold [Hal11]. The most effective method to significantly improve trigger functionality for the HL-LHC may be to employ tracking at the earliest stage possible [CMS07]. The major difficulty implementing tracking triggers at Level 1 is that the data volume is too high to transfer all hits off-detector for decision logic. On-detector data reduction is therefore essential [Hal11].

A new type of module is supposed to provide p_{T} information for the Level-1 trigger. Two sensors are placed with a small spacing close to each other in a sandwich configuration, as illustrated in figure 2.9. The readout chips are connected to both sensors and correlate the hit information of both sensors, providing a simple p_{T} discrimination to the Level-1 trigger.

Two types of modules are under discussion for use in the next tracker. The 2S module is built of two strip sensors and will be used in the outer parts of the tracker, whereas for the PS module in the inner layers, one strip sensor is replaced by a pixel sensor, as illustrated in figure 2.10. There, the discrimination will be performed by the pixel readout chip. The performance of the trigger module concept is studied in chapter 12 in more detail.

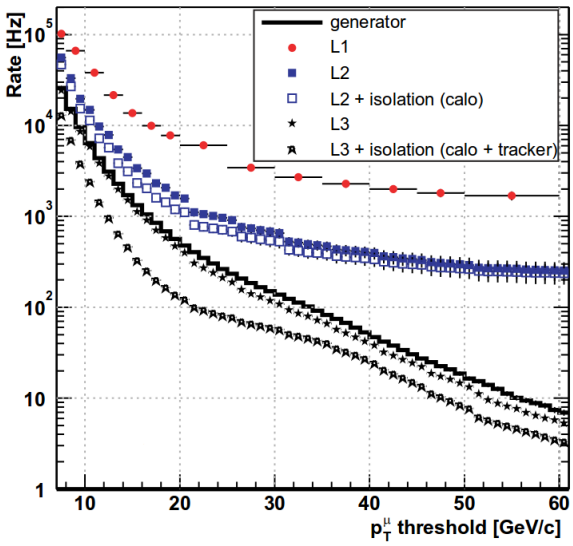

Figure 2.8.: Trigger rate as a function of the transverse momentum threshold for single muons at an instantaneous luminosity of $1 \times 10^{34}\,\mathrm{cm}^{-2}\,\mathrm{s}^{-1}$ [CMS02].

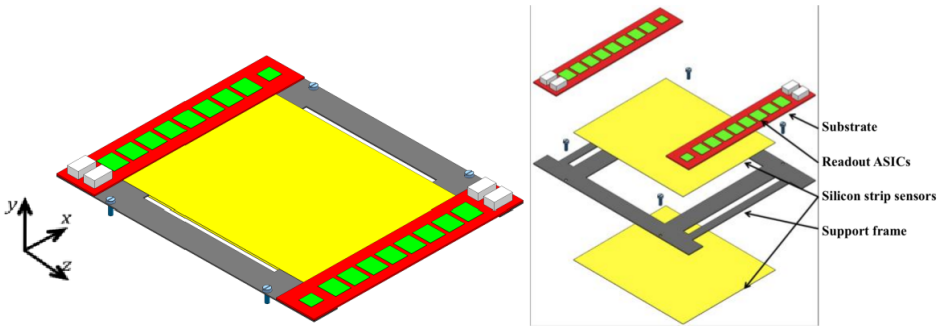

Figure 2.9.: Model of a "2S module", made of 2 Strip sensors read out at the edges by a common set of ASICs. The connection between the sensors and the substrate carrying the ASICs is implemented through wirebonds [Abb11].

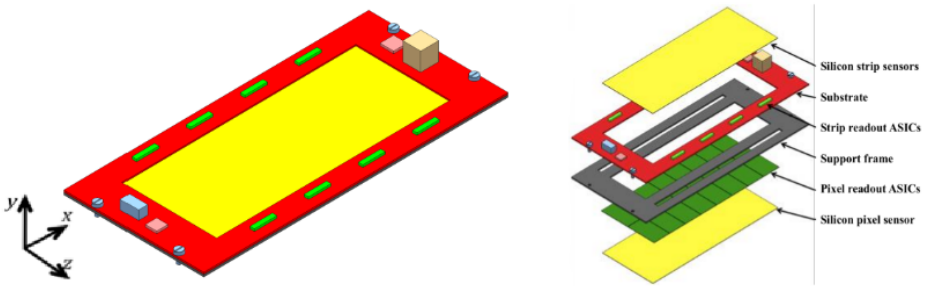

Figure 2.10.: Model of a "PS module". Assembly and connectivity follow the same logic as for the 2S module. In this sketch a single substrate (in red) serves the whole module, carrying the front-end ASICs for the strip sensor, and all the auxiliary electronics for powering and data transmission [Abb11].

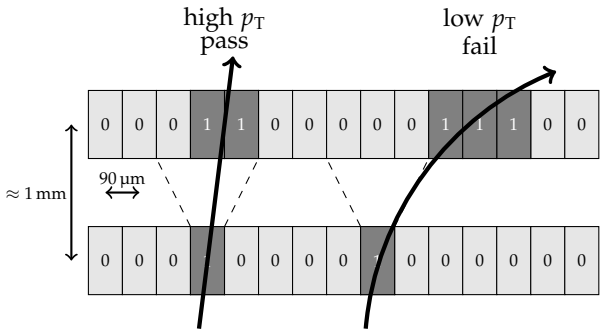

(a) p_T discrimination on the module.

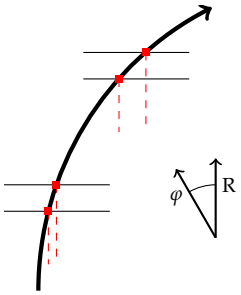

(b) Distance of hits on closely spaced sensors.

Figure 2.11.: (a): Correlation of signals in closely spaced sensors allows the readout chips to discriminate on the tracks transverse momentum and to reject low momentum tracks. The search window on the top sensor around a hit in the bottom sensor is sketched to be three strips. (b): For the same transverse momentum, the distance between the hits in the two sensors depends on the radial position of the module. Due to that, the search window and the sensor spacing have to be adapted in order to obtain the same p_T-cut. Illustrations following Abbaneo [Abb11].

2.3.2 Working principle of the trigger module

In order to provide momentum information to the level 1 trigger, the strong magnetic field of the CMS experiment is exploited. Tracks of charged particles are bend by the magnetic field. Low momentum tracks are bend further than high momentum tracks. Thus, the hits in two closely stacked sensors are displaced by a certain distance depending on the particle momentum. By defining a search window in the top sensor around a hit in the bottom sensor, the readout chips can discriminate on the momentum. To have a good p_T discrimination the search window must be much bigger than the strip pitch [Mer+12]. Only tracks with high momentum are passed out to the trigger. Figure 2.11a illustrates the basic function of the discrimination.

The distance between the hits on the two sensors depends on the radial position of the sensor stack, even for the same transverse momentum, as illustrated in figure 2.11b. To provide a homogeneous trigger threshold over the whole tracker, the spacing between the sensors is varying throughout the tracker in the range of 1.6 to 4 mm, as illustrated by the color coding in figure 2.7. Additionally, the size of the search window has to be adapted.

Theory

The displacement of the particle hit on the second sensor with respect to the first sensor can be calculated easily. Figure 2.12 illustrates the geometry in the Rφ-plane and defines the necessary distances and angles. The bending radius r of the tracks in the magnetic field depends on the particles transverse momentum p_T, and is given by the cyclotron radius:

$$r = \frac{p_T / \mathrm{GeV}\, c^{-1}}{0.3\, q\, B} \tag{2.1}$$

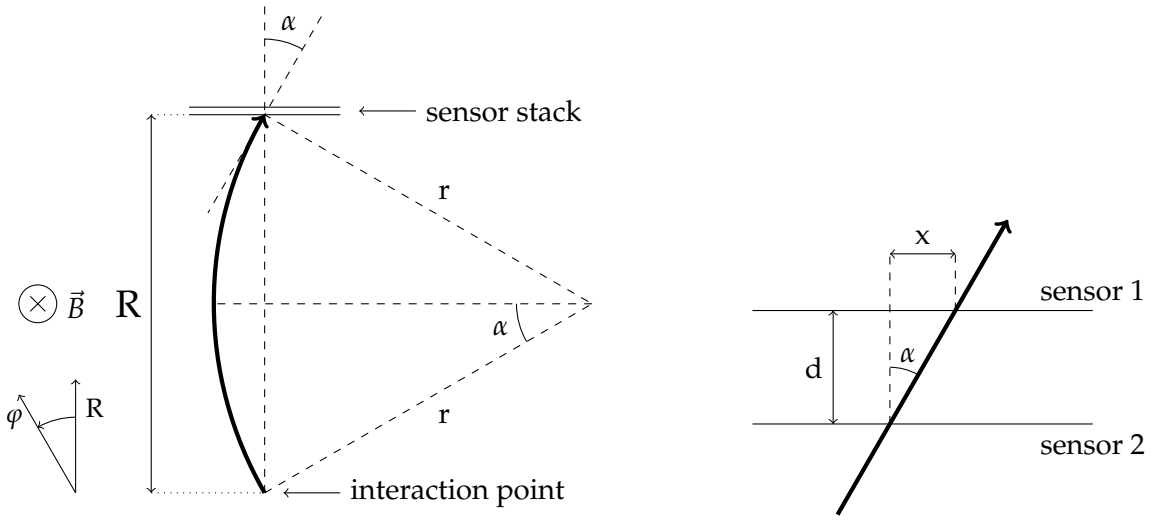

Figure 2.12.: Geometric definitions in the Rφ-plane. Particles with transverse momentum p_T move on circles with radius r, given by the cyclotron motion. They hit a barrel layer at radial distance R from the interaction point at an angle α. The small spacing d in between the two sensors gives rise to a displacement x of the hit on the second sensor.

Particles hit a silicon barrel module at a radial distance R from the interaction point under an angle α given by

$$\alpha = \arcsin \frac{R}{2\,r} = \arcsin \frac{0.3\,q\,R\,B}{2\,(p_T/\mathrm{GeV}\,c^{-1})} \tag{2.2}$$

On short scales, the curvature of the track can be neglected. Therefore, the lateral displacement x on the second sensor with spacing d is given by

$$x = d \tan \alpha \tag{2.3}$$

Using equations 2.2 and 2.3, the trigonometric relation $\arcsin(x) = \mathrm{sgn}(x) \cdot \arctan\left(\sqrt{\frac{x^2}{1-x^2}}\right)$ and by defining $b = \left(\frac{2\,(p_T/\mathrm{GeV}\,c^{-1})}{0.3\,q\,R\,B}\right)^2$, the displacement x is given as

$$x = d\,\frac{1}{\sqrt{b-1}} \tag{2.4}$$

This is valid for tracks that hit the sensor center. Especially in the inner layers where the sensor covers a larger angular slice, the search window has to be corrected for the fact, that the sensor is flat and that even high momentum particles hit the sensor stack at an angle. For that, the search window is centered around the radial projection of the inner hit to the outer sensor. The effect is illustrated in figure 2.13. By applying the offset, the efficiency of the momentum discrimination stays high.

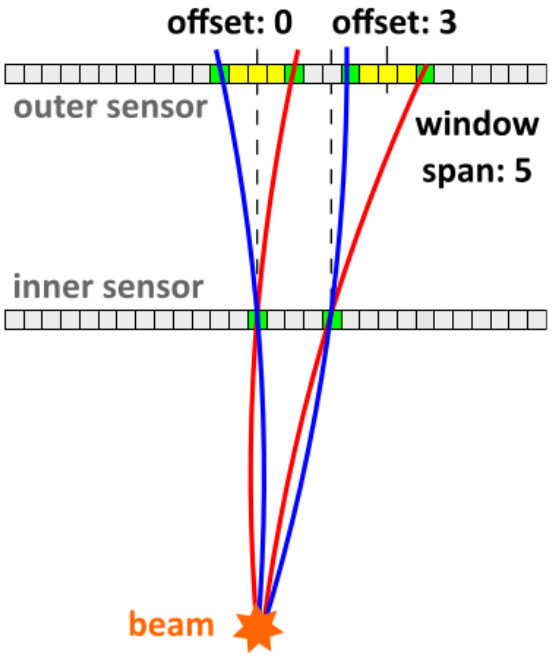

Figure 2.13.: Offset of the search window, [Poz13]. The offset is needed to correct for the fact that the sensors are flat. By applying the offset, the search window is centered around the radial projection of the hit on the inner sensor to the outer one and the efficiency is preserved.

3

Silicon

Most modern high energy physics detectors use silicon sensors in their tracking detectors. Being one of the most abundant elements on earth, silicon is heavily used by the semiconductor industry. Semiconducting materials are elements of the fourth group of the periodic table. Silicon and germanium are most important for industrial applications.

3.1 Basic properties of semiconductors

At $T = 0\,\mathrm{K}$, semiconductors are insulators, because the valence band is populated completely, while the conduction band is empty. At higher temperatures, electrons can be lifted to the conduction band and the material becomes conductive. By doping of the silicon lattice with impurity atoms, the electrical properties of the base material can be altered in a wide range.

As depicted in figure 3.1, solids can be classified into three categories, depending on their electronic band structure:

Metals In metals, the fermi energy lies in the conduction band. This leads to a large concentration of free electrons in the conduction band, even at low temperatures. For that, the conductivity of metals is high.

Insulators The band gap of insulators is large and the conduction band is free of electrons. Electrons can not be excited from the valence band to the conduction band. For that, insulators are non-conductive.

Semiconductors Like in insulators, the conduction band of semiconductors is not occupied at low temperatures. As the band gap is significantly smaller, electrons can be excited from the valence band to the conduction band at room temperature. Therefore, the conductivity of semiconductors depends largely on temperature and impurities and may change over several orders of magnitude.

The band structure of silicon is shown in figure 3.2. The band gap of 1.12 eV is indicated by the gray band. Due to the fact that the maximum of the valence band and the minimum of the

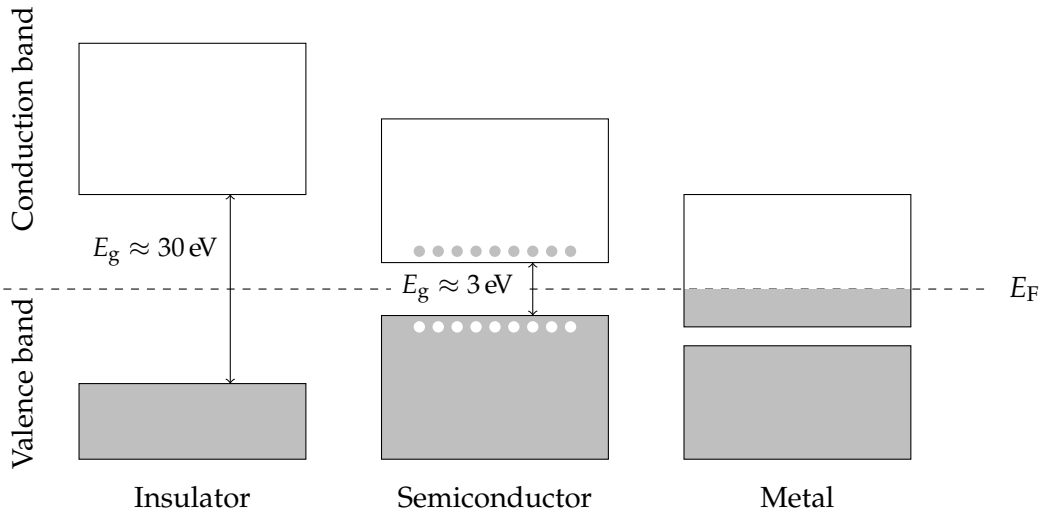

Figure 3.1.: Schematic band structure of an insulator, a semiconductor and a metal. At $T = 0\,\text{K}$ all states up to the Fermi energy E_F are occupied by electrons, all states above E_F are free. In a metal, E_F lies in the conduction band and the conduction band is partly occupied. For that, metals are conductive, even at low temperatures. Insulators and semiconductors have both a completely filled valence band and an empty conduction band at $T = 0\,\text{K}$, as E_F lies in the band gap, they are insulating. In semiconductors, electrons can be excited from the valence band to the conduction band thermally. Therefore, the conductivity of semiconductors depends largely on temperature and impurities and may change over several orders of magnitude. The band gap of insulators is significantly larger, electrons cannot be lifted to the conduction band, and the insulator stays non-conductive.

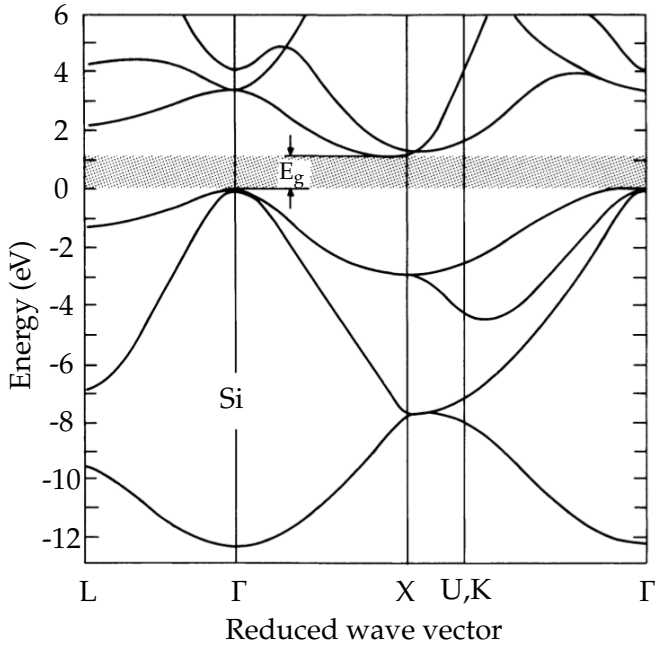

Figure 3.2.: Band structure of silicon, [IL09]. The indirect band gap between the valence band and the conduction band of 1.12 eV is indicated by the gray band. Silicon is an indirect semiconductor, as the maximum of the valence band and the minimum of the conduction band are shifted in momentum space.

conduction band are shifted in momentum space, the transition is indirect. To maintain the conservation of energy and momentum, a phonon has to be excited during the transition of an electron from the valence band to the conduction band and vice versa. The average energy needed to excite an electron to the valence band is therefore larger than the energy value of the band gap.

3.1.1 Doping

To influence the electrical conductivity of a semiconductor, additional impurity atoms are inserted into the lattice by implantation or diffusion. In silicon, mainly elements of the third or fifth group are used, as they provide an additional or a missing electron, as illustrated in figure 3.3. Atoms providing an electron are called donor, atoms providing a hole are called acceptors. The excess electron of donors is not needed for the bonding of the atom in the lattice, it may for that be excited quite easily to the conduction band and participate as a free electron in the conduction of electric current. Acceptors provide only three electrons. For a proper bond in the silicon lattice, four electrons are needed. The missing electron comes from another silicon-silicon bond, where now an electron is missing. The missing electron moves through the lattice as if it was a positive charge carrier. Due to that, the implantation of e.g. a phosphor atom creates a mobile positive charge or a hole, which also participates to the conductivity. In opposite to an intrinsic semiconductor, due to the doping, one kind of free carriers, either negative or positive ones are more abundant in the material. They are majority carriers. Silicon with added donor atoms is called n-doped, as electrons are the majority carriers, silicon with added acceptors is call p-doped, because holes are majority carriers.

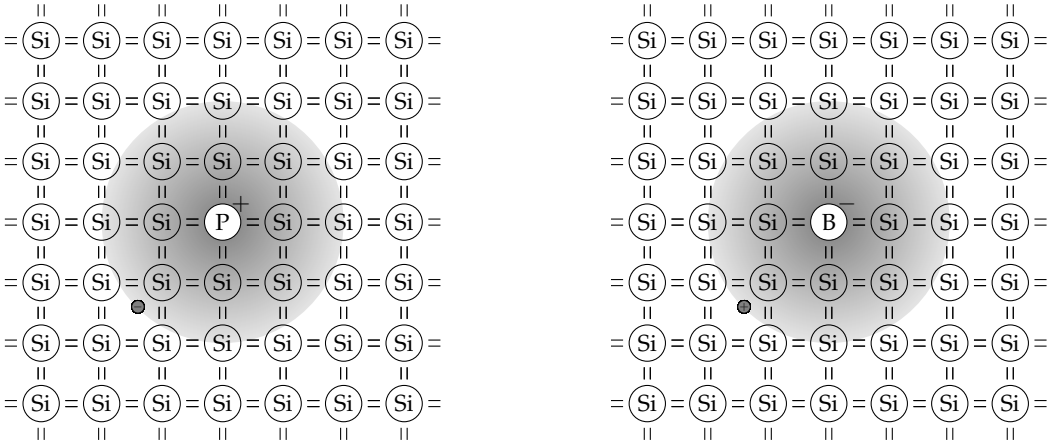

(a) Donor **(b)** Acceptor

Figure 3.3.: Doping of silicon. (a) Donor: the unbound electron moves in the lattice, the fixed phosphor atom is positively charged, (b) Acceptor: the negatively charged atomic kernel of the Boron atom is surrounded by a positive charge. Illustration following Hunklinger [Hun12].

3.1.2 pn-junction

The joint of a n- and a p-doped region in a semiconductor is called pn-junction. Before the joint, the Fermi levels are slightly below the donor or slightly above the acceptor level. After the contact of the n and the p doped region, the Fermi levels are equalized by the diffusion of charge carriers following the concentration gradient. Electrons diffuse to the p region, holes diffuse to the n region. In the opposite doped region, recombination takes place, leaving the now ionized and for that charged impurities atoms in the lattice. They give rise to an electric field which opposes the diffusion, until a state of equilibrium is reached. A depleted space-charge region, free of movable charge carriers has formed. This process is illustrated in figure 3.4. The formation of the electric field is connected to a shift of the electrostatic potential between both regions by the diffusion voltage V_{D}. The diffusion voltage leads to a bend of the valence and conductance bands, as shown in figure 3.5b.

Width of the space-charge region

An important design parameter of a silicon sensor is the full depletion voltage V_{fd}. That is the voltage, that is needed to extend the depleted space-charge region over the total thickness of the sensor bulk. The following derivation is based on Hartmann [Har09] and Sauer [Sau09]. The electrostatic potential $\Phi(x)$ is described by the Poisson equation

$$\frac{\partial^2 \Phi}{\partial x^2} = \frac{1}{\varepsilon_0 \varepsilon_r} \rho(x). \tag{3.1}$$

The charge density $\rho(x)$ is given by

$$\rho(x) = -q \left[n(x) - p(x) + N_A - N_D \right], \tag{3.2}$$

if complete ionization of the dopant is assumed. Here, $n(x)$ and $p(x)$ are the concentrations of electrons and holes. In the space-charge region, they are equal to zero, whereas N_A and N_D are

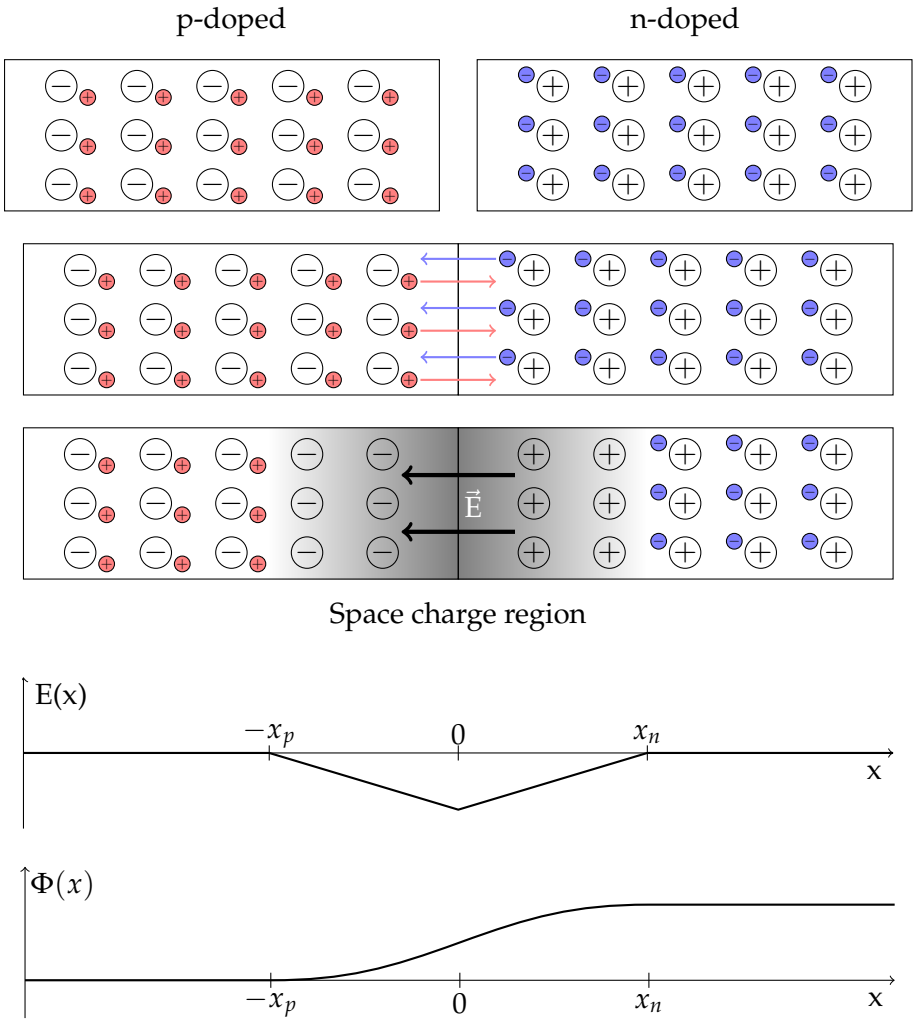

Figure 3.4.: Illustration of a pn-junction. A p-doped and an n-doped silicon bulk material are put in direct contact. Due to the different concentrations of electrons and holes in the different regions, majority carriers diffuse to the opposite doped region, where they recombine. This leads to the formation of a space-charge region without mobile charge carriers. The fixed atomic kernels form an electric field which opposes the diffusion process. In equilibrium, a non-conductive space-charge region has formed.

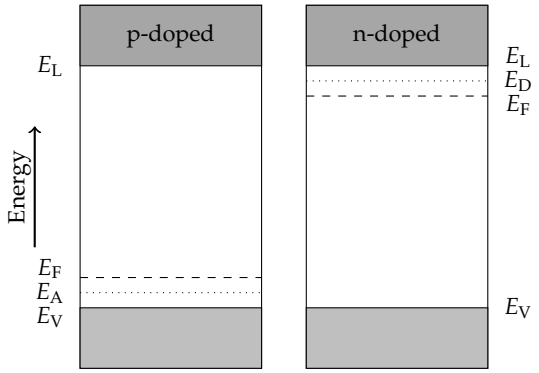

(a) Band scheme before the contact of the n- and p-doped regions.

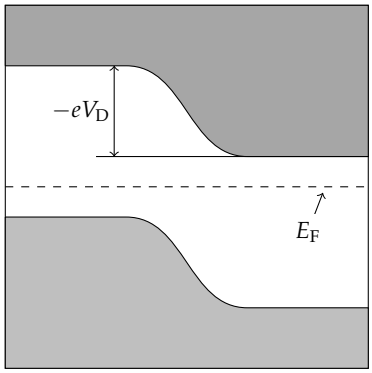

(b) Band scheme after the contact. The valence and conduction band are shifted about the diffusion voltage V_D.

Figure 3.5.: Band scheme of a n- and p-doped semiconductor before and after forming a pn-junction. Before the contact, the Fermi levels are close to the band edges. Due to the diffusion of charges, the Fermi levels are equalized after contact, which leads to the formation of the diffusion voltage V_D and the bending of the bands. Illustration following Hunklinger [Hun12].

the densities of acceptors and donors, respectively. Integration of equation 3.1 results in the strength of the electric field in the n- and p-doped region:

$$E_p(x) = -\frac{qN_A}{\varepsilon_0\varepsilon_r}(x + x_p) \quad \text{for } -x_p \leq x \leq 0 \tag{3.3}$$

$$E_n(x) = \frac{qN_D}{\varepsilon_0\varepsilon_r}(x - x_n) \quad \text{for } 0 \leq x \leq x_n \tag{3.4}$$

with the width of the space-charge region $w = x_n - x_p$. By integrating again using the boundary conditions $\Phi(-x_p) = 0$ and $\Phi(0^+) = \Phi(0^-)$ the potential

$$\Phi_p(x) = \frac{qN_A}{2\varepsilon_0\varepsilon_r}(x + x_p)^2 \quad \text{for } -x_p \leq x \leq 0 \tag{3.5}$$

$$\Phi_n(x) = -\frac{qN_D}{\varepsilon_0\varepsilon_r}\left(\frac{1}{2}x^2 - x_n x\right) + \frac{qN_A}{2\varepsilon_0\varepsilon_r}x_p^2 \quad \text{for } 0 \leq x \leq x_n \tag{3.6}$$

is obtained. The total difference of the potential across the space-charge region defines the diffusion voltage or built-in voltage

$$V_D = \Phi(x_n) = \frac{qN_D}{2\varepsilon_0\varepsilon_r}x_n^2 + \frac{qN_A}{2\varepsilon_0\varepsilon_r}x_p^2. \tag{3.7}$$

Both regions are electrically neutral before the contact. Conservation of charge leads to

$$N_D\, x_n = N_A\, x_p \tag{3.8}$$

which gives a second constraint for x_n and x_p and leads to

$$x_n = \sqrt{\frac{2\varepsilon_0\varepsilon_r}{q}V_D\frac{N_A}{N_D(N_D + N_A)}} \tag{3.9}$$

$$x_p = \sqrt{\frac{2\varepsilon_0\varepsilon_r}{q}V_D\frac{N_D}{N_A(N_D + N_A)}}. \tag{3.10}$$

Finally, the width of the space-charge region is given by

$$w = x_n + x_p = \sqrt{\frac{2\varepsilon_0\varepsilon_r}{q}\frac{N_D + N_A}{N_D N_A}V_D}. \tag{3.11}$$

For the here used sensors, the doping concentrations of acceptors and donors in the different regions differ in several orders of magnitude. Only the doping concentration $|N_{\text{eff}}|$ of the lower doped part is important for the width of the space-charge region. Also an external reverse bias voltage V_{bias} is applied, which adds to V_D. As the external voltage overpasses the diffusion voltage, the diffusion voltage can be neglected. Equation 3.11 simplifies to

$$w = \sqrt{\frac{2\varepsilon_0\varepsilon_r}{q}\frac{1}{|N_{\text{eff}}|}V_{\text{bias}}}. \tag{3.12}$$

The voltage, at which the space-charge region spans the whole sensor bulk thickness d is the full depletion voltage V_{fd}. It is given by

$$V_{\text{fd}} = \frac{q}{2\varepsilon_0\varepsilon_r}|N_{\text{eff}}|\,d^2. \tag{3.13}$$

Capacitance of the space-charge region

Considering the pn-junction as capacitor with two conductive areas separated by a non-conducting dielectric, the capacitance C^* per area is given as

$$C^* = \frac{\mathrm{d}Q^*}{\mathrm{d}V} = \frac{\mathrm{d}Q}{\mathrm{d}w}\frac{\mathrm{d}w}{\mathrm{d}V} \tag{3.14}$$

Using the two assumptions of a large difference in the doping concentration in the two regions and the neglection of V_D as taken for the estimation of the full depletion voltage, the surface charge density Q^* is given as

$$Q^* = \sqrt{2\varepsilon_0\varepsilon_r q\, N_{\text{eff}}\, V_{\text{bias}}}. \tag{3.15}$$

This leads to a capacitance as a function of the applied bias voltage of

$$C^* = \sqrt{\frac{\varepsilon_0\varepsilon_r\, q\, N_{\text{eff}}}{2V_{\text{bias}}}} \tag{3.16}$$

as long as the junction is not fully depleted. Afterwards, the capacitance stays constant, as the space-charge region can not grow further. The doping profile of N_{eff} can be extracted by measuring the capacitance of the space-charge region as a function of the applied voltage by calculating

$$|N_{\text{eff}}| = \frac{2}{A^2\varepsilon_0\varepsilon_r\, q\, \frac{d(1/C^2)}{dV}} \tag{3.17}$$

from the measured capacitance-voltage (CV) characteristics. The slope of the of the voltage dependent portion of the $\frac{1}{C^2}$ curve yields the doping concentration [Spi05].

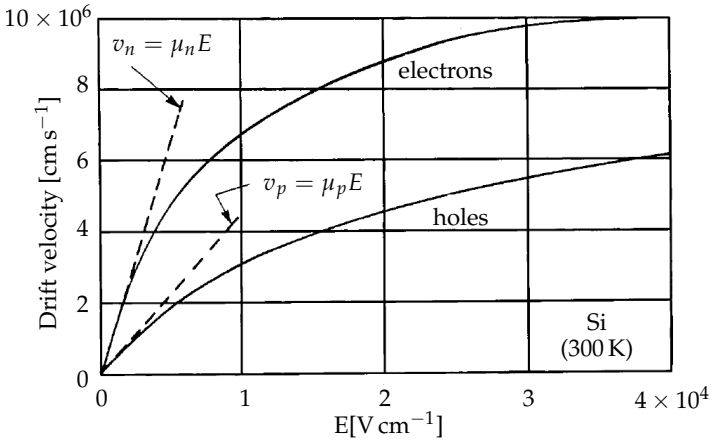

Figure 3.6.: Drift velocity as a function of the electric field. Illustration following Sze [Sze69].

3.2 Carrier transport

Movable charge carriers can be considered as free particles, since they are not connected to a certain lattice position. Their mean kinetic energy is $\frac{3}{2}kT$, the mean velocity at room temperature is of the order of $1 \times 10^7\,\mathrm{cm\,s^{-1}}$. They are scattered at impurity atoms and defects in the silicon lattice and on phonons. The typical mean free path is $1 \times 10^{-5}\,\mathrm{cm}$. This corresponds to a free time of flight of $\tau_c \approx 1 \times 10^{-12}\,\mathrm{s}$ [Lut99].

3.2.1 Drift

Without an electric field in a state of equilibrium, the average motion of the charge carriers due to thermal motion is zero. With the presence of an electric field, the charges are accelerated in between collisions in the direction of the field. The electrostatic force

$$\vec{F} = q\vec{E} + m_e^* \frac{\vec{v}}{\tau} \tag{3.18}$$

leads to a drift of the electron gas with an average drift velocity parallel to the electric field of

$$v_n = \frac{q\tau_c}{m_n} E = \mu_n E \tag{3.19}$$

$$v_p = \frac{q\tau_c}{m_p} E = \mu_p E \tag{3.20}$$

at low electric fields [Lut99]. μ_n and μ_p is the drift mobility of electrons and holes. At high values of the electric field, electrons and holes start losing energy due to the interaction with the lattice and by the emission of phonons or photons. For that, their velocity saturates and does not further increase with the electric field, as illustrated in figure 3.6.

Two effects are mainly contributing to the mobility: ionized impurity scattering and lattice scattering. Depending on the impurity concentration and material temperature, one effect is dominant.

Lattice scattering Above absolute zero temperature, thermal vibrations of the lattice disturb the periodic potential and allow energy to be transferred between the carriers and the

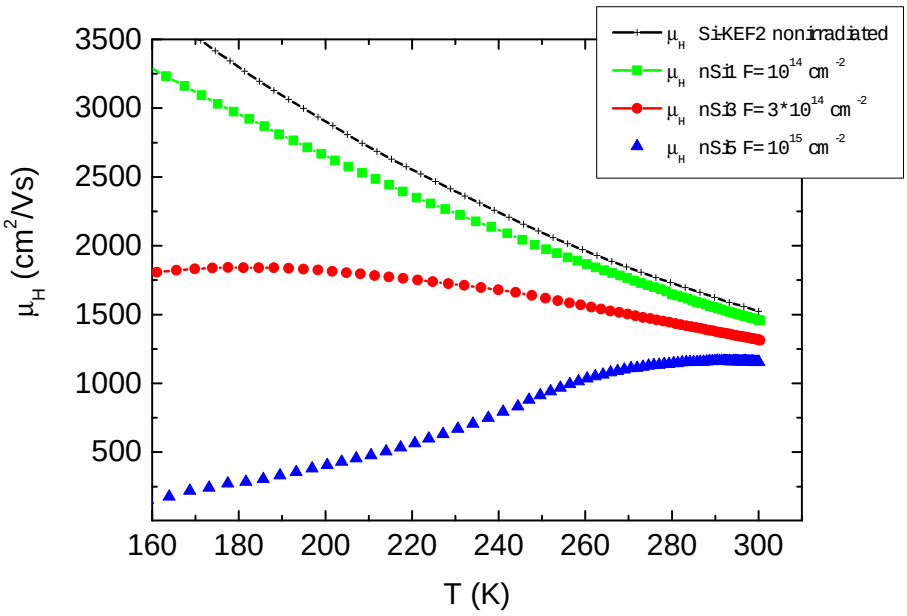

Figure 3.7.: Temperature dependence of the hall mobility of electrons for several irradiated samples obtained by hall effect measurements [Vai+13].

lattice. The amplitude of the vibrations increases with temperature, resulting in an increased probability of scattering carriers and a decreasing mobility. Therefore, lattice scattering dominates at high temperature and at low doping. Lattice scattering is the dominant process limiting the mobility at room temperature [Sin08].

Ionized impurity scattering The carriers experience a coulomb force as they pass an ionized impurity atom. The carrier path is deflected and the mobility decreases. Ionized impurity scattering is the limiting factor of the carrier mobility at low temperatures, as their probability to remain near an ionized impurity and to experience a strong coulomb interaction is larger due to the limited kinetic energy of the carriers. At higher temperatures, the scattering probability decreases because of the faster movement of the carriers [Sin08], resulting in an increase of the mobility with temperature.

Both effects are simultaneously present. Several sources of scattering can be combined to the mobility using Matthiessen's rule:

$$\frac{1}{\mu} = \frac{1}{\mu_{\text{lattice}}} + \frac{1}{\mu_{\text{impurity}}} + \cdots \tag{3.21}$$

At low temperatures, ionized impurity scattering dominates, while at high temperatures, lattice scattering has the most limiting effect on the mobility. For that, the mobility reaches a maximum at an intermediate temperature. Figure 3.7 illustrates the temperature dependence of the hall mobility as obtained by Vaitkus et al. [Vai+13] on several irradiated n-doped silicon samples using the hall effect.

3.2.2 Diffusion

Concentration gradients of charge carrier densities are reduced by diffusion. Due to the unordered random motion of the carriers, more carriers move from areas with high concentration to areas with lower concentration than vice versa. The resulting current is given by

$$\vec{j}_{\text{diff}} = e\left(D_n\vec{\nabla}n - D_p\vec{\nabla}p\right) \tag{3.22}$$

where D_n and D_p are the diffusion constants for electrons and holes and n and p the concentrations, respectively. If the diffusion current and the drift current are carried by the same one type of charge carriers, the diffusion coefficient is linked to the carrier mobility via the Einstein relation [IL09]

$$D_n = \frac{kT}{e}\mu_n \qquad \text{and} \qquad D_p = \frac{kT}{e}\mu_p. \tag{3.23}$$

3.2.3 Lorentz force

In the presence of a magnetic field, besides the electrostatic force, an additional Lorentz force $\vec{F} = q(\vec{v}\times\vec{B})$ acts on the drifting charge carriers. In the case of the electric field and the magnetic field being orthogonal, this leads to a sideways displacement [Lut99]. The drift of the charges is no longer parallel to the electric field, but under an angle, the Lorentz angle. The influence of the Lorentz force to the charge carrier drift will be studied in chapter 9 in detail.

3.2.4 Hall-effect

The Hall effect can be used to measure the mobility of the majority carriers in a uniformly doped semiconducting sample. A magnetic field is applied normal to a current which is drifting through a metal or uniformly doped semiconducting material sample, as illustrated in figure 3.8. The additional Lorentz force F_{L} leads to an accumulation of charge carriers at the remaining two physical edges of the sample until the electric field formed by that compensates the Lorentz force. Then, the charges drift again along the field lines of the initial electric field. The accumulation of charge leads to an external voltage on the device, the Hall voltage U_{H}. It is proportional to the magnetic field [IL09]:

$$U_{\text{H}} = -I\frac{1}{ne}\frac{B}{d} = -IR_{\text{H}}\frac{B}{d} \tag{3.24}$$

with the Hall constant $R_{\text{H}} = \frac{1}{ne}$. With the conductivity $\sigma = n|e|\mu_{\text{H}}$, the hall mobility is given as [GM12]

$$\mu_{\text{H}} = \frac{\sigma}{n|e|} = \sigma|R_{\text{H}}|. \tag{3.25}$$

The Hall mobility μ_{H} differs from the drift mobility μ_{D} by a the Hall factor r_{H} [See91]

$$\mu_{\text{H}} = r_{\text{H}}\,\mu_{\text{D}}. \tag{3.26}$$

The Hall angle is given by the ratio of the Hall field E_x and the applied electric field E_y [See91]

$$\tan(\theta_{\text{H}}) = \frac{E_x}{E_y} = \mu_{\text{H}}\,B_z = r_{\text{H}}\,\mu_{\text{D}}\,B_z. \tag{3.27}$$

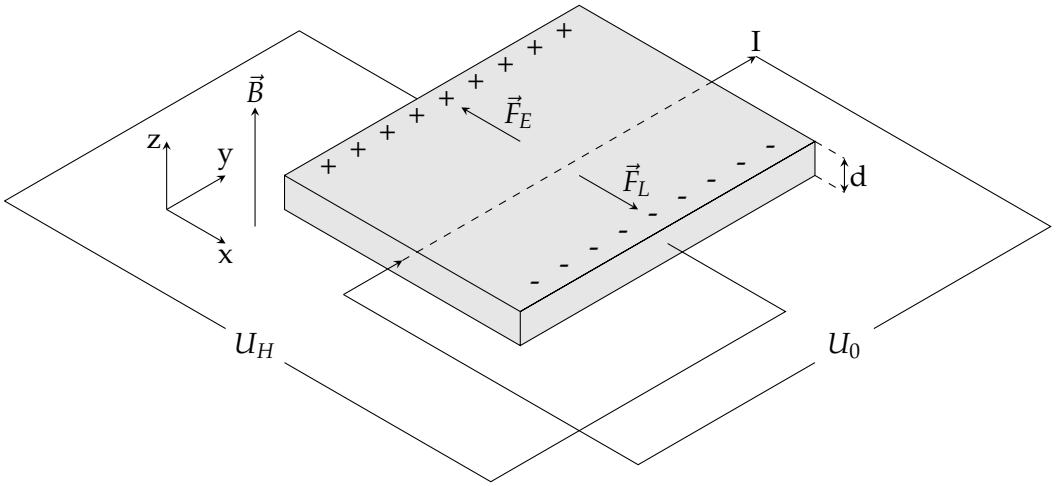

Figure 3.8.: Hall effect: Drifting charges in a uniformly doped piece of semi-conducting material placed in a magnetic field are affected by the Lorentz force. The Lorentz force leads to an accumulation of charge at the edges and the build up of the Hall voltage U_H. The accumulation grows until the formed electric field compensates the Lorentz force.

3.3 Silicon particle detectors

The basic principle of silicon detectors is based on the interaction of either particles or radiation with the silicon material. Due to the interaction, charge carriers are created in the silicon, which can be detected by a readout electronic. Depending on the type and energy of the particle, different effects contribute to the interaction. Charged particles interact with the bulk material via ionization, while low-energy photons interact via the inner photoelectric effect. In silicon, 3.67 eV are needed on average to create one electron-hole pair [Ber+12]. This amount is significantly larger than the size of the indirect band gap, due to the involvement of phonons for energy and momentum conservation. In an intrinsic silicon bulk of the size of 10 cm × 10 cm, the number of free charge carriers is in the order of 1×10^9, the additional about 20 000 charges created by an ionizing particle would be lost. Therefore, the number of free charge carriers has to be reduced by several orders of magnitude [Har09]. This is achieved by using a reverse biased pn-junction for particle detection.

3.3.1 Interaction with charged particles

Charged particles traversing the silicon bulk material lose part of their kinetic energy due to interaction with the shell electrons of the silicon. The average energy loss per track length is given by the Bethe relation [Ber+12][Har09]

$$-\frac{\mathrm{d}E}{\mathrm{d}x} = 4\pi N_\mathrm{A} r_\mathrm{e}^2 m_\mathrm{e} c^2 z^2 \frac{Z}{A}\frac{1}{\beta^2}\left[\frac{1}{2}\ln\left(\frac{2m_e c^2\beta^2\gamma^2 T_\mathrm{max}}{I^2}\right) - \beta^2 - \frac{\delta(\gamma)}{2}\right]. \tag{3.28}$$

In this formula z is the charge of the incident particle, T_max the maximum kinetic energy which can be imparted to a free electron in a single collision, I the mean excitation energy, Z the atomic number, A the atomic mass, N_A the Avogadro's number, m_e the electron mass, c speed of light, r_e classical electron radius, $\beta = \frac{v}{c}$ and $\gamma = \frac{1}{\sqrt{1-\beta^2}}$ and δ density effect correction [Har09].

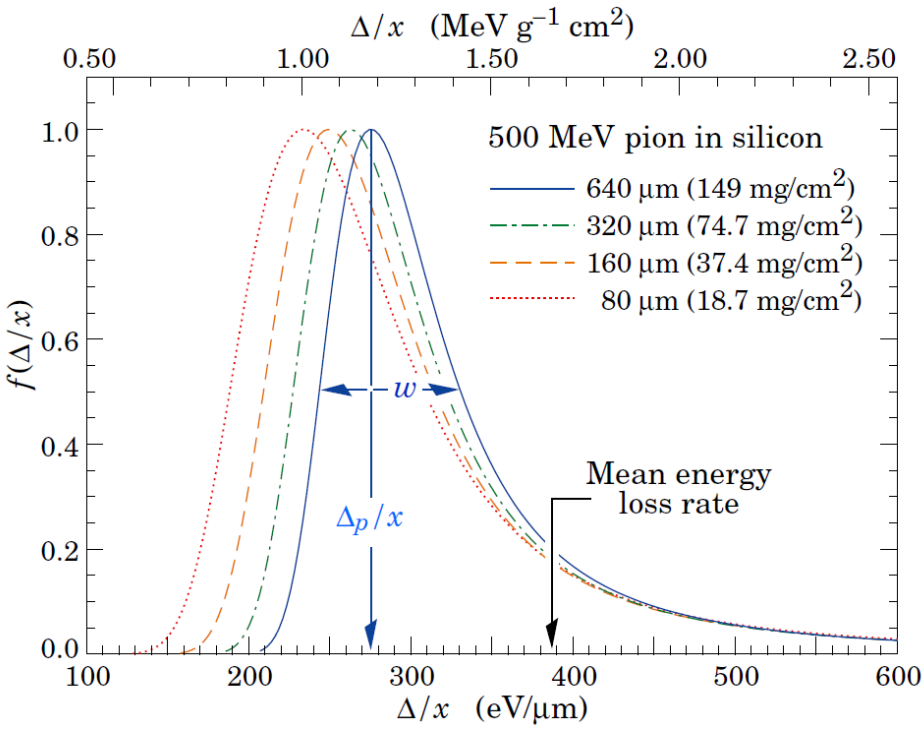

Figure 3.9.: Energy loss of a 500 MeV pion in silicon, [Ber+12]. The most probable value of the energy loss is about 30% lower than the mean energy loss [Har09] and depends on the thickness of the silicon sensor.

In addition to the mean energy loss as given by equation (3.28), statistical fluctuations occur in the ionization process. In a material sample with finite thickness, the number of collisions as well as the transfered energy per collision varies. Depending on the absorber thickness, this leads to an asymmetric landau distribution of the deposited charge with a tail towards higher values. The most probable value of the energy loss is about 30% lower than the mean energy loss [Har09]. Figure 3.9 illustrates the statistical distribution of the energy loss of a 500 MeV pion in silicon.

3.3.2 Interaction with photons

The laser wavelengths used in this work in the range of 680 to 1055 nm correspond to photon energies in the order of 1 to 2 eV. The absorption of this low energetic photons in semiconductors is dominated by the inner photoelectric effect. For high energetic photons and x-rays, also the Compton effect and pair production become important, which are not considered here.

Compared to the outer photoelectric effect, for which an electron leaves the material, the inner photoelectric effect describes the interaction of a photon with an electron in the material for which the electron is excited from the valence band to the conduction band and the photon is absorbed. Due to the different band structure, the absorption process is slightly different in direct and indirect semiconductors.

Direct semiconductor

Photons can excite electrons from the valence band into the conduction band, if their energy $\hbar\omega_\gamma$ is large enough. The photon is absorbed during the process. In direct semiconductors, the energy of the photon has to be at least the size of the band gap, the transition happens vertically in the band scheme, as the momentum of the photon $\hbar k_\gamma$ is small compared to the typical momentum of the electron. The process is illustrated in figure 3.10a. Above the energy threshold given by the band gap, the absorption coefficient of direct semiconductors rises steeply [Hun12]. Electrons with less energy pass the material without being absorbed, the material is transparent.

Indirect semiconductor

In indirect semiconductors the minimum of the valence band is shifted in momentum space compared to the valence band maximum, as illustrated in figure 3.10b. Due to the small photon momentum, no direct transition to the valence band minimum at $\vec{k}_m$ is possible. For the conservation of energy and momentum, a phonon with momentum $\vec{q}$ and frequency ω_q is needed to participate in the interaction. Assuming the minimum of the conduction band at $\vec{k}_m$, the conditions

$$\hbar\omega_\gamma \pm \hbar\omega_q = E_g \qquad \text{and} \qquad \hbar\vec{k}_\gamma \pm \hbar\vec{q} = \hbar\vec{k}_m \tag{3.29}$$

have to be fulfilled. As $\hbar\omega_q \ll E_g$ and $\left|\vec{k}_\gamma\right| \ll \left|\vec{k}_m\right|$, the photon provides the necessary energy and the phonon the necessary momentum. The electron has to interact with the photon and the phonon simultaneously. For that, the indirect process is less likely and the absorption is smaller. As soon as the photon energy is large enough, also the direct transition is possible and the absorption rises steeply [Hun12].

3.3.3 Silicon strip detector

Figure 3.11 shows the basic working principle of a silicon strip detector. Charged particles traversing the silicon sensor interact with the silicon material and create along its track pairs of electrons and holes by ionization of the silicon atoms. These charge pairs recombine on a short timescale, if not separated by an electric field. For that reason, reverse biased silicon pn-junctions are used as particle detectors. The applied bias voltage leads to a depletion of free charge carriers of the silicon bulk and to a formation of an electric field, in which electrons and holes separate and drift to the readout electrodes. This drift is then measurable as a current pulse. To obtain spacial resolution, the pn-junction is segmented in either strips or pixels, providing a one- or two-dimensional sensitivity in the sensor plane. To decouple the readout electronics from the thermally stimulated leakage current, the readout strips are capacitively coupled to the implanted strips. The coupling is achieved by a thin layer of silicon-dioxide separating the aluminum readout strips from the implant.

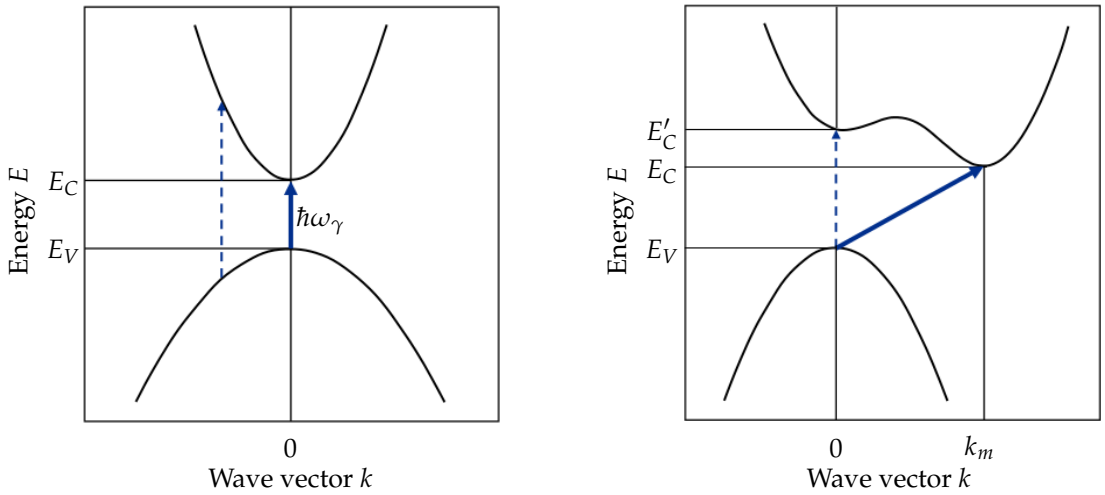

(a) Optical absorption in a direct semiconductor

(b) Optical absorption in an indirect semiconductor

Figure 3.10.: Schematic illustration of the optical absorption in direct and indirect semiconductors. In direct semiconductors, the energy of the incoming photon has to be at least the energy of the band gap. In an indirect semiconductor, a phonon is needed for the conservation of energy and momentum [Hun12].

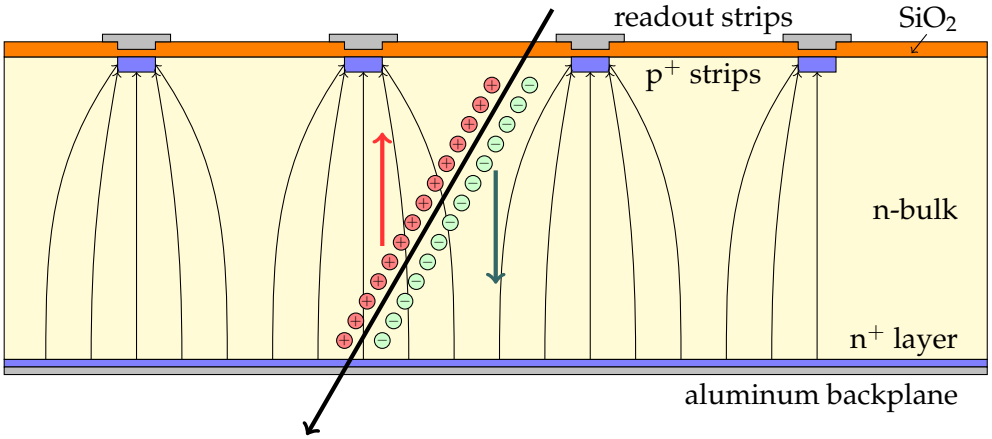

Figure 3.11.: Basic working principle of a silicon strip sensor as particle detector. The sensor bulk is depleted of free charge carriers due to the applied reverse bias voltage and an electric field is formed in the space-charge region. Traversing charged particles create electrons and holes along its track by ionization of the silicon atoms. The charge pairs are separated by the electric field and drift towards the readout electrodes and the sensor backplane. The drift induces a current signal in the ac coupled readout strips, which can be detected by the readout electronics.

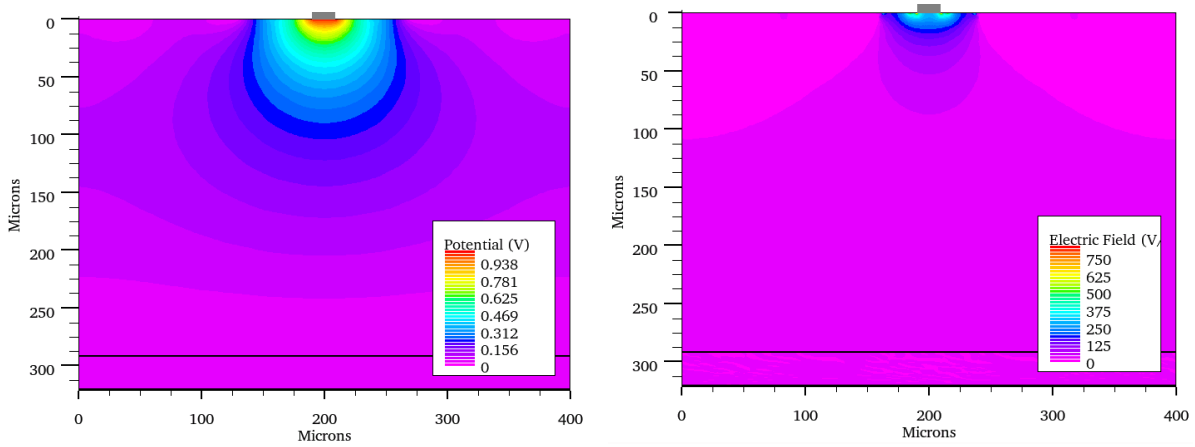

(a) Weighting potential

(b) Weighting field

Figure 3.12.: Weighting potential and weighting field as obtained from a T-Cad simulation of an unirradiated p-bulk sensor at a bias voltage of 300 V.

3.3.4 Shockley-Ramo Theorem

The induced currents in the readout strip by the drifting charges in the silicon bulk can be calculated by using the Shockley-Ramo theorem [Sho38] [Ram39]. The instantaneous current induced to the electrode i is given as

$$I_i = \mathrm{e}\left(\vec{v}\cdot\vec{\nabla}\Phi_{wi}(\vec{x})\right) \tag{3.30}$$

where e is the electron charge and $\vec{v}$ is the instantaneous velocity of the electron [HJ01]. Φ_{wi} is the weighting potential that describes the coupling of a charge at any position to electrode i. The weighting potential applies to a specific electrode and is obtained by setting the potential of the electrode to 1 and setting all other electrodes to potential 0 [Spi05]. If a charge q moves along any path s from position 1 to position 2, the net induced charge on electrode i is [Spi05]

$$\Delta Q_i = q\left(\Phi_{wi}(2) - \Phi_{wi}(1)\right). \tag{3.31}$$

Figure 3.12 shows an example of the simulated weighting potential Φ_{wi} and the weighting field $\left|\vec{\nabla}\Phi_{wi}\right|$ of one strip. The gradient of the weighting potential is highest close to the strip, indicating that the strip is most sensitive to charge drifting close by. While drifting far away from the strip in the sensor bulk, electrons or holes do not contribute much to the induced signal, as the weighting potential is relatively flat.

3.3.5 Noise

Several quantities contribute to the noise of the sensor and the attached readout electronics, as given by Hartmann [Har09]. These are mainly the load capacitance C_d, the leakage current I_L as well as parallel and series resistances R_P and R_D. Noise is expressed as Equivalent Noise Charge (ENC), giving the number of electrons contributing to the noise. The total ENC is the quadratic sum of the individual contributions:

$$ENC = \sqrt{ENC_\mathrm{C}^2 + ENC_{I_\mathrm{L}}^2 + ENC_{R_\mathrm{P}}^2 + ENC_{R_\mathrm{S}}^2}. \tag{3.32}$$

The individual contributions are the shot noise from the leakage current

$$ENC_{I_\mathrm{L}} = \frac{e}{2}\sqrt{\frac{I_\mathrm{L} \cdot t_p}{q_e}}, \tag{3.33}$$

the parallel noise from the bias resistor

$$ENC_{R_\mathrm{P}} = \frac{e}{q_e}\sqrt{\frac{k_\mathrm{B}T \cdot t_p}{2R_\mathrm{P}}}, \tag{3.34}$$

the serial noise from the series resistance, which is mainly the aluminum strip resistance

$$ENC_{R_\mathrm{S}} = C_d\frac{e}{q_e}\sqrt{\frac{k_\mathrm{B}TR_\mathrm{S}}{6t_\mathrm{p}}} \tag{3.35}$$

and the most significant part is the load capacitance

$$ENC_\mathrm{C} = a + b \cdot C_\mathrm{d}. \tag{3.36}$$

Here, a and b are specific parameters for the used preamplifier in the readout chip, whereas e is the Euler number, q_e the electron charge, t_p the peaking time of the shaper and T the operation temperature.

3.3.6 Lorentz angle

Because of the layout of the sensor edges, no accumulation of charge can build up due to the magnetic field. No Hall voltage can build up and for that no electric field compensates the Lorentz force acting on the drifting charge carriers. All charges created in the silicon bulk, either thermally stimulated or by ionization by an incident particle, are deflected by the Lorentz force. The angle under which they drift towards the strips and the backside electrode is called Lorentz angle. It is given by the ratio of the velocities in the direction of the electric field v_z and the orthogonal direction v_x. In first order, the Lorentz angle is similar to the Hall angle as defined in equation 3.27 [Hau00]

$$\tan(\theta_L) = \frac{v_x}{v_z} = \mu_\mathrm{H}B_y = r_\mathrm{H}\,\mu_\mathrm{D}\,B = \tan(\theta_\mathrm{H}). \tag{3.37}$$

4

Radiation damage

The silicon sensors in the CMS Tracker are exposed to a dense particle and radiation field. Interactions of passing particles with the silicon atoms result in defects in the lattice. This defects influence the properties of the detector. In this chapter, the microscopic generation of defects in the silicon bulk and the surface oxide is briefly introduced. Afterwards, the impact on the macroscopic parameters of the sensors is illustrated.

4.1 Microscopic effects

The created defects due to radiation are divided into defects in the sensor bulk and defects in the silicon-dioxide layer.

4.1.1 Bulk damage

Besides the ionizing interaction of incoming particles with the sensor material, non-ionizing interactions may occur. Interactions with the atomic nuclei lead to displacements of atoms from their place in the crystal lattice. A single displacement of an atom to an interstitial position leaving a vacancy on its original place is called Frenkel pair, as illustrated in figure 4.1. The dislocated atom is called primary knock on atom (PKA). It can move further through the lattice where it can interact with further atoms along its path, if enough energy is transferred during the primary interaction. The accumulation of several lattice defects close to each other is called defect cluster.

The type and density of the created defects depends on the type and energy of the incoming particles. Charged hadrons interact mainly via coulomb interactions with the lattice atoms and create mostly point like defects, whereas neutral hadrons interact only via nucleus-nucleus scattering and create mainly cluster defects. Figure 4.2 illustrates a simulation of the defect distribution in a $1\,\mu m^3$ piece of silicon after irradiation with 10 MeV protons, 24 GeV protons and 1 MeV neutrons. The number and spatial distribution of created vacancies depends strongly on the particle type and energy. For better comparison, the particle fluence is usually

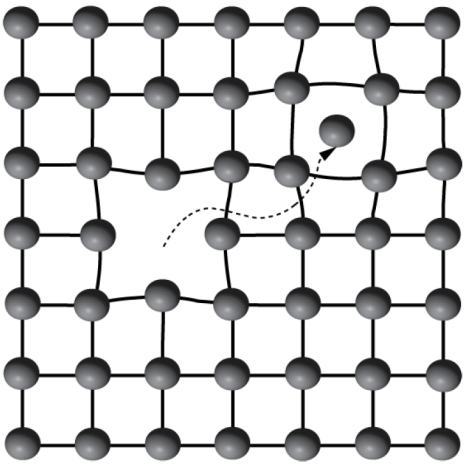

Figure 4.1.: Frenkel pair: A silicon atom is knocked out of its lattice position into an interstitial position, leaving a vacancy at its original position in the lattice [Jun11].

scaled to an equivalent fluence Φ_{eq} creating the same amount of damage as created by 1 MeV neutrons, with $[\Phi_{eq}] = n_{eq}/cm^2$. Therefore, the NIEL scaling hypothesis is used.

NIEL scaling

The non ionizing energy loss (NIEL) is the energy, that a traversing particle loses due to displacement of atomic nuclei from their lattice positions. The created damage in the bulk material is assumed to scale linearly with the NIEL. Figure 4.3 illustrates the displacement damage function $D(E)$ as a function of the incoming particle energy for electrons, protons, pions and neutrons. The damage function is normalized to 95 MeV mb for 1 MeV neutrons. The ordinate represents the damage relative to 1 MeV neutrons. In the following, all particle fluences are normalized to the equivalent fluence of 1 MeV neutrons.

4.1.2 Surface damage

As the silicon bulk, also the silicon-dioxide layer is damaged by ionizing radiation. In contrast to silicon, displacements in the crystal lattice can be neglected, but ionization processes are not completely reversible. Most of the charge carrier pairs created by ionizing particles recombine immediately. Electrons are much more mobile in the oxide layer than holes ($\mu_{e,SiO_2} \approx 20\,cm^2\,V^{-1}\,s^{-1}$, $\mu_{h,SiO_2} \approx 2 \times 10^{-5}\,cm^2\,V^{-1}\,s^{-1}$) [Wun92]. The electrons drift towards a positively charged readout electrode and are removed from the material. The immobile holes remain in the material and move slowly towards the interface of the silicon and silicon-dioxide, where they are trapped in deep levels [Wun92]. By that, a positive charge layer forms directly at the interface. In p-bulk silicon sensors, this leads to an accumulation of electrons from the bulk leakage current at the interface and shortens the n-implanted strips. Isolation of the strips is maintained by the implantation of p^+ (p-stop) surrounding each n^+ strip. The p^+ implants push away the accumulation layer at the Si-SiO_2 interface and reestablish the isolation of the strips. Another possible isolation technique is a diffuse layer of p-dopants close to the surface (p-spray) [Har09]. Figure 4.4 illustrates the two different techniques, as well as a combination of both.

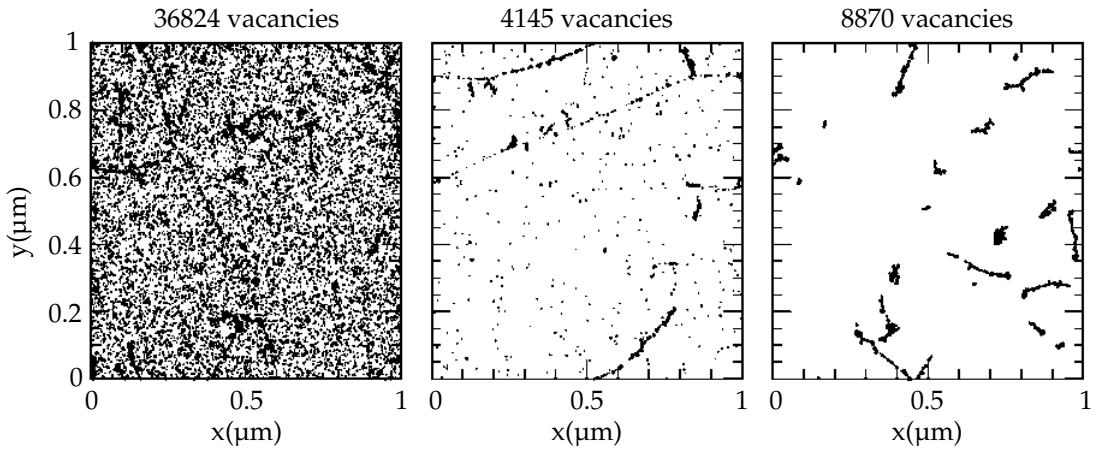

Figure 4.2.: Simulated initial distribution of vacancies produced by 10 MeV protons (left), 24 GeV protons (middle) and 1 MeV neutrons (right) [Huh02]. The plots show a projection over 1 µm depth and correspond to a particle fluence of $1 \times 10^{14}\,\mathrm{cm}^{-2}$.

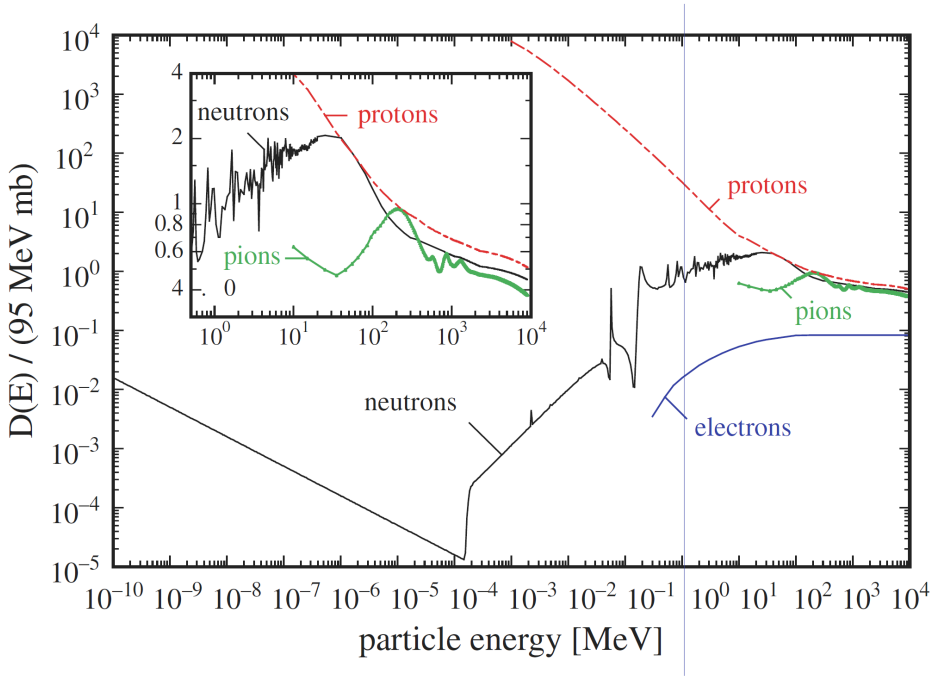

Figure 4.3.: Displacement damage function D(E) for electrons, pions, protons and neutrons, normalized to 95 MeV mb for 1 MeV neutrons. Due to this normalization, the ordinate represents the damage equivalent to 1 MeV neutrons [Mol99].

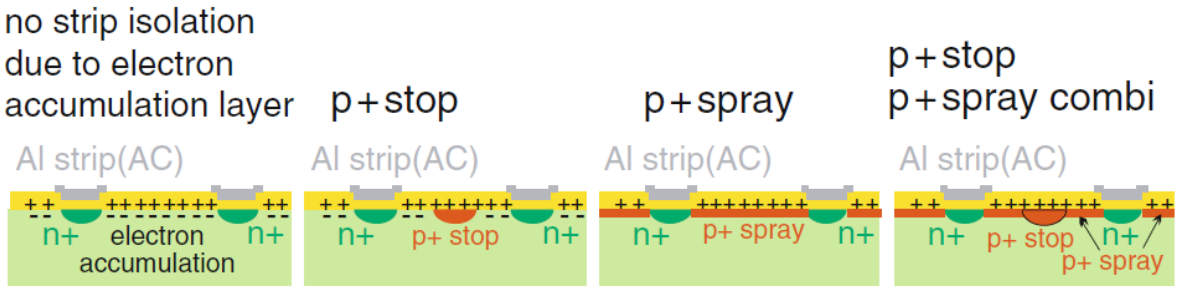

Figure 4.4.: Different strip isolation techniques, illustration by Hartmann [Har09].

4.2 Macroscopic effects

Depending on their energy state in the band gap, defects alter the macroscopic parameters of the sensor in several ways, as illustrated in figure 4.5. Levels close to the center of the band gap serve as centers for carrier generation and recombination. Electrons can be excited from the valence band to the defect level and from there on to the conduction band by thermal stimulation more easily than directly to the conduction band. Due to that, energy states close to the band gap center create free charge carrier pairs and give rise to the increased leakage current after irradiation.

Defects close to the band edges can be ionized easily. If they form charged states, an additional contribution to the effective doping concentration and space charge of the material is given. For that, these defects alter the full depletion voltage of the sensor bulk.

Electrons and holes generated by an ionizing particle can be trapped by intermediate states. They are immobile, do not drift towards the electrodes and do not contribute to the signal. After the detrapping time, which may be longer than the integration time of the readout chip, the carriers are released again and drift to the electrodes. Due to their delayed drift, the contribution to the signal is lost. This effect reduces the charge collection efficiency of the sensor.

4.2.1 Leakage current

The leakage current of a silicon diode or sensor is known to rise linearly with equivalent NIEL irradiation fluence. This has been measured in many different materials and using different irradiation types as shown in figure 4.6. The current increase due to irradiation ΔI per volume V scales linearly with equivalent fluence Φ_{eq}:

$$\frac{\Delta I}{V} = \alpha \, \Phi_{\text{eq}} \tag{4.1}$$

where the proportionality factor α is called current related damage rate [Mol99]. This damage rate α is used to compare the increase of leakage current due to irradiation in the investigated test sensors. To obtain comparable results, the annealing of the leakage current and the damage rate has to be taken into account.

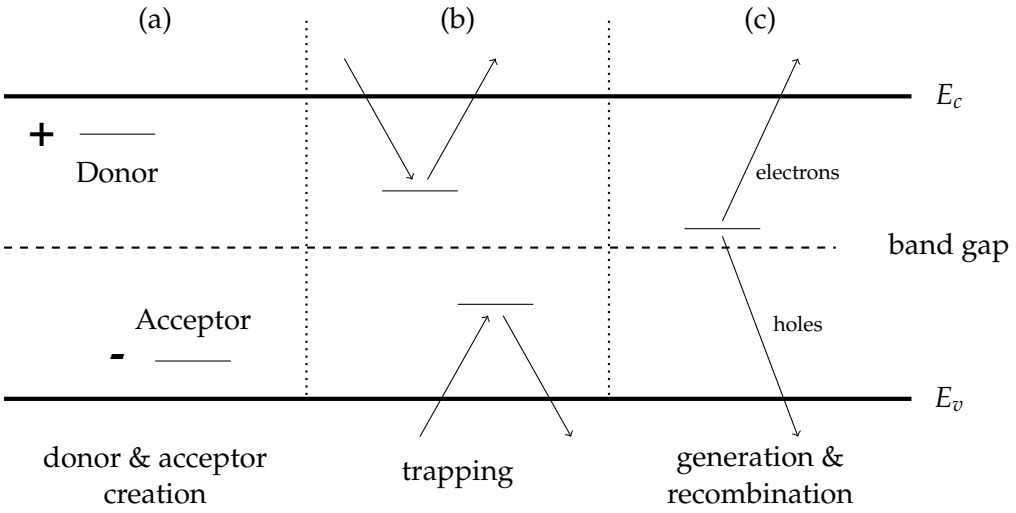

Figure 4.5.: Effects on detector parameters due to defect levels in the band gap. Defects corresponding to levels close to the band edges are mostly ionized and contribute to the space charge (a). States close to the band gap center serve as generation and recombination centers for electrons and holes. These defects are responsible for the increased generation current after irradiation (c). Intermediate states capture electrons and holes and trap them for a certain time. Trapped signal charges can not drift towards the readout electrodes in the integration time and for that do not contribute to the signal (b). Illustration reproduced following Moll [Mol99].

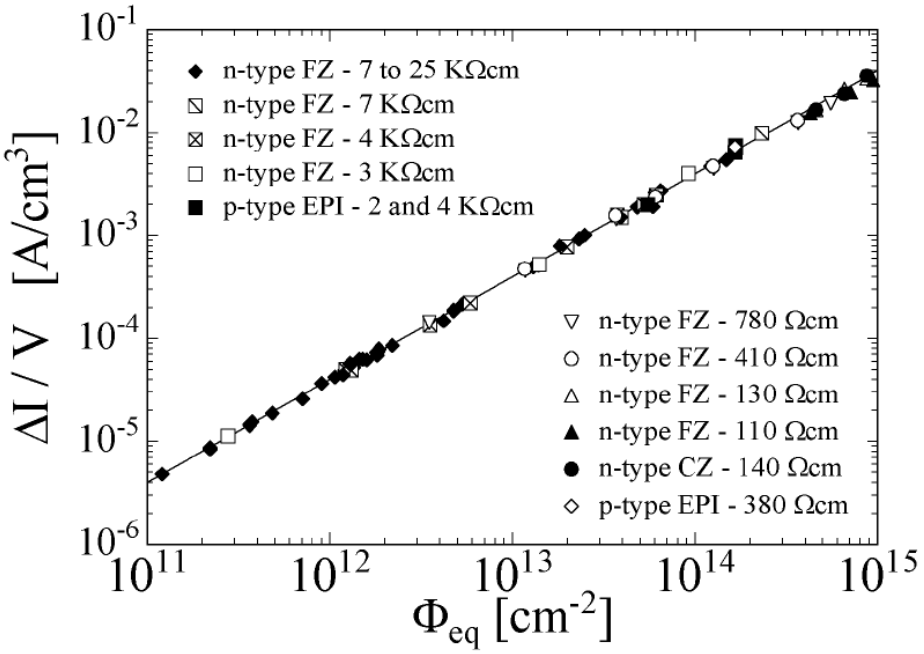

Figure 4.6.: Linear increase of leakage current with irradiation fluence [Mol99]. The increase is independent of the sensor material and its initial bulk resistivity and type of bulk doping.

Temperature scaling

The temperature dependence of the bulk generation current can be described as

$$I(T) \propto T^2 \exp(-1.21\,\mathrm{eV}/2kT) \tag{4.2}$$

both for non-irradiated and irradiated sensors [Chi13]. This scaling has been extracted by Chilingarov [Chi13] from measured leakage currents in the temperature range of -30 to 30 °C and has been found to be valid for all kind of sensors. In this thesis, the leakage currents of irradiated devices have been measured at a temperature of -20 °C. The scaling factor of the measured leakage current to the value at room temperature of 21 °C is according to equation (4.2)

$$\frac{(294\,\mathrm{K})^2 \exp(-1.21\,\mathrm{eV}/2k294\,\mathrm{K})}{(253\,\mathrm{K})^2 \exp(-1.21\,\mathrm{eV}/2k253\,\mathrm{K})} = 64.7$$

The expected value of the damage parameter α at 21 °C after 20 minutes at 60 °C annealing using the parametrization by Moll [Mol99] is $5.01 \times 10^{-17}\,\mathrm{A\,cm^{-1}}$. Scaled to the measurement temperature of -20 °C, the expected value of α is $0.77 \times 10^{-18}\,\mathrm{A\,cm^{-1}}$.

4.2.2 Full depletion voltage

Radiation induced defects may be electrically active and thus contribute to the fixed space charge in the silicon bulk. By that, they have an impact on the sensors full depletion voltage. The evolution of the full depletion voltage has been investigated intensively and has been parametrized in the so called Hamburg Model given by Moll [Mol99]. Figure 4.7 depicts the qualitative behavior of the depletion voltage of a n-bulk sensor under irradiation. During the creation of defects, acceptor-like defects dominate in most material types. Due to that, the created acceptors compensate the donors in the n-bulk and reduce the effective doping concentration. The full depletion voltage of the sensor gets lower and lower.

At a certain fluence point, the created acceptors predominate the donors, and the sensor bulk behaves effectively like it is p-doped. This is called type inversion. After that point, the depletion voltage rises again with further irradiation. The sensor is still operative after type inversion, but the pn junction is now formed at the backside of the sensor and the depletion zone starts growing from there. P-bulk sensors do not undergo type inversion, as acceptors are already the dominant dopant. The depletion voltage rises from its initial value with irradiation. For that, the depletion voltage of p-bulk sensors tends to be higher after irradiation than the depletion voltage of n-bulk sensors of the same thickness.

However, this descriptive picture is no longer completely valid after high irradiation fluences above $1 \times 10^{15}\,\mathrm{n_{eq}/cm^2}$, as shown by Swartz et al. [Swa+04].

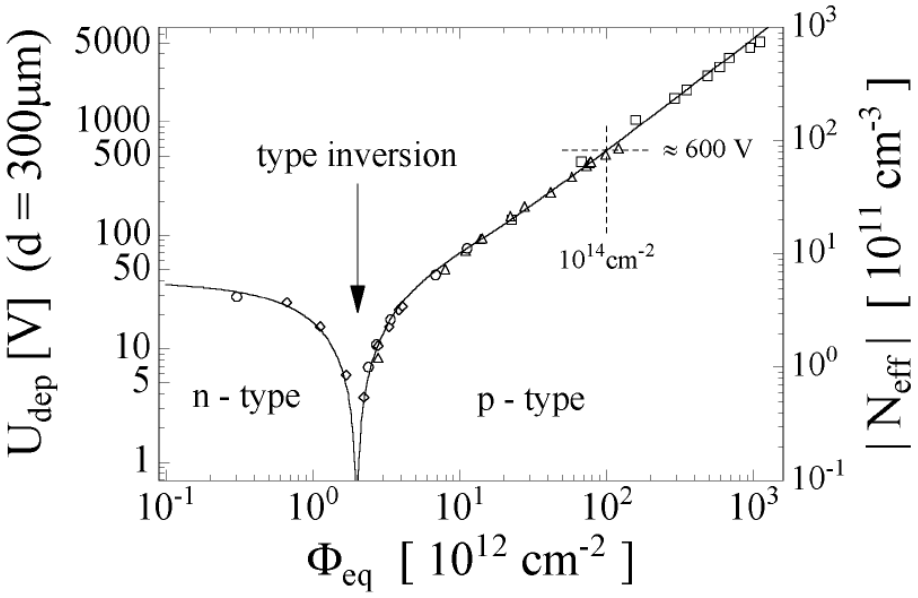

Figure 4.7.: Evolution of full depletion voltage with fluence [Mol99].

4.2.3 Charge collection efficiency

The collected charge is an important parameter for describing the sensors performance. A high charge signal gives rise to a good hit recognition efficiency and resolution. Due to the rise of the depletion voltage and trapping of charge carriers after irradiation of the sensors, the signal obtained from irradiated sensors is usually reduced. Figure 4.8 illustrates the collected signal as a function of the fluence for various irradiated p-bulk sensors as summarized by Affolder, Allport, and Casse [AAC10]. The collected signal starts to be reduced after irradiation with a few $1 \times 10^{14}\,\mathrm{n_{eq}/cm^2}$, leading to a signal of only 5000 electrons after an irradiation of $1 \times 10^{16}\,\mathrm{n_{eq}/cm^2}$.

For comparison of irradiated sensors, their charge signal is scaled to the charge signal of a non-irradiated sensor of the same type. This quantity is called charge collection efficiency.

4.2.4 Annealing

Radiation induced defects in the sensor bulk are not stable, but may drift through the material and recombine with other defects or material impurities. By that, more stable states are created in the silicon lattice, which may have different electrical properties than the initially created defects. The annealing of defects is almost stopped at temperatures below 0 °C but can be accelerated by heat. The annealing behavior of the leakage current and the effective doping concentration have been parametrized by Moll [Mol99] in the Hamburg model.

Annealing of the sensor reduces the damage parameter α and with it the leakage current of the sensor. Figure 4.9 shows the α factor as a function of annealing time at different annealing temperatures, as parameterized by Moll [Mol99]. The annealing of the leakage current is used in this thesis to convert annealing times at different temperatures, by stating that the α factor corresponds to a certain equivalent annealing time at room temperature, independent of the annealing temperature at which it has been reached.

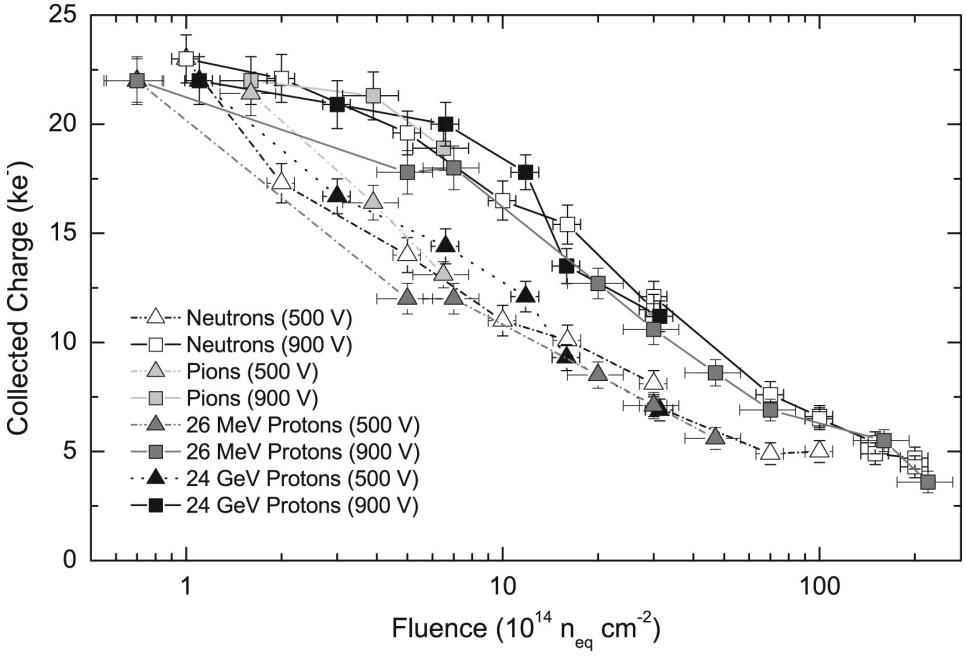

Figure 4.8.: Collected charge at biases of 500 V and 900 V as a function of fluence for n-in-p FZ sensors irradiated with neutrons, 280 MeV pions, 26 MeV protons and 24 GeV protons up to $2.2 \times 10^{16}\,n_{eq}/cm^2$ [AAC10].

Also the effective bulk doping undergoes annealing effects. Here, the parameterization by Moll [Mol99] is divided into three different parts, as shown in figure 4.10. A stable increase of the effective doping concentration, which is independent of the annealing time, forms the first part of the model. A beneficial reduction of the effective doping concentration on a relatively short time scale of a few weeks at room temperature and an increase of the effective doping concentration after longer annealing treatment form the non-stable parts of the parameterization. The interplay of these three factors lead to an initial reduction of the full depletion voltage of the sensor, followed by a steady increase after a few weeks equivalent room temperature annealing.

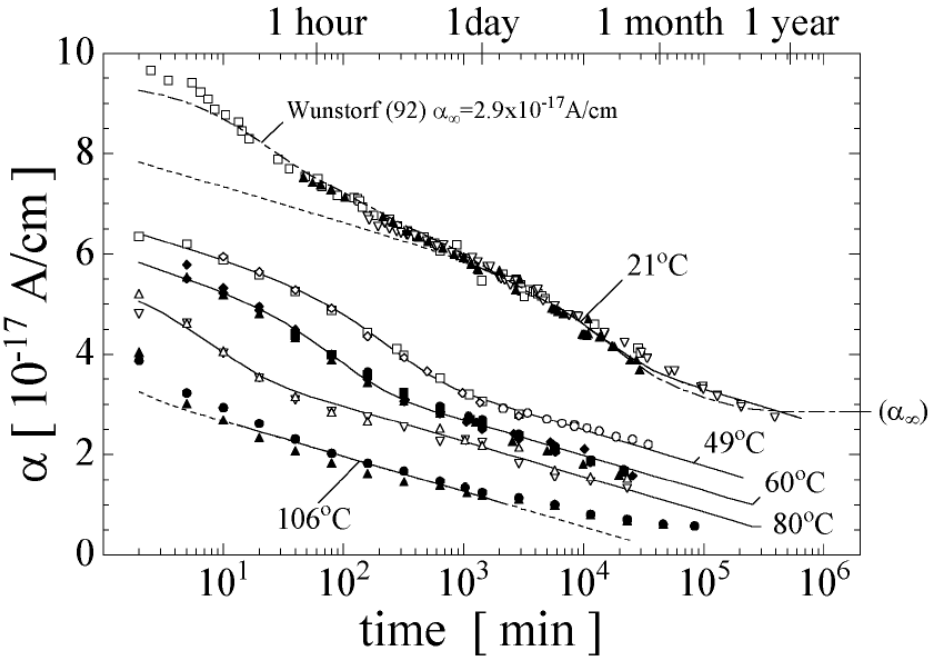

Figure 4.9.: Annealing of damage rate α at different annealing temperatures between 21 °C and 106 °C [Mol99]. Annealing always decreases the damage rate, a saturation is only visible after several thousand minutes of annealing at 106 °C.

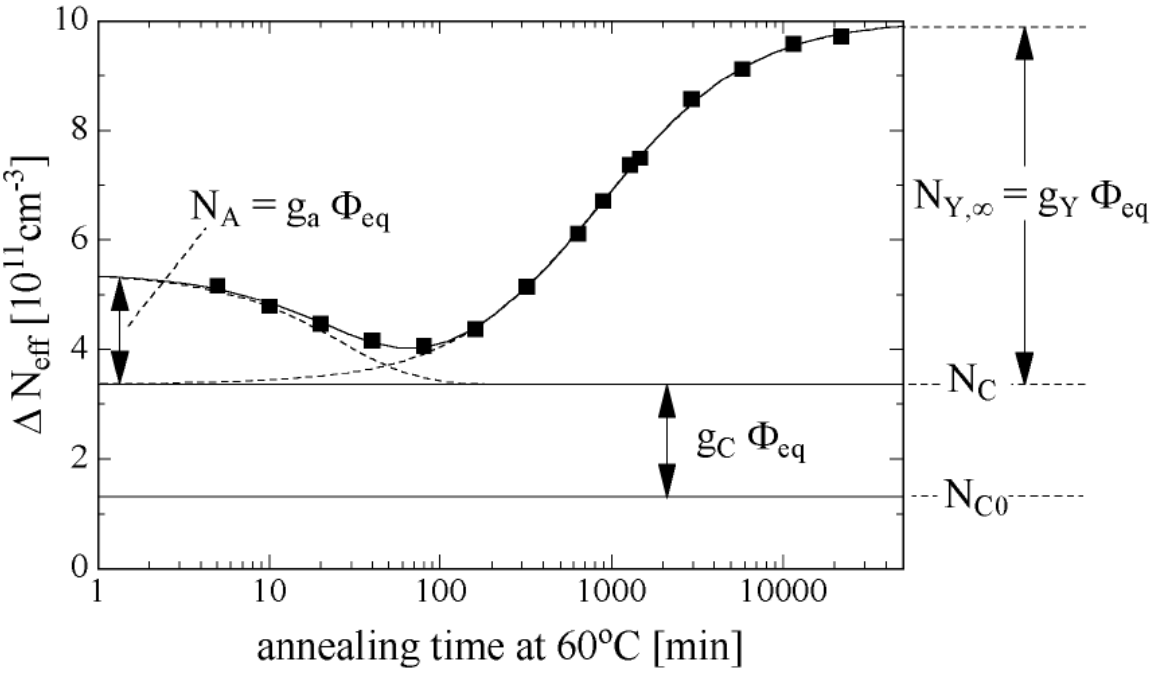

Figure 4.10.: Annealing of the effective doping concentration [Mol99].

5

HPK Campaign

In order to find a suitable silicon base material for the upcoming upgrade of the CMS Tracker after the third long shutdown of the LHC, the CMS Tracker collaboration started a large campaign to investigate the properties of thin single sided silicon sensors. Over 100 wafers carrying several test sensors have been produced by a single company, Hamamatsu Photonics K.K. (HPK) in Japan. After initial characterization, the sensors did undergo an elaborated irradiation and measurement program, ranging from lab measurements in probe stations, TCT- and beta setups at the participating institutes to beam tests at particle accelerators at CERN, Fermilab and DESY.

As the luminosity of the LHC will increase by a factor of five to ten after its extension to the HL-LHC, the new tracker has to cope with much higher radiation levels and track densities. A large part of the campaign is thus dedicated to radiation hardness studies of the various base materials and sensor layouts.

5.1 Sensors

Sensors have been produced on three different silicon base materials, namely float zone (FZ), magnetic czochralski (MCz) and epitaxial (Epi) silicon, in a p-on-n as well as a n-on-p process. On the p-bulk wafers, two different strip isolation techniques (p-stop and p-spray) have been applied.

Several wafers with the same mask design but different silicon base material and thickness have been ordered. Wafer thickness range from 50 to 320 µm in both n and p bulk. Table 5.1 summarizes all available material combinations and the respective sensor thicknesses.

The wafer specially designed for this campaign carries several different test sensors. Simple diodes and standard test sensors are placed on the wafer, as well as several sensors with geometry variations (multi-geometry sensors) and new structures like a sensor with an integrated pitch adapter in the first metal layer and a four-fold segmented strip sensor with edge readout. A schematic layout of the wafer is shown in figure 5.1. A large part is covered by two multi-geometry strip sensors (Multi-SSD or MSSD) and two multi-geometry pixel

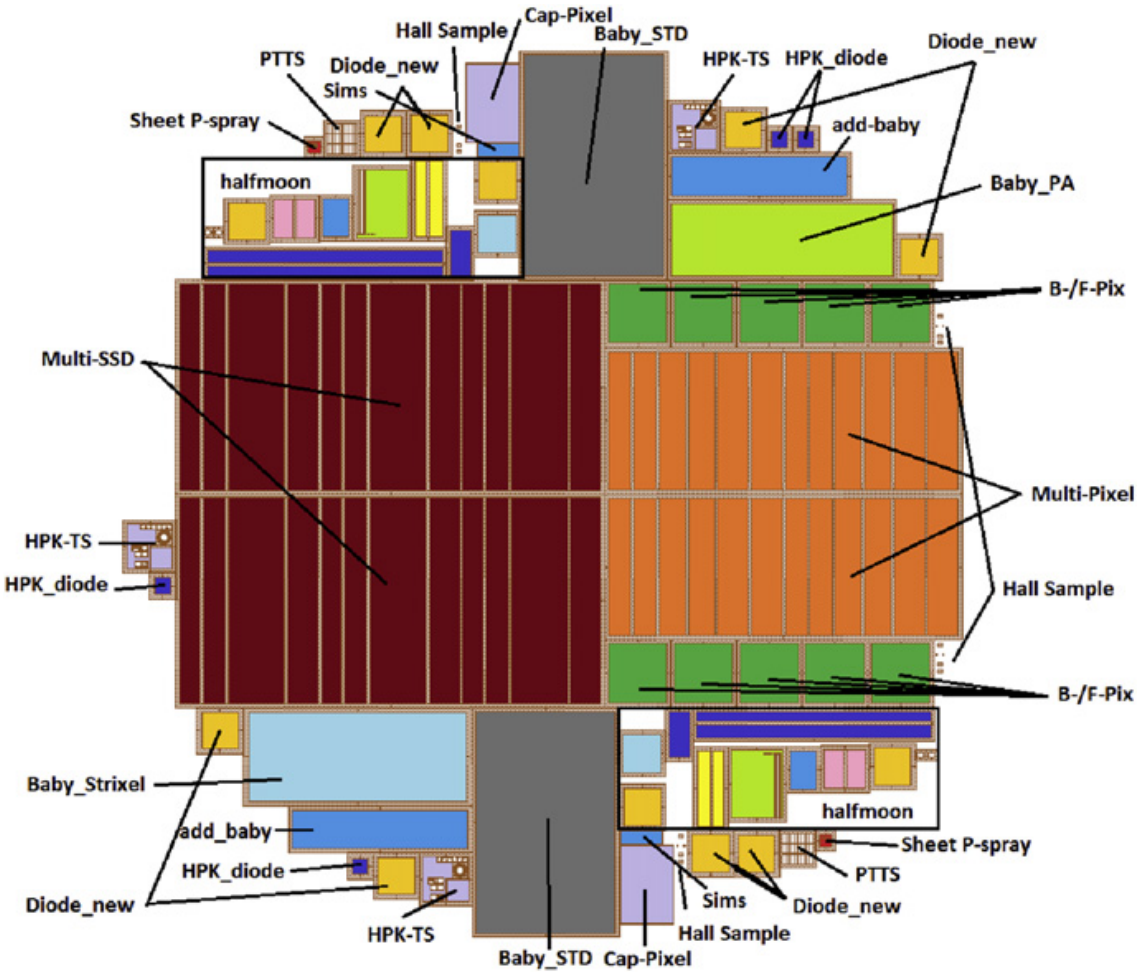

Figure 5.1.: Wafer layout [Hof11]. Several diodes, test sensors and dedicated test structures are placed on a 6 inch wafer. The largest area is covered by two multi geometry strip sensors and two multi geometry pixel sensors in the central part. Smaller test sensors and diodes are placed in the upper and lower periphery.

sensors (Multi-Pixel or MPix) in the center of the wafer. The surrounding area is populated with smaller strip sensors, diodes and test structures.

5.1.1 Naming scheme

The naming scheme used to identify the single structures on the different wafers is

MaterialThicknessDoping_Wafer_TypeOfStructure_PositionOnWafer

The available combinations of material type and thickness are listed in table 5.1. Doping indicated the polarity of the sensor, either p-on-n (N) or n-on-p. The n-on-p wafers were delivered with two different strip isolation techniques, p-stop (P) and p-spray (Y).

Table 5.1.: Overview of the available material types

name	physical thickness / µm	active thickness / µm	on carrier
FZ320	320	320	no
FZ200	320	200	yes
FZ120	320	120	yes
FTH200	200	200	no
MCz200	200	200	no
Epi100	320	100	yes
Epi50	320	50	yes

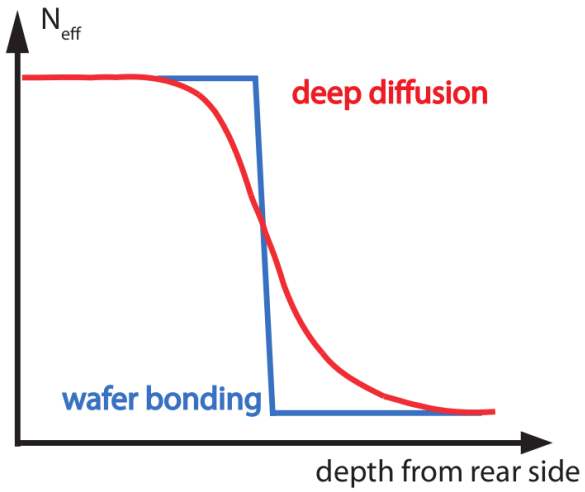

Figure 5.2.: Doping profile of the sensor backside. Comparison between the deep diffusion profile and the usually used wafer bonding. The wafer bonding profile is very steep, whereas the profile obtained by deep diffusion is washed out. Illustration by Junkes [Jun11].

5.1.2 Deep diffusion

For the float zone sensors labeled with FZ, a special process was used by the vendor to reduce the active thickness of the silicon bulk. Usually, thinning of sensors is performed by wafer bonding the sensor wafer to a carrier and thinning the sensor wafer physically to the desired thickness. Here, a process called deep diffusion was applied, where the reduction is achieved by the diffusion of dopant atoms very far into the sensor backside. This highly doped region cannot be depleted and therefore does not contribute to the active sensor volume. A drawback of this technique is the soft transition between the highly doped backside and the active sensor volume, compared to the wafer bonding process, as depicted in figure 5.2. In contrast to that, the sensors labeled with FTH200 are thinned down to a physical thickness of 200 µm.

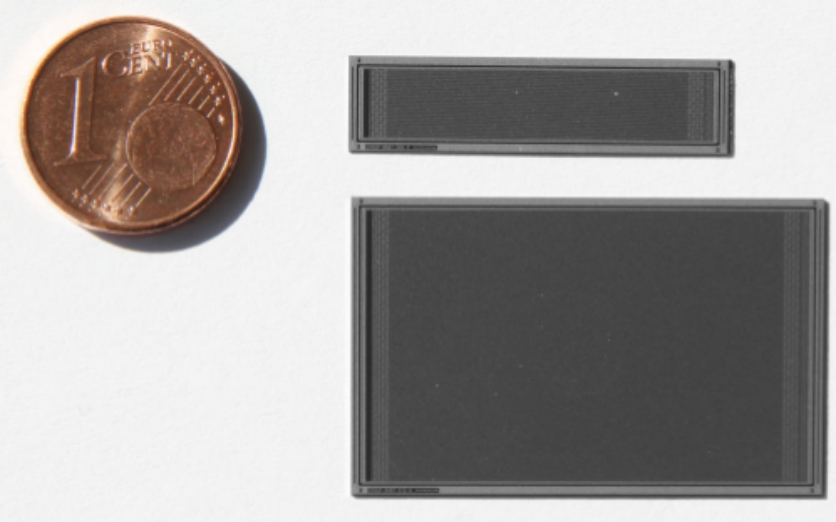

Figure 5.3.: add-baby (top) and Baby_STD (bottom) sensor. For comparison of the size, a 1 cent coin is placed next to the sensors, photo by Randoll [Ran13]. The add-baby sensor has 64 strips, the Baby_STD sensor has 256 strips. Both sensor types have a strip pitch of 80 µm.

5.1.3 Standard sensors

The sensors investigated in this work are mainly the "add-baby" sensors, which are strip sensors in a standard layout with 64 strips and a strip pitch of 80 µm. They are used to study the influence of the magnetic field on the sensor properties, especially the Lorentz angle. This work will be presented in chapter 9. The larger "Baby_STD" sensors with 256 strips at 80 µm pitch were mainly used for charge collection measurements and electrical characterization of the strip parameters after irradiation, as presented by Hoffmann [Hof13]. Figure 5.3 shows a Baby_STD sensor in the bottom and an add-baby sensor in the top part. For comparing the absolute size of the sensors, a 1 cent coin is taken as a reference scale.

5.1.4 Multi geometry sensors

The multi geometry strip sensors (MSSD) allow the investigation of the influence of the strip geometry (pitch and strip width) on the sensor performance. Due to their large surface, they are mainly examined in beam tests, which will be presented in chapter 10. The multi geometry strip sensors consist of 12 regions, each with a different strip geometry. Four different strip pitches (70 µm, 80 µm, 120 µm and 240 µm) and three different width-to-pitch ratios (0.13, 0.23, 0.33) are implemented. Each region consists of 32 strips. Figure 5.4 shows a MSSD sensor while table 5.2 gives a detailed overview of the geometry of the different regions.

Table 5.2.: Overview of the different regions of the MSSD [Hof13]

Region	Pitch / µm	Implant width / µm	Alu width / µm	w/p
1-120	120	17	24	0.133
2-240	240	35	42	0.142
3-80	80	11	18	0.125
4-70	70	9.5	16.5	0.121
5-120	120	29	36	0.233
6-240	240	59	66	0.242
7-80	80	19	26	0.255
8-70	70	16.5	23.5	0.221
9-120	120	41	47	0.333
10-240	240	83	90	0.342
11-80	80	27	34	0.325
12-70	70	23.5	30.5	0.321

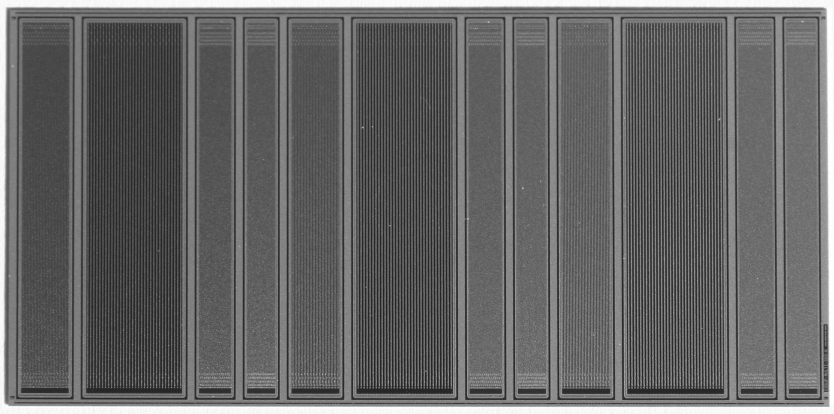

Figure 5.4.: Multi geometry strip sensor. 12 regions with different strip pitch and strip width are placed on one sensor. Each region consists of 32 strips. Photo by Randoll [Ran13].

Table 5.3.: Irradiation steps

Radius / cm	Proton fluence / $1 \times 10^{14}\,n_{eq}/cm^2$	Neutron fluence / $1 \times 10^{14}\,n_{eq}/cm^2$	Total fluence / $1 \times 10^{14}\,n_{eq}/cm^2$
—	0	0	0
60	2.5	4	6.5
20	10	5	15
15	15	6	21
10	30	8	38
7.5	50	8	58

Table 5.4.: Annealing steps

initial 10 min at 60 °C after neutron irradiation initial 10 min at 60 °C after proton irradiation			
Step	Temperature / °C	Time / min	Sum at room temperature / days
1	60	136	27
2	80	15	78
3	80	30	204
4	80	60	417

5.2 Irradiation and annealing

In order to simulate the damage created by passing particles in the CMS Tracker, test sensors are irradiated with protons and neutrons to fluences equivalent to the expected fluences in the detector after ten years of operation. Figure 5.5 depicts the expected particle fluence in the CMS Tracker at a LHC energy of 7 TeV per beam after an integrated luminosity of 1 fb^{-1}. Fluences are plotted separately for charged and neutral hadrons. The chosen irradiation steps in the HPK campaign have been obtained by scaling the particle flux with the NIEL damage function and by extrapolating to the anticipated total integrated luminosity of 3000 fb^{-1} during the HL-LHC lifetime.

In the inner regions, charged hadrons dominate the particle spectrum, while in the outer areas, neutral hadrons are the dominating particles. The variance of the mixing ratio between charged and neutral particles with the radius in the tracker is reflected in the irradiation steps defined in the HPK campaign. Table 5.3 summarizes the irradiation steps in the campaign by listing the expected proton and neutron irradiation fluence for the different radii in the tracker.

Following the irradiation steps, a short annealing of 10 minutes at room temperature is applied to the sensor, before any investigation is performed. This is to suppress the influence of an eventual annealing during handling and transport. After the second irradiation, a detailed annealing study has been performed on the standard sensors. Table 5.4 lists the annealing times and temperatures of the steps performed during this work. For the charge collection efficiency measurements done by Hoffmann [Hof13] and Frech [Fre12], the first step has been subdivided even further.

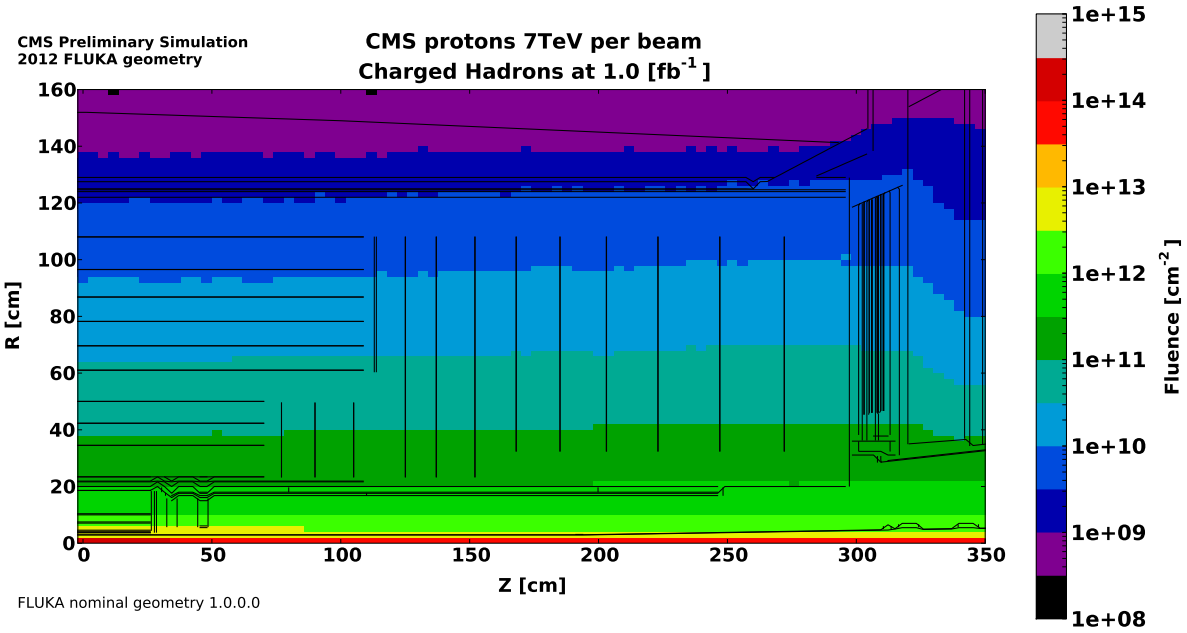

(a) Charged hadrons

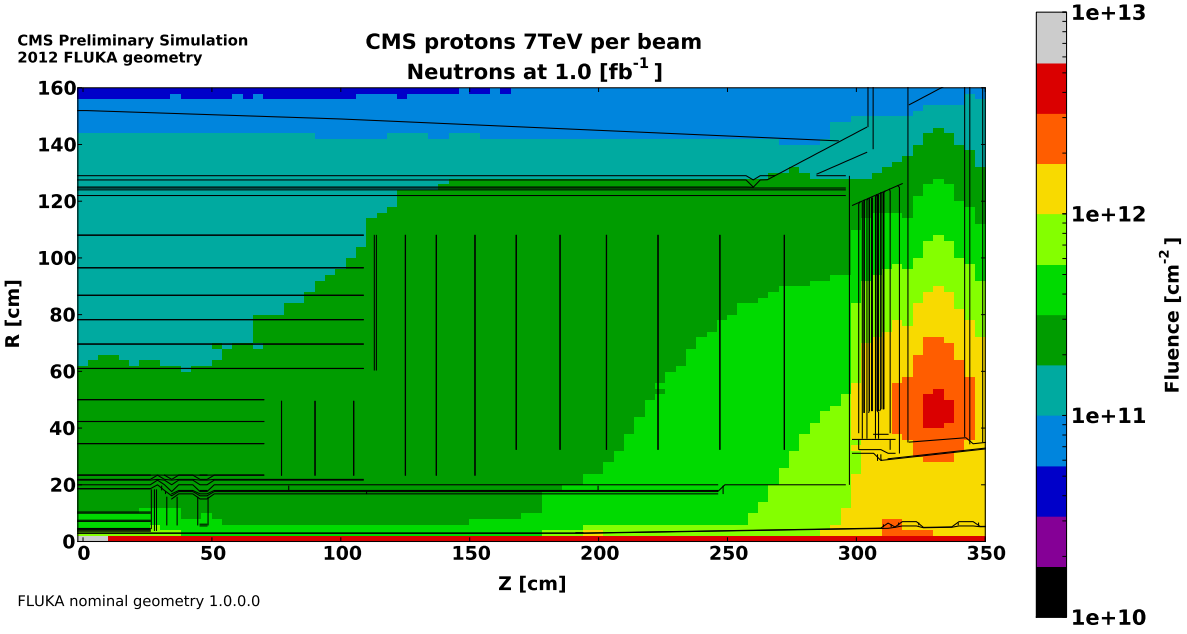

(b) Neutrons

Figure 5.5.: Expected particle fluence in the CMS Tracker per 1 fb^{-1} at an energy of 7 TeV per beam [BRIL2013]. The flux of charged hadrons (a) falls with the radius, while the flux of neutrons (b) is relatively constant. For that, the flux in the inner region is dominated by charged hadrons, while in the outer regions, neutral hadrons dominate.

Part II.

Methods

6

Equipment and Methods

In this chapter, the used measurement techniques and setups are summarized. After a short presentation of the sensor test stations used for the electrical characterization of the sensors, the various methods to measure the Lorentz angle are introduced. The test beam facility at DESY and the performed analysis are outlined afterwards. Finally, the used irradiation facilities are introduced.

6.1 Sensor test stations

6.1.1 Probe station

Electrical characterization of the sensors is performed in a semi-automatic probe station, as shown in figure 6.1. The sensor is placed on a peltier-cooled aluminum jig and the contact pads on the sensor are contacted with probe needles. A relay switching matrix provides the correct connections to the measurement devices. The station allows the measurement of sensor characteristics like leakage current and total sensor capacitance as well as the characterization of individual strip parameters. For that, the cold jig can be moved by stepper motors to allow for a semi-automatic connection of several consecutive strips. The structure of the probe station and the possible measurements are outlined in more detail by Hoffmann [Hof13] and Erfle [Erf09].

(a) Probestation 1 **(b)** Probestation 2

Figure 6.1.: Probestations, photo by Hoffmann [Hof13].

6.1.2 ALiBaVa station

For the characterization of the sensors with particles, the ALiBaVa[1] system [MH09] may be used. It is a fast readout system for silicon strip sensors based on the beetle readout chip used by the LHCb experiment for the readout of their silicon vertex detector. The ALiBaVa system is subdivided into two parts. The daughter board carries two beetle readout chips. It is connected to the mother board via a flat ribbon cable. This allows the mother board to be placed outside the housing of the test station and thus protecting it from humidity and radiation.

Figure 6.2 illustrates the setup at IEKP. The sensor is placed on the daughter board and is connected to the readout chip via wire bonds. A radioactive Sr90 source or a laser is placed over the sensor. Electrons emerging the source and hitting the sensor create charge signals which are read out by the beetle chip. A scintillator below the sensor provides trigger information. The event information is passed on to the mother board, where it is digitized and passed on to the readout computer. For cold operation of irradiated sensors at usually $-20\,°C$, the base plate is mounted on a copper bridge which is cooled by peltier elements. To avoid condensation on the sensor, the box is flushed with dry air.

[1] A Liverpool Barcelona Valencia Readout system

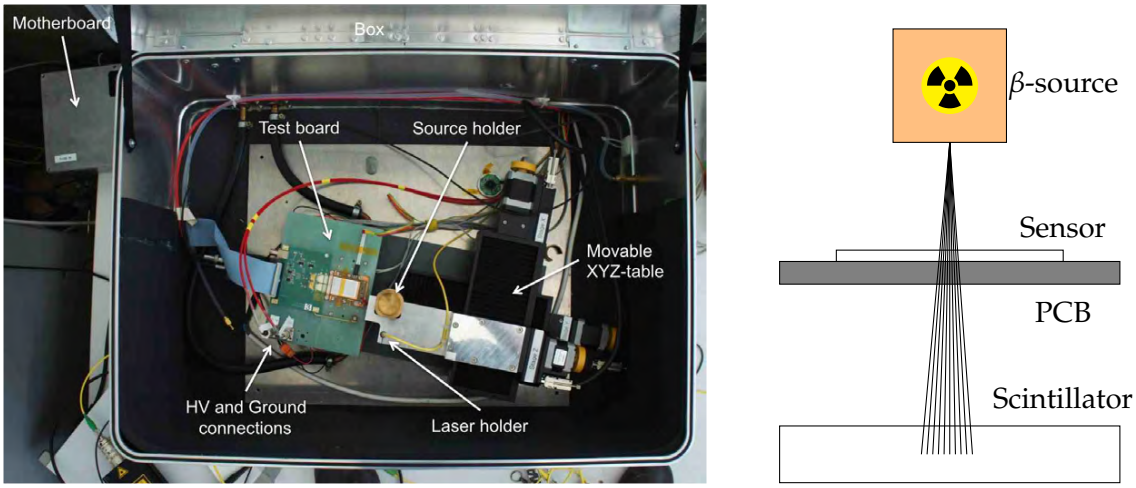

(a) Photo, [Hof13]. **(b)** Illustration

Figure 6.2.: ALiBaVa setup. A strip sensor is mounted onto a GFK test board and placed on a cooled copper bridge. A radioactive source or a laser are used to illuminate the sensor. Strip signals are read out by the readout chips on the daughter board.

6.2 Lorentz angle

Several methods to measure the Lorentz angle of electrons and holes inside a silicon sensor exist. Unlike the grazing angle method or the method presented in chapter 6.2.2 and used in the CMS Tracker using inclined particle tracks, the laser method as given in chapter 6.2.1 can be used without a tracking system surrounding the silicon sensor.

6.2.1 Laser method

The laser method has been used several times to measure the Lorentz deflection in silicon sensors (e.g. by de Boer et al. [Boe10]), the newly built measurement setup and a few selected results have already been outlined by Nürnberg and Schneider [NS13].

Method

Charge is induced to the sensor by a short laser pulse to the backside of the sensor while being placed inside a strong magnetic field, as shown in figure 6.3. While drifting towards the readout electrodes, the charge is deflected by the magnetic field. The amount of displacement can thus be measured as a function of the magnetic field.

The absorption of light in silicon is strongly dependent on the wavelength. Two different laser wavelengths are used here. Light with a wavelength of 1055 nm (from now on referenced as infrared light) has an absorption length of about 1 mm, which is more than three times the sensor thickness. Thus, electrons and holes are created along the whole path of the laser light, very similar to a charged ionizing particle (figure 6.3, right). In opposite to that, light with a wavelength of 880 nm (from now on referenced as red light) penetrates only about 25 µm and thus creates charge only close to the sensor back surface (absorption length parametrized by Rajkanan, Singh, and Shewchun [RSS79], compare also table 7.3). Depending on the type of sensor doping, one type of charge carriers (electrons or holes) is collected at the backside

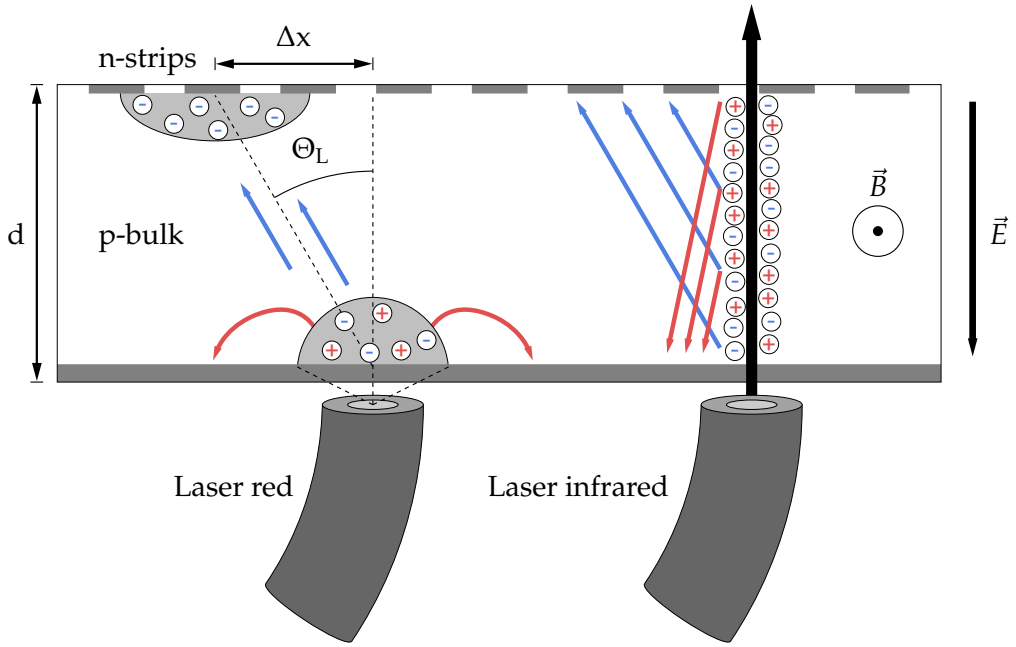

Figure 6.3.: Measurement method: A short laser pulse to the sensor backside induces charge in the sensor volume, depending on the absorption of the laser light. One type of charges drifts towards the readout strips, while the opposite charge drifts towards the sensor backside. During the drift, the charge is deflected by the Lorentz force. By varying the strength of the magnetic field, the shift can be measured as a function of the magnetic field [NS13].

electrode, while the other type drifts through the whole sensor volume and is collected at the readout strips (figure 6.3, left). During the drifts, the carriers are deflected by the magnetic field. By varying the magnetic field and comparing the position of the read out charge to the case without magnetic field, the Lorentz angle Θ_L and the Hall mobility μ_H can be calculated as

$$\tan\left(\Theta_\mathrm{L}\right) = \frac{\Delta x}{d} = \mu_\mathrm{H}\, B \tag{6.1}$$

from the observed shift Δx at the magnetic field B. To study the basic properties like the hall mobility of electrons and holes, the red laser is used. As the charge is created very localized at the sensor back surface, only one type of carriers drifts through the sensor and the drift distance d is the whole sensor thickness. As the infrared laser deposits charge like an ionizing particle in the whole sensor depth, it is best suited to study the effect of the magnetic field to the overall sensor performance in a tracking detector.

The different absorption is reflected in the shapes of the reconstructed charge distributions. Figure 6.4 shows exemplary the reconstructed amount of charge for several neighboring strips close to the laser hit for magnetic fields between 0 T and 8 T. Using red laser light, the charge cloud is displaced as a whole, its shape is only broadened by the larger lateral diffusion due to the elongated drift distance (figure 6.4a). As opposed to that, using infrared laser light, the amount of displacement of the charge from the incidence position depends on their position in the sensor. Charges that drift only a short distance to the electrode are displaced less than charges that drift a longer distance. This leads to a smearing and broadening of the reconstructed charge in one direction (figure 6.4b).

Per measurement step, 500 events without laser signal are taken in order to get the pedestal value per strip. Afterwards 500 events with laser signal are recorded. To reduce the influence of electronics noise to the measurement, the 500 single laser shots are averaged strip by strip before the analysis is performed. The pedestal subtracted and averaged charge signals are then fitted with a Gaussian function, as shown in figure 6.4. The central value is taken as the position of the charge cloud and is stored in the measurement database.

Magnet

The magnet used for the measurements is the JUMBO at Institute for Technical Physics at KIT, shown in figure 6.5. Its superconducting coil consists of NbTi and Nb_3Sn wires and has to be cooled for proper operation to 4.2 K. Therefore, the coil is mounted inside a liquid helium cryostat [Sch+10]. A warm tube is used to insulate the measurement setup thermally from the liquid helium. By that, the sensors can be operated at normal operation temperatures of around $-20\,°\mathrm{C}$. The strength of the magnetic field is tuned by the current in the coil. For a field of 8 T, a current of approximately 200 A is necessary. For reproducibility and monitoring reasons, the current is measured via the voltage drop on a shunt resistor of approximately $0.6\,\mathrm{m}\Omega$.

Figure 6.6 illustrates the strength of the magnetic field in the area of the sensors. The deviations from the nominal field value are in the order of $\pm 2\,\%$ [Klä11].

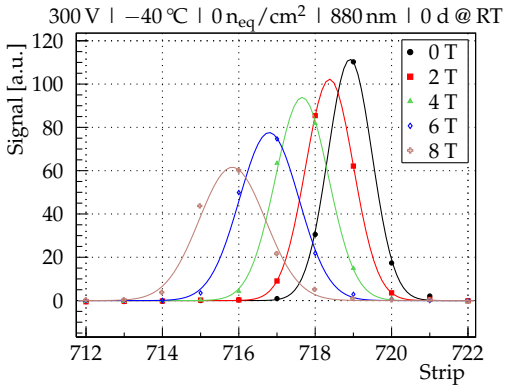

(a) Displacement of charge created with 880 nm laser. The charge is displaced as a whole and not changed in shape. The broadening is a result of the longer drift.

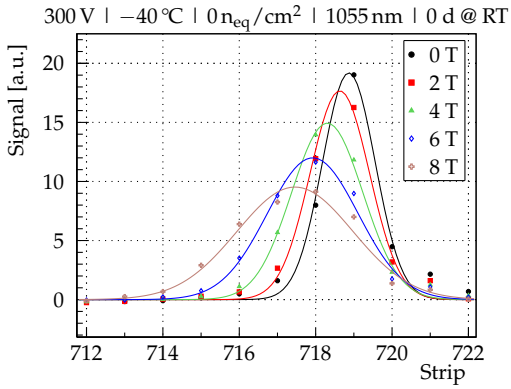

(b) Displacement of charge created with a 1055 nm laser. The distribution is broadened towards lower strip numbers, due to the different drift distances of charge carriers.

Figure 6.4.: Comparison of the shapes of the reconstructed charge distributions on the readout strips using two different laser wavelengths at different magnetic fields. The raw signals per strip are averaged over 500 laser shots after pedestal subtraction, and fitted with a Gaussian function. Its central value is counted as reconstructed position.

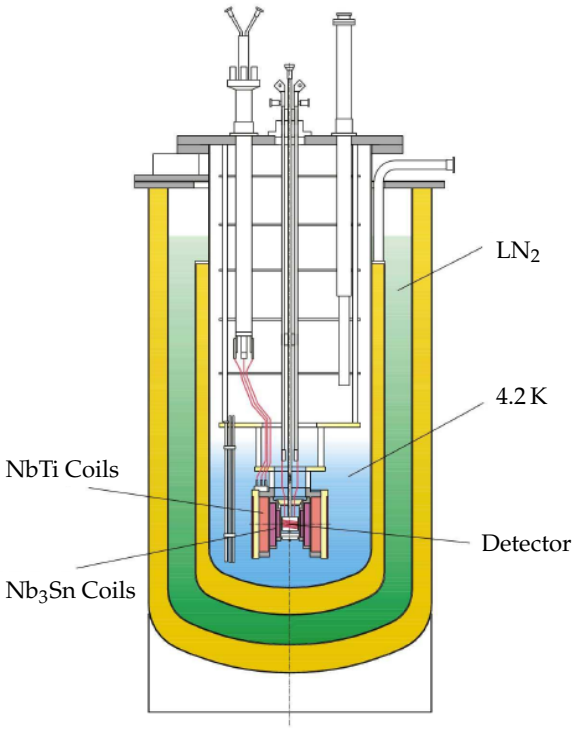

Figure 6.5.: JUMBO superconducting magnet [RHS00]. The coil is located in a cryostat filled with liquid helium. An additional warm tube can be inserted into the cryostat which insulates the sensors from the helium. This allows measurements at temperatures up to room temperature.

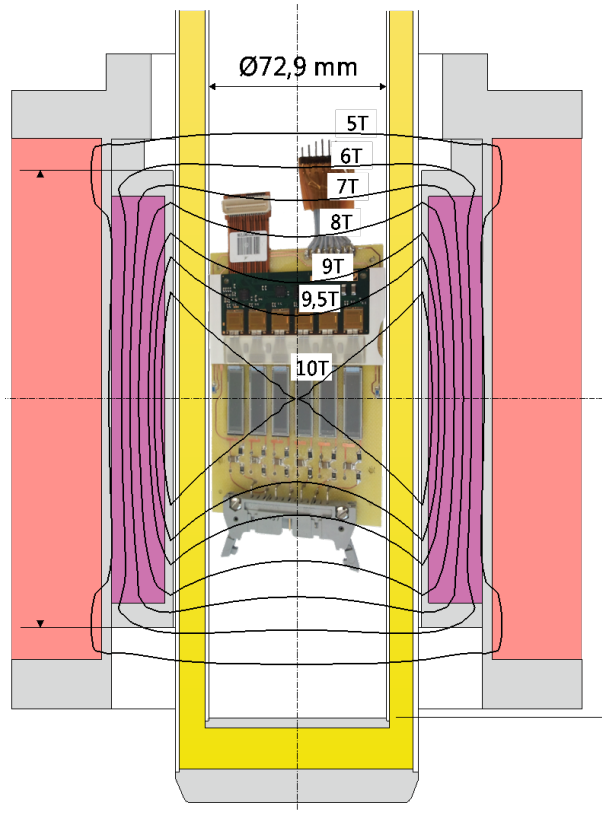

Figure 6.6.: Detailed view of the magnetic field configuration in the area of the sensors for a nominal field of 10 T. The deviations from the nominal field value in the area where the sensors are placed are in the order of ±2 %, [Klä11].

Data acquisition

For performing the Lorentz angle measurements, the silicon sensor has to be attached to a readout system. For that purpose, the ARC system has been used. The APV Readout Control (ARC) Test Setup is a compact, cost efficient test and diagnostic tool which is suited for full operation and characterization of front-end hybrids and Silicon-Detector modules [Axe+01]. Figure 6.7 gives an overview of the setup built around the ARC system. Main component of the setup is a controlling PC, which reads out the sensors and controls the bias voltages and the temperature. The board carrying the sensors is connected to the ARC front end board, which buffers and amplifies the signals before passing them to the ARC Board, where they are digitized and sent to the readout PC. For illumination of the sensor backside, two lasers are used. The pulse width of the laser pulse is in the order of 30 to 1000 ps [Pil]. The light is divided via a 1 to 6 optical splitter and led via optical fibers towards the sensor backside. Triggering of the readout and the laser pulses is performed via the ARC LED pulser board, which generates a regular trigger signal. The bias voltage is provided by an eight channel high voltage power supply, remote controlled by the PC via a CAN bus protocol.

Cooling system

The necessary cooling of the sensors is done by flushing the magnets warm tube with cold nitrogen gas. Warm nitrogen gas gets cooled down by a heat exchanger in liquid nitrogen, which has a temperature of $-196\,°C$. The cold gas is mixed with warm gas to preselect the appropriate temperature. The mixing ratio is controlled manually. Fine regulation of the temperature inside the warm tube is done via a heating coil close to the setup, that heats the gas to the correct temperature. The heating current is regulated by a PID controller implemented on the readout PC, the maximal heating power is 100 W.

PCB

Up to six sensors of the same type are mounted on a printed circuit board, carrying all necessary parts to bias and read out the sensors. One sensor is kept non-irradiated as a reference, while the other sensors are irradiated to different fluences according to table 5.3 with protons and neutrons prior to assembly. Openings in the board allow the illumination of the sensor backside with laser light, in order to induce a signal to the sensor. The alignment of the sensors on the PCB guarantees, that the openings in the aluminum grid on the sensor backside are centered in the PCB openings. Figure 6.8 depicts a completely equipped board with six sensors, a CMS Tracker readout electronics board and connectors for high voltage supply, detector readout and temperature control.

To hold the sensors at the correct position in the magnet, the board is mounted to a glass fiber bar fitting the magnet bore, as illustrated in figure 6.9. An aluminum support structure protects the sensors from mechanical damage and fixes the optical fibers used for laser illumination. The six fiber pairs can be moved individually by adjusting screws for about 1 mm with high precision. Detailed technical drawings of all parts are attached in chapter A.

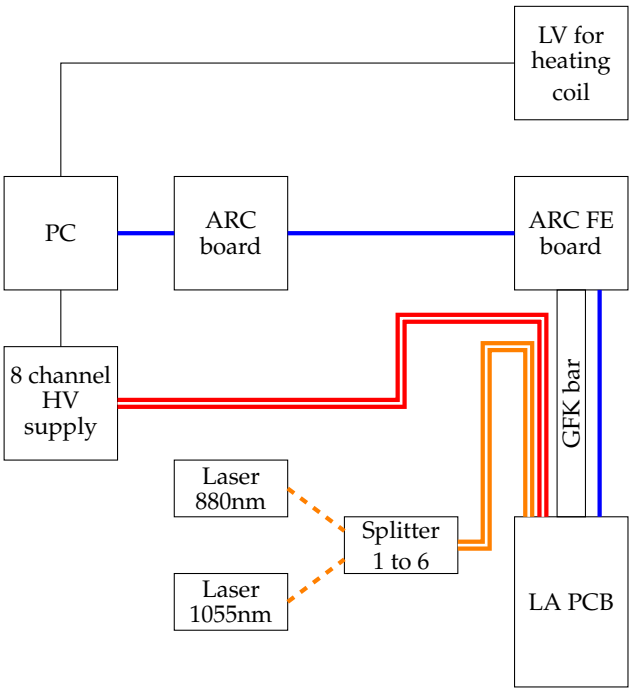

Figure 6.7.: Schematic overview of the measuring setup. The sensors are read out by the measurement PC via the ARC front-end board and the ARC board. The PC controls also the eight channel high voltage supply and the low voltage supply for temperature regulation via the heating coil. Signals are alternatively induced by two different lasers. The light is split by an optical 1 to 6 beam splitter, to allow the illumination of up to six sensors in parallel. Data cables for the readout are shown in blue, high voltage cables in red and optical fibers in orange. Double lines symbolize 6 parallel cables. Illustration following Schmenger [Sch11].

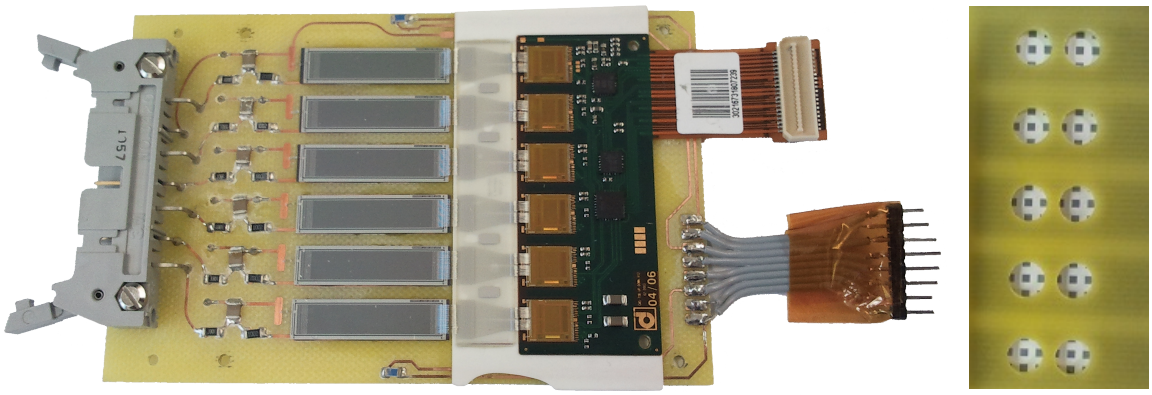

Figure 6.8.: Lorentz angle PCB: Up to six sensors of one type are mounted on a printed circuit board, together with the components needed for sensor bias and read out. Openings in the backside allow for illumination with laser light. The openings in the backside aluminum are aligned to the holes in the PCB [NS13].

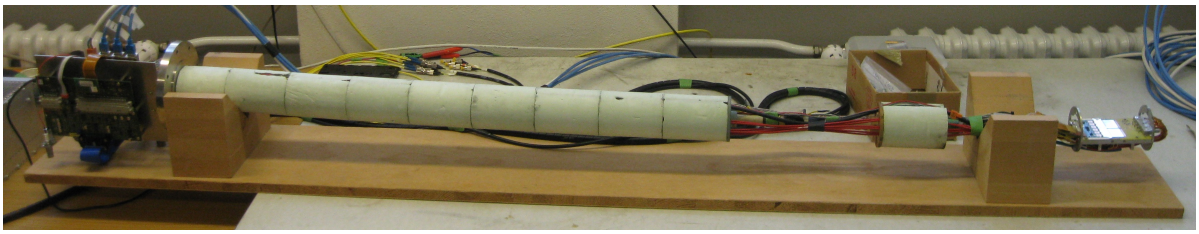

(a) GFK bar with attached sensor PCB

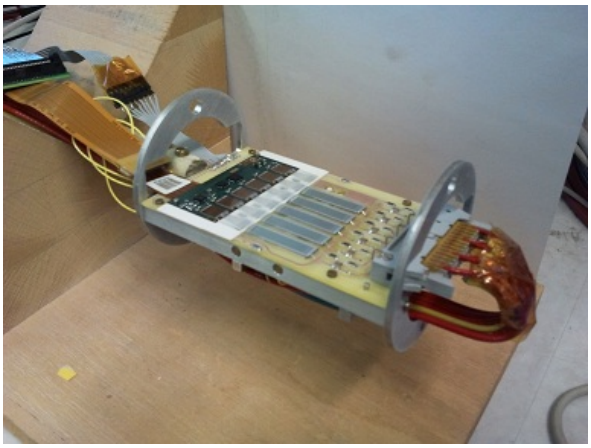

(b) Aluminum support structure

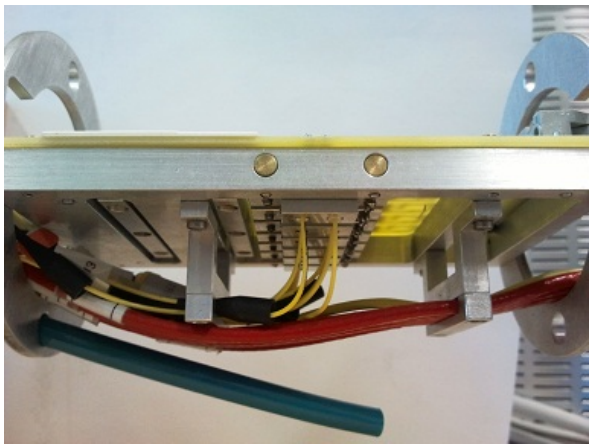

(c) Moveable laser fibers

Figure 6.9.: The PCBs are mounted onto an aluminum support structure (b). This structure protects the board from mechanical damage and holds the optical fibers used for laser illumination of the sensor backside (c). To place the sensors in the magnet, a GFK bar is used, to which the sensor PCB and parts of the readout electronics are attached (a).

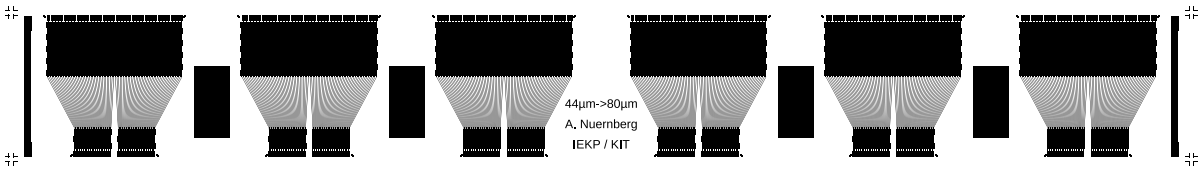

Figure 6.10.: Pitch adapter designed for the Lorentz angle PCBs. Six similar sets of routing lines are placed on a glass substrate.

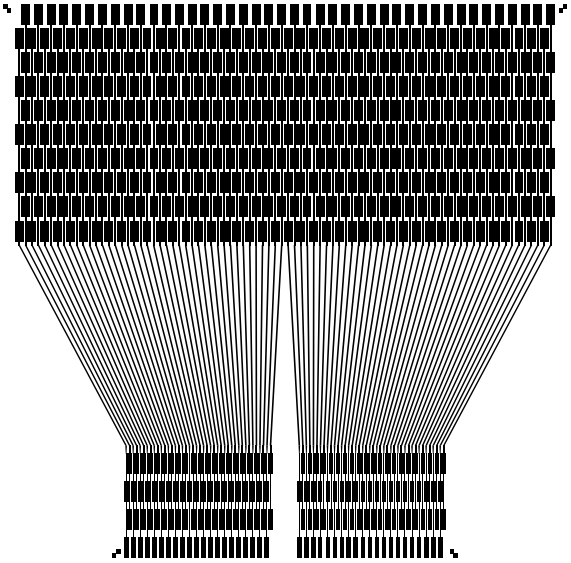

Figure 6.11.: Detailed view of the pitch adapter. The input pads of the readout chip are wire bonded to the pads at the lower part, the sensor readout pads are wire bonded to the top pads. Five rows of pads for connecting sensors and two rows of pads for connecting readout chips make the pitch adapter reusable several times.

Pitch adapter

The pitch of the sensor readout strips of 80 µm does not match to the pitch of the input pads of the APV readout chips of 44 µm. No direct wire bond connections can be made between sensor and chip. Usually, aluminum routing lines on a glass substrate are used to adapt the different pitches. For the measurements, a pitch adapter has been designed, taking the placement of the six sensors and the geometry of the PCB into account. Figure 6.10 shows the total layout of the pitch adapter. Six similar adapters are placed on the glass substrate, suitable to connect a single sensor to a readout chip. At the left and right edges, a single line for connecting the hybrid ground potential to the sensors is placed. A detailed view of the routing is given in figure 6.11. In the lower part, the pads match the layout of the input pads of the readout chips, while the pads on the top part match the sensor strip pitch. As the bond pads can not be reused for an infinite number of times, five rows of bond pads are foreseen, to make the pitch adapter and the connected readout hybrid reusable.

Performed measurements

More than 40 sensors produced by two different vendors have been tested at different conditions inside the magnetic field, covering the foreseen operational conditions and expected particle fluences in the CMS Tracker at HL-LHC. N-bulk sensors with p-implanted strips as well as p-bulk sensors with n-implanted strips have been evaluated. In addition to the sensors produced by HPK, p-bulk sensors produced by Micron have been investigated in the Lorentz angle studies. The following parameters have been chosen for the measurements:

- Temperature: $-20\,°C$, $-30\,°C$ and $-40\,°C$
- Magnetic field: 0 to 8 T in 0.5 T steps
- Voltage
  - at 4 T and 8 T: ramp from 50 to 1000 V in 50 V steps
  - 2 fixed voltages otherwise: 300 V and 600 V for the non-irradiated sensors, 600 V and 1000 V for the irradiated samples
- 2 laser wavelengths: 880 nm and 1055 nm
- 5 irradiation steps according to several radii in the CMS tracker ranging from 40 cm down to 7.5 cm
- annealing: 0 days, 20 days and 420 days of equivalent room temperature annealing, intermediate steps investigated without magnetic field

The irradiation fluences are summarized in table 5.3, separated in neutral and charged hadron irradiation. The ratio between charged and neutral hadron dose is changing with the radius, this has been reflected in the neutron and proton fluences.

6.2.2 Lorentz angle in the CMS Tracker

The evolution of the Lorentz angle in the CMS Tracker is monitored by the Tracker Detector Performance Group. The here presented work has been carried out within that group.

Basic principle

The measurement of the Lorentz angle in the CMS Tracker is based on the fact, that the average size of the reconstructed clusters depends on the incidence angle of the particles relative to the sensor surface. Without the presence of a magnetic field, the cluster size is minimal at perpendicular track incident. This is for two reasons. First, the amount of created charge is minimal at perpendicular incident, as the path length of the ionizing particle through the sensor bulk is shortest. Second, and more important, is the minimal distribution of charge towards neighboring strips, as a perpendicular hitting particle does not hit several strips. Usually only one or two strips are hit, for that, the average cluster size is small.

This is changed in the presence of a magnetic field. Due to the Lorentz force, the charges are deflected while drifting towards the readout strips, and the minimal cluster size is no longer obtained at perpendicular incident. The minimum is now at incident under the Lorentz angle,

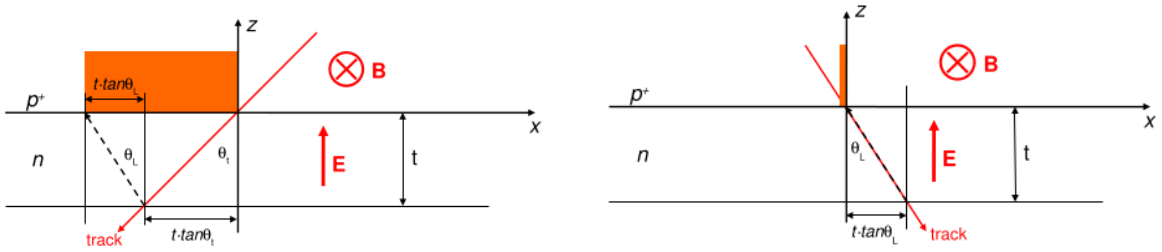

(a) Track incidence at a generic angle

(b) Track incidence under the Lorentz angle

Figure 6.12.: Cluster formation in presence of a magnetic field. Tracks incident with a generic angle (a) and with an angle equal to the Lorentz angle (b) are considered. The cluster is represented by the orange rectangle [Ciu+07].

as it is depicted by figure 6.12 [Ciu+07]. This fact is used to determine the Lorentz angle by searching for the track incidence angle under which the average cluster size is minimal.

A track hitting the sensor at a generic angle creates a large charge cluster, indicated by the orange rectangle in figure 6.12a. A track hitting at the Lorentz angle, creates charges along the way they drift towards the electrodes. Thus, their distribution is not broadened by the magnetic field, and the average cluster size stays minimal.

This shift of the minimal cluster size is being used to estimate the Lorentz angle of the drifting charges in the silicon sensors inside the CMS tracker. All strip sensors in the tracker are n-bulk sensors, for that, the Lorentz angle of holes can be investigated by plotting the average cluster size (or a derived quantity) over the incidence angle of the particles. The incidence angle is determined by the tracking of particles over several layers of silicon sensors. For that reason, this method requires a tracking system surrounding the investigated sensors. This can be either a beam telescope during a test beam or a full scale tracking detector like the CMS Tracker.

Figure 6.13 illustrates the distribution of incidence angles of charged particles for three layers of the tracker, namely the first layer of the inner barrel and the first and last layer of the outer barrel. Due to the bending by the Lorentz force, in the outer barrel almost all particles hit the silicon sensors at an angle. Because of that, the population of the histograms used to estimate the Lorentz angle is dependent on the tracker layer. Because of that, not all methods give reliable results for all layers.

Estimation methods

Different quantities are being investigated as a function of the track incidence angle. Besides the average cluster size [Ciu+07], the average cluster variance [BG09] and the probability of finding a cluster of size one [BG09] show an extrema around the Lorentz angle and thus serve as an estimator for it. As fitting function, equation 6.2 is used [Swa13]. It describes a v-shaped function with two linear arms and a rounded extreme, which can be either a minimum or a maximum.

$$f(x) = a + b\sqrt{1 - \left\lfloor \frac{|x-d|}{2\,(x-d)} \right\rfloor \cdot (x-d)^2 \cdot c^2 + \left\lceil \frac{|x-d|}{2\,(x-d)} \right\rceil \cdot (x-d)^2 \cdot e^2} \tag{6.2}$$

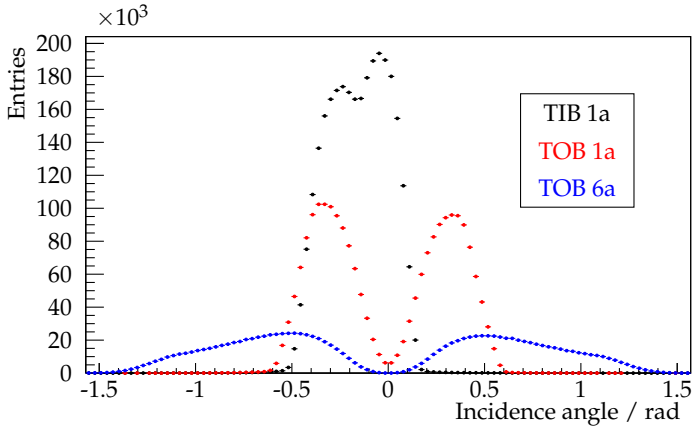

Figure 6.13.: Angular distribution of particles in the CMS Tracker.

Here, a is an overall offset, b is an RMS constant, c and e describe the slopes of the left and right arm and d is the angular position of the minimum, which represents the Lorentz angle after the fit. The following section describes the used methods to estimate the Lorentz angle exemplary on a proton-proton collision data for the innermost layer of the Tracker Inner Barrel.

Width method

Figure 6.14 gives an example, showing the average cluster size obtained in TIB layer 1 as a function of the tangent of the track incidence angle. The v-shaped function given by equation 6.2 composed of two linear parts is fitted to the histogram. The intersection of the two parts is taken as fit value for the minimum of the distribution.

Average variance method

Instead of looking at the average cluster size directly, several other quantities can be derived from the cluster properties, as shown by Betchart and Gotra [BG09]. Also the cluster variance

$$\sigma^2 = \frac{\sum_{\text{strips}} \int_i^{i+1} x^2 q_i \, \mathrm{d}x}{\sum_{\text{strips}} q_i} - \left(\frac{\sum_{\text{strips}} \int_i^{i+1} x q_i \, \mathrm{d}x}{\sum_{\text{strips}} q_i} \right)^2 \tag{6.3}$$

changes with the particle incident angle and is minimal at the Lorentz angle. The variance has the advantage of being more robust against changes in the clustering threshold. It is being investigated for clusters composed of two (avgv2) and three strips (avgv3) separately, resulting in two independent estimators for the Lorentz angle. Clusters containing more than three strips are quite seldom and thus are neglected from the analysis. Figure 6.15 shows two example distributions of the average cluster variance as a function of the track incidence angle for two (figure 6.15a) and three (figure 6.15b) strip clusters separately. A clear and very pronounced minimum is visible in both distributions.

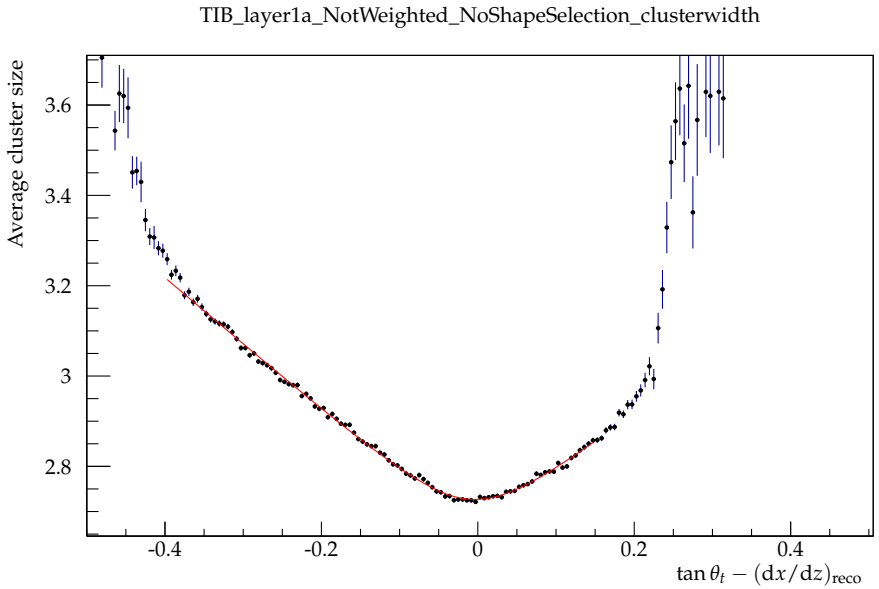

Figure 6.14.: Average cluster size as a function of track incidence angle

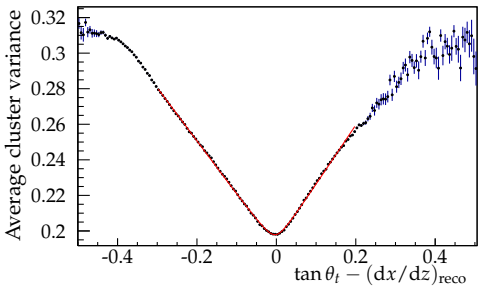

(a) Average variance of two strip clusters

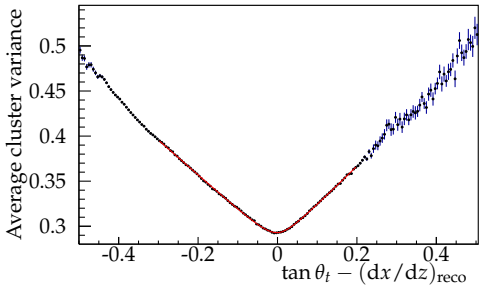

(b) Average variance of three strip clusters

Figure 6.15.: Average variance methods: the average cluster variance as given by equation 6.3 is plotted as a function of the track incidence angle for layer 1 of the TIB. (a) gives the distribution of two strip clusters, (b) gives the distribution for three strip clusters. The cluster variance is expected to be minimal at track incidence under the Lorentz angle. A minimum which can be fitted by a v-shaped function is visible in both plots.

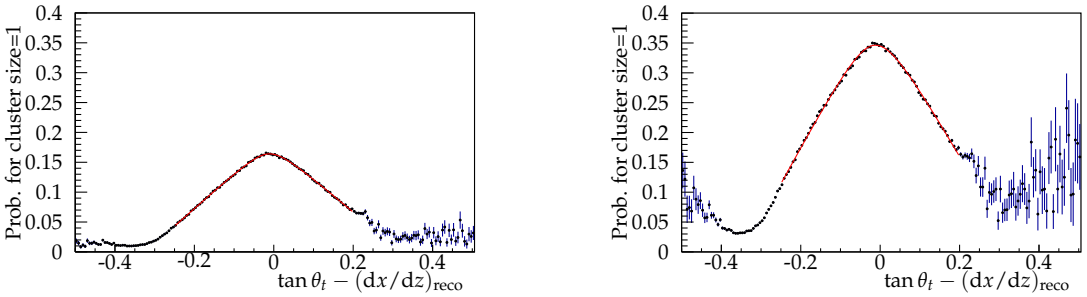

(a) prob1 **(b)** prob12

Figure 6.16.: Maximum probability methods: The probability of finding a cluster with cluster size one is plotted as a function of the track incidence angle. The normalization is either on all clusters (a) or only on clusters of size one and two (b). Both curves show a maximum at the Lorentz angle which is fitted by a v-shaped function.

Probability method

A third method is based on the fact, that the probability of having clusters containing only one strip is smallest if the cluster size is smallest [BG09]. The probability is obtained by dividing the histogram showing the number of clusters with size one as a function of the track incident angle by the histogram showing the number of either all clusters over the track angle or only the one and two strip clusters over the track angle. This two methods are called the prob1 and prob12 method. By that, the resulting histogram represents the probability for a size one cluster over the track angle. It shows a maximum at the Lorentz angle, which can be fitted by the same v-shaped function to estimate the Lorentz angle of the drifting holes. Figure 6.16a shows an example distribution for the prob1 method while figure 6.16b depicts an example for the prob12 distribution. Both histograms show a peak which can be fitted using equation 6.2.

Module level analysis

For the methods to work properly, the histograms have to be populated with a sufficiently large number of clusters. As the particle density depends on the distance of the module to the interaction point, at first order, only the radius of the tracker layer is considered. The z coordinate is neglected and the Lorentz angle is averaged over a whole tracker layer. This either reduces the amount of needed computing time and memory, because only one histogram per tracker layer has to be filled and fitted. It allows also the investigation of smaller runs with less tracks, as the minimum number of entries per histogram can be reached more easily.

For large runs, the Lorentz angle can be investigated not only as an average over all modules of a layer but can be analyzed individually on a module level. This allows the investigation of the dependence of the Lorentz angle for example on the ϕ and z coordinate or the module temperature.

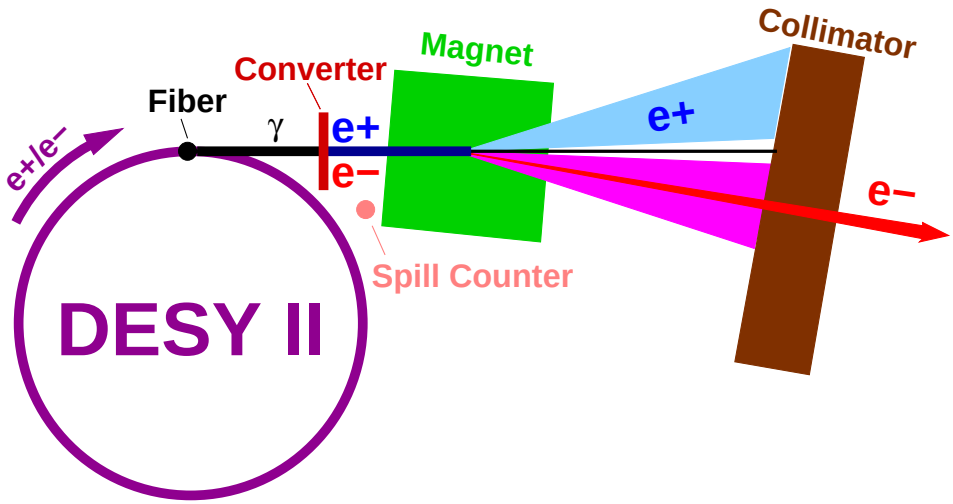

Figure 6.17.: Schematic layout of the test beam at DESY [Desy]

6.3 Test beam

Test beam measurements are commonly used to study the performance of tracking detectors. Usually, a reference telescope provides precise track information, allowing a more sophisticated investigation of the sensor under test, compared to e.g. a β-setup like the ALiBaVa setup. Especially, important parameters like efficiency and spacial resolution can only be evaluated properly with reference tracking. For the here presented studies, multi-geometry strip sensors as introduced in chapter 5.1.4 have been operated in a beam telescope at the DESY accelerator in Hamburg using the ARC read out system.

6.3.1 Desy accelerator complex & test beam area

DESY II is a synchrotron with a revolution frequency of 1.024 MHz. Figure 6.17 illustrates the basic layout of the accelerator. A bremsstrahlung beam is generated by a carbon fiber located in the primary beam. The photons are converted back to electron positron pairs by a converter target, which is a metal plate in the photon beam. The electron positron pairs are then spread out by a dipole magnet and a collimator cuts out the final electron or positron beam which is passed on to the test beam area. By tuning the magnet current, the momentum of the particles passing the collimator window can be chosen. No further beam optics are used.

The energy of the synchrotron varies with time. With a rate of 12.5 Hz, the beam energy is ramped to the nominal beam energy of 6 GeV and down to injection energy of 450 MeV again. Due to energy conservation, electrons reach the test beam area only during times, where the primary beam energy is larger than the energy chosen by the user for the test beam. For that, the test beam is modulated by that frequency. The software of the ARC read out system has been adapted to that time structure of the beam. During the beam-on period, the event data of several events is stored in the fast internal memory of the ARC board and passed on to the DAQ PC during the following beam-off period. During data transfer, the acquisition system is blocked. The shift of the data transfer to the beam-off time resulted in an improved acquisition rate. For the measurements presented here, an electron beam energy of 4.6 GeV has been chosen, compromising between particle rate and multiple scattering in the telescope.

6.3.2 Telescope

The used telescope consists of six planes of MIMOSA monolithic active pixel sensors [Rub12], which are located inside an aluminum support structure. The planes are mounted on a frame of aluminum profiles, allowing the easy positioning of the telescope planes along the beam axis. The device under test (DUT) is usually placed in the center of the telescope. For that, the telescope is divided into two arms consisting of the three upstream and the three downstream planes.

The active area of the pixel sensors is 10.6 mm $\times$ 21.2 mm. Each sensor consists of 576 $\times$ 1152 pixels with a pitch of 18.5 µm. The sensors are thinned down to a thickness of 50 µm [Desy]. As the size of the pixel sensors is much smaller than the MSSD sensor, the DUT has to be shifted during data taking, in order to cover all 12 regions. For that, the sensor is mounted on a xy and rotary stage, allowing the precise positioning of the sensor in the beam. In total, 4 positions are needed to cover the whole sensor.

The sensor is placed in an insulating box, which is mounted to the xy stage. To operate the sensor at temperatures below $-20\,°C$, the aluminum frame of the module is attached onto a cooling plate, which itself is cooled by an external chiller. To avoid condensation on the cold sensor, the cold box is flushed with nitrogen gas. By that, the irradiated sensors can be operated at voltages up to 900 V without the risk of damage due to humidity or a thermal runaway.

Figure 6.18 shows a photograph of the telescope in the DESY test beam area, together with the MSSD setup while figure 6.19 depicts a sketch of the used telescope geometry.

Due to the long integration time in the order of 100 µs of the telescope sensors, several particle tracks may be contained in one telescope readout frame. The MSSD is read out much faster, the shaping time of the APV chips is 25 ns. For that the signal of only one particle is usually obtained by the test sensor. To be able to decide, which particle track actually triggered the readout, a second non-irradiated strip sensor has been installed, which is read out synchronously to the MSSD by the same readout system. Using that method, it is possible to decide which track actually triggered the readout. This allows for a proper estimation of the efficiency of the DUT.

6.3.3 Trigger and timing

The trigger logic unit (TLU) is connected to all DAQ systems that are read out during data taking. The TLU distributes the trigger signal to all of them. The output signals of up to four scintillators are used to generate the trigger. At DESY, two scintillators are located in front of the telescope, the other two behind the telescope. The coincidence of all four scintillators generates a trigger signal, which is distributed to all DAQ systems.

After receiving a trigger signal, the connected DUT is expected to raise the BUSY signal. During the active phase of this signal, no further triggers will be sent. After having read out the DUT and being ready to receive the next trigger, the BUSY signal is released. This simple handshake is depicted by figure 6.20a [Cus09].

To be able to synchronize the data streams of the telescope events and the DUT events during the analysis more easily, the TLU optionally distributes a consecutively numbered trigger ID to all connected systems. For that, the DUT has to send an additional TRIGGER-CLOCK signal. During each clock cycle on that line, the TLU shifts out one bit of the trigger ID over the trigger line. This is called trigger handshake protocol, as depicted in figure 6.20b [Cus09] and has been

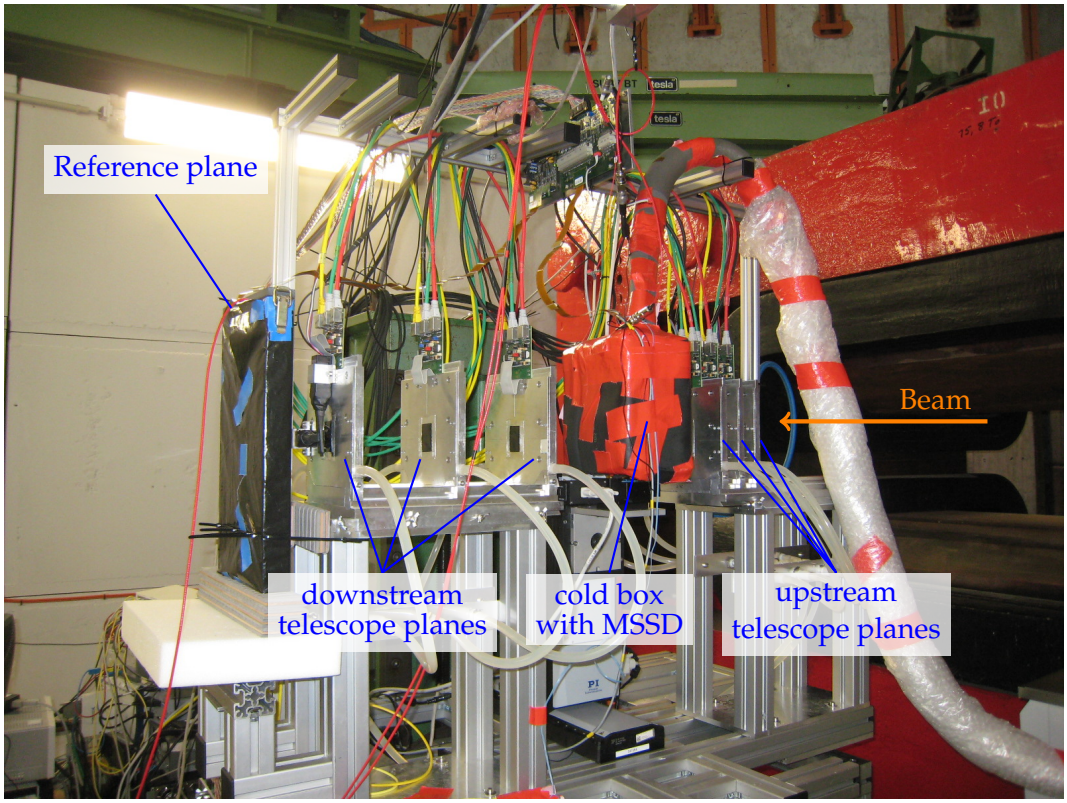

Figure 6.18.: Datura telescope in the test beam area 21. Six telescope planes are mounted on movable rails for easy adjustment. In the center of the telescope, the cold box containing the MSSD is located on the xy and rotary stage. After the three downstream telescope planes and after the downstream scintillator, the reference strip sensor is attached. The electron beam is hitting the telescope from the right side of the picture.

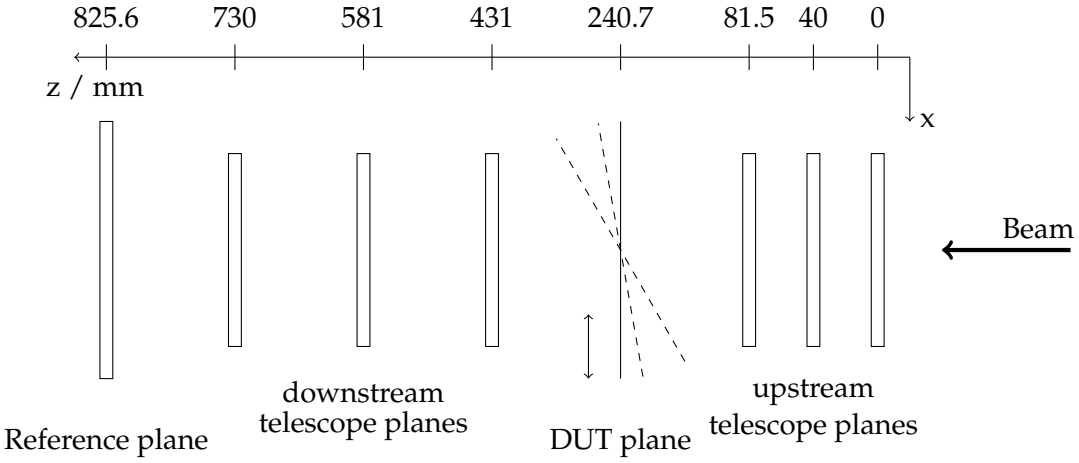

Figure 6.19.: Telescope geometry. The eight planes forming the telescope are shown with their z positions in the global coordinate frame. The 10° and 30° rotation of the DUT plane is indicated by the dashed line. In addition, the DUT is shifted along the global x direction in order to cover all regions of the sensor.

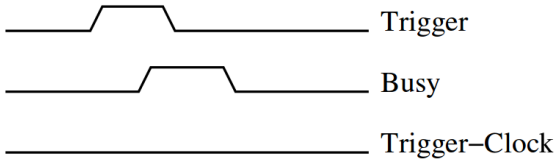

(a) Simple handshake

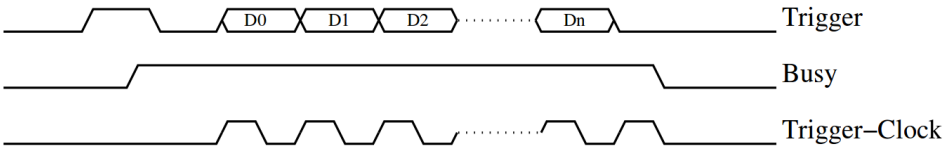

(b) Trigger handshake protocol

Figure 6.20.: Trigger handshake between TLU and DUT, [Cus09]

used during the data taking. For that, the handshake has been implemented in the ARC read out software using the parallel port of the PC.

6.3.4 MSSD module

In order to test the sensors with particle beams, the sensor has been attached to a readout electronics board. Figure 6.21 depicts a module used in the beam test studies. All twelve regions of the MSSD are read out by APV chips on a CMS Tracker front-end hybrid via several pitch adapters. The applied bias voltage is filtered by a R-C-R low-pass filter and is common to all regions. The aluminum base plate serves as cooling contact for the sensor. The module design is adopted from earlier MSSD testbeam campaigns using a silicon strip telescope, as presented e.g. by Auzinger [Auz13] and Mäenpää [Mäe13].

6.3.5 EUTelescope analysis framework

The analysis of the test beam data is performed using the EUTelescope framework [Eut]. The EUTelescope library is a set of processors in the so-called Marlin framework provided in the ILCSoft package [Rub10]. The general analysis work flow follows figure 6.22 and [Bul+07].

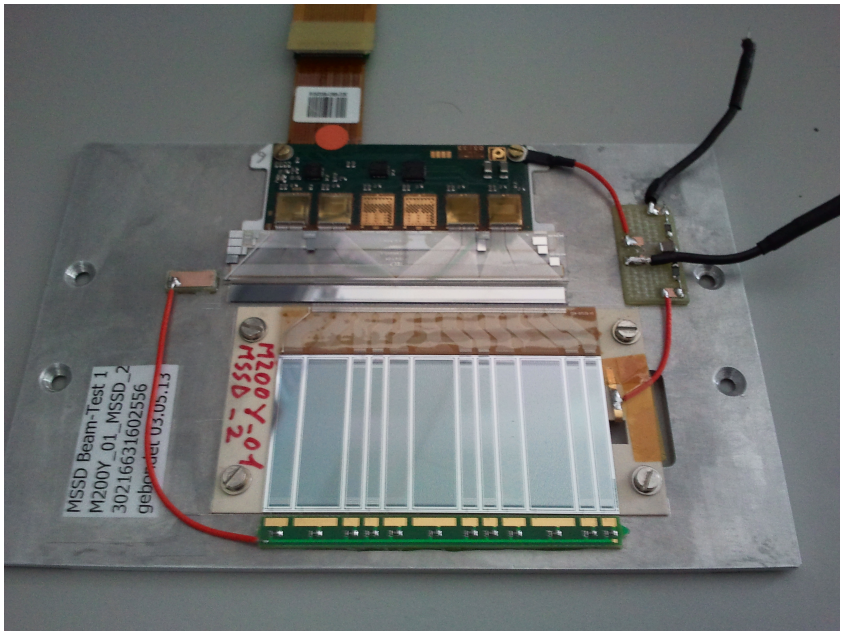

Figure 6.21.: MSSD module as used in the test beam studies

Definitions

Charge collection efficiency is the fraction of charge q that a sensor delivers compared to the read out charge q_0 obtained from a fully depleted non-irradiated sensor of the same type. It is a measure for the sensor degradation due to irradiation or under-depletion.

$$CCE = \frac{q}{q_0} \tag{6.4}$$

Hit efficiency is the fraction of the number of expected hits in a certain area of the sensor n_{expected} to the actually measured number of hits n_{measured}. The expected number of hits is derived from the track information, the number of measured hits is obtained by the reconstructed DUT data.

$$\eta_{\text{hit}} = \frac{n_{\text{measured}}}{n_{\text{expected}}} \tag{6.5}$$

Occupancy is the average fraction of strips which contribute to a reconstructed charge cluster, either due to a passing ionizing particle or due to noise. To avoid ambiguities in the track reconstruction and to reduce the probability of merging charge clusters originating from different particle tracks, the occupancy may not overpass a certain limit given by the tracking algorithm.

Gain factor is the conversion factor between the measured signal height in adc counts s_{adc} to the actual signal height measured in number of electrons $s_{\text{electrons}}$. The determination of the gain factor is performed by using the digital header preceding each event sent by the readout chips. It has a known signal height corresponding to a signal generated by 8 times the signal of a Minimal Ionizing Particle in a 300 µm thick silicon sensor, and is $8 \times 24\,000$ electrons $= 192\,000$ electrons, as given by Raymond et al. [Ray+00]. However,

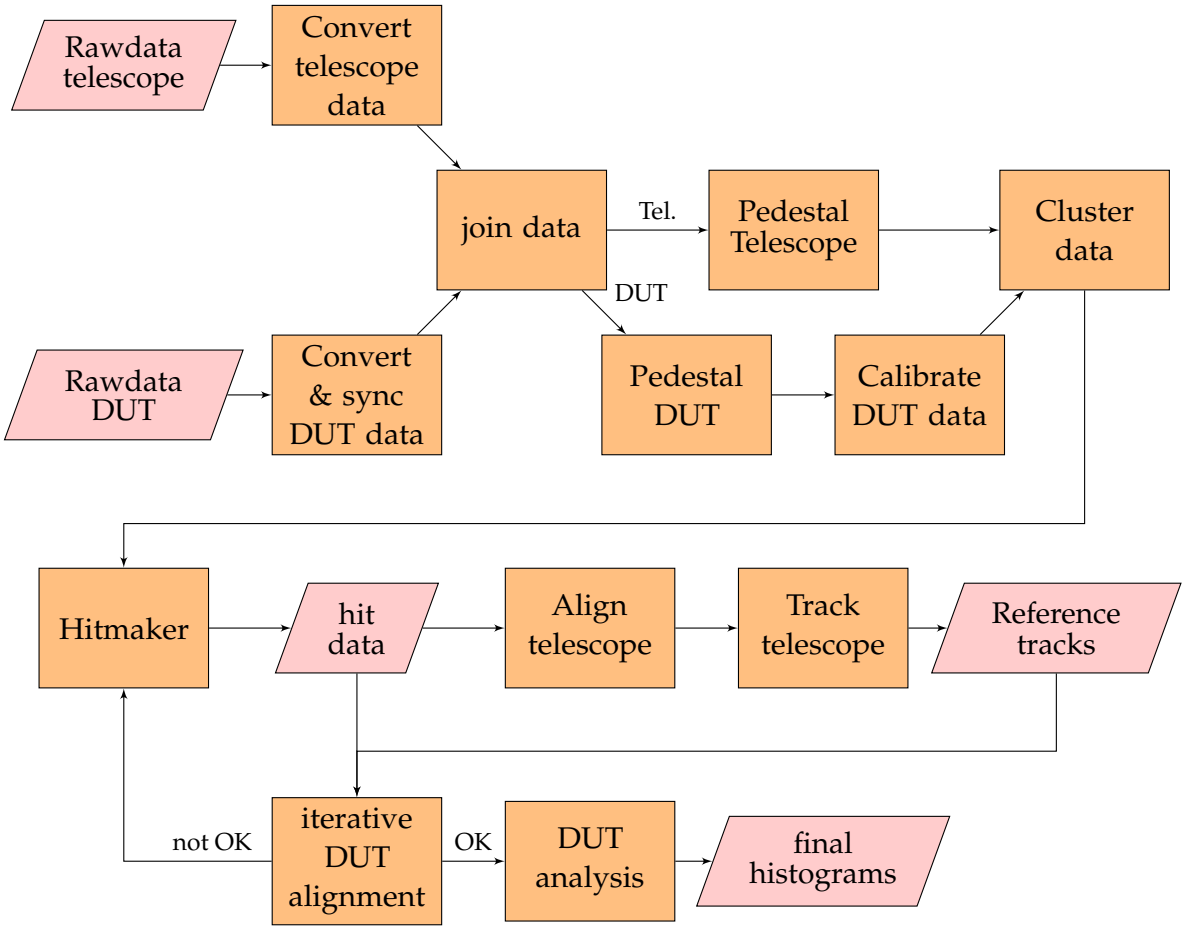

Figure 6.22.: Basic analysis work flow: The raw detector data is converted to the lcio data format, which is used in the EUTelescope framework. After the calibration of the data, charge clusters are created on the sensor planes, which are then converted by the hitmaker to three dimensional space points in the telescope frame of reference. From the hit information, tracks are formed which are used to either properly align the sensors towards each other and to perform the characterization of the device under test.

the factor had to be scaled down for this analysis to 135 000 electrons in order to match the expected signal of 14 000 electrons in the non-irradiated 200 µm thick sensor. The size of the header in adc counts $s_{\text{adcheader}}$ is averaged by the conversion processor over all four readout chips and all events of a given run, the analysis processor performs the conversion of the adc signal to electrons using this average number by calculating:

$$s_{\text{electrons}} = \frac{135\,000\,\text{electrons}}{s_{\text{adc, header}}} s_{\text{adc}} \tag{6.6}$$

Track matching is the process of assigning hits on the reference sensor or the DUT to tracks reconstructed by the telescope planes. The hit with the minimal distance between the interpolated track penetration point to the hit is assigned to the track. In addition, this distance may not be larger than 500 µm.

Reference track is the track, that was matched successfully to a hit on the reference sensor. It is used for further analysis of the DUT. To avoid ambiguities, events with multiple hits on the reference sensor are excluded from the analysis.

Residual is the distance between the interpolated track penetration point and the assigned hit along the local x or y coordinate of the sensor. As the DUT and the reference sensor are strip sensors, here only the residual in x-direction is important, whereas for the pixel sensors of the telescope planes, x and y residuals are meaningful. If the relative alignment of the sensors towards each other is known precisely, the distribution of the residuals is Gaussian shaped and centered around zero. The width of the residual distribution is an indication to the resolution of the sensor, although it is folded with the telescope resolution.

Data conversion & syncronization

The first step is in the analysis chain is the conversion of the raw data to the lcio format, which is used throughout further analysis steps as data model. Here, a custom processor has been created for the conversion of the DUT data, while the telescope events can be converted using the EUTelescope framework. Using the trigger IDs present in each event, the custom converter takes care of synchronizing the two data streams. It has been sufficient, to synchronize the first events of each run to each other. Due to the reliable veto mechanism, the following events stay synchronized. A desynchronization as observed by Troska [Tro12] did not occur. The two distinct streams are joined to a single lcio-file directly after conversion, in order to maintain synchronization throughout the following steps. Following that, the estimation of the noise and pedestal distribution and the pedestal subtraction from the raw data is performed on the DUT data.

Clustering

The zero suppressed telescope data contains all pixel information, exceeding a certain signal level. A traversing particle may hit more than one pixel, especially at an angular incident. For that, the raw hits can not be used for transformation into geometrical space points, as each hit pixel would become an individual hit point. Neighboring hit pixels, usually originating from the same particle track have to be combined to charge clusters.

For the DUT data, no zero suppression is applied. During the clustering process, strips carrying a signal which surpasses a 5σ signal threshold serve as seed for charge clusters. Neighboring strips are added to the cluster, if their signal is larger than two times the noise. To reject noise contributions occurring at the edge strips of the regions or from the not connected readout channels, a filtering processor is used. Here, additional cuts like total charge and total signal to noise ratio could be defined. Masking of damaged or unconnected strips can also be performed here.

The cluster position in the local coordinate system s_{hit} is obtained by calculating the center-of-gravity of the charge cluster, where c_i is the charge on strip i and s_i is the strip number of strip i. The sum runs over all strips which build the cluster.

$$s_{\text{hit}} = \frac{\sum_{i=1}^{N} c_i \, s_i}{\sum_{i=1}^{N} c_i} \tag{6.7}$$

Hitmaking

The clusters are obtained in local coordinates (strip or pixel numbers) on each sensor plane. To be able to perform a track finding in the telescope, the geometry of the telescope setup and the strip or pixel geometry of the individual planes has to be taken into account. The local coordinate system of the sensor planes is converted to the global coordinate system, by applying shifts and rotations of each sensor plane. To cope with the special geometry of the MSSD, the hitmaker processor has been adapted, taking the different strip pitches of the regions into account.

Telescope alignment

The geometry description provides information on the orientation of the sensor planes in the global coordinate system. This positions are reached by the sensors only within mechanical and practical precision. To improve the geometry description, the positioning of the sensors relative to each other can be estimated using actual particle tracks. In EUTelescope, this is done using the Millepede 2 algorithm [Blo07]. The standard EUTelMille processor is used for simple track finding and creating the input data for the track based alignment process by Millepede. As output, corrective values to the ideal geometry are calculated. During this analysis stage, only the six telescope planes are considered.

Tracking

Knowing the alignment constants, the geometrical description of the telescope is more realistic. After correcting the sensor hit positions for the misalignment, track fitting is performed. The EUTelTestFitter processor provided by the EUTelescope framework is used without modifications. Compared to a straight line fit, the EUTelTestFitter takes multiple scattering of the particle beam on the sensor layers into account, thus leading to a better track estimation.

Analysis

Using the track information, the DUT data is analyzed. The first step is the matching of hits on the reference sensor to tracks. For that, the fitted particle hits in the two most downstream telescope planes are extrapolated linearly to the reference sensor plane. After a manual prealignment, which is needed to be performed only once for all runs as the reference sensor was never moved, the track closest to a reference hit is considered as the track that triggered the readout.

The referenced track is extrapolated from the two planes directly in front of the MSSD to the DUT plane, and the residual between the track point and the closest reconstructed hit is calculated.

After aligning the sensor, the output histograms are filled. These are on the one hand distributions per sensor, like a hit map, an efficiency map, an overall residual distribution and residual profiles along the local x and y axis. On the other hand, distributions per sensor region are created. These include the total cluster signal, the cluster seed signal, the cluster size and the residual distribution. In addition to that, the cluster signal, the seed signal, the cluster size and the efficiency in the strip unit cell are evaluated for each region individually.

During the analysis step, the gain calibration of the obtained signal is applied. Therefore the average header height in adc counts as obtained during the conversion step and equation 6.6 are used to convert the signal height from adc counts to an absolute electron count.

DUT Alignment

The alignment of the MSSD and the reference sensor is done iteratively, by fitting the residual distributions and calculating corrective values for the position and angular alignment of the planes. Convergence is usually reached after three to five alignment steps. Several different profiles of the mean residual along the sensor axes are considered, each sensitive to a misalignment in a certain direction. In particular, these are:

- the slope of mean residual along sensor y direction is sensitive to a rotation around z axis,
- the mean value of residual along sensor y direction is sensitive to a x misalignment of the sensor,
- the slope of mean residual along sensor x direction is sensitive to a rotation around y axis and
- the slope of mean residual as a function of the incidence angle in x is sensitive to a z misalignment

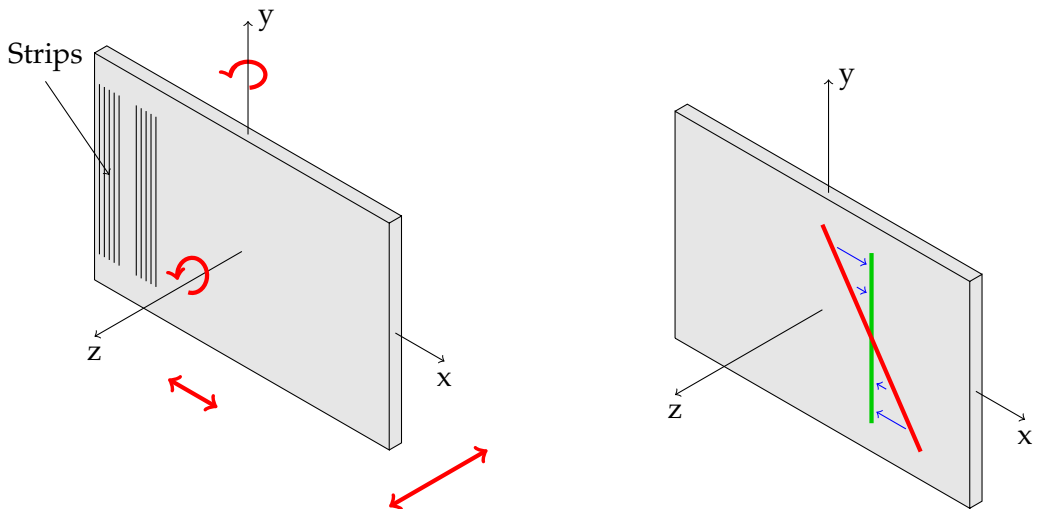

(a) Degrees of freedom **(b)** Example for misalignment around z-axis

Figure 6.23.: DUT alignment. (a): Summary of the four degrees of freedom in which the alignment is performed. (b): Example for the influence of a misalignment around the z-axis (tilt not to scale). The reconstructed position of several particle hits using the telescope tracks is illustrated by the green line, the reconstructed position using the sensor is due to a misalignment tilted and is represented by the red line. The residuals are indicated by the small blue arrows. In the top part of the sensor, the mean of the residual in x-direction is positive, in the bottom part it is negative.

as illustrated in figure 6.23a. Figure 6.23b illustrates the first item in detail. If the sensor is rotated around the z-axis, the reconstructed particle position using the DUT (shown in red) differs from the extrapolated hit from the telescope track (shown in green). The residual (indicated by the blue arrows) depends on the y-position of the particle hit.

Initial alignment parameters are obtained from the geometry description in the run logbook, reflecting the ideal position of the DUT in the telescope. In a first alignment step, only the offset along the x axis and the rotation around the z axis are corrected, as the residuals are most sensitive to a misalignment of the sensor in these parameters. In addition, the alignment parameters may be correlated to each other. After convergence, the other two degrees of freedom are included in the alignment process. The last remaining two degrees of freedom, namely a shift in the strip direction and a rotation around the local x axis, are not important here, because the strip sensor is insensitive to a misalignment in these degrees. In fact, the y coordinate of the strip hit is interpolated from the track information, as it can not be reconstructed from the strip sensor alone.

Figure 6.24a shows an example of the mean residual distribution used to align the DUT before and after the alignment correction of the first stage. In this example, the DUT is rotated 7 mrad around the z-axis due to the slope of the distribution and shifted 71 µm along the x-axis due to the offset of the distribution in order to correct for the misalignment. Afterwards, the sensor is aligned in the remaining two degrees of freedom. Figure 6.24b illustrates the x-residual distribution before and after the alignment procedure. After alignment, the distribution is narrowed down and centered around zero.

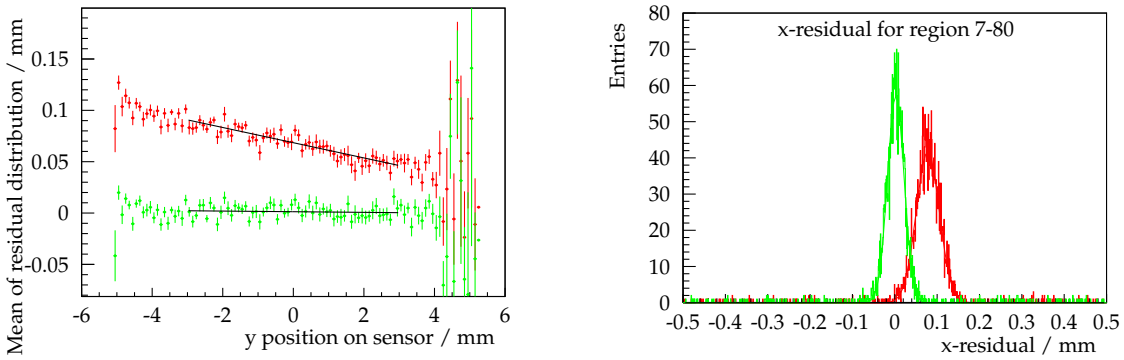

(a) x-residual distribution along the y axis before and after alignment around the z-axis

(b) x-residual distribution before and after alignment

Figure 6.24.: DUT alignment. (a): Residual distribution along the y-axis before (in red) and after (in green) applying the alignment procedure. To correct for the misalignment in this example, the sensor is rotated 7 mrad around the z-axis and shifted 71 µm along the x-axis. (b): Residual distribution before alignment (in red) and after (in green) applying all alignment steps. After alignment, the distribution is narrowed and centered around zero.

Sub strip

Due to the good spacial resolution of the telescope [ZN07], reference tracks reconstructed by the telescope planes enable the study of cluster properties with sub strip resolution. This allows a deeper comparison between the performance of the different strip geometries. The interpolated track impact point on the sensor in the global reference frame is converted back to the local frame of the sensor by applying the alignment corrections and hit making steps in reversed order. From that local coordinate, the position of the track hit in the unit cell of the sensor is evaluated.

The geometry of the strip unit cell has been defined as illustrated by figure 6.25. The strip center is located at x=0.5, whereas the midpoint in between two neighboring strips is located at x=0 and x=1. The width of the unit cell is of the size of the strip pitch. This choice is similar to the definition used by Mäenpää [Mäe13].

6.4 Irradiation facilities

The proton and neutron irradiation of the sensors used in this thesis have been performed at the cyclotron of the ZAG Zyklorton AG in Karlsruhe and the at the Reactor Infrastructure Center of the Jožef Stefan Institute in Ljubljana.

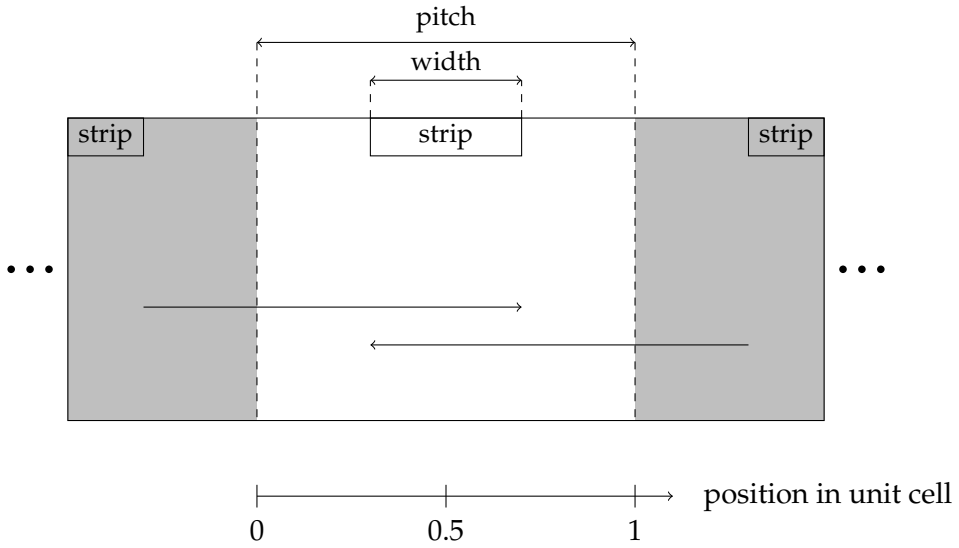

Figure 6.25.: Geometry definition for sub strip resolved considerations. The signal of all strips is periodically folded into one strip unit cell (shown in white). The coordinate system is chosen in that way, that the strip center is located at x=0.5. The center of the inter strip space is located at x=0 and x=1. The total width of the unit cell corresponds to the strip pitch.

6.4.1 Neutron irradiation at JSI

Irradiation of the sensors with neutrons has been performed at the 250 kW TRIGA Mark II light-water reactor at the Reactor Infrastructure Center of the Jožef Stefan Institute in Ljubljana. For irradiation purposes, several channels in the reactor core can be used. The highest achievable neutron flux is in the central channel, where it reaches almost $2 \times 10^{13}\,\mathrm{cm^{-2}\,s^{-1}}$ at the full reactor power of 250 kW. For the irradiation of the sensors in this work, one of the outer irradiation channels has been used, where the neutron flux is around $7 \times 10^{12}\,\mathrm{cm^{-2}\,s^{-1}}$ at full reactor power [SZT12]. The aimed fluence range for the irradiations in this work of 4×10^{14} to $8 \times 10^{14}\,\mathrm{n_{eq}/cm^2}$ can be reached within a few minutes. The accuracy of the irradiation fluence is 10 %. Figure 6.26 gives an overview of the different channels of the reactor. For the irradiation of larger samples, the triangular irradiation channel TIC is used, while for small test sensors and diodes the irradiation channel F19 is taken.

6.4.2 Proton irradiation at ZAG

Proton irradiation has been performed at a compact cyclotron operated by the Zyklotron AG in Karlsruhe [ZAG]. The energy at extraction is 25.3 MeV leading to an energy of the protons when reaching the samples of approximately 23 MeV, the beam current is limited to approximately 1.5 µA to avoid heating the samples. Additionally, the samples are placed in a thermally insulated box which is flushed with cold nitrogen gas in order to prevent an annealing of the samples during irradiation. The beam spot has a size of 4 to 8 mm, which means that larger samples have to be scanned in order to be irradiated homogeneously. For that, the irradiation box is placed on a programmable XY-stage. After irradiation, dosimetry is performed using ^{57}Ni-activity measurement in nickel foils which are attached to the samples during the irradiation procedure [Irr]. The estimated error on the irradiation fluence is 20 %.

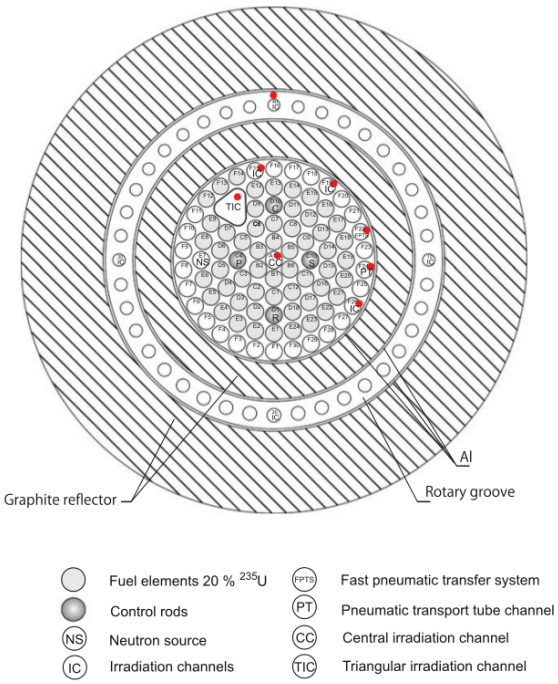

(a) Irradiation channels [SZT12]

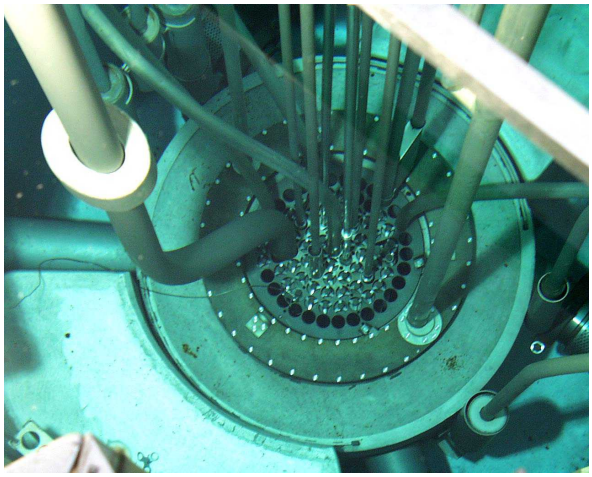

(b) Reactor [RIC]

Figure 6.26.: TRIGA Reactor at JSI

Figure 6.27 gives an overview of the proton irradiation setup. The beam pipe is coming from the left side of the picture, the samples are placed behind a capton window in the box, which can be seen on the right side of the picture, mounted on the XY-stage.

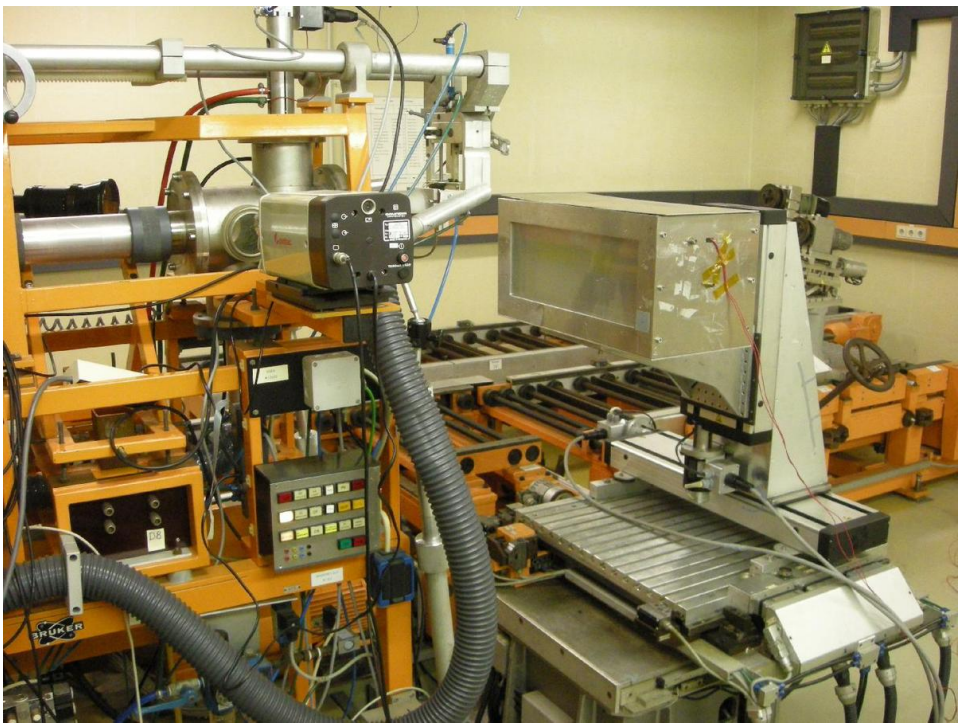

Figure 6.27.: Proton irradiation setup in front of the beam pipe. The samples are placed in a box, which is flushed with cold nitrogen gas to prevent an annealing of the samples during the irradiation. The box in mounted on a movable XY-stage to allow the scanning of samples larger than the beam spot size [Irr].

7

Simulation models and applications

For a better understanding of the formation of the read out signal, simulations of the microscopic processes during the drift of the charge carriers are very helpful. This chapter describes the various approaches that have been pursued in reproducing the performed measurements as shown in chapter 9. Two different models and algorithms are summarized here. A simple one dimensional drift model and a full scale finite-element simulation using a commercial T-CAD product used mainly in semiconductor industry.

The different methods described here vary in the accuracy and detail of the individual steps. By that, savings in computing time can be achieved, on the cost of accuracy or simulated details. The general procedure is common to both methods:

1. Definition of sensor geometry
2. Calculation of the electric field in the sensor bulk
3. Placement of charge carriers in sensor bulk (interaction with particle beam or laser light)
4. Propagation of charge to readout electrodes and sensor backplane
5. Calculation of signal induced in the readout electrodes
6. Shaping of signal according to readout electronics

The first part of this chapter describes the developed models on the basis of the performed Lorentz angle measurements, whereas the extrapolation to results obtained using particles from a beta source and beam test measurements is given in the second part.

7.1 Simple model

Expanding the simulation described by Bartsch et al. [Bar+03], a new simulation model has been implemented. The workflow has been previously published by Nürnberg and Schneider [NS13]. In contrast to Bartsch et al. [Bar+03], the model is capable to take the Gaussian laser beam spot and the absorption of the laser light in the silicon bulk into account. This is managed by tracking several thousand electrons or holes individually through the sensor bulk volume. The field dependent drift mobility and the deflection due to the Lorentz force are taken into account, while propagating the particles towards the readout strips. As described by Hamel and Julien [HJ01], charge that is moving close to the readout strips contributes most to the signal. For the sake of convenience and for saving computing time, only the type of charge carriers that is drifting towards the readout strips is considered here, as it contributes most. This model has been integrated into the analysis software, which has been used to analyze the measured data. Due to that, every condition can serve as an input to the model quite easily.

7.1.1 Parametrization of the electric field

At first order, the electric field in a depleted silicon sensor depends only on the z-position in the sensor bulk. Its strength rises linearly from the sensor backplane towards the readout strips, while the integrated electric field over the whole sensor thickness has to match the applied external bias voltage. The simplest parametrization is a perfectly linear increase as it is given by Bartsch et al. [Bar+03]:

$$E(z) = \frac{U_{\text{bias}} - U_{\text{depl}}}{d} + 2\,\frac{U_{\text{depl}}}{d}\left(1 - \frac{z}{d}\right) \tag{7.1}$$

with U_{bias} the applied external reverse bias voltage, U_{depl} the measured full depletion voltage of the sensor and d the sensor thickness.

7.1.2 Parametrization of the drift mobility

The drift mobility of electrons and holes is strongly dependent on the electric field. In general, the velocity of the charge carriers is the product of the drift mobility μ_{D} and the electric field.

$$v = \mu_{\text{D}} E$$

Electrons and holes are accelerated by the electric field. In a vacuum, the acceleration is not disturbed and the charges get more and more energy. In a solid, scattering occurs and the charges move at an average speed, the drift velocity.

Figure 7.1 shows an example of the drift velocity of electrons as a function of the electric field at different temperatures, taken from Jacoboni et al. [Jac+77]. At low electric fields, a linear increase is visible, resulting in a constant drift mobility. However, at larger electric fields, the velocity saturates and the mobility is reduced.

The continuous lines in figure 7.1 are the best fitting curves to the data points as obtained by Jacoboni et al. [Jac+77] using

$$v_{\text{D}} = v_{\text{m}} \frac{E/E_{\text{c}}}{\left[1 + (E/E_{\text{c}})^{\beta}\right]^{1/\beta}}$$

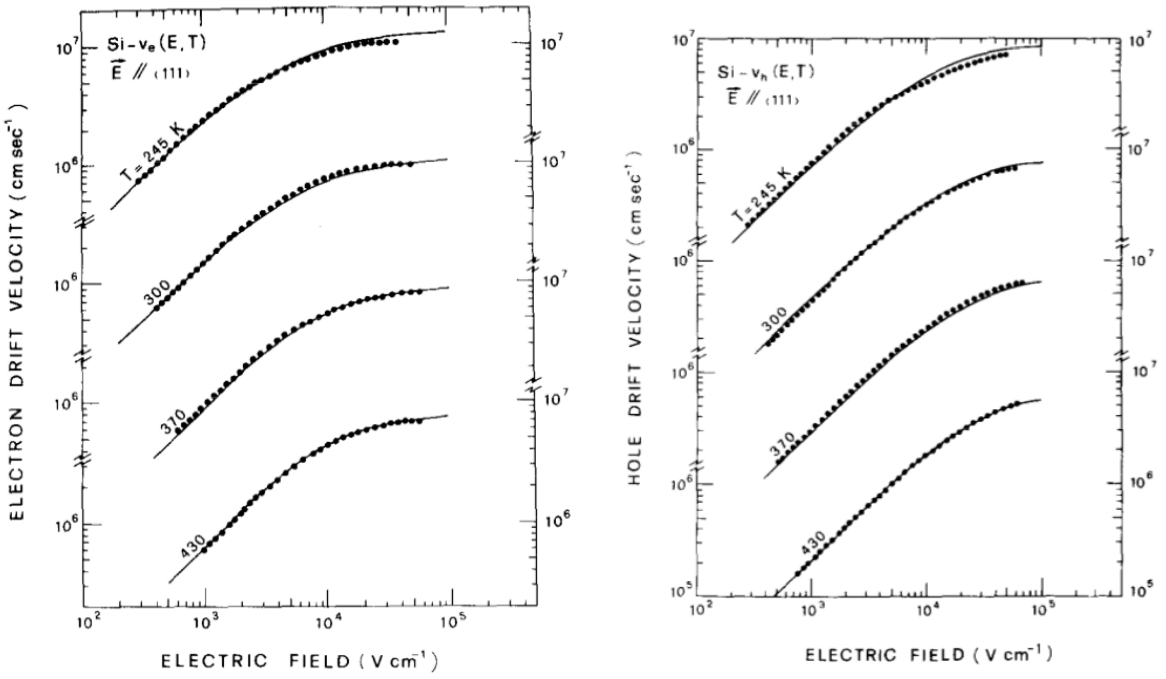

(a) Electron drift velocity

(b) Hole drift velocity

Figure 7.1.: Drift velocity of electrons and holes in high-purity silicon for $E \| < 111 >$ as a function of the electric field at four different temperatures. The points represent the experimental data and the continuous lines are the best-fitting curves [Jac+77]. At high electric fields, a saturation of the drift velocity with increasing field is observed. This corresponds to a reduced drift mobility at high fields.

Table 7.1.: Best fit parameters of drift velocity obtained by Jacoboni et al. [Jac+77]

parameter	electrons	holes	unit
v_m	$1.53 \times 10^9 \times T^{-0.87}$	$1.62 \times 10^8 \times T^{-0.52}$	$\mathrm{cm\,s^{-1}}$
E_c	$1.01 \times T^{1.55}$	$1.24 \times T^{1.68}$	$\mathrm{V\,cm^{-1}}$
β	$2.57 \times 10^{-2} \times T^{1.55}$	$0.46 \times T^{0.17}$	
T is measured in degrees Kelvin			

and the parameters given in table 7.1. E_c is related to the saturation drift velocity by $v_\mathrm{m} = \mu E_\mathrm{c}$ where μ is the low field mobility.

From that, the field dependent mobility can be evaluated as given by Canali et al. [Can+75]

$$\mu(E) = \frac{v_\mathrm{m}/E_\mathrm{c}}{\left[1 + (E/E_\mathrm{c})^\beta\right]^{1/\beta}} \tag{7.2}$$

Figure 7.2 shows an example of that parametrization in an 300 µm thick p-bulk silicon sensor at a reverse bias voltage of 300 V. The electric field rises towards the strips according to equation 7.1 while the drift mobility for electrons is reduced, following equation 7.2.

7.1.3 Absorption of light and placement of charges

The absorption of light in silicon is strongly dependent on the wavelength. In order to perform a proper simulation of the Lorentz angle measurements performed with a laser, as described in chapter 9, the absorption length of the light has to be known.

A parametrization of the absorption coefficient is given by Rajkanan, Singh, and Shewchun [RSS79] with a stated accuracy of 20%. Figure 7.3 shows the absorption coefficient of silicon at different temperatures. The solid lines are best fits to the data points using

$$\begin{aligned} \alpha(T) &= \sum_{i=1,2 j=1,2} C_i A_j \left[\frac{\left(\hbar\omega - E_{\mathrm{g}j}(T) + E_{\mathrm{p}i}\right)^2}{\exp(E_{\mathrm{p}i}/kT) - 1} + \frac{\left(\hbar\omega - E_{\mathrm{g}j}(T) - E_{\mathrm{p}i}\right)^2}{1 - \exp(-E_{\mathrm{p}i}/kT)} \right] \\ &+ A_\mathrm{d} \left[\hbar\omega - E_\mathrm{gd}(T)\right]^{1/2} \end{aligned} \tag{7.3}$$

where the different contributions are different transitions in the silicon band structure. The first part are the indirect transitions at 1.1557 eV and 2.5 eV, where a phonon is involved. The second contribution is a direct band gap at 3.2 eV. Table 7.2 gives the best fit parameters obtained by Rajkanan, Singh, and Shewchun [RSS79] on the experimental data.

The size of the direct and indirect band gaps E_gd and $E_{\mathrm{g}i}$ are dependent on temperature. For that, the parameterization by Varshni [Var67]

$$E_\mathrm{g}(T) = E_\mathrm{g}(0) - [\beta T^2/(T + \gamma)]$$

was used by Rajkanan, Singh, and Shewchun [RSS79] for the fit. For silicon, the parameters are $\beta = 7.021 \times 10^{-4}\,\mathrm{eV\,K^{-1}}$ and $\gamma = 1108\,\mathrm{K}$ [Var67]. These values are assumed to be valid for all three transitions.

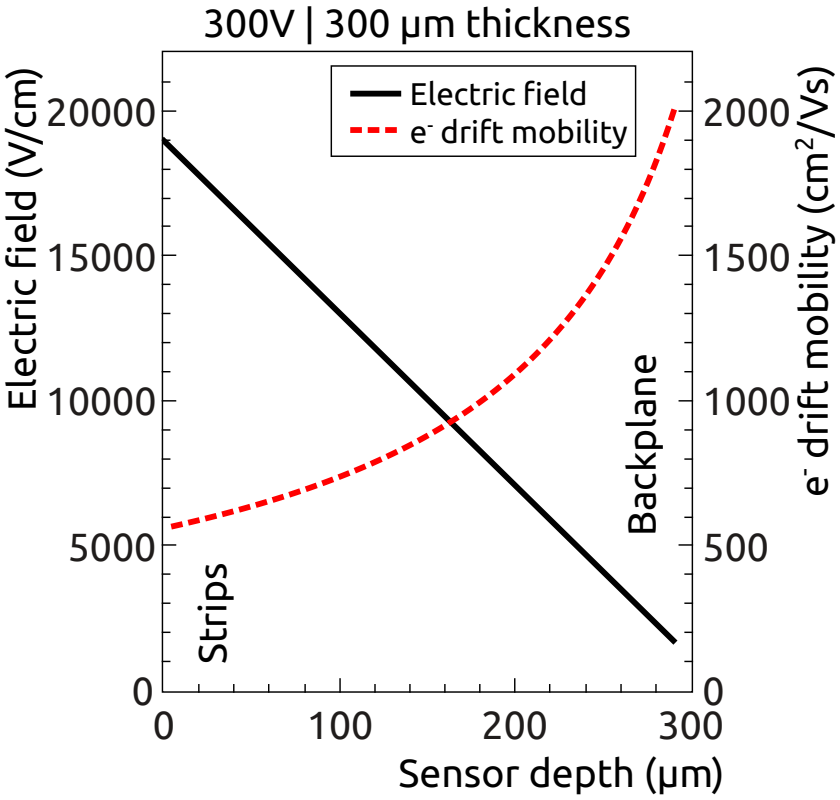

Figure 7.2.: One dimensional electric field and mobility distribution [NS13]. The electric field rises linearly towards the strips, the drift mobility of electrons is lowered with increasing electric field.

Table 7.2.: Best fit parameters for absorption coefficient obtained by Rajkanan, Singh, and Shewchun [RSS79]

Quantitiy	Value	Comment
$E_{g1}(0)$	1.557 eV	Indirect gap
$E_{g2}(0)$	2.5 eV	Indirect gap
$E_{gd}(0)$	3.2 eV	Direct gap
E_{p1}	1.827×10^{-2} eV	
E_{p2}	5.773×10^{-2} eV	
C_1	5.5	
C_2	4.0	
A_1	$3.231 \times 10^{2}\,\mathrm{cm}^{-1}\,\mathrm{eV}^{-2}$	
A_2	$7.237 \times 10^{3}\,\mathrm{cm}^{-1}\,\mathrm{eV}^{-2}$	
A_d	$1.052 \times 10^{6}\,\mathrm{cm}^{-1}\,\mathrm{eV}^{-2}$	

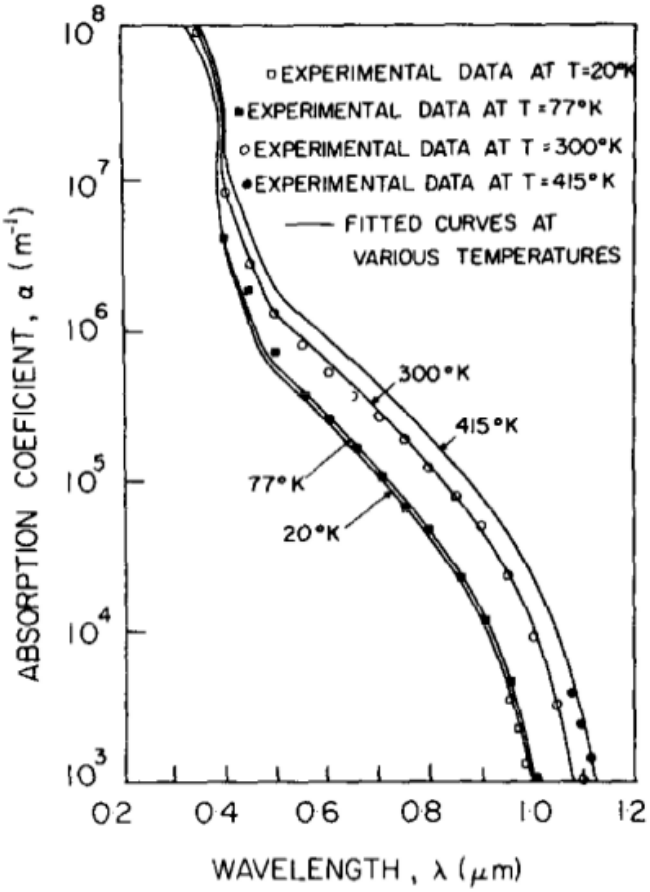

Figure 7.3.: Fitted absorption coefficient of silicon at T = 20, 77, 300 and 415K [RSS79]

.

Table 7.3.: Absorption lengths for the three used wavelengths

wavelength / nm	absorption length / µm
680	3.9
880	25.5
1055	1143.5

The absorption length is the reciprocal value of the absorption coefficient. The intensity of the light drops exponentially, and the absorption length is the length after that the intensity of the light has dropped to a factor of $\frac{1}{e}$ of its initial value at the sensor surface.

$$I(z) = I_0 \times \exp\left(-\frac{z}{\alpha}\right) \tag{7.4}$$

For the measurements, laser light with a wavelength of 680 nm, 880 nm and 1055 nm has been used, the absorption lengths according equation 7.3 are given in table 7.3. Light with 1055 nm wavelength penetrates the whole sensor volume, as the absorption length is larger than 3 to 5 times the sensor thickness, while light with a wavelength of 880 nm penetrates only 25 µm and thus creates charge only close to the sensor backside. The highly doped region connecting the sensor bulk to the backside aluminum is approximately 10 to 20 µm deep. The 680 nm laser penetrates only 4 µm into the sensor bulk and thus cannot be seen from the sensor backside.

Ionization charges are created in the sensor proportional to the intensity of the laser light. Knowing the wavelength, spot size and possibly the incidence angle of the used laser, charges can be created virtually in the silicon bulk. An example for that is shown in figure 7.4, where an 1055 nm laser pulse on the sensor backside is simulated. The assumed spot size is 30 µm and the incidence is perpendicular to the sensor surface at x=0. 2000 charge carriers are placed, following the absorption law given in equation 7.4 over the sensor depth and a Gaussian profile in the x-direction. During this step of the simulation, the polarity of the sensor is not yet important, as electrons and holes are created pairwise. As stated above, in the simplest form of the simulation code, only the type of charge carriers that drifts towards the readout strips is considered. For that, here generic charge carriers are created, while their polarity is defined during the following steps.

7.1.4 Drift towards the strips

After placement of the charges, their polarity has to be defined. For convenience, only the type of charges that drifts towards the strips is considered. Electrons in a p-bulk sensor and holes in an n-bulk sensor. The drift of the charges towards the strips is evaluated stepwise by dividing the drift distance along the z-axis in 1000 equally distributed steps of the size dz. For each particle and each step, the local shift dx due to the magnetic field is calculated and applied to the particles position for each particle while moving it towards the sensor surface with a step size of dz

$$\mathrm{d}x = \mathrm{r_H}\, \mu_\mathrm{D}(E(z))\, B\, \mathrm{d}z \tag{7.5}$$

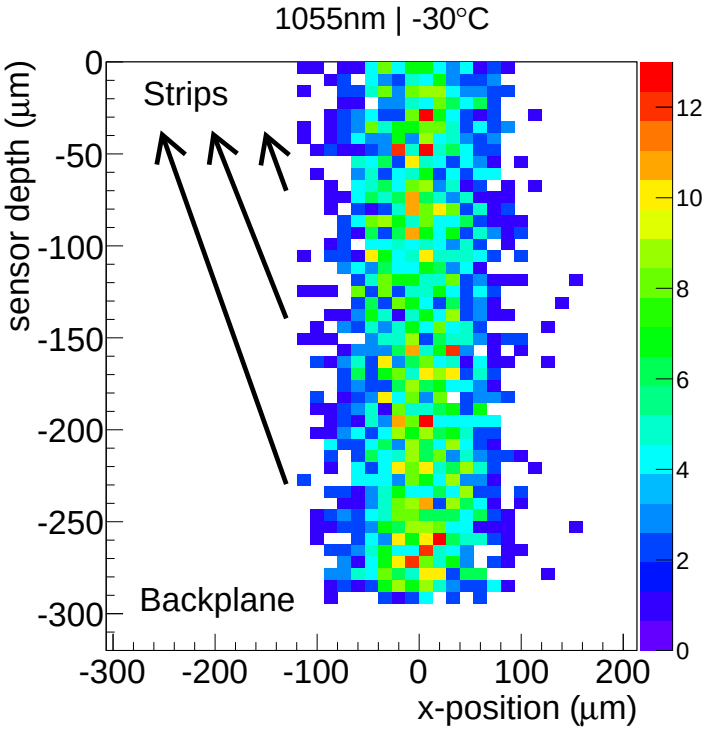

Figure 7.4.: Placement of charge carriers in the silicon bulk after a simulated incidence of a laser pulse of the wavelength 1055 nm [NS13]. Charges are created according to the absorption law, given in equation 7.4, using the absorption coefficient given by equation 7.3.

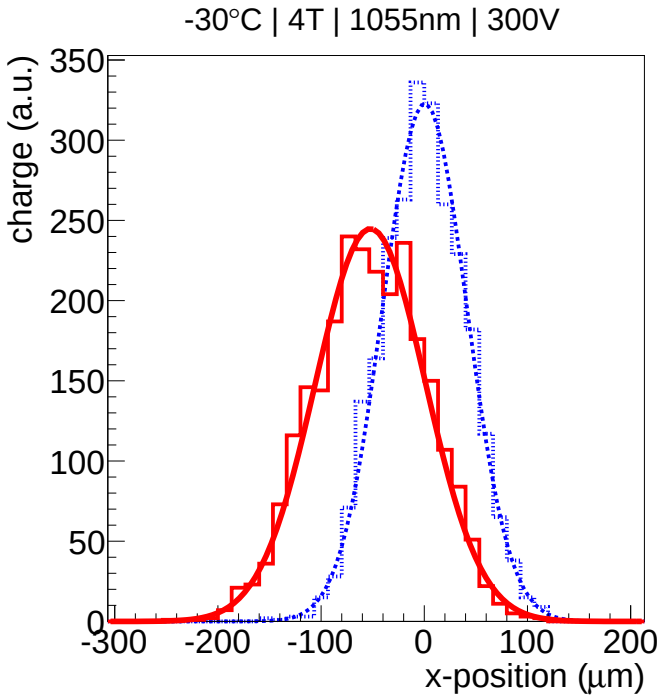

Figure 7.5.: Shift of charge carriers after simulated drift, [NS13]. The blue distribution is the projection of the charge towards the sensor surface as it is created by the infrared laser pulse, while the red distribution shows the position of the charges after being tracked towards the sensor surface, taking the deflection due to the magnetic field into account. The total Lorentz shift is evaluated by fitting a Gaussian to each distribution and taking the difference in the central values. In this case, electrons have been assumed to drift in a p-bulk sensor, the deflection is about 50 µm.

resulting in a deflection of the particle on its way towards the strips. At each position, the local electric field is given by equation 7.1 and is used to calculate the drift mobility of the particle using equation 7.2. The magnetic field B is assumed to be homogeneous across the sensor volume. After all particles have been tracked and have reached the sensor surface, their distribution can be investigated again. An example is shown in figure 7.5, where the deflection due to the magnetic field is clearly visible. The blue distribution shows the projection of the placed particles towards the sensor surface as they are placed by the laser, while the red distribution shows the positions after the propagation towards the sensor surface taking equation 7.5 into account. The difference between the central value of the two fitted Gaussian corresponds to the simulated Lorentz shift. In the case of figure 7.5, electrons have been assumed to drift in a p-bulk sensor, the deflection is about 50 µm at a magnetic field of 4 T and a bias voltage of 300 V.

7.1.5 Binning to strips & eta distribution

After the propagation of the charge carriers to the sensor surface with high spatial resolution, the charge is assigned to the nearest strip, where all charges are summed up. This is necessary in order not to pretend a higher position resolution of the simulated sensor. In addition to that, it allows the post processing of the simulated charge cluster. In this case, a charge sharing model has been implemented, which emulates a sharing of charge following the η-algorithm commonly used during hit reconstruction, e.g. described by Belau et al. [Bel+83]. Therefore a measured η-distribution has been parameterized and is applied to the simulated charge in a reversed way. By that, a more realistic charge distribution in the cluster can be achieved and the agreement to the measured data is slightly improved.

7.2 Applications

The simple model described in chapter 7.1 can be used to study and investigate not only the Lorentz angle, but also other properties of the drifting charges and the created clusters in general. This comparison between simulation and measurement data is performed for various sensors and multiple test setups, ranging from a beta setup at the laboratory to a full scale beam telescope at a test beam area.

Charge deposition by an ionizing particle is a statistical process. Two particles hitting the sensor at exactly the same position will not necessarily create the exact same charge cluster. Due to the relatively fast computation time of the simple model in the order of seconds per event and the possibility to use modern multi-core computers for event-based parallelization[1], statistical analyses of the cluster parameters can be performed. For the reproduction of the statistical fluctuations in the ionization process, the simple model has been combined with a Geant4 simulation of the investigated setup.

7.2.1 Simulation of the ALiBaVa setup

The input to the simulation model is a Geant4 [Ago+03] [All+06] simulation of the ALiBaVa setup as shown in chapter 6.1.2. Mainly, the brass collimator housing the radioactive source and the scintillating material below the sensor have been rebuilt. Figure 7.6 depicts the used geometry. The collimator is a cylindric piece of brass with an 0.8 mm opening at the bottom. Inside, the radioactive isotope ^{90}Sr is placed. Electrons emerging the collimator hit the silicon sensor, which is placed on a 1 mm thick printed circuit board. Below that, the scintillating material is located. There, neither the correct thickness and geometry have been rebuilt nor are the physics processes of the scintillation reproduced. Only the deposited energy is taken into account for event triggering.

The β-decay of the radioactive isotope ^{90}Sr creates electrons, which either hit the silicon sensor and deposit energy in the scintillating material or get absorbed by the brass collimator.

The beta decay of ^{90}Sr is given in equation 7.6

$$^{90}\mathrm{Sr} \rightarrow^{90} \mathrm{Y} \rightarrow^{90} \mathrm{Zr} \tag{7.6}$$

[1] here, OpenMP has been used as shared-memory parallel programming API in C/C++, [OMP]

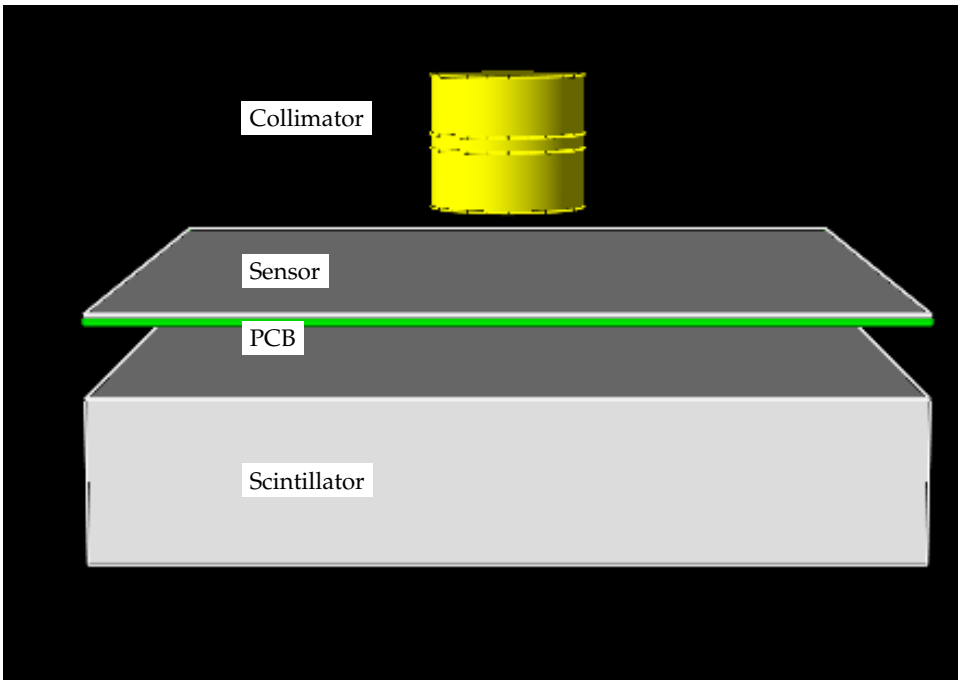

Figure 7.6.: Geometry of the Geant4 simulation

Radioactive ^{90}Sr decays via a β^--decay to ^{90}Y with a maximal decay energy of the electron of 0.546 MeV. ^{90}Y itself undergoes a β^--decay to the stable ^{90}Zr with a decay energy of 2.283 MeV [Ber+12]. The simulated energy spectrum of the electrons originating from the decay and hitting the silicon sensor is shown in figure 7.7a. Both decays can clearly be distinguished. Electrons, that hit the sensor do not necessarily contribute to the signal read out of the sensor. The electrons can be absorbed in the sensor itself or the underlying PCB before hitting the scintillator trigger and thus are not counted. This is depicted in figure 7.7b, where only the part of the energy spectrum is shown, that is able to fire the scintillator trigger. Most of the low energy electrons below approximately 600 keV are not able to reach the scintillator and are cut out of the spectrum.

The incidence position and angle as well as the energy deposit of all particles that hit the silicon sensor and fire the trigger are fed into the simulation model, in order to get charge clusters on the sensor. An ionization energy of 3.6 eV per created electron-hole pair is assumed, as given by Beringer et al. [Ber+12]. In order to model the loss of cluster signal in irradiated sensors found in the beam test studies, the energy deposit obtained from the Geant simulation is modulated with an additional weighting function $f(x)$, where x is the position in the strip unit cell as defined by figure 6.25:

$$f(x) = -\frac{l}{2}\cos(2\pi \cdot x) + 1 - \frac{l}{2}. \tag{7.7}$$

This describes a reduction of the total charge in the area in between the strips. For the simulation of the beam test results, l has been chosen to 0.2. This results in a reduction of the total charge to 80 % between the strips, reflecting the measured loss on the 70 µm, 80 µm and 120 µm pitch regions.

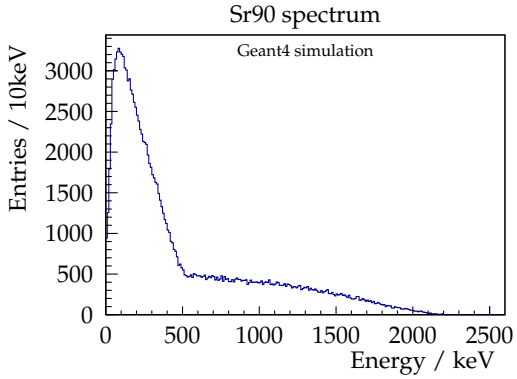

(a) Total energy spectrum of simulated decay electrons hitting the silicon sensor.

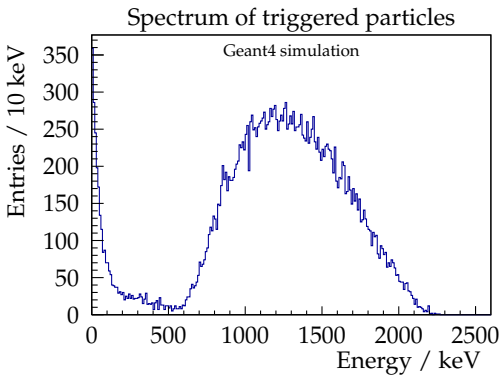

(b) Energy spectrum of particles that hit the silicon sensor and afterwards fire the scintillator trigger.

Figure 7.7.: Geant4 simulated energy spectrum of the Sr90 source

As an example, a comparison between the obtained hit position on an 200 µm thick non-irradiated p-bulk float zone sensor and the simulation model is shown in figure 7.8a. The strip pitch of the sensor is 80 µm. The black dots represent the number of clusters found on that particular strip, while the red solid line shows the output of the simulation model. Both datasets have been normalized to the same number of total entries, no other scaling or fine-tuning has taken place. The shape of the distribution is reproduced by the simulation model, indicating that the geometry of the collimator and the other parts of the setup are modeled correctly.

An important cluster parameter is the average size of the charge clusters. Using an analogue readout chip as used in the current CMS Tracker, the hit position can be interpolated by taking the shape of the charge cluster and the distribution of charge on the involved strips into account. This is only possible on clusters that are composed of at least two strips. Figure 7.8b shows in black the distribution of cluster sizes obtained in the ALiBaVa setup on a 200 µm p-bulk sensor. Clusters of size one and two strips are dominant, clusters with size three or more do not appear very frequently. In red, the output of the simulation model is shown. Again, the simulation reproduces the properties of the clusters quite well, only a small excess on clusters with size three can be noted.

7.2.2 Extension

The model can not only be used to reproduce measurements taken at the ALiBaVa setup, but is capable to extrapolate cluster properties e.g. the cluster size or the binary cluster search as a function of the track incidence angle. Generalizing the simulation setup of the ALiBaVa system, the collimator has been removed and the radioactive source placed directly on top of the sensor. Now, particles are hitting the sensor under a wide angular range, both along and perpendicular to the strip axis. For simplicity reasons, a flat energy spectrum in the range of 0.5 to 2 MeV has been chosen for the electrons, approximating the energy spectrum shown in figure 7.7b.

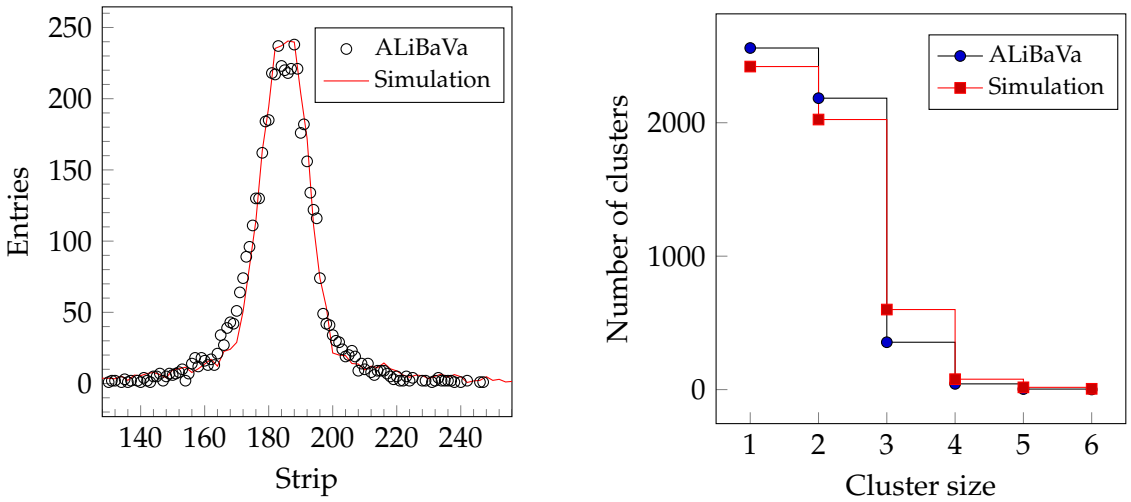

(a) Comparison between simulated and measured hitmap

(b) Distribution of cluster sizes

Figure 7.8.: (a): Comparison between simulated and measured hitmap. The black dots show the number of entries per strip as measured in the ALiBaVa setup, while the solid red line represents the output of the simulation model. The two datasets are normalized to the same number of total entries. (b): Distribution of cluster sizes obtained in the ALiBaVa setup in black and the corresponding simulation in red. Clusters containing one and two strips are dominating, while clusters with size three and more strips are rare. This is reproduced by the simulation.

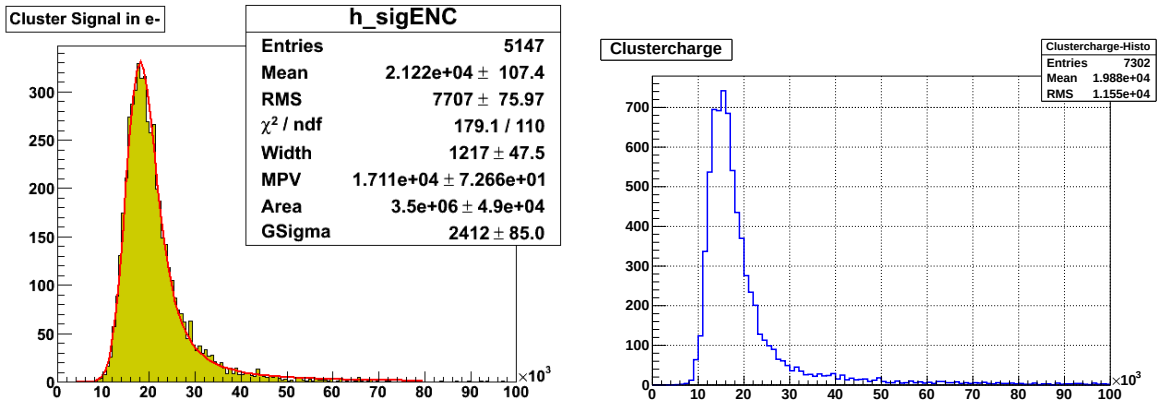

(a) ALiBaVa

(b) Simulation

Figure 7.9.: Cluster pulse height spectrum obtained in a 200 µm thick non-irradiated float zone silicon sensor (a) and simulated spectrum (b). Both distributions show a most probable value of 15000 to 17000 electrons, the shape of the landau distribution is similar.

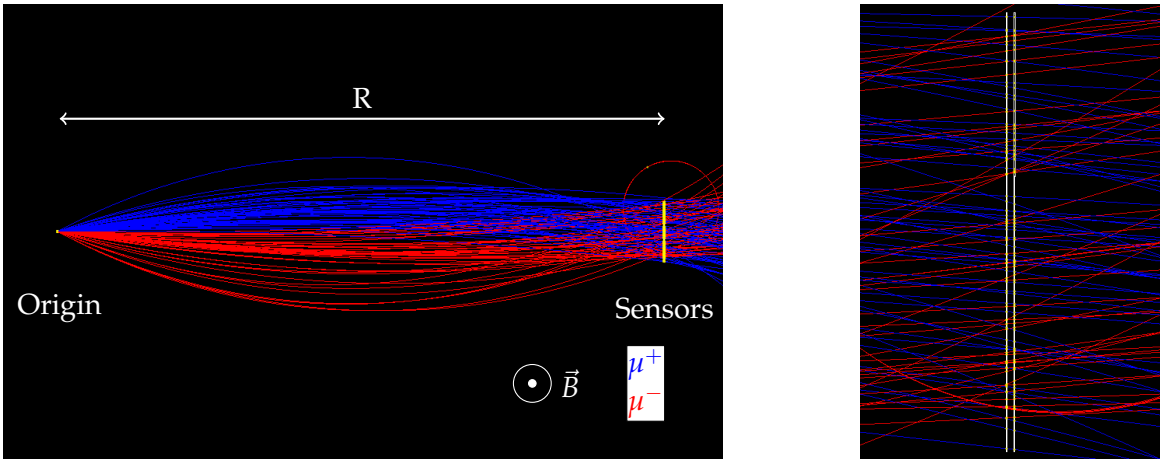

(a) Overview **(b)** Detailed view

Figure 7.10.: (a): Geometry of the Geant4 simulation used to study the trigger efficiency of the 2S module concept. 50 Muons (red) and 50 antimuons (blue) originating the interaction point are hitting a stack of two silicon sensors. The initial momentum of the particles is uniformly distributed in the range of 1 to 10 GeV c^{-1}, the initial momentum direction is set in such a way, that the particle is hitting the sensor stack at a randomized position. (b): Detailed view of the sensor stack. Clearly the offset between the hits on the two sensors can be noted.

7.2.3 Trigger module

In order to study the performance of the trigger module concept, the simulation model outlined in chapter 7.2 has been used. The geometry of the Geant simulation is extended and consists of two closely spaced silicon parts located in a distance R from the particles origin point, as shown in figure 7.10. The size of the sensors is 10 cm $\times$ 10 cm with 1024 strips each. Muons and antimuons are propagated in a 3.8 T magnetic field towards the stack of silicon sensors. The initial momentum is chosen to be uniformly distributed in the range of 1 to 10 GeV c^{-1}, the initial momentum direction is set in such a way, that the particle is hitting the sensor stack at a randomized position, as illustrated in figure 7.10. The distance between the origin of the particles and the sensor, as well as the sensor spacing is chosen to correspond to one of the barrel layers in the current layout for the new tracker.

7.3 T-CAD

The finite elements method is a technique for the numerical solution of partial differential equations. The object is divided into a large number of small and simple elements of finite size. Taking initial values and boundary conditions, the differential equation is solved for these simpler elements using numerical methods and combined to a full solution of the problem. This technique is largely used for the solution of many kind of problems in natural science and engineering.

Silvaco Atlas is a finite elements program for the physics-based simulation of the electrical, optical and thermal behavior of semiconductor devices in two and three dimensions [Sil]. With Silvaco Atlas, a magnetic field can be include in the calculation. Thus it allows the simulation

of the Lorentz angle measurements shown in chapter 9, where the silicon sensors have been operated in magnetic fields of up to 8 T.

7.3.1 Basic steps

The basic work flow when simulating a sensor with a finite elements simulation program is:

1. Definition of the sensor geometry and doping profiles
2. Generation of the simulation mesh
3. Obtain stationary solution at a certain bias voltage
4. Optional: perform transient simulation after particle or laser incident.

As first step, the sensor geometry has to be defined. This is done by applying the used materials and their properties like doping to specific regions in the simulation volume. Figure 7.11a shows a cutout of the used geometry to simulate a strip sensor in detail. In orange, the silicon bulk is shown, covered by a thin layer of silicon dioxide. In that oxide layer, the aluminum readout strips are embedded. The silicon bulk is homogeneously doped either with phosphor or boron. To form the pn-junction, the strip implants are placed using the opposite doping type, as shown by figure 7.11b. The backplane contact is formed accordingly using a Gaussian doping profile. After the regions and doping profiles are defined, the mesh can be created. The mesh divides the volume into small triangles. On the so formed grid, the simulation is solved numerically, respecting the boundary conditions and continuity equations among the mesh points. External connections, like the high voltage on the sensor backplane are considered in the calculation via boundary conditions set to the affected nodes.

The number of mesh points directly influences the needed computing time for solving the differential equations. On the other hand, with a too coarse mesh the accuracy of the solution might be poor, or the calculation might not converge to a static solution at all. The definition of the mesh is for that a crucial step in the simulation process. Here, a fine mesh is created in areas with high gradients in the doping profile near the strip. A coarse mesh is defined in areas with relatively constant doping concentration, like the sensor bulk.

After defining the geometry and the mesh, the backplane contact is ramped in small steps to the desired bias voltage. Per step, the electric field in the sensor has to be evaluated. During the ramp up, the silicon bulk gets more and more depleted and the electric field is formed. Figure 7.13 depicts the strength of the electric field in the sensor bulk as a function of the sensor depth, cut exactly in the center of a readout strip. With rising bias voltage, the field starts growing from the strip side towards the backplane. Except for deviations near the strips due to the focusing of the field lines, the field shows a linear decrease towards the backside. This is comparable to the parameterization given by equation 7.1 used in the one dimensional model, which is shown exemplified in figure 7.2. Near the strips, the field lines bend towards the strip implants, thus leading to an additionally increased strength of the electric field in that area. This effect is shown in figure 7.12b, where the direction of the field vectors is indicated by the arrows. In the bulk area, the field is parallel, pointing towards the sensor backplane.

Finally, after the calculation of the stationary solution of the electric field, time resolved transient simulations can be performed. Charge carriers are created in the device by injection of an ionizing particle or a laser beam. Theses carriers are then propagated in the device for a

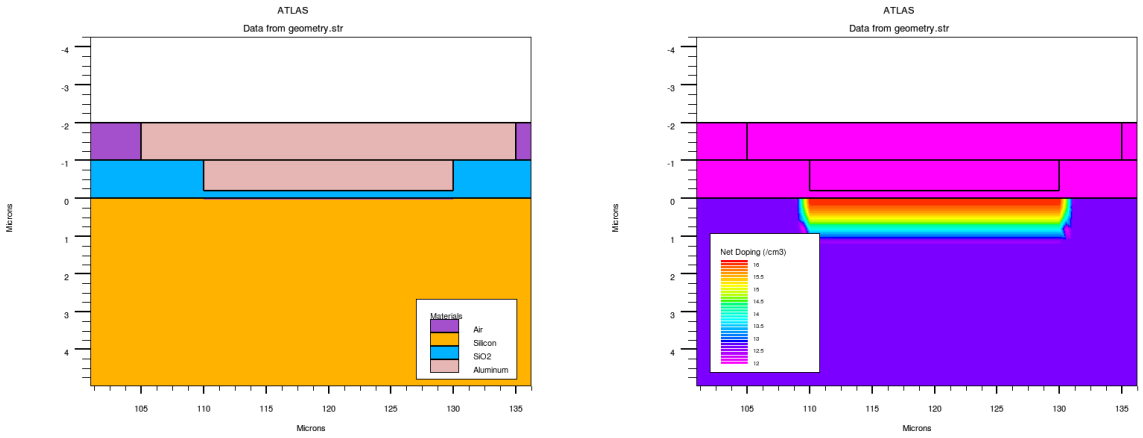

(a) Materials **(b)** Doping

Figure 7.11.: Zoom to the strip region. The geometry and the used materials describing the readout strip geometry (a) and concentration of dopants in the silicon material (b).

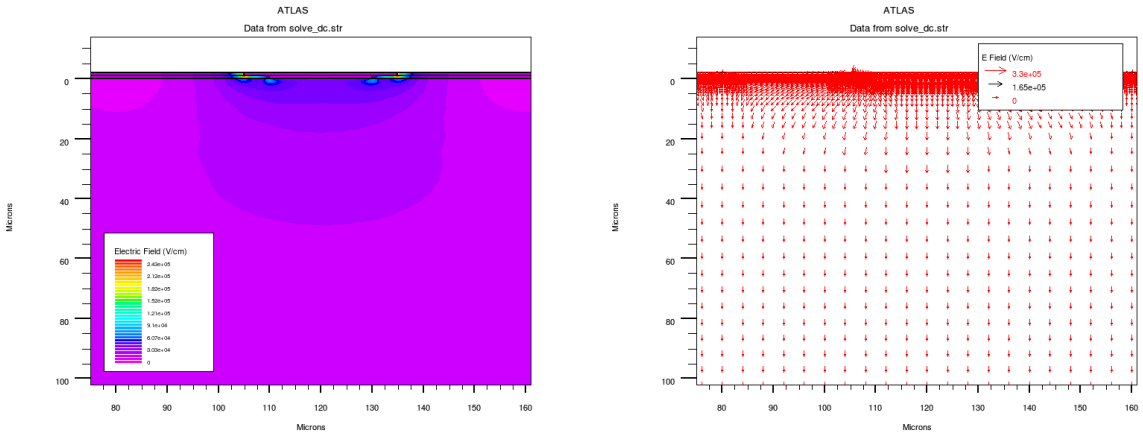

(a) Absolute strength of the electric field **(b)** Direction of the electric field

Figure 7.12.: Electric field near a readout strip. Due to the focusing of the field lines near the readout strip, the strength of the electric field is increased. In the bulk, the field is pointed towards the backside of the sensor.

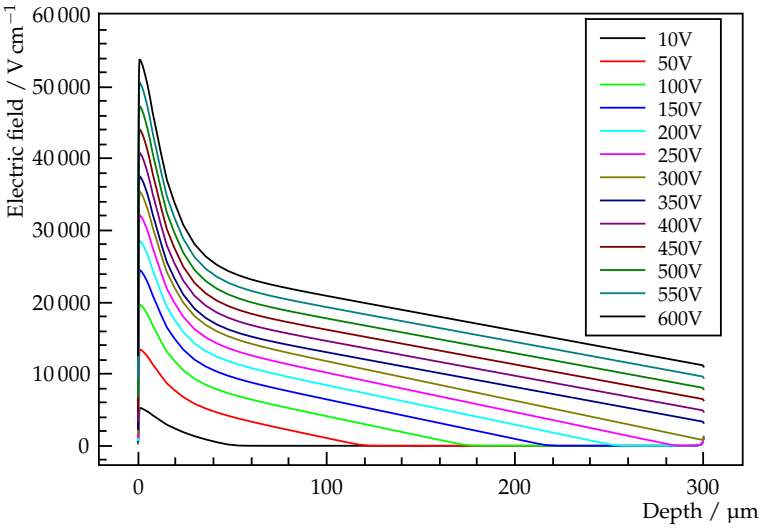

Figure 7.13.: Strength of the electric field in the sensor bulk at several steps during the ramp up of the applied backplane voltage. A cut exactly in the center of a readout strip is shown. The strips are located at 0 µm, the backplane is at 300 µm. With increasing voltage, the electric field grows towards the sensor backside, showing a linearly increasing strength towards the strips. Close to the strips, the field is increased additionally by focusing effects.

given time period. During their drift, additional current is induced in the readout electrodes. Integrated over the readout time, this corresponds to the charge signal that a readout chip would obtain. Figure 7.14 shows the electron density distribution in a p-bulk sensor at nine consecutive time steps after an 880 nm laser pulse has been injected to the sensor backside in the center between strip one and two. The electrons drift towards the readout strips, the holes are collected by the backside electrode. Due to the definition of a 4 T magnetic field, the electrons are deflected by the Lorentz force and do not drift straight towards the readout strips. By varying the strength of the magnetic field, the Lorentz angle measurements depicted in chapter 9 can be reproduced.

The time resolved current in all five simulated readout strips is shown in figure 7.15b for a time period of 10 ns. The second and third strip carry most of the signal, as these are the strips, that collect most of the induced charge (compare figure 7.14). After a time of approximately 10 ns, all charges created by the laser have been collected at the electrodes of the device and the induced current in the readout electrodes is zero again. For comparison, figure 7.15a shows the induced currents in the readout strips without the presence of the magnetic field. Now, strip one and two collect the most charge, as the laser is hitting in the center between these two strips.

The integrated charge signals are fed to the same analysis code as the measurement data. By that, it can be assured, that simulated and measured data are analyzed and interpreted in a similar way.

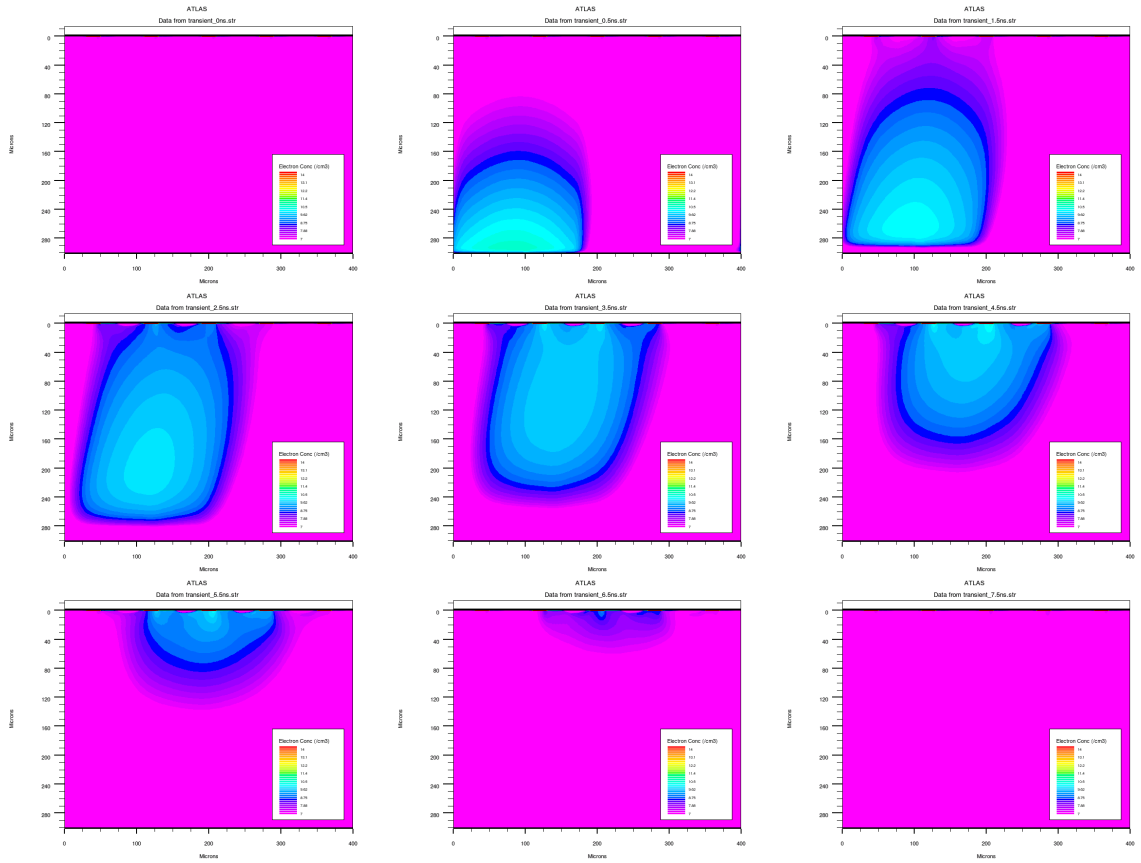

Figure 7.14.: Transient simulation: electron density distribution at nine consecutive timesteps after the injection of a 880 nm laser pulse to the sensor backside. The electron density is color coded in a logarithmic way, ranging from concentrations of 1×10^7 to $1 \times 10^{14}\,\mathrm{cm}^{-3}$. The electrons that are created at the backside of the sensor drift towards the readout strips and are deflected by a 4 T magnetic field.

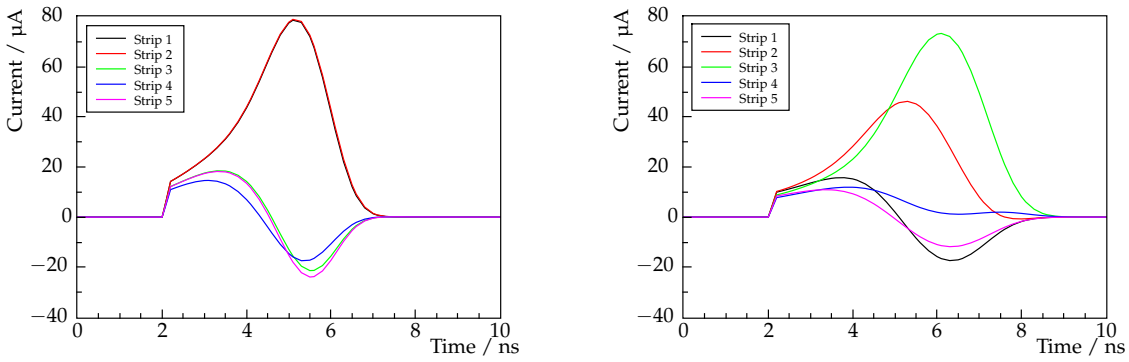

(a) Transient 0T **(b)** Transient 4T

Figure 7.15.: Time resolved current in the ac-coupled readout electrodes. After the laser incident, the drifting charges induce a current in the strips. After approximately 10 ns, all created charges have been collected at the electrodes and the current is zero again. At zero magnetic field, strip one and two collect exactly the same amount of charge, as the laser incident is in the middle of these two strips. With larger magnetic field, the charge gets deflected and strip two and three collect most of the signal.

Table 7.4.: Modified Five-defect model, based on [Dal+13] [Dal13].

Type	Energy / eV	Concentration / cm^{-3}	σ_{e^-} / cm^{-2}	σ_{h^+} / cm^{-2}
Acceptor	$E_C - 0.525$	$3 \times F$	1×10^{-14}	1.4×10^{-14}
Acceptor	$E_C - 0.45$	$4 \times F$	8×10^{-15}	2×10^{-14}
Acceptor	$E_C - 0.4$	$4 \times F$	8×10^{-15}	2×10^{-14}
Donor	$E_V + 0.5$	$0.6 \times F$	4×10^{-15}	4×10^{-15}
Donor	$E_V + 0.45$	$2 \times F$	4×10^{-15}	4×10^{-15}

Table 7.5.: Two-defect model for proton irradiation, [Ebe13]

Parameter	Donor	Acceptor
Energy / eV	$E_V + 0.48$	$E_C - 0.525$
Concentration / cm^{-3}	$5.598\,\mathrm{cm}^{-1} \times F - 3.949 \times 10^{14}$	$1.189\,\mathrm{cm}^{-1} \times F - 6.434 \times 10^{13}$
σ_{e^-} / cm^{-2}	1×10^{-14}	1×10^{-14}
σ_{h^+} / cm^{-2}	1×10^{-14}	1×10^{-14}

7.3.2 Defect levels

Radiation induced damage of the silicon lattice generates new energy states for electrons and holes in the otherwise forbidden band gap. This damage can be included in the simulation by adding effective energy levels in the band gap. These energy states are chosen in a way that they reproduce the macroscopic properties of the sensor, like leakage current, depletion voltage and charge collection efficiency. Table 7.4 summarizes an effective five-defect model obtained by Dalal et al. [Dal+13] on diodes and strip sensors in the HPK campaign. The model consists of three acceptor states at 0.525 eV, 0.45 eV and 0.4 eV below the conduction band and two donor states 0.5 eV and 0.45 eV above the valence band. The defect concentration depends on the fluence and is parametrized linearly. Each defect level has a cross section for an interaction with an electron or hole, describing the probability of releasing or capturing a charge carrier.

Being electrically active, the states contribute to the effective doping concentration and so have an influence on the distribution of the electric field in the sensor bulk. By that, they influence also the Lorentz shift, as shown by the measurements in chapter 9. Figure 7.16 illustrates the effect of the defects on the distribution of the electric field in a p-bulk sensor at a bias voltage of 600 V. After an irradiation to a fluence of $1 \times 10^{15}\,\mathrm{n_{eq}}/\mathrm{cm}^2$, the electric field is concentrated near the strips and the backside of the sensor.

Figure 7.17 illustrates a comparison between the field distribution in the sensor using the modified 5-trap model outlined in table 7.4 and the 2-trap model developed by Eber [Ebe13] outlined in table 7.5 using a different T-CAD simulation package, namely Synopsys Sentaurus Device [Syn]. Qualitatively, the shapes of the field distributions are similar.

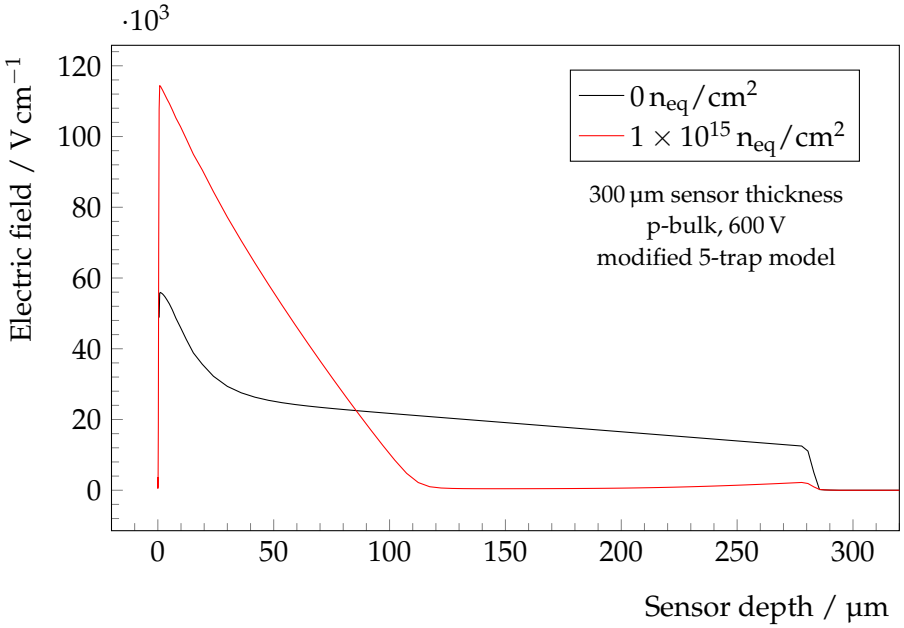

Figure 7.16.: Electric field distribution in a silicon strip sensor. Comparison between an non-irradiated sensor and a sensor irradiated to $1 \times 10^{15}\,\mathrm{n_{eq}/cm^2}$ using the five-trap model as given by table 7.4.

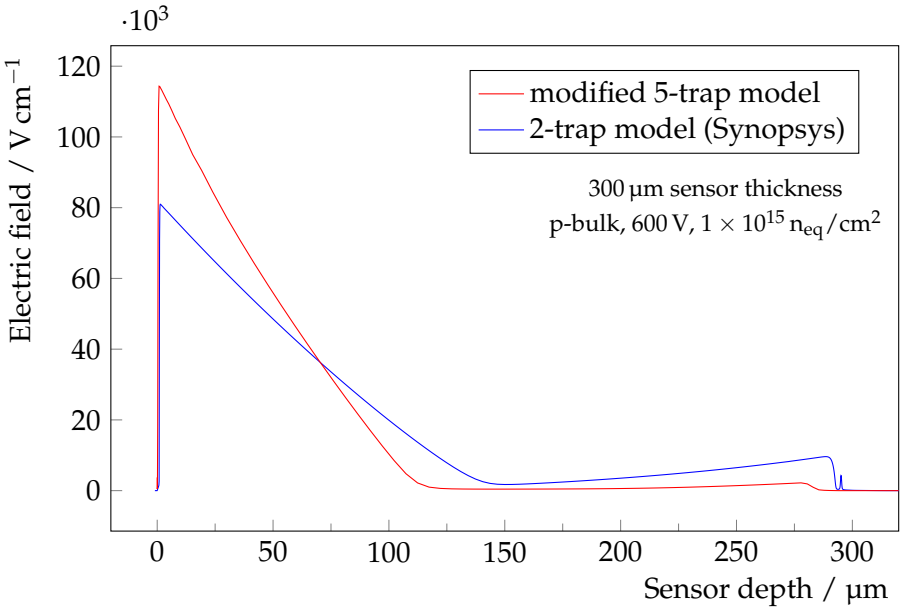

Figure 7.17.: Electric field distribution in an irradiated silicon strip sensor after a fluence of $1 \times 10^{15}\,\mathrm{n_{eq}/cm^2}$. Comparison between the field distribution obtained with the modified 5-trap model as given in table 7.4 using Silvaco Atlas and the two trap model developed by Eber [Ebe13] using the Synopsys Sentaurus Device package.

Part III.

Results and discussion

8

Sensor qualification

Properties of silicon sensors change under irradiation with particles. For the damage during operation in a tracking detector at a LHC experiment, non-ionizing interactions of charged and neutral hadrons with the sensor bulk material are the most important interactions. Displacement of atomic nuclei from the silicon lattice introduce defects in the material, which are manifested as additional energy states for electrons in the otherwise forbidden band gap. Depending on the electric properties and the exact energy level, defects influence the macroscopic properties of the sensor in several ways.

Prior to the further investigation of the sensors used for the measurements in this work, the sensors have been characterized in order to investigate the influence of the performed irradiation to the macroscopic sensor parameters, especially the leakage current and the full depletion voltage.

8.1 Leakage current

The leakage current of all irradiated HPK test sensors which have been investigated in this work has been measured before and after each irradiation step. The leakage current scales with the sensor thickness, as can be seen from figure 8.1a where the measured IV characteristics of 3 irradiated n-bulk sensors are shown as an example. The 320 µm thick sensors show always a higher leakage current than the 200 µm and 120 µm thick devices, except for the beginning breakdown at high voltages of the thinnest sensor.

For a better comparison among the sensors and to the expectation from the Hamburg model, figure 8.2 shows the leakage current of the investigated baby strip sensors normalized to the sensor bulk volume as a function of the irradiation fluence. The linear increase as expected from equation 4.1 is clearly visible. The leakage current is independent of the type of bulk doping and, in the p-bulk sensors, independent on the strip isolation technique of either p-stop or p-spray. The small offset between the neutron only irradiated sensors and the mixed neutron and proton irradiated sensors comes from an additional annealing of 10 min at 60 °C after the second irradiation. As expected, the damage created by the neutrons is thus a bit further

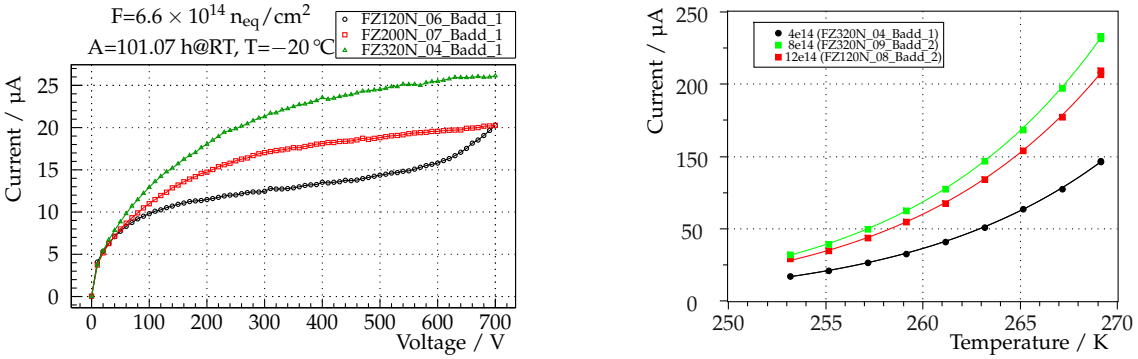

(a) IV characteristic of FZ n-bulk sensors

(b) IT-curves

Figure 8.1.: (a) The IV characteristic of three float zone n-bulk sensors with different thickness is shown. All three sensors follow the characteristic square root shaped increase of the current with bias voltage. The absolute value of the current scales with the sensor thickness. In the 120 µm thick sensor, a beginning soft break down is visible at voltages above 500 V. (b): Measured leakage current as a function of the sensor temperature, for three different irradiated float zone n-bulk sensors. The lines are fit to the data points according to equation 4.2, but with the effective band gap as an additional free parameter.

annealed and the leakage current is a bit smaller compared to the neutron only irradiated sensors.

In order to extract the damage rate α, the measured leakage currents have been normalized to the sensors volume. Now, all data points fit more or less on a straight line. Fitting and evaluating the slope results in an average damage rate of

$$\alpha = (1.3 \pm 0.2) \times 10^{-18}\,\mathrm{A\,cm^{-1}}$$

at the temperature of $-20\,°\mathrm{C}$ for the mixed irradiated sensors. The leakage current in some sensors is 10 to 50 % higher than the expectation, which is however based on measurements on diodes rather than strip sensors.

The leakage current is strongly dependent on the sensor temperature. As an example, figure 8.1b shows the measured leakage current as a function of the temperature for three different irradiated sensors in the range of -20 to $-4\,°\mathrm{C}$. The lines are fits to the data points according to the expected temperature scaling given by equation 4.2, the effective band gap obtained from the average of the three fits is (1.193 ± 0.004) eV, which is close to the recommended value of 1.21 eV by Chilingarov [Chi13].

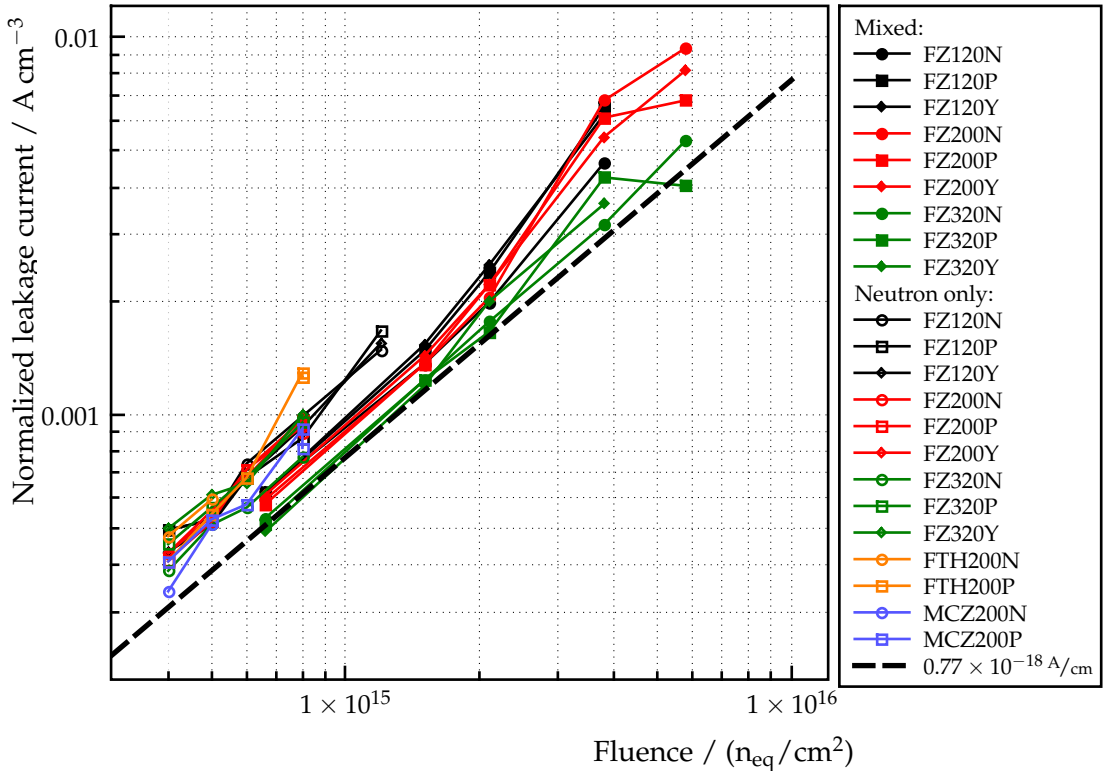

Figure 8.2.: Leakage current as measured for all investigated irradiated HPK sensors. The current has been normalized to the sensor bulk volume. The fact that the datapoints now lie on top of each other shows that the leakage current is proportional to the sensor volume. The dashed line indicates the expected value corresponding to a damage factor α of 0.77×10^{-18} A cm^{-1} after the proton irradiation and the applied annealing of 20 minutes at 60 °C. Data partly published by Dierlamm [Die12].

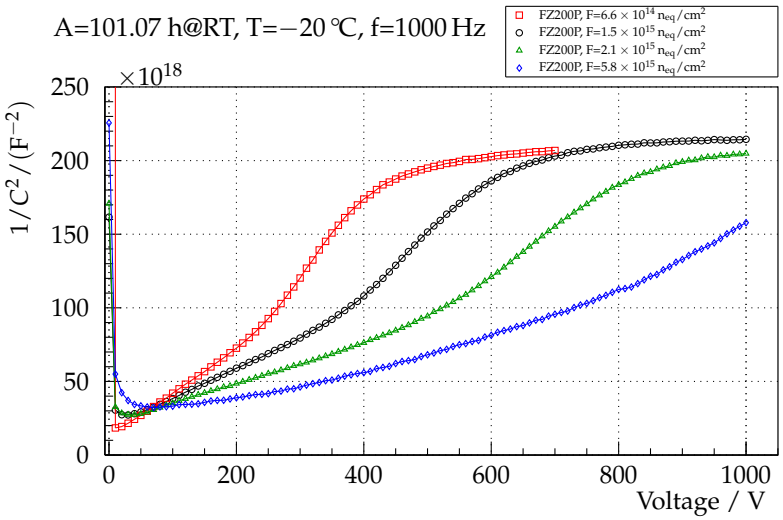

Figure 8.3.: Capacitance voltage characteristic: The inverse squared capacitance of four irradiated 200 µm thick float zone sensors is plotted as a function of the applied bias voltage. With rising bias voltage the capacitance lowers, until the sensor is fully depleted. At this point, the capacitance stays constant, even if the bias voltage is increased further. The depletion voltage increases with irradiation fluence, as the kink is moving to the right with fluence.

8.2 Full depletion voltage

The full depletion voltage of all investigated sensors has been evaluated by measuring the total capacitance as a function of the applied bias voltage. By plotting the inverse capacitance as a function of the applied bias voltage, the depletion voltage can be evaluated as the voltage, at which the capacitance curve shows a kink and turns into a constant. Figure 8.3 depicts four exemplary curves, showing the capacitance obtained in irradiated 200 µm thick float zone sensors. Summarizing, figures 8.4a to 8.4c show the obtained depletion voltages of all investigated HPK sensors as a function of the irradiation fluence before and after each irradiation step. A rise of the depletion voltage is visible for all irradiated sensors, also the n-bulk sensors. Already after the lowest irradiation point of $4 \times 10^{14}\,\mathrm{n_{eq}/cm^2}$ the n-bulk is type inverted and the depletion voltage is higher than before irradiation. Even though the initial drop is not visible, the depletion voltage of the n-bulk sensor is systematically lower than the depletion voltage of the p-bulk sensors. As expected, the depletion voltage is lower in the thin sensors than in the thick sensors. At high fluences and in the 320 µm thick sensors, the silicon bulk can not be fully depleted at the highest applied bias voltage of 1000 V. For these sensors, only a lower limit can be given.

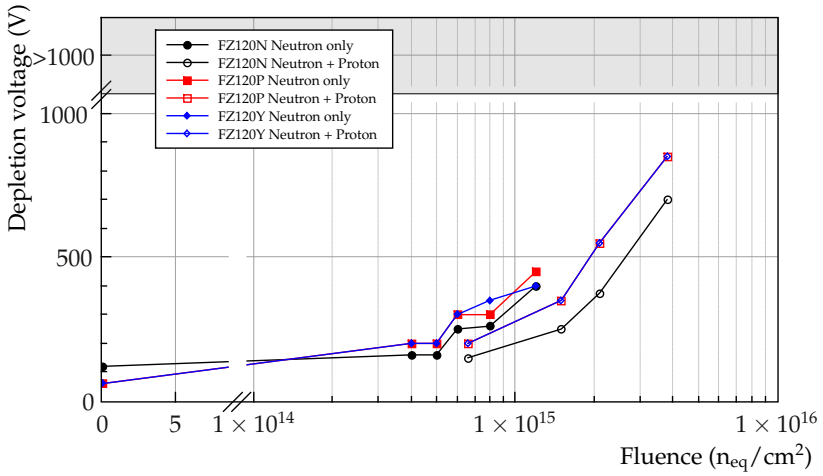

(a) FZ120

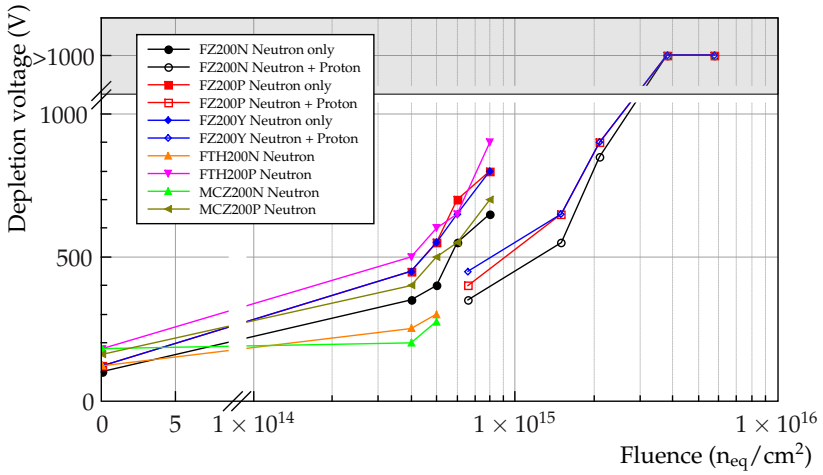

(b) FZ200, FTH200 & MCZ200

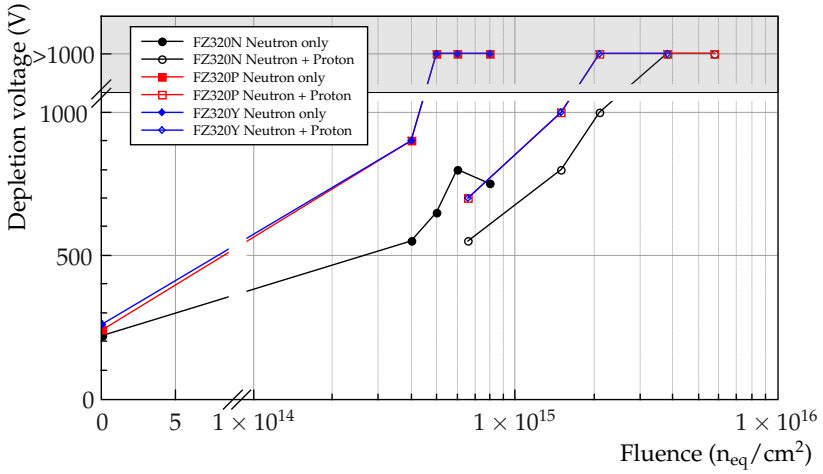

(c) FZ320

Figure 8.4.: Depletion voltage as a function of irradiation fluence, as measured in all investigated HPK sensors. The plots are divided by sensor thickness. The depletion voltage is lower in the thin sensors than in the thicker ones. Because of the type inversion effect, the n-bulk sensors show a lower depletion voltage than the p-bulk sensors. Data partly published by Dierlamm [Die12].

Table 8.1.: Calibration factors for the different laser fibers and mapping to the different sensors.

Fiber	calibration factor	Irradiation HPK / (n_{eq}/cm^2)	Irradiation Micron / (n_{eq}/cm^2)
1	0.721	5.8×10^{15}	—
2	0.965	3.8×10^{15}	1×10^{15}
3	0.875	2.1×10^{15}	—
4	1.1	1.51×10^{15}	2.6×10^{14}
5	0.748	6.61×10^{14}	—
6	0.721	0	1×10^{15}

8.3 Charge collection efficiency and annealing

8.3.1 Lorentz angle sensors

As a side product of the performed Lorentz angle measurements outlined in chapter 6.2.1, the charge collection efficiency of the sensors has been investigated. All sensors are illuminated from the backside with a 1055 nm laser, which penetrates the whole sensor thickness, like an ionizing particle would do. The generated charge is collected at the readout strips. For calibration of the laser intensities among the different lines of the beam splitter, a non-irradiated sensor has been used. Table 8.1 lists the applied calibration factors.

Figure 8.5 shows the charge collection efficiency (CCE) after 77 days of equivalent room temperature annealing as a function of the irradiation fluence of the 320 µm thick float zone HPK sensors with n-bulk and p-bulk at a bias voltage of 600 V. A drop of the charge collection efficiency with irradiation fluence is visible for both material types. While the p-bulk sensors give a detectable charge signal even after the highest irradiation fluence of $5.8 \times 10^{15}\,n_{eq}/cm^2$, the loss of signal in the n-bulk sensors is much more pronounced. There, only below fluences of $2.1 \times 10^{15}\,n_{eq}/cm^2$, a signal could be detected. At $2.1 \times 10^{15}\,n_{eq}/cm^2$, the signal could only be extracted due to the averaging of 500 events. The increased CCE at this point compared to the previous fluence may additionally be influenced by non-Gaussian noise contributions. The sensors irradiated to the even higher fluences showed a steeply increasing noise and no detectable signal. The faster loss of signal in the n-bulk sensors can be explained with the fact, that they collect holes at the readout strips. Due to the lower mobility of holes compared to electrons and their longer drift time in the sensor bulk, they are more likely to be trapped by defects and do no longer contribute to the readout signal.

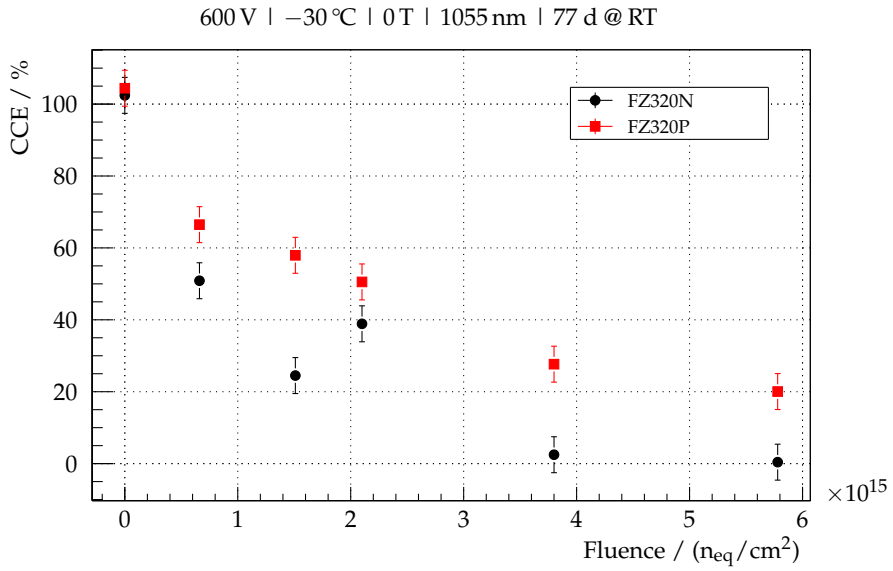

Figure 8.5.: Charge collection efficiency of irradiated FZ320 sensors as a function of the irradiation fluence. The maximum of the beneficial annealing of 77 days room temperature equivalent is shown. For both kinds of bulk doping, a drop of CCE is visible. While the p-bulk sensors show a signal even after the highest irradiation fluence of $5.8 \times 10^{15}\,\mathrm{n_{eq}/cm^2}$, the n-bulk sensors give no signal at fluences greater than $2.1 \times 10^{15}\,\mathrm{n_{eq}/cm^2}$.

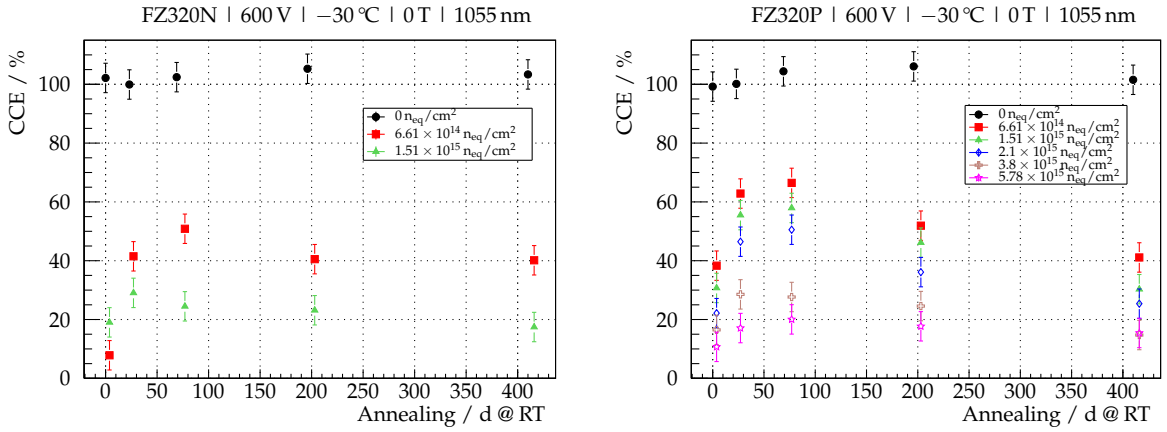

(a) FZ320N

(b) FZ320P

Figure 8.6.: Charge collection efficiency of (a) FZ320N and (b) FZ320P sensors at a bias voltage of 600 V as a function of the equivalent room temperature annealing. The signals are induced using a 1055 nm laser. The scaling is relative to the non-irradiated sensor. During the first 75 days, the signal in the irradiated sensors recovers, while it drops again after longer annealing times.

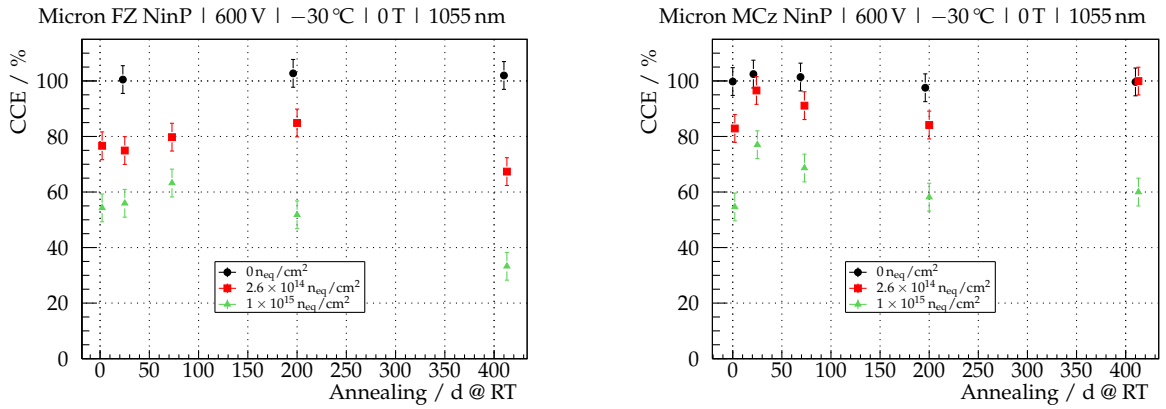

(a) float zone **(b)** magnetic czochralski

Figure 8.7.: Charge collection efficiency of Micron (a) float zone and (b) MCz sensors at a bias voltage of 600 V as a function of the equivalent room temperature annealing. For the MCz sensors, the over all charge collection is higher and they do not suffer as pronounced as the FZ sensors on reverse annealing effects.

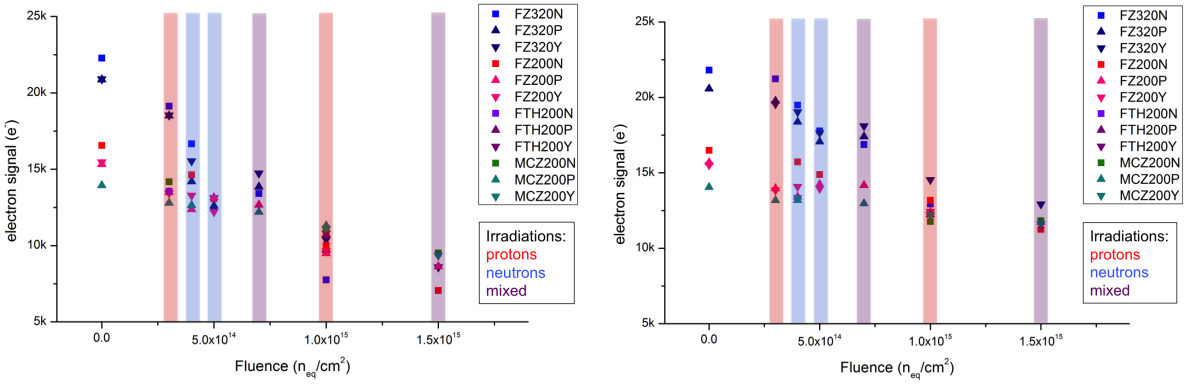

(a) 600V **(b)** 900V

Figure 8.8.: Collected charge as a function of the irradiation fluence [Hof13].

8.3.2 ALiBaVa

For comparison, the results on charge collection as a function of the irradiation fluence and the annealing time as obtained by Hoffmann [Hof13] using the ALiBaVa setup are summarized by figures 8.8 and 8.9. The overall shape of the results obtained with the radioactive source is similar to what has been measured using the infrared laser. In figure 8.8, the collected charge as a function of the irradiation fluence is shown for the various materials available in the HPK campaign. At 900 V, the advantage of the higher signal of the 300 µm sensors can be seen up to $1.5 \times 10^{15}\,\mathrm{n_{eq}/cm^2}$, while at 600 V this almost relativizes already at a fluence of $7 \times 10^{14}\,\mathrm{n_{eq}/cm^2}$ [Hof13].

The dependence of the electron signal of sensors irradiated to $1.5 \times 10^{15}\,\mathrm{n_{eq}/cm^2}$ on the annealing time is shown in figure 8.9 at (a) 600 V and (b) 900 V. The signal of the 200 µm sensors keeps constant, while the signal for the 300 µm sensors decreases. At higher voltages, the decreased signal of the 300 µm sensors is comparable to the signal of the thin sensors

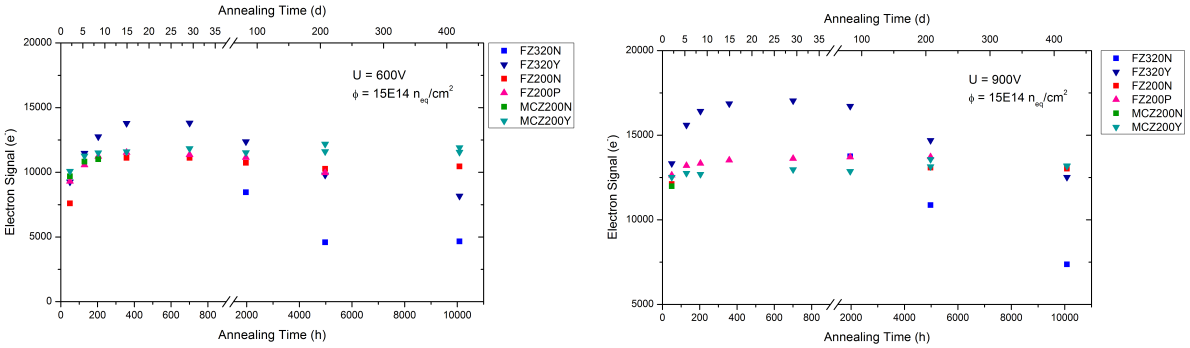

(a) 600V **(b)** 900V

Figure 8.9.: Dependence of the electron signal of sensors irradiated to 1.5×10^{15} n_{eq}/cm^2 on the annealing time [Hof13].

at an annealing time of about 400 days at 21 °C. Only the signal of the FZ320N decreases dramatically [Hof13].

8.4 Noise

Besides the charge collection efficiency, which determines the size of the signal, also the noise is an important parameter. The ratio between signal and noise affects directly the hit reconstruction efficiency and resolution. Using several different readout systems in different institutes during lab measurements (e.g. by Erfle [Erf14]) and beam tests, especially the n-bulk sensors in the HPK campaign have been found to be affected by an increased noise after irradiation with protons. The effect depends on the applied bias voltage and the state of annealing of the sensor. To study the effect in more detail, a dedicated noise run has been performed on two irradiated n-bulk MSSD modules. Figure 8.10 shows the width of the Gaussian kernel fitted to the noise distributions as a function of the applied bias voltage. The 12 regions are considered separately. A clear hierarchy in the turn-on voltage of the noise among the regions is observed. With rising bias voltage, the regions with the largest electric field at the strips are affected first, namely the regions with the largest strip pitch and the smallest width to pitch ratio. Step by step, all other regions show an increase in the noise as well, until at a bias voltage of 1000 V all regions are affected. The increase in noise prevents a proper operation of the sensors, as after irradiation a high bias voltage is needed to gain a large signal.

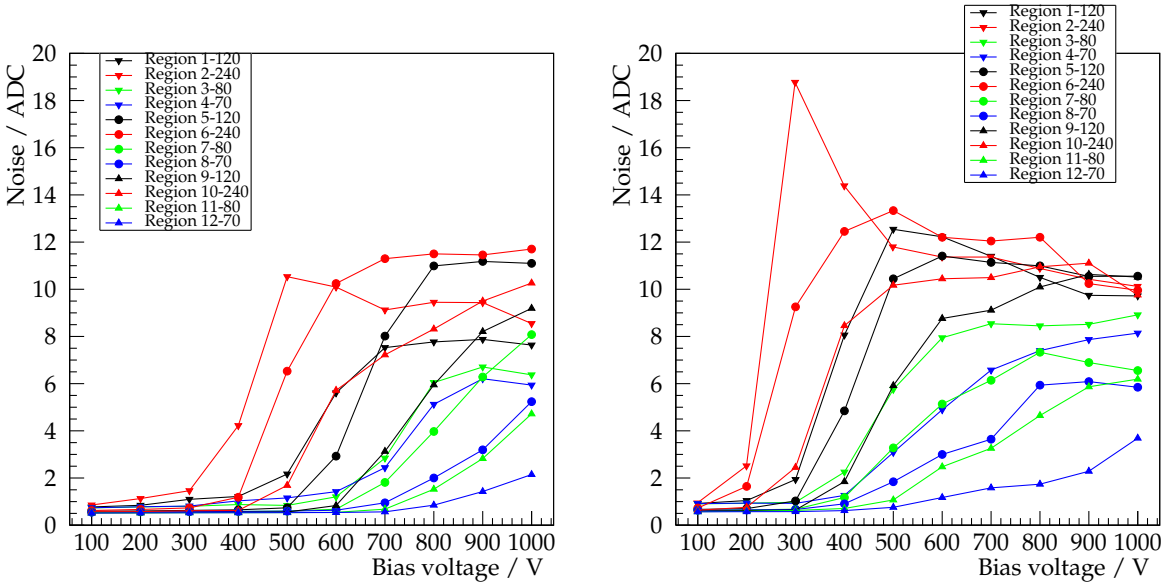

(a) FTH200N **(b)** MCz200N

Figure 8.10.: Width of the Gaussian kernel of noise distributions of proton irradiated n-bulk MSSD sensors as a function of the bias voltage, separately for the 12 different strip geometry regions. The sensors are irradiated to a fluence of $1.5 \times 10^{15}\,\mathrm{n_{eq}/cm^2}$, the annealing is approximately 110 days@RT.

8.4.1 Random Ghost Hits

In addition to the broadened noise distribution, a non symmetric noise contribution which is faking particle hits is present in the n-bulk sensors. Being as large as real charge clusters, the ghost hits can not be distinguished from clusters originating from particle tracks. In order to quantify the effect, the ghost hit occupancy has been calculated as the number of strips above a 5σ noise cut divided by the number of events and strips on the sensor. Figure 8.11 illustrates the occupancy as a function of the bias voltage. As for the symmetric noise, also the ghost hits appear hierarchically ordered from region to region. Despite the increasing noise at high voltages, the strip occupancy reaches levels of over 5 to 10 %, which impedes the operation as a tracking detector.

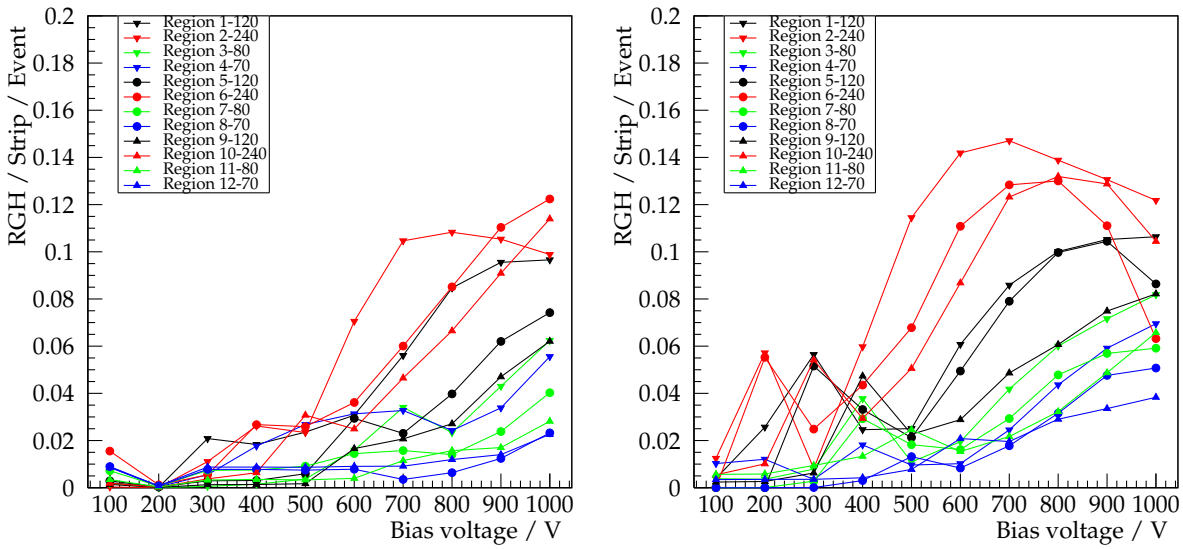

(a) FTH200N **(b)** MCz200N

Figure 8.11.: Occupancy of irradiated n-bulk MSSD sensors by random hits during a pedestal run as a function of the bias voltage. Being as high as 5 to 10 % in some regions, the noise occupancy impedes the operation as a tracking detector.

9 Lorentz angle

Charges created in the silicon sensors of the CMS Tracker by ionizing particles are affected by the magnetic field present in the CMS detector. This leads to a systematic shift in the read out position of the charge and to a degradation of tracking performance, if not corrected during track reconstruction. As the sensors are exposed to a harsh radiation field, sensor properties are going to change and the shift will evolute with time and integrated luminosity. To be able to predict the evolution of the Lorentz angle with sensor degradation, irradiated test sensors have been operated at various conditions in a superconducting magnet at the Institute for Technical Physics of KIT. In addition, the Hall mobility of the holes in the silicon sensors of the CMS Strip Tracker has been measured using particle tracks.

9.1 Non-irradiated sensors

In the following part, the non-irradiated sensors are investigated, starting with the dependence of the Lorentz angle and hall mobility of electrons and holes on the magnetic field, the applied bias voltage and the temperature. Afterwards, an overview over the obtained results in the irradiated sensors is given, adding the dependence of the irradiation fluence and equivalent annealing time.

9.1.1 Magnetic field

Figure 9.1a shows the obtained shift for various non-irradiated sensors with various thickness and both types of bulk doping at a bias voltage of 300 V as a function of the magnetic field. Here, the 1055 nm laser was used. First of all, a clear linear increase of the Lorentz shift with the magnetic field is visible. Due to the different charge sign, the shift of electrons is in the opposite direction than the shift of holes. The direction of the magnetic field and the orientation of the sensors in the magnet is in such way, that the resulting shift of holes is in the positive direction and the shift of electrons in the negative direction. Compared to the shift of holes, the absolute shift of electrons is about three to four times larger. This is due to the higher mobility

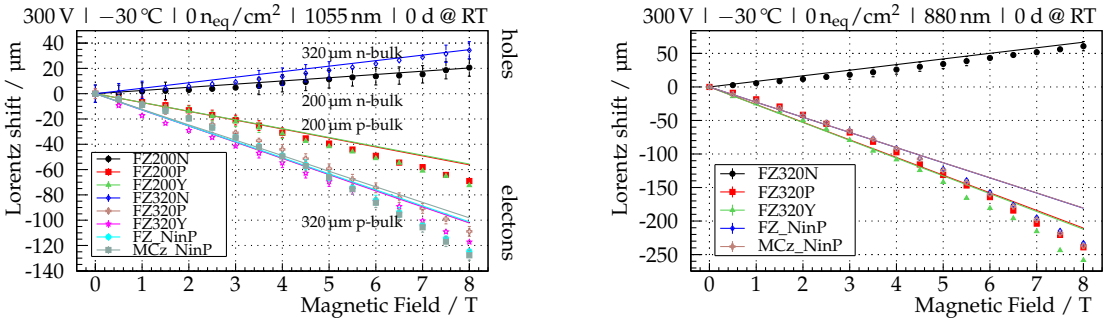

(a) 1055 nm laser

(b) 880 nm laser

Figure 9.1.: Lorentz shift as a function of the magnetic field for electrons and holes, measured using the 1055 nm and the 880 nm laser. The Lorentz shift shows a linear increase with the magnetic field. The shift of holes is in the opposite direction to the shift of electrons, and the shift of electrons is about four times larger than the shift of holes. This is due to the higher mobility and larger hall scattering factor of electrons. The shift is larger in 320 µm thick devices compared to 200 µm thick sensors as the drift distance is longer. As expected, the shift using the 880 nm laser is about twice as large as the resulting shift using the 1055 nm laser. The solid lines represent the output of the simulation model.

and higher hall scattering factor of the electrons. The shift is larger in 320 µm thick sensors than in 200 µm thick sensors, which is a geometric effect. The angle under which the charge is deflected is proportional to the magnetic field, and not to the sensor thickness. Due to the larger drift distance in thick sensors, the overall shift is larger.

To study the properties of electrons and holes separately, the 880 nm laser is more suitable. Figure 9.1b shows the obtained Lorentz shift in 320 µm thick sensors. Also here, the four times larger shift of electrons compared to the shift of the hole signal is visible. Comparing the shift measured with the different laser wavelengths, the 880 nm laser signal is shifted twice as far as the signal created by the 1055 nm laser. The infrared laser creates charge along the whole sensor depth, thus the obtained shift is an average over the whole sensor thickness.

Taking the shifts shown in figure 9.1b, the tangent of the Lorentz angle Θ_L and the hall mobility μ_H can be calculated following equation 6.1. The resulting Lorentz angle is shown in figure 9.2a as a function of the magnetic field and figure 9.2b shows the hall mobility μ_H as a function of the magnetic field in the range from 2 to 8 T. At lower fields, the shifts are quite small and below the resolution of the measurement. As expected from the Lorentz shift, the resulting hall mobility of electrons is about a factor four larger than the hall mobility of holes.

Several p-bulk sensors have been investigated with different strip isolation techniques as mentioned in chapter 5 and produced by two different vendors. There is no systematic difference in the Lorentz shift observable. This indicates, that the Lorentz angle in non-irradiated sensors is not influenced by the details of the production technique of neither the strip implants nor the bulk material.It depends mainly on operational parameters like the bias voltage or temperature.

During normal operation of the CMS detector, the magnetic field is supposed to be 3.8 T in the tracker volume. Figure 9.3b shows the obtained Hall mobility in the tracker layers during a cosmic run at a magnetic field of 3.8 T. The mobility is slightly higher in the TIB layers than in the TOB layers. This systematic difference lays in the different thicknesses of the silicon

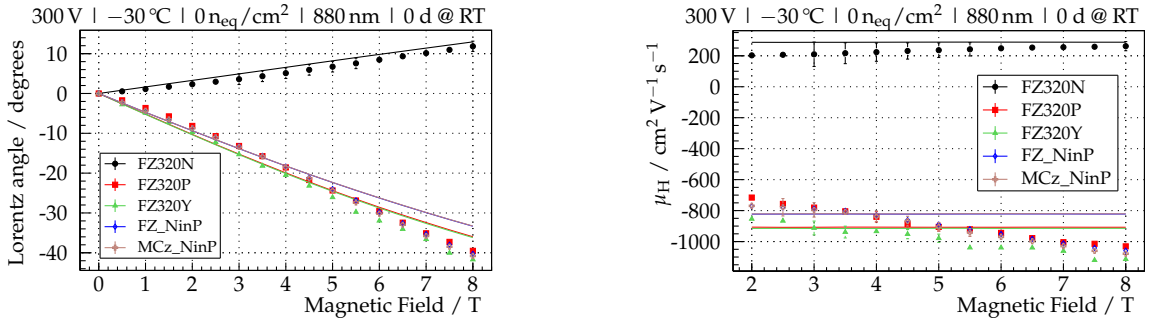

(a) Lorentz angle

(b) Hall mobility

Figure 9.2.: Lorentz angle and Hall mobility of electrons and holes as a function of the magnetic field in the range from 0 to 8 T. The hall mobility μ_H is independent of the thickness of the sensor and the magnetic field. The hall mobility of electrons is about a factor four larger than that of holes. Partly because of the higher drift mobility, partly because of the higher hall scattering factor. The solid lines represent the simulation model.

Table 9.1.: Mean and RMS values of the tangent of the Lorentz angle over all tracker layers obtained during a 0 T run.

Method	mean value of $\tan(\theta_L)$	RMS
prob1	−0.0026	0.04
prob12	−0.000 94	0.003
avgv2	0.000 68	0.003
avgv3	0.000 34	0.01
clusterwidth	−0.000 51	0.004

sensors in TIB and TOB. TIB sensors have a thickness of 300 µm whereas TOB sensors have a thickness of 500 µm. This leads to a lower electric field in the TOB sensors and thus to an increased mobility. Within the sub detectors the mobility shows no clear trends, indicating that the mobility is dominated by the sensor geometry and not yet by radiation damage. Otherwise a radial trend is to be expected.

During maintenance periods, the magnet is ramped down and cosmic particles have been recorded without the presence of a magnetic field. The resulting Lorentz angle is shown in figure 9.3a for the different layers of the tracker using all four estimators. The resulting Lorentz angle is zero within statistical fluctuations for all layers and methods, as expected. Table 9.1 shows the mean and rms values over all tracker layers for the different methods. Within the statistical fluctuations, the mean values are compatible with zero, the rms values are lowest for the average variance method using two-strip clusters and the prob12 method. This indicates a higher precision for these two methods compared to the others.

The 0 T analysis can not be performed with collision tracks. They are all originating from the center of the detector and are hitting the silicon modules without being bend by the Lorentz force at a perpendicular angle. A study of the cluster size as a function of the incidence angle is not possible. Cosmic particles hit the detector modules at different angles, even without magnetic field.

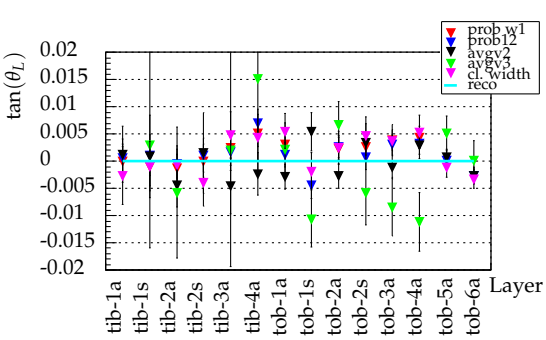

(a) Lorentz angle in the different layers of the CMS tracker during a Cosmic run without magnetic field. As expected, the resulting Lorentz angle is zero within statistical fluctuations for all layers and methods.

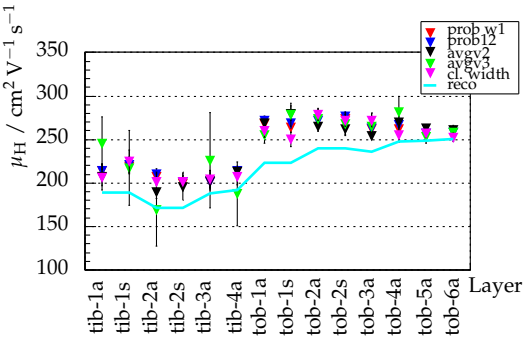

(b) Hall mobility as a function of tracker layer obtained for a cosmic run at a magnetic field of 3.8 T. The mobility is slightly lower in the TIB layers, originating from the thinner sensors used there, compared to the TOB.

Figure 9.3.: Lorentz angle in the CMS tracker.

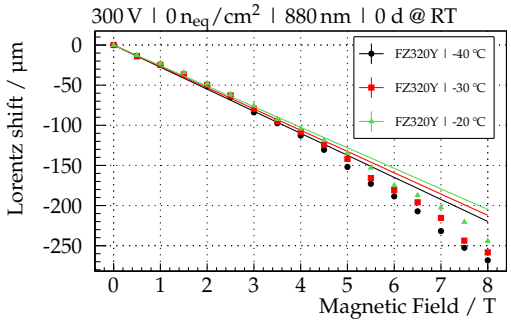

(a) Electrons

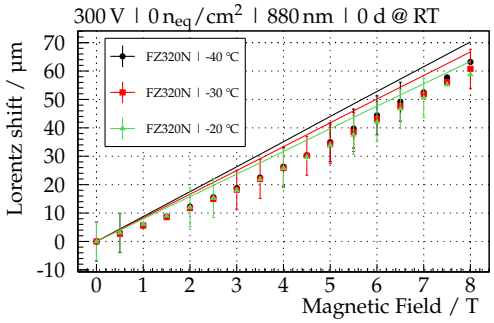

(b) Holes

Figure 9.4.: Lorentz shift of electrons (a) and holes (b) in non-irradiated sensors at different temperatures. At high magnetic fields, the temperature dependence of the shift is visible, with higher temperature the shift is lowered.

9.1.2 Temperature

The mobility of charge carriers in a semiconductor is dependent on the temperature. With increasing temperature, the mobility is lowered, as discussed in chapter 3.2. This trend is also reflected in the Lorentz angle. Due to the limited temperature range of -20 to -40 °C and the limited resolution of the measurement, the effect is best visible at high magnetic fields and low bias voltages.

Figure 9.4 shows the Lorentz shift and Hall mobility of electrons and holes in non-irradiated 320 µm thick floatzone sensors as a function of the magnetic field for three different temperatures. For both, electrons and holes, the mobility decreases with rising temperature and the effect is more pronounced for electrons than for holes.

Summarizing the measurements of the temperature dependence of the Lorentz shift and hall mobility of electrons in non-irradiated devices, figure 9.5a gives an overview over the Hall mobility in all 320 µm thick p-bulk sensors at 8 T and 300 V using the red laser. A trend to larger shifts at lower temperature is visible. The sensors produced by Micron show a slightly

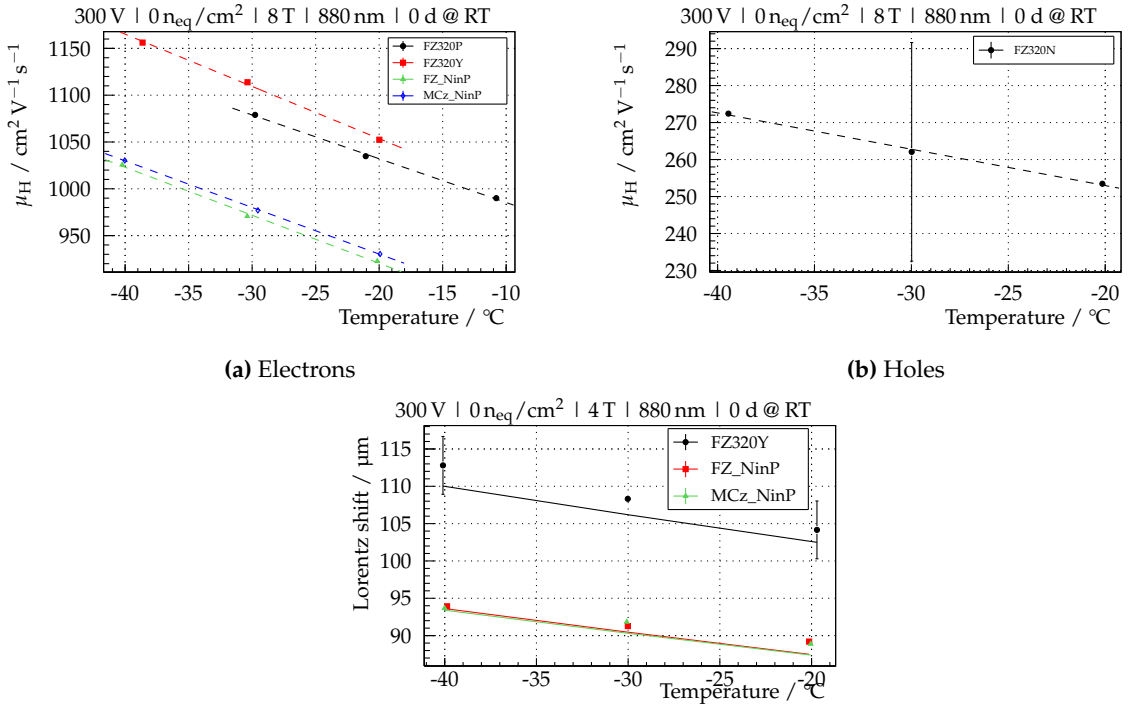

(a) Electrons

(b) Holes

(c) Electrons: comparison to simulation

Figure 9.5.: Hall mobility of electrons (a) and holes (b) as a function of the silicon temperature in the range from −40 to −10 °C as measured in 320 µm thick sensors at a bias voltage of 300 V and a magnetic field of 8 T. The hall mobility drops with increasing temperature. The dashed lines are linear fits to the measurements. (c): Comparison of the measured mobility values for electrons to the outcome of the simulation model.

smaller Lorentz shift, but the temperature coefficient is similar to the results from the HPK sensors. The dotted lines are linear fits to the data points, indicating an averaged temperature coefficient of the Lorentz shift of electrons to be

$$\left(\frac{d\,\Delta x}{dT}\right)_{e^-,300\,\mathrm{V},8\,\mathrm{T}} = -1.2\,\frac{\mu\mathrm{m}}{\mathrm{K}}. \tag{9.1}$$

The hall mobility μ_H changes in a similar way with temperature. The hall mobility decreases if the temperature is increased, the resulting temperature coefficient for the hall mobility of electrons at 300 V is

$$\left(\frac{d\,\mu_\mathrm{H}}{dT}\right)_{e^-,300\,\mathrm{V}} = -4.9\,\frac{\mathrm{cm}^2}{\mathrm{V\,s\,K}}. \tag{9.2}$$

Considering holes, the temperature dependence of the Lorentz shift and the hall mobility is not as pronounced as for electrons. As for electrons, the Lorentz shift and the hall mobility of holes drops with rising temperature. Figure 9.5b depicts the Hall mobility of holes obtained in a 320 µm thick n-bulk sensor at 8 T and a bias voltage of 300 V. From the fit, the resulting temperature coefficients are

$$\left(\frac{d\,\Delta x}{dT}\right)_{h^+,300\,\mathrm{V},8\,\mathrm{T}} = -0.228\,\frac{\mu\mathrm{m}}{\mathrm{K}} \tag{9.3}$$

and

$$\left(\frac{d\,\mu_\mathrm{H}}{dT}\right)_{h^+,300\,\mathrm{V}} = -0.982\,\frac{\mathrm{cm}^2}{\mathrm{V\,s\,K}}. \tag{9.4}$$

The silicon temperature of the sensors in the CMS Tracker is monitored by the Detector Control Unit (DCU) chip located on each front-end hybrid. Due to different locations in the tracker and several closed cooling loops, the temperature of the modules ranges from approximately 5 to 40 °C in the warmest areas in 2011 and 2012. This spread can be used to estimate the temperature dependence of the hall mobility, by correlating the mobility value obtained in each individual module to the temperature of the module. Figure 9.6 shows the obtained hall mobility per module as a function of the measured silicon temperature. Here, only axial TIB modules have been considered using the avgv3 method. The spread of the mobility values at a certain temperature is quite large. This prevents a direct correction of the obtained hall mobility for temperature effects, but it still allows an analysis of the average temperature behavior. The temperature coefficient is estimated by calculating the average mobility value per temperature bin and fitting a linear function in the temperature range of 15 to 30 °C where a linear behavior is visible, as shown in figure 9.6. The fit range has been limited to a temperature range with a large amount of entries per temperature slice and areas with very high spread have been excluded. By that, the temperature coefficient for holes can be estimated to

$$\left(\frac{d\,\mu_\mathrm{H}}{dT}\right)_{h^+,300\,\mathrm{V}} = (-0.92 \pm 0.25)\,\frac{\mathrm{cm}^2}{\mathrm{V\,s\,K}}.$$

This value is close to and within errors compatible to the value obtained during the laser measurements of $(-0.98 \pm 0.06)\,\mathrm{cm}^2\,\mathrm{V}^{-1}\,\mathrm{s}^{-1}\,\mathrm{K}^{-1}$. Also the absolute offset of the fitted slope of

$$\mu_\mathrm{H}(0\,°\mathrm{C}) = (207.6 \pm 5.7)\,\mathrm{cm}^2\,\mathrm{V}^{-1}\,\mathrm{s}^{-1}$$

is close to the value obtained from the laser measurement of $\mu_\mathrm{H}(0\,°\mathrm{C}) = (194 \pm 35)\,\mathrm{cm}^2\,\mathrm{V}^{-1}\,\mathrm{s}^{-1}$, if scaled to 0 °C. The small deviation can be due to the fact, that the mobility is measured in different temperature ranges and in different sensors. The fact that the temperature coefficient is compatible among both evaluations serves as a cross-check and confirms the obtained trend.

9.1.3 Bias voltage

The Lorentz shift is strongly dependent on the applied bias voltage, as illustrated in figure 9.8a. The reverse bias voltage leads to a depletion of free charge carriers in the sensor and to an electric field in the sensor bulk. With increasing bias, the depletion zone starts to grow from the pn-junction into the sensor bulk, until it is extended over the whole sensor. For an non-irradiated sensor, the depleted sensor depth is proportional to the square root of the applied voltage, as given by equation 3.12. In this bias voltage range, an increase of voltage will lead to an increasing shift, as the drift distance gets larger and larger. At the point where

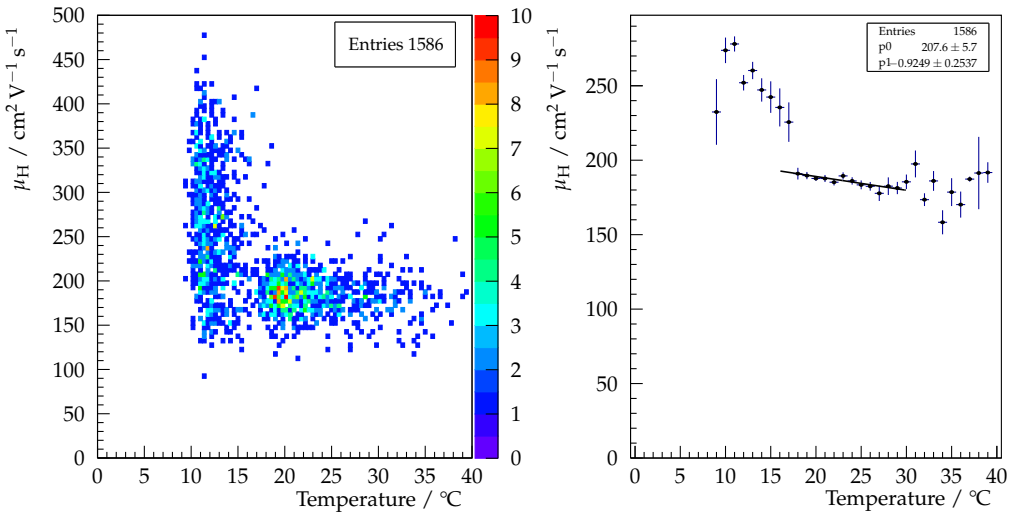

Figure 9.6.: Hall mobility as a function of the silicon temperature: The left plots shows the obtained hall mobility on all TIB modules as a function of the temperature using the avgv3 method. By averaging per temperature bin and fitting a slope to the temperature range of 15 to 30 °C, the temperature coefficient can be obtained, as shown in the right graph.

the depletion zone reaches the sensor edge, a further increase of voltage will only increase the strength of the electric field, as the depletion zone can not grow any further. That increased field leads to a decreasing Lorentz shift, due to the reduced mobility of the charge carriers, as illustrated by figure 9.7.

Figure 9.8a shows the Lorentz shift of electrons obtained in different non-irradiated p-bulk sensors with different depletion voltage and different thickness at a magnetic field of 4 T as a function of the bias voltage in the range between 25 to 600 V. The bulk doping concentration of all three sensors is different, as can be extracted from capacitance measurements.

For the measurement of the Lorentz shift, the infrared laser was used, in order to obtain a signal, even if the sensor is strongly underdepleted. Below the depletion voltage, the shift rises with the applied bias voltage. Above full depletion, the electric field in the sensor grows stronger and stronger, which leads to a decreasing shift in that regime. If the sensor is fully depleted, the concentration of dopants in the sensor bulk does no longer play a role considering the Lorentz shift, as the shift is the same for all three 320 µm thick sensors. Again, the 200 µm thick sensors show a smaller Lorentz shift.

The measurement of the Lorentz shift of holes in a 320 µm and a 200 µm thick n-bulk floatzone sensor at 4 T is shown in figure 9.8b. As for electrons, the shift of holes rises, if the sensor is underdepleted. The largest shift is obtained at the full depletion voltage. Above that voltage, the shift drops again. The shift is larger in the 320 µm thick device and the shift of holes is always a factor three to four times smaller than the shift of electrons at the same bias voltage.

Several times during a year, a bias voltage scan on the modules in the CMS Tracker is performed with stable proton-proton collisions in the detector [Bar11b]. The main purpose of the scans is the monitoring of the full-depletion voltage of the silicon sensors. The same data can also be used to estimate the Hall mobility as a function of the bias voltage. Figure

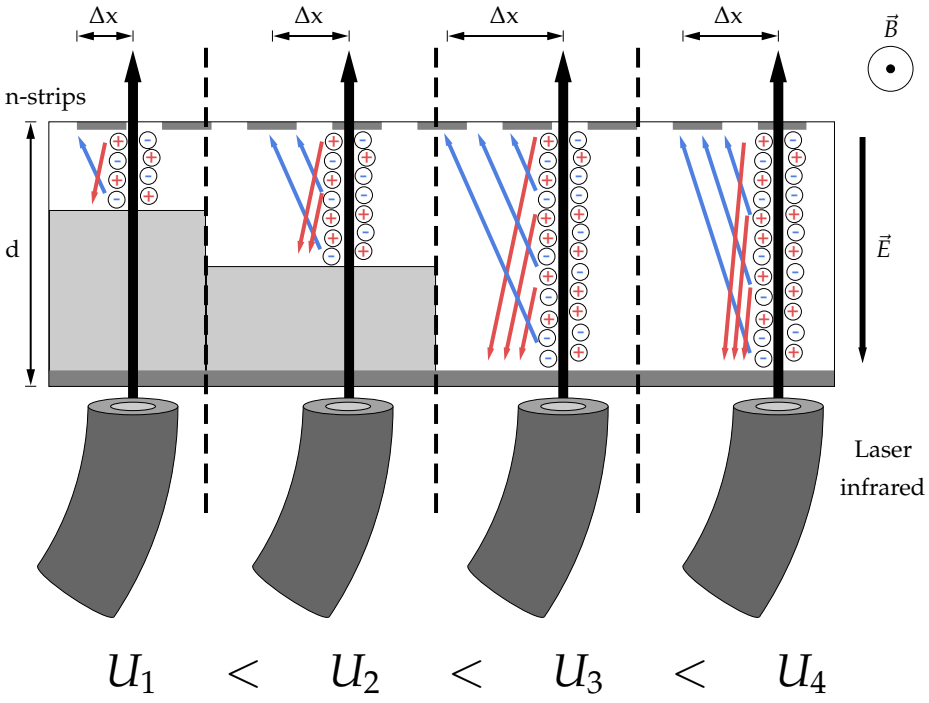

Figure 9.7.: Lorentz shift at different bias voltages. As long as the sensor is under depleted (U_1), only a fraction of the sensor thickness is active and contributes to the readout signal. For that, the Lorentz shift is relatively small. With increasing bias voltage (U_2), the depletion zone increases and the Lorentz shift rises, until the whole sensor volume is depleted (U_3). From that point on (U_4), the Lorentz shift decreases again with increasing bias voltage as the electric field in the sensor gets stronger and leads to a reduced mobility of the charge carriers, resulting in a decreasing Lorentz shift.

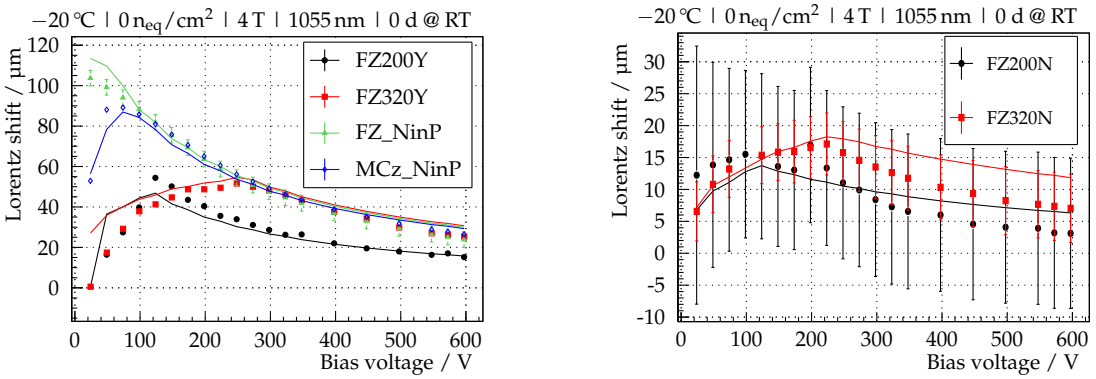

(a) Electrons

(b) Holes

Figure 9.8.: Lorentz shift of electrons (a) and holes (b) as a function of the bias voltage for four non-irradiated p-bulk sensor. The range, in which the shift increases, is the range in which the sensors are not yet fully depleted. After reaching depletion, the shift is independent of the bulk doping concentration and the shift in all three sensors is the same. The shift is smaller for 200 µm thick devices.

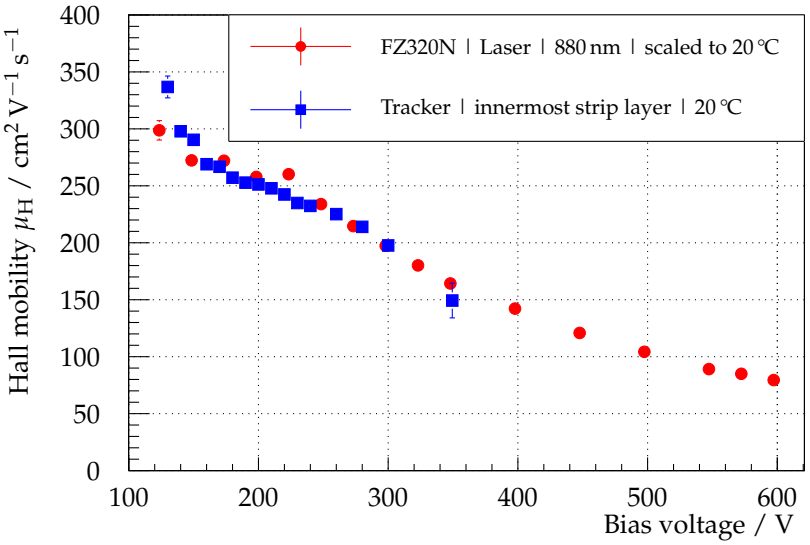

Figure 9.9.: Hall mobility of holes as a function of the bias voltage applied to the silicon sensor. Results obtained in Layer 1 of TIB are compared to measurement results obtained on a 320 µm thick n-bulk sensor using the laser method. For better comparability, the laser data has been scaled to a temperature of 20 °C. Both data sets show a falling trend of the Hall mobility with bias voltage, the absolute values agree very well.

9.9 compares the obtained Hall mobility in TIB layer 1 with the Hall mobility measured on a FZ320N sensor using the laser method. Both datasets agree very well, after scaling to the same temperature of 20 °C using equation 9.4. The falling trend of the Hall mobility with the bias voltage is consistent between both measurement methods.

9.1.4 Additional simulations

Simple model

The influence of the magentic field and the Lorentz deflection of the charge carriers has been studied using the simulation model outlined in chapter 7.1. Especially, inclined particle tracks relative to the sensor surface have been investigated. The inclination alters the cluster in several ways. As example, a 200 µm thick n-bulk sensor with 80 µm pitch has been chosen. Figure 9.10 shows the most probable value of the cluster charge and the most probable value of the seed charge as a function of the incidence angle of the particle in a plane perpendicular to the strips. Due to the longer distance of the particle in the sensor bulk, the total charge of the cluster is increasing with the incidence angle. An inclined track is more likely to deposit charge on several neighboring strips. For that, the charge of the seed strip is decreasing, although the total charge is increased.

Without magnetic field, the cluster properties are symmetric around perpendicular track incidence. This symmetry vanishes with the presence of a magnetic field, as the charges are shifted to a certain direction. For that, the same particle hits have been processed taking the Lorentz shift due to a 3.8 T magnetic field into account. The resulting charge distributions are overlayed in figure 9.10. As expected, the distributions are no longer symmetric. Due to the Lorentz shift, especially the seed charge distribution is altered, whereas the total cluster charge

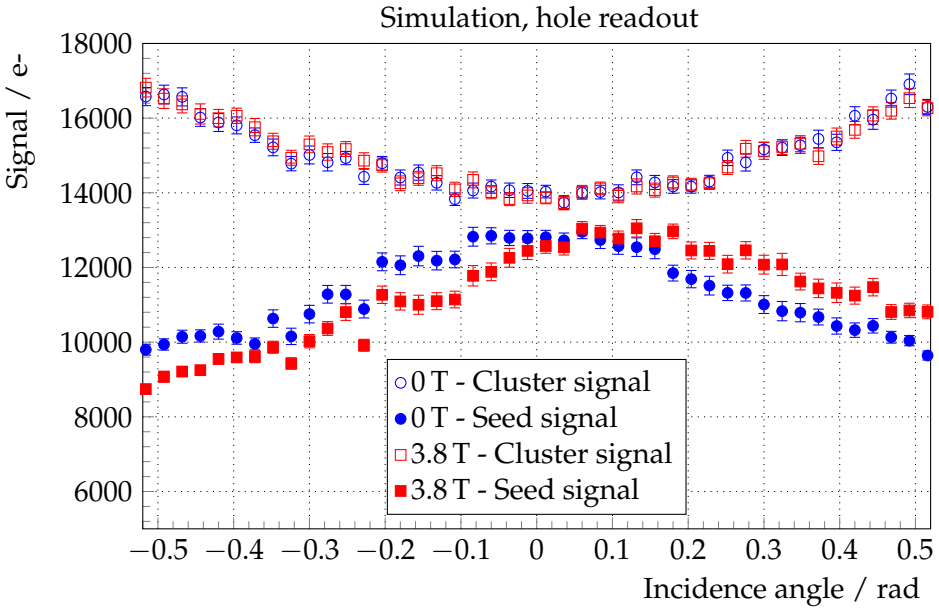

Figure 9.10.: Cluster charge (open symbols) and seed charge (closed symbols) as a function of the track incidence angle in a simulated 200 µm thick n-bulk sensor. The cluster charge increases with the angle due to the longer path length of the particle in the sensor, whereas the seed charge decreases due to the larger sharing of charge among neighboring strips. With a magnetic field of 3.8 T, the seed charge distribution is shifted due to the Lorentz deflection of the holes. The cluster charge distribution is not changed by the magnetic field. For the total charge, only the path length of the particle in the sensor material is important.

is independent of the magnetic field, as it depends mainly on the path length in the silicon bulk.

The average cluster size is increasing with the incidence angle, as shown in figure 9.11. As the seed charge, also the cluster size is no longer minimal at perpendicular incident of the particle, the minimum is shifted by the Lorentz angle.

By fitting the v-shaped function used in the analysis of the CMS data as given by equation 6.2, the hall mobility of the simulated holes can be estimated from the position of the minimum. With the magnetic field turned on, the fitted minimum is at 0.089 rad, which results in a hall mobility of

$$\mu_{\mathrm{H}} = \frac{\tan\theta_{\mathrm{min.}}}{B} = (215 \pm 8)\,\frac{\mathrm{cm}^2}{\mathrm{V\,s}}$$

when scaled to 0 °C which is in good agreement to either the results obtained in the laser measurements and the CMS Tracker. This demonstrates that both measurement methods give comparable estimations of the Lorentz angle and Hall mobility.

Figure 9.12 illustrates the simulated residual distribution now in a 200 µm p-bulk sensor with a 3.8 T strong magnetic field and without magnetic field at perpendicular particle incident. The difference in distance between the reconstructed hit defined as center-of-gravity of the charge cluster and the true particle hit point known from the Monte-Carlo simulation is taken as residual. Without field, the distribution is symmetrically centered around zero and the width of the fitted Gaussian is 22.5 µm. With magnetic field, the charges are deflected to one direction.

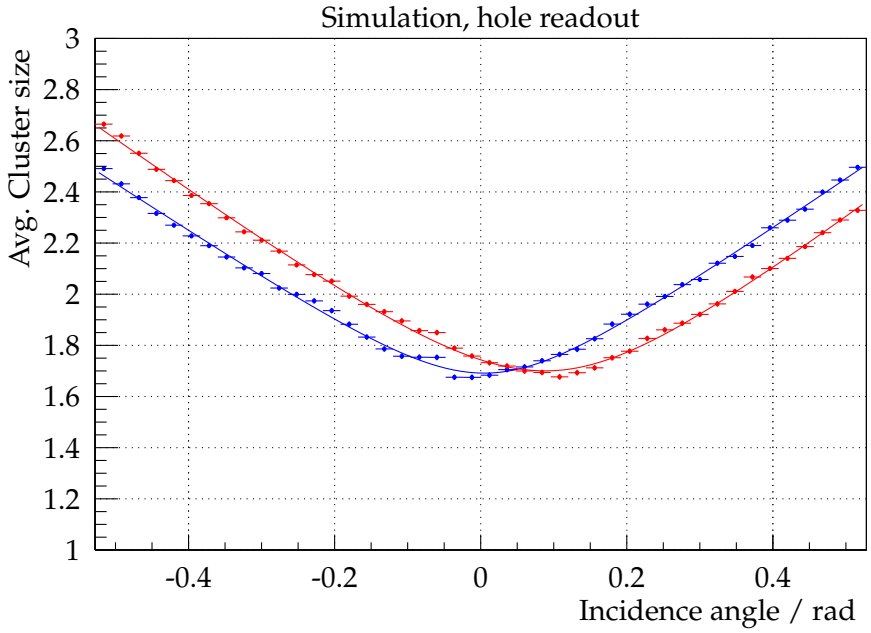

Figure 9.11.: Simulated cluster size as a function of the track incidence angle at 0 T (in blue) and 3.8 T (in red). The cluster size is increasing with the track angle. Due to the magnetic field, the minimal cluster size is no longer at perpendicular track incidence, but is shifted by the Lorentz angle. As for the analysis in the CMS Tracker, a v-shaped function is fitted to the distribution, in order to extract the hall mobility of the charges from the position of the minimum.

For that, also the reconstructed particle position is shifted and the residual distribution is no longer symmetric around zero. This shift is the reason, why the Lorentz deflection has to be taken into account during the event reconstruction in the CMS Tracker. In this case of a 200 µm thick p-bulk sensor, the shift of the residual distribution is about 23.1 µm, which is close to the measured Lorentz shift of electrons for such a sensor (compare to the black curve in figure 9.8a) as obtained with infrared laser light. Due to the increased charge sharing, the average cluster size is increasing. This allows a better estimation of the particle hit, as the center-of-gravity can be used, if more than one strip is hit. For that, the width of the residual distribution is narrowed to 13.5 µm due to the Lorentz shift.

T-CAD

Figure 9.13 shows a comparison of a measured and a simulated magnetic field scan in the range between 0 to 8 T at a bias voltage of 300 V using the T-CAD simulation, as outlined in chapter 7.3. The simulated geometry corresponds to non-irradiated 320 µm thick n-bulk and p-bulk sensors with a pitch of 80 µm, as used for the measurement. Charge has been induced by a 880 nm laser pulse at a bias voltage of 300 V. Measurement and simulation show a linear increase of the Lorentz shift with the magnetic field and the overall agreement of the simulated to the measured points is given. The quantitative difference between the hall mobility and hall scattering factors of electrons and holes – leading to a larger shift of electrons – and the direction of the shift are reproduced by the simulation. Also other cluster parameters like the increasing width of the fitted Gaussian after the drift with increasing magnetic field are

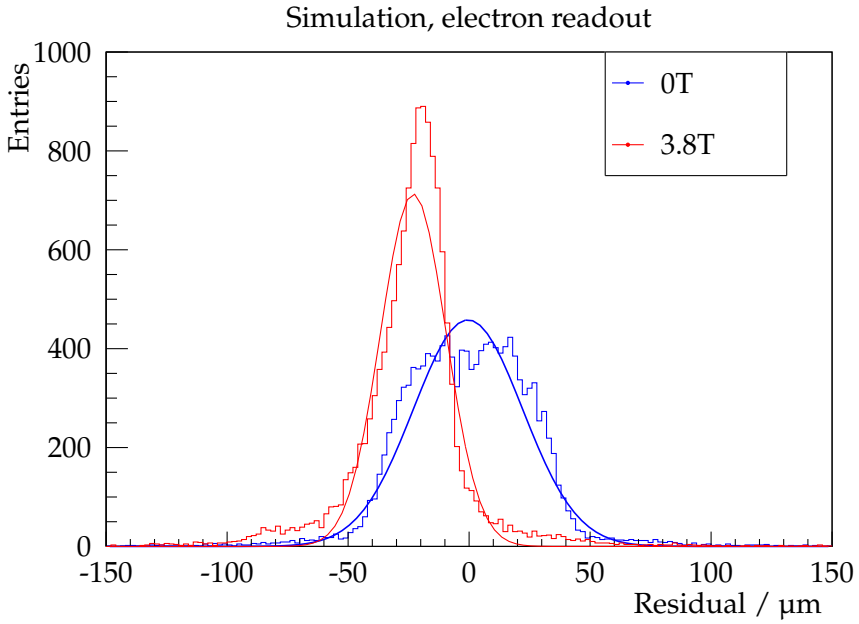

Figure 9.12.: Simulated residual distribution with and without magnetic field in an non-irradiated 200 µm thick p-bulk sensor at 300 V. The difference in distance between the reconstructed hit defined as center-of-gravity of the charge cluster and the true particle hit point known from the Monte-Carlo simulation is taken as residual. Due to the Lorentz shift, the mean of the distribution is shifted. The increased charge sharing due to the magnetic field, leads to a better resolution of the sensor, manifested in a narrower residual distribution.

reproduced, as can be seen from figure 9.14. The larger spread of the charge with increasing magnetic field in the p-bulk sensor can probably be explained by the longer drift distance of the charge and therefore larger diffusion in the silicon bulk. Nevertheless, the size of the charge cloud stays constant in the n-bulk sensor.

A comparison between the simulated and measured Lorentz shift at 4 T as a function of the applied bias voltage is shown in figure 9.15. Here, the used laser wavelength is 1055 nm, in order to obtain a charge signal at low bias voltages where the sensor is still underdepleted. Similar to the measured data, the shift increases with rising bias voltage, until the sensor is fully depleted. From that point, the Lorentz shift decreases again.

9.2 Irradiated sensors

Radiation induced damage has multiple effects on the Lorentz angle. First of all, the depletion voltage of the sensor is modified as discussed in chapter 4.2, which may lead to a different electric field distribution in the sensor. As the electric field has a strong impact on the mobility of electrons and holes, an effect on the Lorentz angle is to be expected. Furthermore, radiation induced defects can alter the mobility of the charge carriers itself, which will also lead to changes in the Lorentz angle.

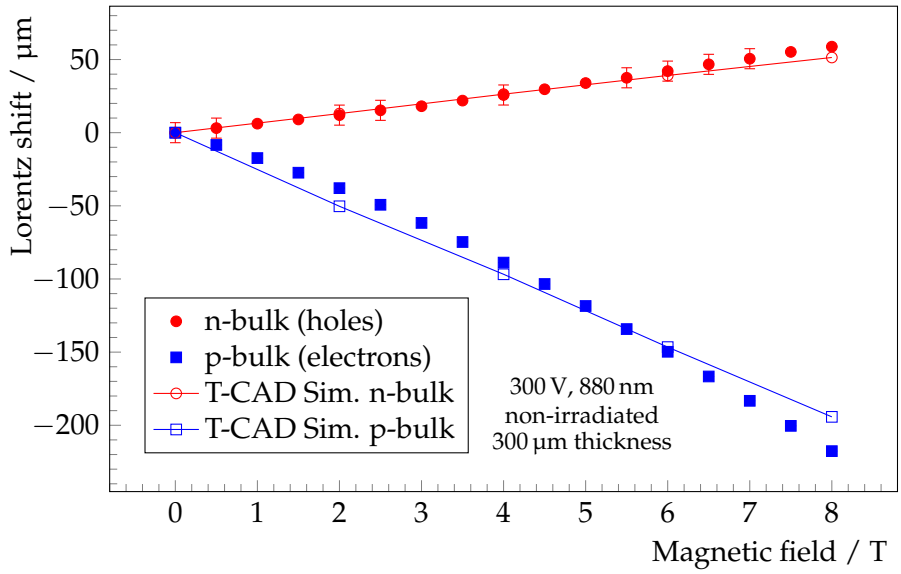

Figure 9.13.: Measured and simulated lorentz shift in a 320 µm thick n- and p-bulk silicon sensor as a function of the magnetic field in the range of 0 to 8 T. The applied bias voltage is 300 V in both cases. For both types of bulk doping, the simulated curves are in agreement with the measured data.

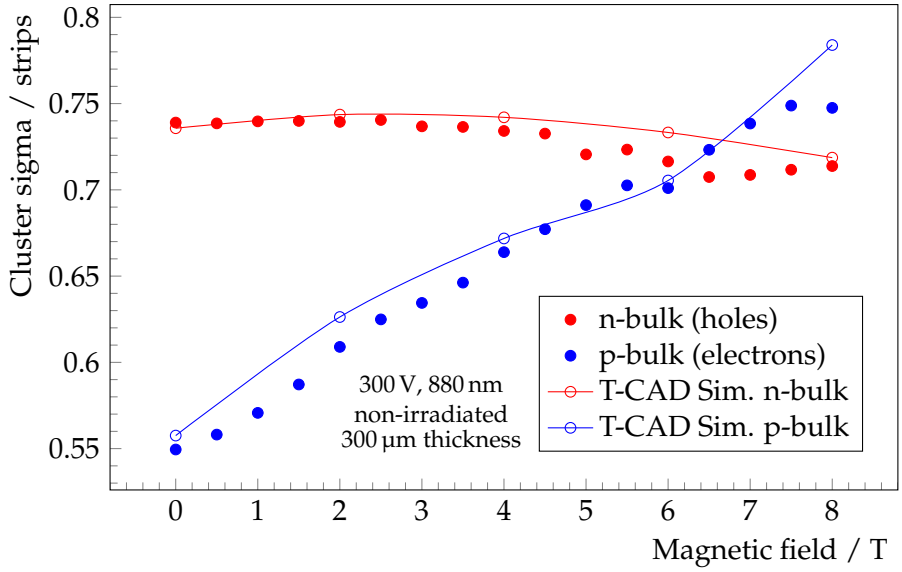

Figure 9.14.: Comparison of the simulated and measured width of the charge distribution after the drift towards the strips at different magnetic field in the range of 0 to 8 T. The width of the charge distribution is larger with increasing magnetic field in the p-bulk sensor, possibly due to the longer drift time and distance and therefore larger diffusion of the charge cloud in the silicon bulk. It stays constant for the n-bulk sensor though.

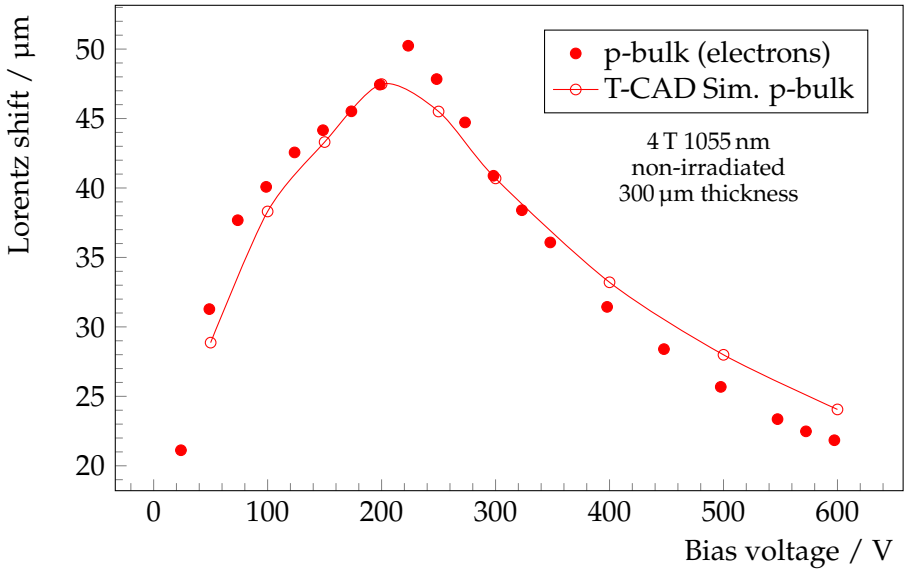

Figure 9.15.: Measured and simulated Lorentz shift in a 320 µm thick p-bulk sensor as a function of the bias voltage. The shift is rising up to the depletion voltage due to the growing active thickness of the sensor. Above that point, the shift drops again due to the increasing electric field in the sensor bulk and the reduction of the mobility.

9.2.1 Magnetic field

Figure 9.16 shows the obtained Lorentz shift as a function of the magnetic field for holes and electrons after irradiation with several different fluences and an applied bias voltage of 600 V to all sensors. Still, a linear increase of the Lorentz shift with the magnetic field is visible. For electrons, a drop of the shift with increasing fluence can be observed, while for holes the shift increases as long as the sensor can be fully depleted. As soon as the full depletion voltage exceeds the applied bias voltage, the Lorentz shift drops to almost zero. This is here the case after an irradiation of $1.5 \times 10^{15}\,\mathrm{n_{eq}/cm^2}$.

The solid lines in figure 9.16 represent the outcome of the simulation model. To account for the radiation damage, the increase of the full depletion voltage of the senors has been included into the model. For electrons, the prediction of the model fits quite well to the data point after irradiation. The reduced shift is reproduced correctly, except for small deviations at high magnetic fields above 6 T. Considering holes, the prediction is not as good as for electrons. As for electrons, the increase of the full depletion voltage leads to a reduced shift at high fluences above $1 \times 10^{15}\,\mathrm{n_{eq}/cm^2}$. However, at lower fluences, the increase of the Lorentz shift is not reproduced correctly. Here, additional effects may contribute to an inreased mobility of the charge carriers. As shown earlier in chapter 8.4, the n-bulk sensors which are used for the determination of the Lorentz shift of holes suffer from an increased noise after irradiation. The noise decreases precision of the measurement and reduces the significance of the results.

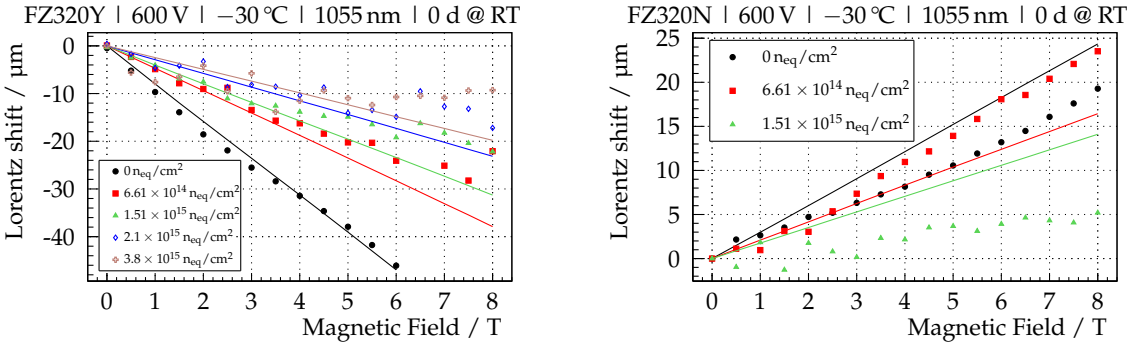

(a) Electrons **(b)** Holes

Figure 9.16.: Lorentz shift of holes and electrons as a function of the magnetic field for irradiated 320 µm thick sensors. The solid lines represent the outcome of the simulation model.

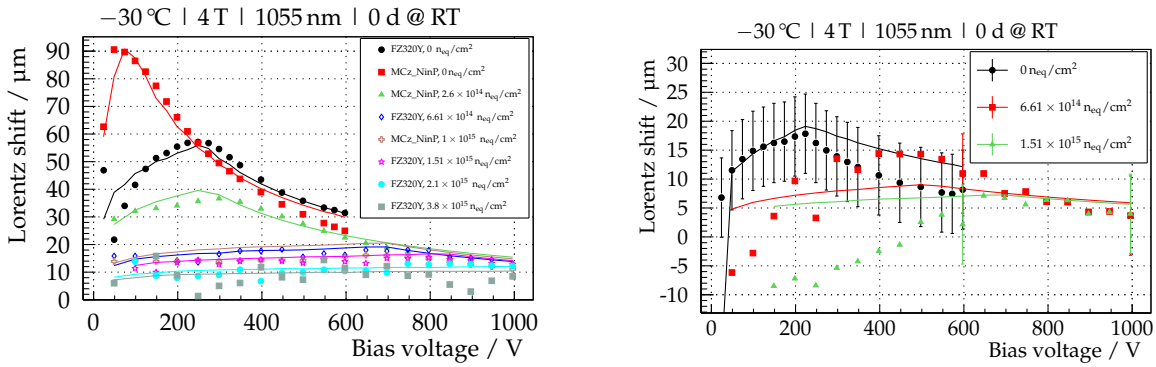

(a) Electrons **(b)** Holes

Figure 9.17.: Shift of electrons and holes as a function of the applied bias voltage for irradiated sensors. The solid lines represent the outcome of the simulation model.

9.2.2 Bias voltage

After irradiation, the distribution of the electric field in the sensor bulk changes. Thus, also the dependence of the Lorentz shift from the bias voltage changes. Figure 9.17a shows the Lorentz shift of electrons as a function of the applied bias voltage for an non-irradiated and four irradiated FZ320Y sensors. While the non-irradiated sensor shows first a rising and later on a falling behavior, the irradiated sensors show a more or less constant and small shift. After irradiation, the depletion zone is no longer as sharp and well defined as in non-irradiated devices. For that, a simple explanation as given in figure 9.7 is no longer applicable.

Considerning the holes in n-bulk sensors, the picture is not that clear. In the sensor irradiated to $6.6 \times 10^{14}\,\mathrm{n_{eq}/cm^2}$, the Lorentz shift is nearly as large as in the non-irradiated sensor. After higher irradiaton, a negative shift has been observed. However, the n-bulk sensors suffer from a strongly increased noise, as shown in chapter 8.4. The signal induced by the laser pulse is obscured by the noise and can only be detected due to the averaging of several hundred of events. On the one hand this reduces the resolution of the measurement, on the other hand, the noise effect itself may influence the drift of the charges.

9.2.3 Irradiation and annealing

Figure 9.18a shows the obtained Lorentz shift of electrons for 320 µm thick p-bulk sensors at 4 T and 600 V after three different states of annealing. Both, HPK and Micron sensors are shown. First of all, a constant drop of the shift with irradiation fluence can be noted. Starting from approximately 25 µm without irradiation, the shift drops to 10 µm and below after an irradiation of $5.8 \times 10^{15}\,n_{eq}/cm^2$. The lines indicate the output of the simulation model. For the solid lines, the measured full depletion voltage of the sensors has been taken as input to the simulation. In the dashed area, the depletion voltage is outside the range where it could be measured. The depletion voltage has been extrapolated from the measurements at lower fluences.

The Lorentz shift of holes is depicted in figure 9.18b. In contrast to the shift of electrons , the Lorentz shift of holes at first rises with irradiation fluence, as long as the full depletion voltage of the sensor can be reached. After that point, where the sensors are not fully depleted anymore, the shift drops again. Due to an increased noise and reduced signal, the n-bulk sensors with an irradiation above $2.1 \times 10^{15}\,n_{eq}/cm^2$ could not be measured anymore. At a fluence of $1.5 \times 10^{15}\,n_{eq}/cm^2$ and higher, the sensors are heavily affected by noise. The measured Lorentz shift is small.

For measuring the Lorentz angle, three different states of annealing have been considered. The first set of measurements was performed on the sensors right after irradiation. The second step was performed in the phase of beneficial annealing, after approximately 20 days of equivalent room temperature annealing. This amount of annealing is probably to arise to a tracking detector in an experiment during maintenance periods, in which the proper cooling of the sensors is not always guaranteed. The third and last set of measurements was done after a significant amount of long-term annealing, equivalent to 420 days at room temperature. A full detector will probably not be annealed to that stage. This last step was taken to estimate the effects of long term annealing and if it affects the Lorentz angle in a way negative to the detector performance. Than, special care would have to be taken during maintenance periods, to avoid annealing of the sensors.

The annealing has a significant influence on the Lorentz shift of electrons. A clear correlation of the Lorentz shift to the full depletion voltage of the sensors is observed. Short-term annealing equivalent to 20 days at room temperature lowers the full depletion voltage (compare figure 4.10) and increases the Lorentz shift, while long-term annealing decreases the shift and increases the full depletion voltage again.

Despite of the dependence of the full depletion voltage from the annealing treatment, for holes, the annealing of the sensors has almost no impact on the Lorentz angle. This may be due to the overall smaller Lorentz shift compared to electrons and the limited resolution of the measurement.

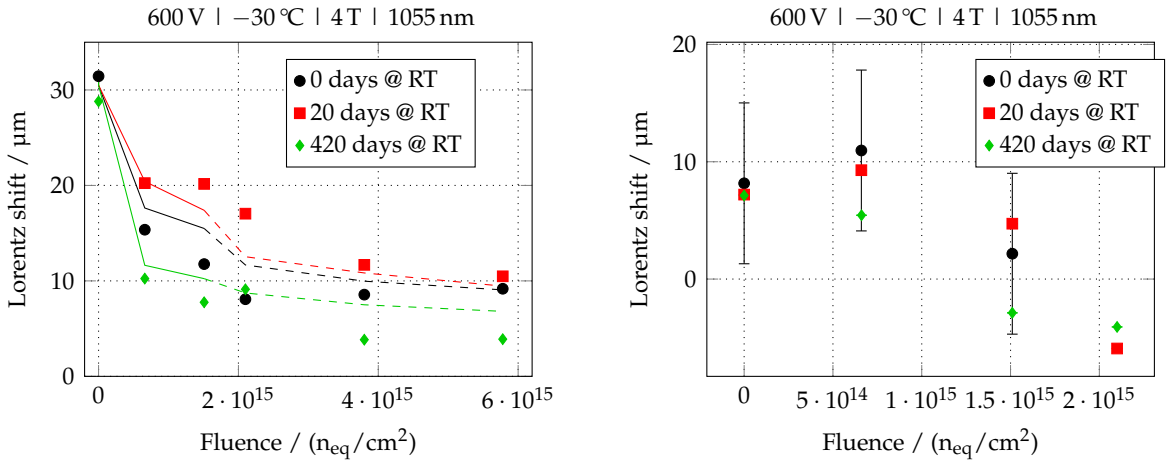

(a) Electrons **(b)** Holes

Figure 9.18.: Lorentz shift of electrons and holes as a function of the irradiation fluence and annealing time.

9.2.4 Temperature dependence of the electron shift

Similar to the non irradiated case, the temperature dependence of the Lorentz shift of electrons is shown in figure 9.19a as a function of the sensor temperature in the range of −40 to −20 °C. The applied bias voltage is 600 V on all sensors. As shown earlier, the overall shift of electrons is reduced with irradiation fluence.

A qualitatively different temperature behavior is obvious. While the Lorentz shift is decreasing with temperature in the non irradiated sensor, the slope is changed after irradiation and the shift is increasing with temperature. To extract the temperature coefficient, linear fits have been applied to the data points. The resulting temperature coefficient is shown in figure 9.19b as a function of the irradiation fluence for three different p-bulk sensors. All three sensor types show a similar change in the sign of the temperature coefficient after irradiation. For the higher irradiated sensors, no measurement of the temperature dependence was possible due to thermal runaway at −20 °C.

9.2.5 Simulation of the residual distribution

As for the non-irradiated case, the residual distribution has been simulated. Figure 9.20 illustrates the residual distribution in a 200 µm thick p-bulk sensor at 600 V bias using the parameters derived from the test beam studies that will be presented in chapter 10, corresponding to a fluence of $1.5 \times 10^{15}\,\mathrm{n_{eq}/cm^2}$ and an annealing of 13 days at room temperature.

Similar to the non-irradiated simulation, the residual distribution is shifted due to the magnetic field. Due to the higher bias voltage, the Lorentz shift is smaller. The shift of the mean of the distribution is 13.9 µm. The magnetic field leads to a gain in the spacial resolution of the sensor, represented by the width of the distribution. The distribution is narrowed from 23.4 µm without magnetic field to 19.6 µm in a 3.8 T field.

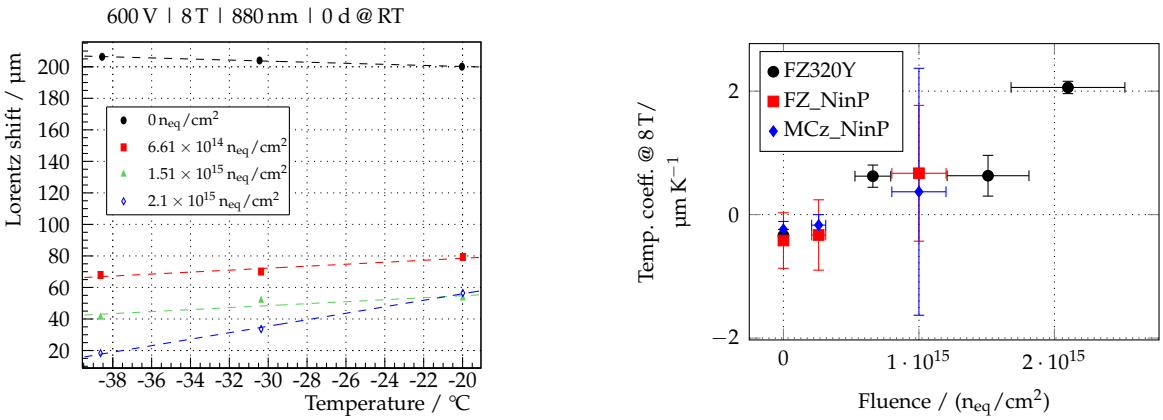

(a) Lorentz shift vs. temperature

(b) Temperature coefficient vs. fluence

Figure 9.19.: Temperature dependence of the Lorentz shift of electrons after irradiation. In the non irradiated sensor, the temperature coefficient is negative. After irradiation, the sign is changed. (a): Different irradiation states of the FZ320Y sensors are shown. The temperature coefficient changes its sign with irradiation, leading to a Lorentz shift with temperature after irradiation. The dashed lines indicate linear fits to the data points. (b) Summary of the fitted temperature coefficients as a function of the irradiation fluence.

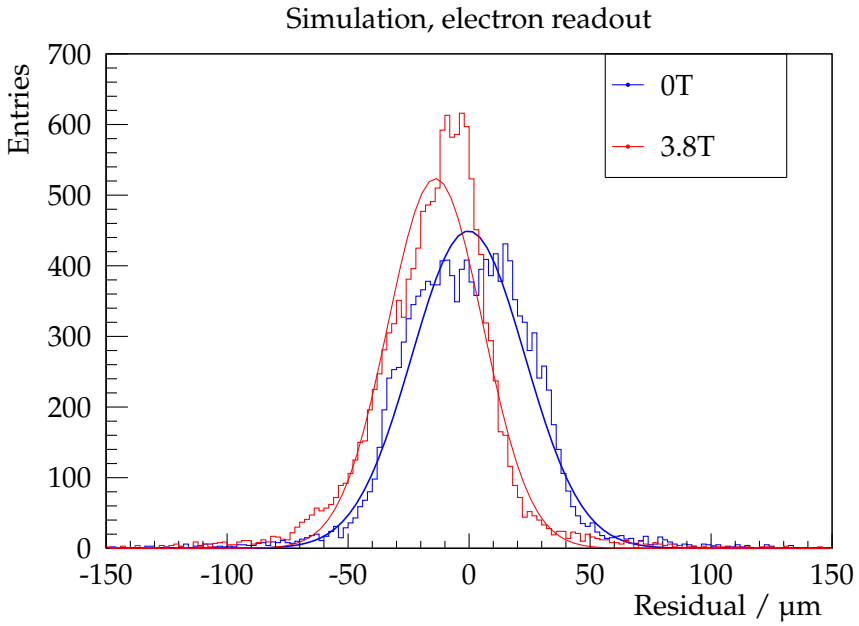

Figure 9.20.: Simulated residual distribution with and without magnetic field in an irradiated 200 µm thick p-bulk sensor at 600 V. The difference in distance between the reconstructed hit defined as center-of-gravity of the charge cluster and the true particle hit point known from the Monte-Carlo simulation is taken as residual. Due to the Lorentz shift, the mean of the distribution is shifted. The increased charge sharing due to the magnetic field leads to a better resolution of the sensor, as manifested in a narrower residual distribution.

10 Test beam

This chapter describes studies on irradiated multi geometry strip sensors performed at the test beam facility at the DESY II accelerator. The main objective is the investigation of the efficiency and resolution for tracks hitting the sensor perpendicular and at an angle of 10° and 30° for the various geometries implemented on the multi-geometry strip sensors (MSSD).

10.1 Investigated sensors

In total, seven MSSDs have been assembled to modules like the one shown in figure 6.21 and investigated during the measurement time at DESY. Six sensors are irradiated with protons to a fluence of $1.5 \times 10^{15}\,\mathrm{n_{eq}/cm^2}$, whereas one sensor is non-irradiated. Table 10.1 summarizes the sensor type and polarity as well as the fluences and annealing states of the sensors. All irradiated sensors have been operated at 500 V, 600 V, 750 V and 900 V at a temperature below −20 °C, the non-irradiated sensor has been biased at 100 V and 150 V. The module tilt angle has been 0°, 10° and 30°.

Table 10.1.: Sensor types investigated in test beam

Sensor	Fluence / ($\mathrm{n_{eq}/cm^2}$)	Annealing / (d @ RT)
MCZ200P_03_MSSD_2	0	0
FTH200P_07_MSSD_1	1.5×10^{15}	13
FTH200Y_02_MSSD_2	1.5×10^{15}	13
FTH200N_23_MSSD_1	1.5×10^{15}	112
MCZ200P_01_MSSD_2	1.5×10^{15}	13
MCZ200Y_05_MSSD_1	1.5×10^{15}	13
MCZ200N_06_MSSD_2	1.5×10^{15}	112

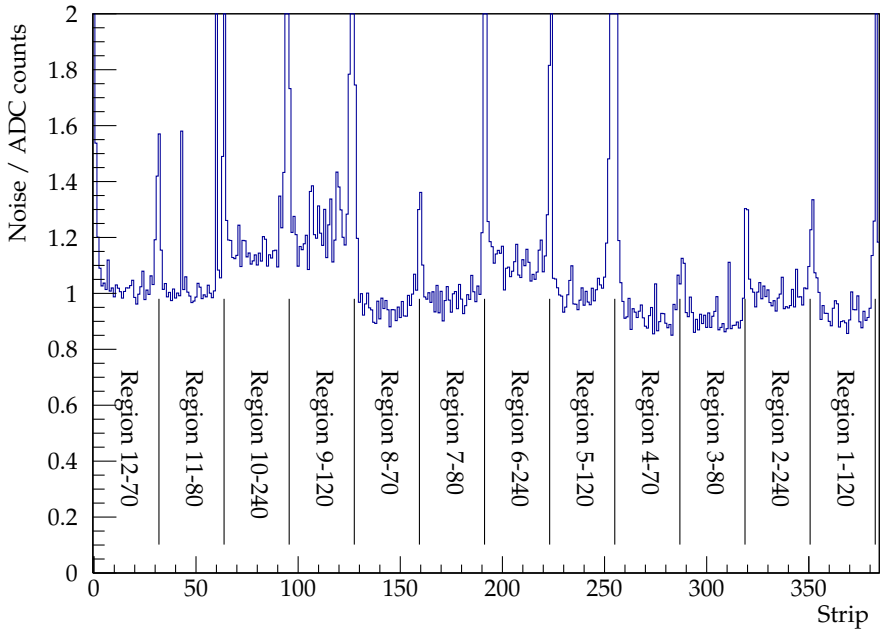

Figure 10.1.: Noisemap of the irradiated FTH200Y MSSD: Large pitch regions show a systematically higher noise than regions with small strip pitch. This is due to the larger area covered, which leads to a higher leakage current collected by these strips and to a higher load capacitance on the inputs of the readout chip. One ADC count corresponds to approximately 950 electrons ENC.

10.2 Results at perpendicular particle incident

In the following, the results obtained from data taken at perpendicular particle incident are presented. In the first part, the overall cluster propierties and sensor performance of the irradiated FTH200Y sensor is shown. In the second part, sub-strip resolved studies are presented.

10.2.1 Noise

The noise of the sensor and the connected readout system influences the overall performance of the sensor. In order to be reconstructed correctly, charge clusters must poke out of the noise. Usually, a signal to noise ratio cut of five is used for the cluster recognition with an analogue readout chip. Figure 10.1 depicts the noise value in ADC counts as a function of the strip number of the irradiated FTH200Y MSSD. The noise distribution is flat among the strips of a specific region. Only the outer most two strips show a higher noise value. They are for that excluded from the analysis.

Generally, a tendency of having higher noise in the regions with larger strip pitch can be noted. This is due to the fact that the large pitch regions cover a larger silicon volume and for that collect a higher bulk leakage current. The increased current contributes to the noise, as given by equation 3.33.

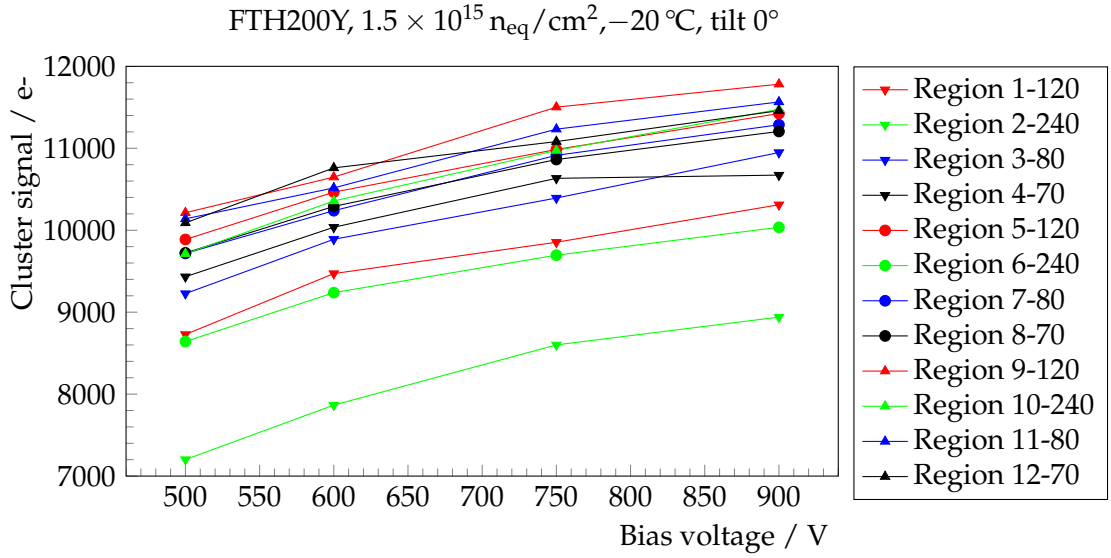

Figure 10.2.: Cluster signal in electrons as a function of the applied bias voltage, obtained on the irradiated FTH200Y MSSD sensor. All twelve regions are shown. Only a slight increase of the signal is visible for all regions, indicating that the sensor is fully depleted. The signal reaches around 13 000 electrons. Only regions 1,2 and 6 show a slightly lower signal.

10.2.2 Cluster signal

Similar to the investigation in a beta setup, the signal obtained from the sensors is evaluated. The signal is being evaluated using a clustering algorithm, applying a 5σ seed cut and a 2σ neighbor cut. Only clusters that are assigned to referenced particle tracks are taken into account. The histograms of the cluster charge distribution are fitted by a convoluted Landau and Gaussian function, in order to obtain the most probable value of the deposited charge. Summarizing, figure 10.2 shows the obtained cluster signals for all 12 regions of the irradiated FTH200Y sensor as a function of the bias voltage. For all regions, the cluster signal increases only slightly with the applied voltage, indicating that the sensor is almost fully depleted. This agrees to the capacitance measurements, which indicate a full depletion voltage of around 450 V. The signal reaches around 12 000 electrons, which is approximately 80 % of the expected value of 14 000 electrons for a non-irradiated 200 µm thick sensor. Nevertheless, regions 1, 2 and 6 show a slightly reduced signal compared to all other regions, which differ only about $\pm$500 electrons.

10.2.3 Cluster size

The size of the reconstructed charge cluster depends mainly on the strip pitch and the particle incidence angle. With larger pitch, the charge spreads on less strips compared to a small strip pitch and thus the charge clusters are smaller. Inclined tracks are more likely to pass several strips, especially at small strip pitch. For that, the cluster size increases with the track inclination angle.

The size of the charge cluster has an impact on the spatial resolution of the strip sensor. For clusters containing at least two strips, the hit position can be interpolated using either the center of gravity or η-method, and thus the estimated track penetration point is more accurate.

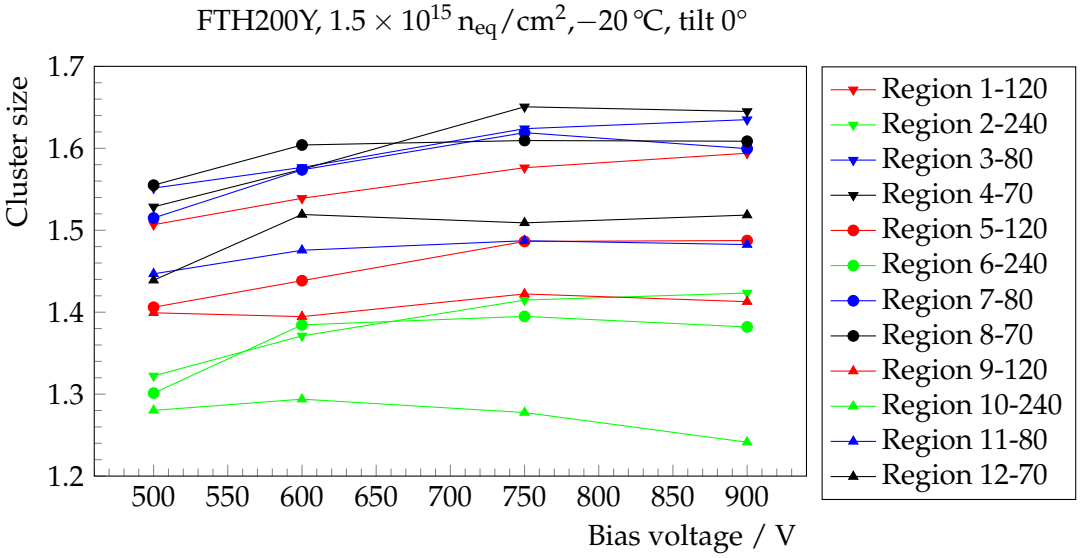

Figure 10.3.: Average cluster size on an irradiated FTH200Y MSSD as a function of the applied bias voltage at perpendicular particle indident. For most regions, a slight increase in cluster size is visible, corresponding to the slightly increasing total cluster signal. As expected, the regions with small strip pitch show the largest cluster size and the clusters are smaller on regions with larger strip pitch. In addition to that, the cluster size depends on the strip width to pitch ratio. At the same pitch, a larger strip width results in smaller clusters.

Even with a binary readout, the resolution is improved for clusters with at least two strips by taking the center of gravity. The cluster size as a function of the bias voltage is shown in figure 10.3. As to expect, the cluster size depends mainly on the strip pitch. On regions with small strip pitch, the charge spreads over several strips more easily and for that the average cluster size is increased. Additionally, the cluster size depends on the ratio of strip pitch to strip width. At the same pitch, the clusters are smaller on regions with wider strip implants. With increasing bias voltage, a slight increase in the total cluster signal has been observed. Due to the larger total charge, the probability for neighboring strips to pass the signal-to-noise cut is larger and thus the average cluster size increases slightly with the applied bias voltage.

10.2.4 Width of residual distribution

The spatial resolution of a tracking device is one of the most important parameters. In first order, it is given by the width of the residual distribution of the reconstructed hit position on the sensor to the track. For that, the particles track is reconstructed using the telescope planes only. The track is extrapolated to the DUT and compared to the position of the reconstructed cluster. If the alignment of the modules relative to each other is correctly known, the residual distribution is Gaussian shaped and centered around zero. An eventual misalignment can be estimated by investigating the mean value of the residuals at various points on the sensor individually.

The width of the residual distribution is a first indicator on the spatial resolution of the sensor. The narrower the distribution, the closer is the reconstructed hit on the sensor to the

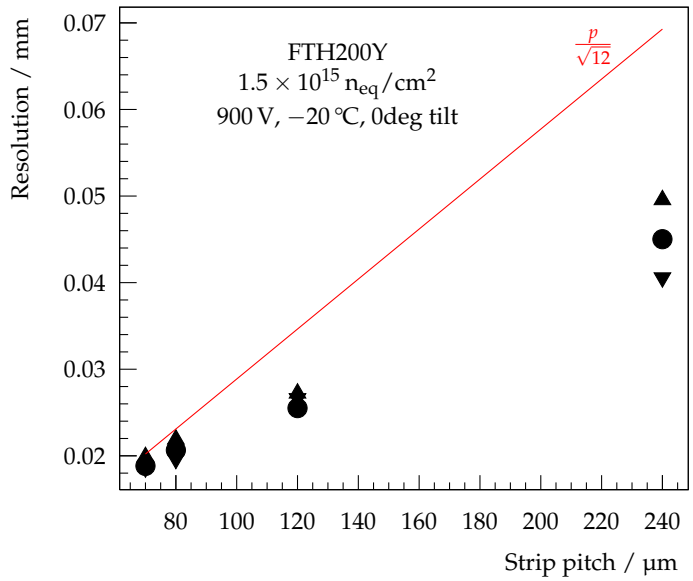

Figure 10.4.: Sensor resolution of the irradiated FTH200Y MSSD as a function of the strip pitch. As expected, the width of the residual distribution follows the strip pitch. The red line indicates the binary resolution of $\frac{p}{\sqrt{12}}$.

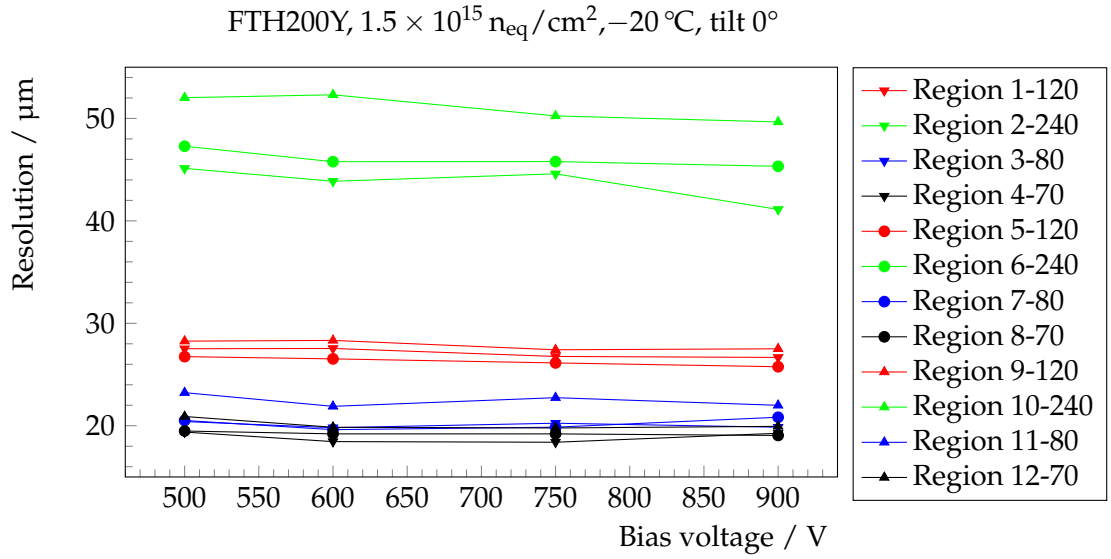

Figure 10.5.: Sensor resolution of the 12 regions of the irradiated FTH200Y MSSD as a function of the bias voltage. The resolution is strongly dependent on the strip pitch, no trend with the bias voltage is observed above 500 V.

true penetration point of the track. The theoretical estimation for the width of the residual distribution under the assumption of a binary clustering is

$$\sigma = \frac{\mathrm{p}}{\sqrt{12}} \tag{10.1}$$

The resolution using an analogue readout where the pulse height information of the individual strips is taken into account is expected to be better than that value. Additionally, here the hit on the DUT has not been used for track fitting. In a tracking detector all layers would contribute to the track fit, for that the spatial resolution is expected to be slightly better. Figure 10.4 depicts the width of the residual distribution as a function of the strip pitch of the individual region. For all regions, the residual distribution is narrower than the value given by equation 10.1, indicating the benefit due to the interpolation of the hit position using the analogue readout.

Figure 10.5 illustrates the width of the residual distributions of an irradiated FTH200Y MSSD on all 12 regions as a function of the applied bias voltage. Besides the obvious dependence on the strip pitch, the width of the residual distributions is independent of the applied bias voltage, at least in the investigated range above 500 V, where the sensor is fully depleted.

The width of the residual is a composition of the spatial resolution of the sensor and the tracking resolution of the telescope. In order to correct for the telescope resolution, the uncertainty of the interpolated track on the sensor plane has to be known. In addition, the DUT has not been included in the track fit, which usually results in a broadening of the residual distribution.

10.2.5 Efficiency

The efficiency of the sensor is evaluated by comparing the expected number of hits in a certain area of the DUT due to the reconstructed reference tracks to the actual number of reconstructed hits. An efficiency close to 100 % means that most of the tracks lead to a reconstructed hit on the sensor, whereas an efficiency close to 0 % means that almost no tracks have been seen as charge cluster on the DUT. Figure 10.6 shows the mean efficiency per region of the same sensor as a function of the bias voltage. For most regions, the average efficiency is in the range of 80 to 90 % and varies only less with the bias voltage. The small variation is consistent with the minor variation of the total cluster signal as shown in figure 10.2.

10.2.6 Substrip

Exploiting the good spatial resolution of the reference telescope, cluster parameters have been analyzed with sub-strip resolution. This means, the cluster properties can be studied depending on the position of the particle hit relative to the strip. In the following part, the cluster signal, the seed signal, the cluster size and the efficiency of the sensor are investigated as a function of the track position. Afterwards, the efficiency of the sensor regions is studied depending on the cluster seed cut, the strip pitch, the strip width to pitch ratio and the silicon base material type. For clearness, additional plots of the cluster charge, the seed charge and the cluster size have been moved into appendix B.

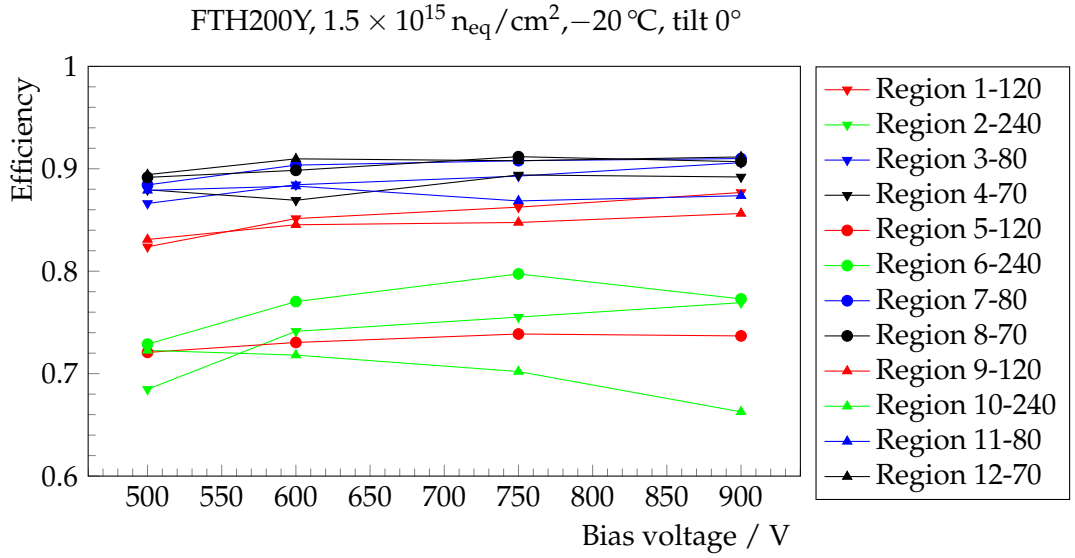

Figure 10.6.: Average efficiency per region of an irradiated FTH200Y sensor as a function of the bias voltage. For most regions, the average efficiency is in the range of 80 to 90 % and constant with the bias voltage. The 240 µm pitch regions are slightly less effective, compared to the other regions. This corresponds to a drop in the charge collection efficiency as described in section 10.2.6.

Cluster signal and seed signal

Figure 10.7 illustrates exemplary the total cluster signal as a function of the penetration point of the track, folded into one single strip unit cell. Region 6-240 and 7-80 of the irradiated FTH200Y sensor has been chosen. Region 7 has the same strip geometry than the other strip sensors on the HPK wafer. On regions with 240 µm pitch, the resolution is best, for that region 6 has been added as a comparison.

In the vertical direction of the plot, a histogram of the cluster signal is is shown. In each bin, the landau distribution is visible in the color coding. The black line represents the most probable value of the landau distribution in each bin. Clearly, a drop of the signal for tracks hitting the midpoint between the strips at x=0 and x=1 is notable, while the signal is highest for tracks passing the sensor directly on the strip at x=0.5. Towards the center of the pitch close to x=0 and x=1, it can be noted already by eye, that the most probable value approaches the clustering cut, which is in this case approximately at 4000 electrons.

The seed signal distribution shown in figure 10.8. Due to the charge sharing, the charge on the leading strip of the cluster is reduced even further. This adds to the loss of the total collected charge. The most probable value of the seed charge drops for both regions to approximately 5000 electrons between two neighboring strips. This is close to the clustering cut. Because of that, especially betrween the strips, clusters might be lost.

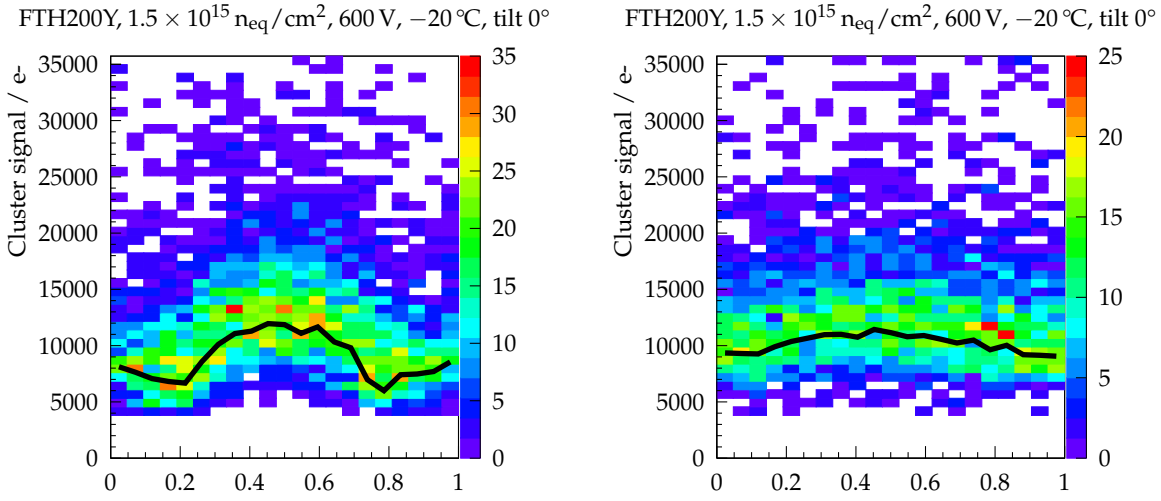

(a) Region 6-240 **(b)** Region 7-80

Figure 10.7.: Cluster signal in the strip unit cell: Depending on the position of the track in the strip unit cell, the cluster signal is shown. Each vertical bin contains a charge distribution, which has been fitted with a convoluted landau and Gaussian function. The black line represents the most probable value of the fit in each bin. The cluster signal is significantly higher, if the particle hits directly on a strip (at x=0.5) and is reduced for tracks hitting between two neighboring strips (at x=0 and x=1). The effect is most pronounced on regions with large strip pitch (a), but is also visible on small pitch regions (b).

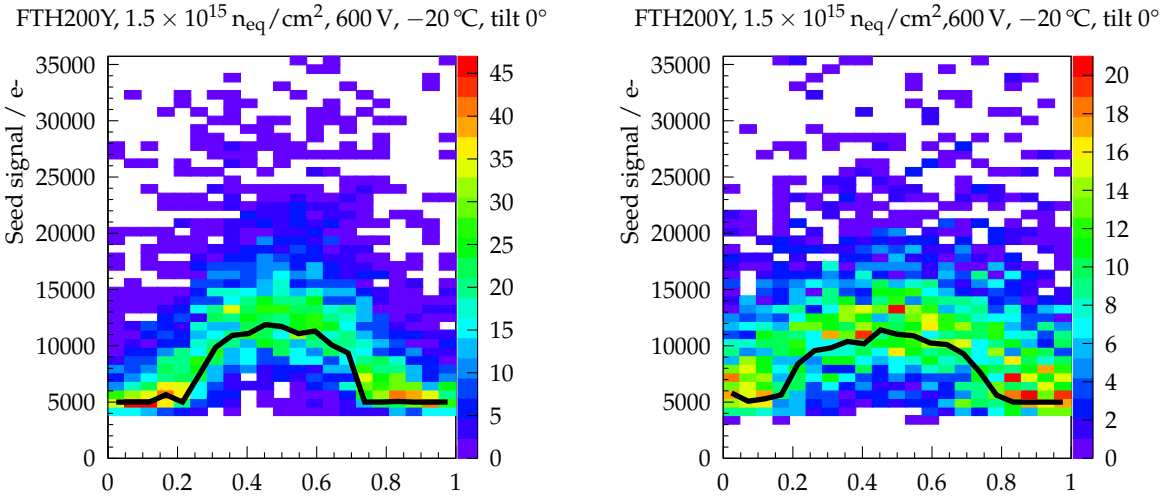

(a) Region 6-240 **(b)** Region 7-80

Figure 10.8.: Seed signal in the strip unit cell: Charge sharing between neighboring strips reduces the signal of the leading strip in the cluster. The most probable value of the seed charge in each bin is represented by the black line. In the vicinity of the strip implant at x=0.5, the seed charge approximately 10 000 electrons, while it drops below 6000 electrons between two strips at x=0 and x=1. This is close to the threshold of the clustering algorithm, bearing a risk of losing clusters.

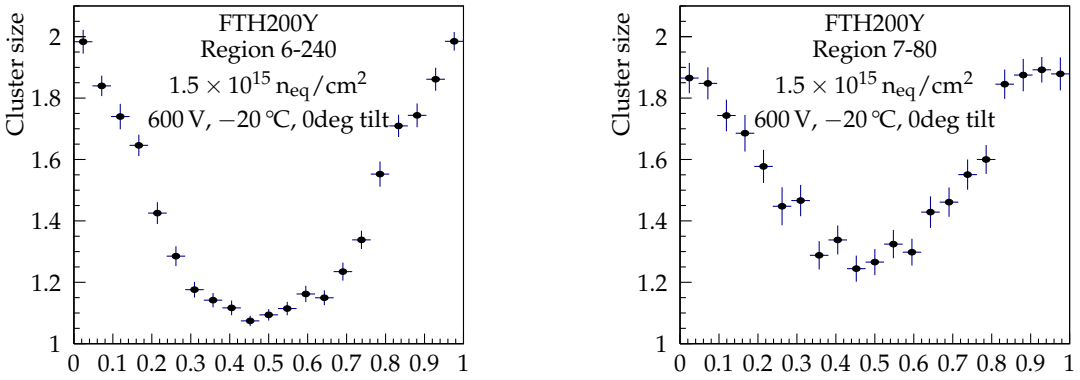

(a) Region 6-240

(b) Region 7-80

Figure 10.9.: Cluster size in the strip unit cell: The average cluster size is strongly dependent on the inter strip position of the track hit. Charge originating from tracks hitting in the area between two strip is likely to be shared by the two closest strips. For them, the cluster size is more likely to be two strips, whereas the charge created by tracks hitting directly on a strip is mostly collected by that single strip. The cluster size is more likely to be only one strip.

Cluster size and efficiency

The charge of tracks passing the sensor between two strips is shared among the strips. Both strips may pass the selection cuts and the cluster has an average size of two strips, in contrast to tracks hitting directly on a strip. There, the charge is collected mostly by that strip and the average cluster size is smaller. This is illustrated by figure 10.9, where the average cluster size in the unit cell of region 6 and 7 of the irradiated FTH200Y MSSD is shown.

A certain fraction of clusters is expected to have seed charge values below the most probable value. As the most probable value is approaching the noise cut for the seed strip, the possibility of losing clusters is not negligible. The efficiency of both considered regions of the sensor as a function of the strip hit position is shown in figure 10.10. The large pitch region shows a clear drop of efficiency in the region between both strips. Only close to the strip implant, the efficiency reaches a constant value close to 90 %. In contrast to that, the efficiency of the 80 µm pitch region stays constant at a level between 80 to 90 % over the whole unit cell. Besides the reduction of the seed signal due to various effects, the efficiency is influenced by the noise of the sensor, as the seed cut is defined as a multiple of the noise value of each strip. As already shown in figure 10.1, the noise of region 6-240 is approximately 15 to 20 % higher compared to region 7-80. This increases the seed cut by the same amount, which makes the efficiency estimation of region 6-240 more sensitive to a reduction of the seed signal.

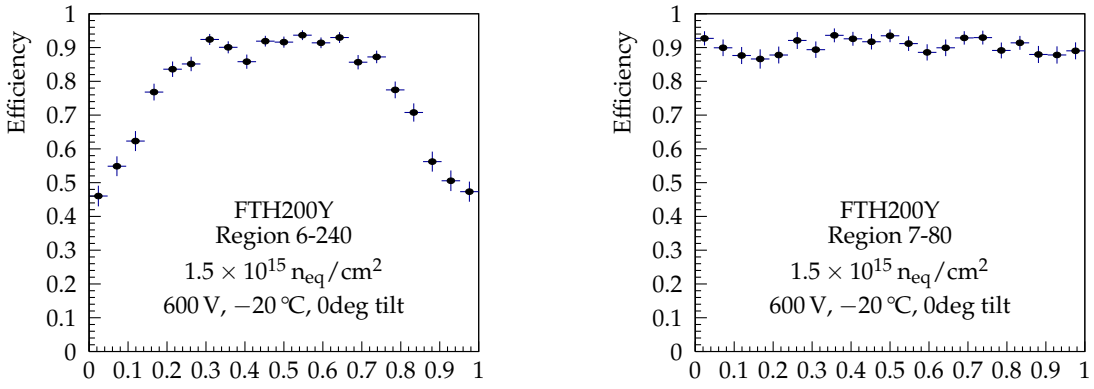

(a) Region 6-240 **(b)** Region 7-80

Figure 10.10.: Efficiency in the strip unit cell: The reconstruction efficiency of the track on the sensor with a 5σ seed cut for region 6 with 240 µm pitch (a) and region 7 with 80 µm pitch (b) is shown. On the large pitch region, the efficiency drops between the strips to values below 50 %. Directly on the strip, the efficiency is close to 90 %. On the small pitch region, no efficiency drop is observed, the efficiency is approximately 85 % in the whole unit cell.

Dependence of charge loss on cluster cut

The efficiency is an interplay between available charge on the seed strip, detector and readout noise as well as applied cluster cut during the analysis phase. The reduction of the seed charge between the strips can result in a detector inefficiency as observed in figure 10.10a when the seed signal to noise ratio drops below the cluster cut.

The cluster cut defines the ratio between noise occupancy and detector efficiency. Figure 10.11 illustrates the dependence of the efficiency in the strip unit cell for a clustering cut of 3σ, 5σ and 7σ times the noise level for region 6-240 and 7-80 of the irradiated FTH200Y sensor. With increasing cluster cut, the reduced seed signal between the strips on region 6 is more likely to be lower than the cut. For that, the efficiency is lowered with increasing seed cut in that region, as expected. Directly on the strip, the signal is still large enough to pass the cut, there the efficiency stays constant. On region 7, the reduction of the seed signal is not as pronounced as on region 6. For that, the drop of efficiency with increasing cut is not as strong. Only at a seed cut of 7σ, a slight reduction of the detector efficiency in the area between the strips occurs.

Dependence of charge loss on strip pitch

Figure 10.12 illustrates the efficiency in the strip unit cell for all four strip pitches of the intermediate width to pitch regions with width to pitch ratio of approximately 0.23. The observed charge loss leads to a drop of efficiency in the strip unit cell for the 120 µm and 240 µm pitch regions in the area between the strips, whereas the 70 µm and 80 µm pitch regions have a uniform detector efficiency over the strip unit cell, as desired. The loss of signal and efficiency is most pronounced on the 240 µm pitch region.

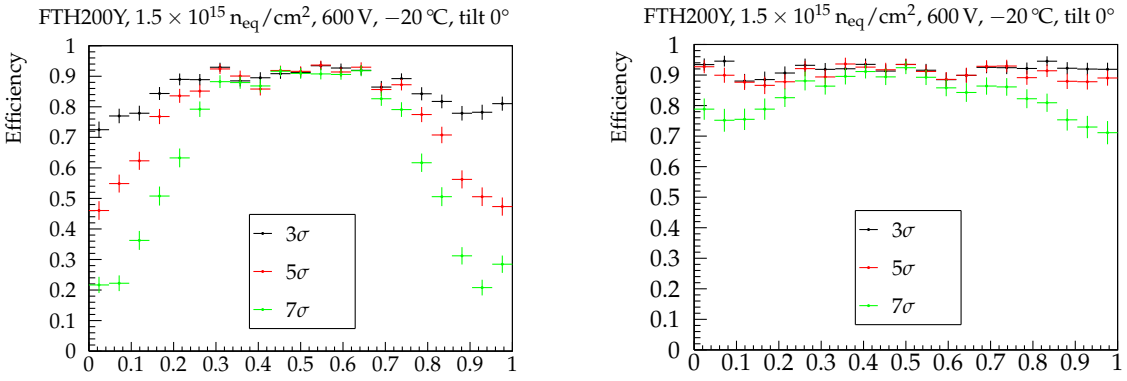

(a) Region 6-240

(b) Region 7-80

Figure 10.11.: Efficiency as a function of the track position in the strip unit cell for different cluster cuts: The efficiency of regions 6 and 7 is shown for a cluster seed cut of 3σ, 5σ and 7σ above the noise level. The drop of efficiency on the 240 µm pitch region is enhanced with rising cluster cut. On the 80 µm region, only a slight reduction of the efficiency at a cluster cut of 7σ is observable.

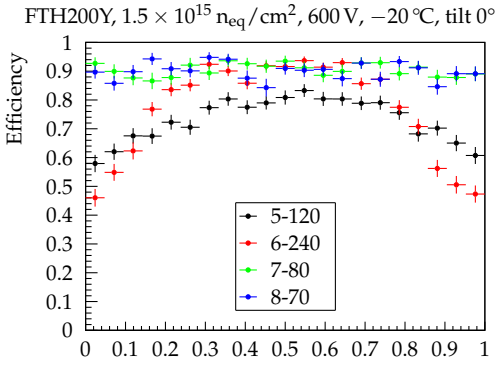

Figure 10.12.: Efficiency as a function of the position in the strip unit cell for the four different strip pitches.

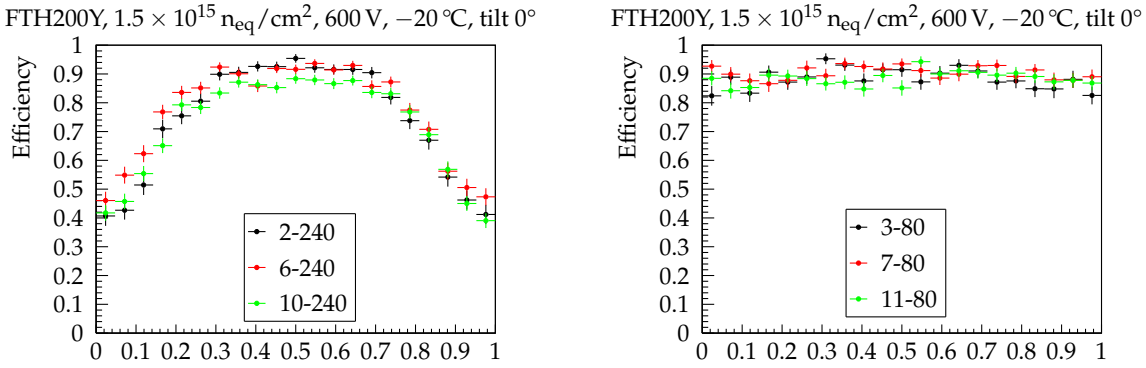

(a) 240 µm pitch

(b) 80 µm pitch

Figure 10.13.: Efficiency in the strip unit cell as a function of the position of the track incident. A comparison between the three different strip width to pitch ratios is shown for the 240 µm and the 80 µm pitch regions.

Dependence of charge loss on width to pitch ratio

The size of the charge loss depends not only on the strip pitch. At a given strip pitch, the amount and the spatial distribution of the reduced signal depends also on the the width of the strip implant.

Figure 10.13 illustrates the efficiency in the strip unit cell for the three different width to pitch ratios implemented on the sensor. The 240 µm pitch regions as well as the 80 µm pitch regions are shown. As before, the efficiency of the 240 µm pitch regions suffers from the observed charge loss between the strips, whereas the efficiency of the 80 µm pitch region is constantly high in the strip unit cell. No clear trend is observed with the strip width to pitch ratio. The efficiency on the 240 µm regions drops to approximately 50 % independent of the width to pitch ratio.

10.2.7 Comparison of different silicon base materials

Four different p-bulk sensors have been irradiated to the same fluence of $1.5 \times 10^{15}\,\mathrm{n_{eq}/cm^2}$. Two sensors are processed on float-zone silicon, two sensors are processed on magnetic-czochralski silicon wafers. On each type of sensor material, one sensor was processed with p-stop strip isolation, the other one with p-spray. The different strip isolation techniques result in different configurations of the electric field near the sensor surface and may for that have an influence on the observed charge loss between the strips.

A comparison of the efficiency in the strip unit cell of the different materials is given in figure 10.14. Here, a slight advantage of the MCZ200P material is visible, especially in the 240 µm pitch region. In contrast to that, the FTH200P material is least efficient. Both p-spray sensors show an efficiency intermediate between the p-stop sensors and behave very similar. The same trend is observed on the 80 µm region, but less pronounced.

All materials behave very similar and no clear conclusion on the best performing material can be made from this study.

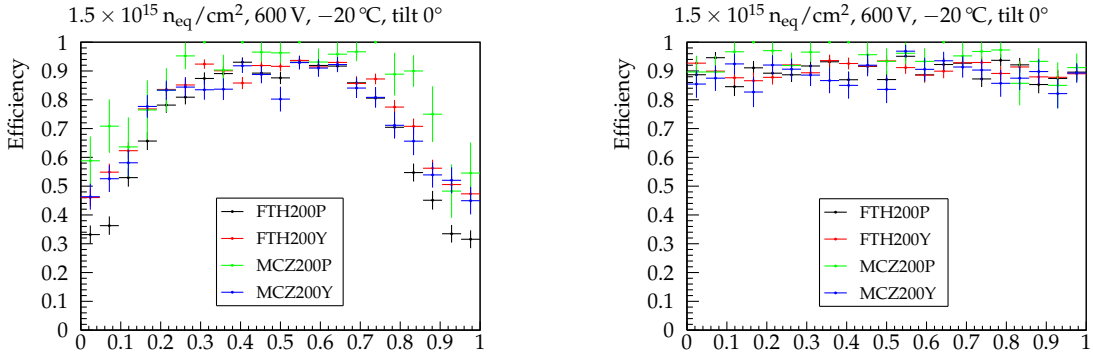

(a) Region 6-240 **(b)** Region 7-80

Figure 10.14.: Efficiency in the strip unit cell for all four irradiated p-bulk sensors. A slight advantage of the MCZ200P sensor showing a higher efficiency is visible, especially on the 240 µm pitch region.

10.3 Inclined track incidence

In addition to the perpendicular particle incidence, the DUT has been rotated, so that the particle beam hits the sensor at an angle of 10° and 30°. This is the more realistic operation condition, as in the CMS detector, the particle tracks are bend by the magnetic field and only high energetic particle tracks hit the sensor at an almost perpendicular angle. The analysis is performed in the same way as for perpendicular incident. In the following part, important sensor parameters are investigated as a function of the track incidence angle.

10.3.1 Signal

For inclined tracks, the path length of the track in the sensor is increased by a factor of $\frac{1}{\cos\theta}$. Due to the constant ionization per path length, the total created charge is increased. Figure 10.15 illustrates the total cluster charge of all twelve regions as a function of the track incident angle relative to the sensor surface. As expected, the signal increase is visible on all regions by approximately the same amount of charge.

10.3.2 Seed signal

The seed signal changes even more with the track incidence angle. Due to the increased path length and the increased total deposited charge in the sensor, also the signal of the seed strip could be increased. But considering the seed signal only, a second effect contributes. Due to the inclination, the charge sharing towards neighboring strips is increased. This may lead to a reduction of the seed charge. The interplay between both effects depends on the sensor geometry, mainly on the strip pitch.

Figure 10.16 depicts the charge of the seed strip as a function of the track inclination angle for the twelve regions of the MSSD. On the large pitch regions, the effect of the increased charge is dominant, the seed signal increases. On the regions with small strip pitch, the increased charge sharing dominates and the seed charge is more or less constant or even reduced.

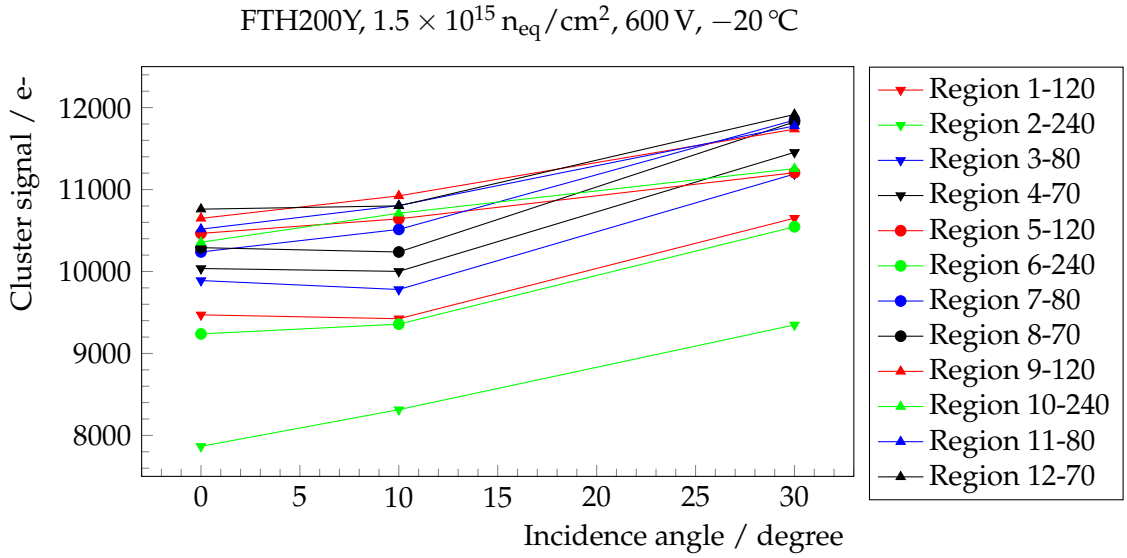

Figure 10.15.: Cluster charge as a function of the track incidence angle relative to the sensor surface. All twelve regions of an irradiated FTH200Y MSSD at a bias voltage of 600 V are shown. Due to the larger path length of the particle in the sensor, the deposited charge is increasing, which directly results in a larger cluster signal.

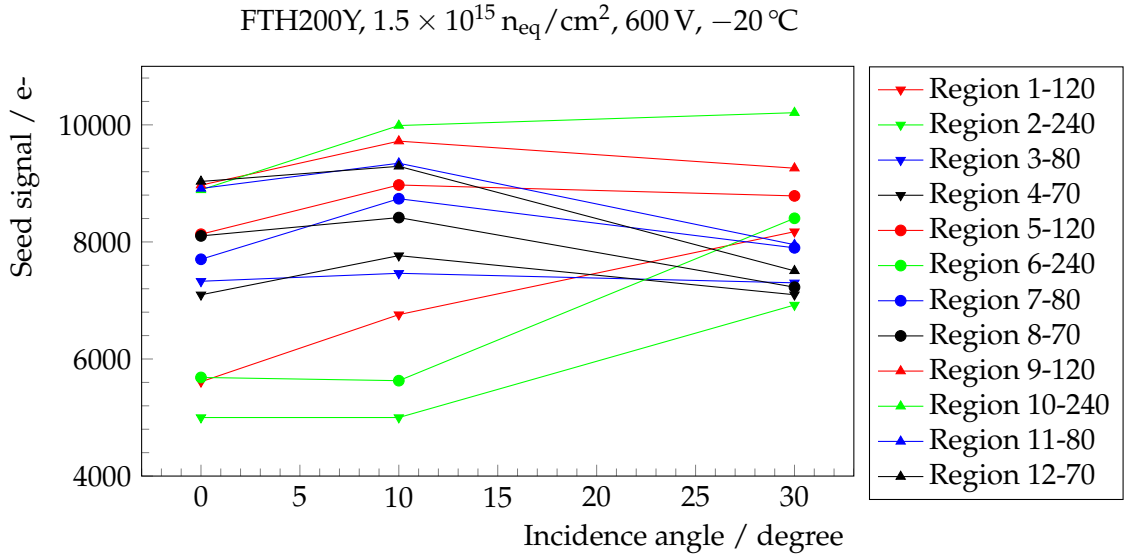

Figure 10.16.: Seed signal as a function of the track incidence angle. For the small pitch regions, the charge sharing effect is dominant and the seed charge is decreasing with the incidence angle. At larger strip pitch, charge sharing is suppressed and the seed signal increases similarly to the cluster charge.

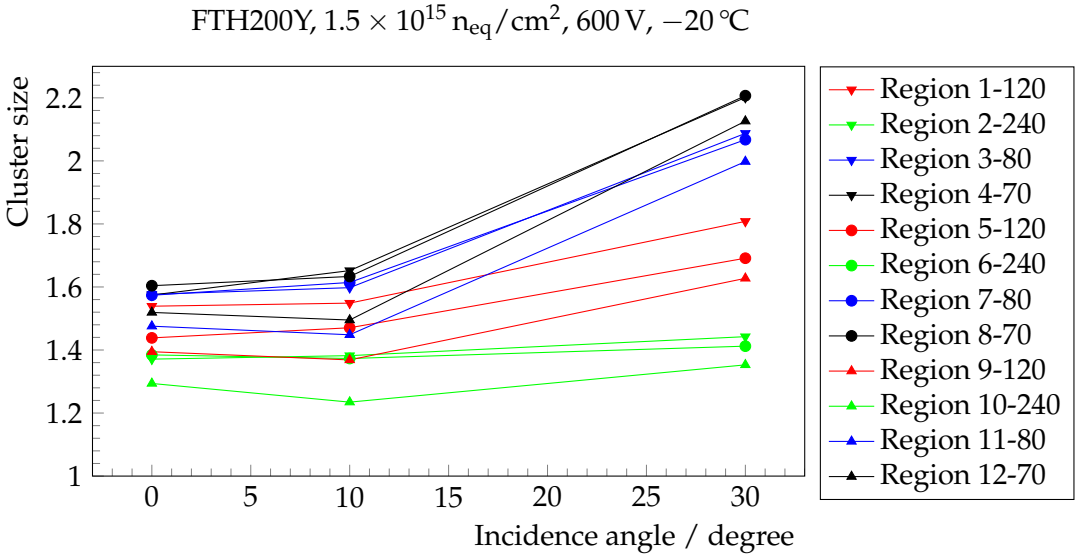

Figure 10.17.: Mean cluster size as a function of the track incidence angle as obtained on an irradiated FTH200Y sensor at 600 V bias voltage. As expected, the mean cluster size rises with the track angle. The rise is largest for the regions with lowest strip pitch. In addition, regions with small width to pitch ratio show systematically larger clusters than regions with large width to pitch ratio. This indicates a stronger charge sharing among neighboring strips, if the gap between the strips is reduced.

10.3.3 Cluster size

The mean size of the charge cluster increases with the track incidence angle, because of the larger possibility of the track hitting the influence zone of several strips. This probability is largest on regions with small strip pitch. Figure 10.17 depicts the mean cluster size as a function of the tilt angle of the MSSD in the beam telescope. As expected, the cluster size increases with rising tilt angle. The rise is strongest for the regions with the smallest strip pitch of 70 µm and less pronounced on the regions with larger strip pitch. At 30°, a clear ascending ordering with the strip pitch is noted. In addition to that, the cluster size shows a dependence on the strips width to pitch ratio. On regions with small w/p-ratio the resulting charge clusters are larger compared to regions with the same strip pitch but larger w/p-ratio. This indicates a stronger coupling and crosstalk between the strips, when the spacing between the strip implants and aluminum readout strips is reduced.

10.3.4 Resolution

Figure 10.18 illustrates the width of the residual distribution as obtained on the twelve regions of the irradiated FTH200Y MSSD as a function of the track incidence angle. Clearly, the ordering of the residual distributions with the strip pitch is visible, whereas no trend with the incidence angle is obvious.

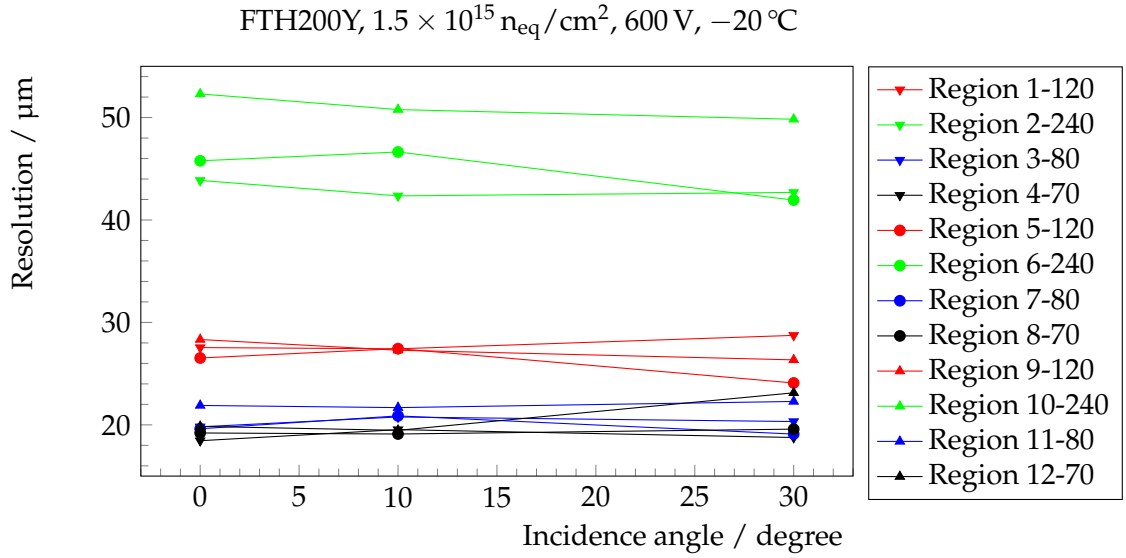

Figure 10.18.: Sensor resolution as a function of the track incidence angle at a bias voltage of 600 V. No significant dependence of the width of resolution from the incidence angle is visible.

10.3.5 Efficiency

The efficiency of the different regions as a function of the track incidence angle is shown in figure 10.19. Most regions, especially the 70 µm and 80 µm regions maintain an efficiency close to 90 %. This is the expected behavior from the seed signal distribution, which also did not show any dramatic loss for these regions with the incidence angle.

10.4 Simulation

Using a beam telescope to study the charge clusters allows for a sub-strip resolved analysis of the properties. On the simulation side, knowing the true impact point of the particle from the Monte Carlo data makes a simulation of the the whole telescope setup and subsequent analysis chain unnecessary. The predictions of the one-dimensional model outlined in chapter 7.2 is compared to the obtained test beam results. The dependence of the cluster properties from the incidence angle and the sub-strip properties have been investigated. As the model does not include the detailed strip geometry, it is not possible to reproduce the influence of the strip width on the results. For comparison to the simulation, the width to pitch ration of 0.23 has been chosen.

Several thousand particles hitting the silicon sensor at similar conditions as in the test beam are simulated. Each event results in a simulated charge distribution on the strips. Clustering of the simulated data is performed in a similar way as on the measured data, with a 5σ seed cut and a 2σ neighbor cut. The simulated strip data is overlaid with a Gaussian noise with a width of 1100 electrons.

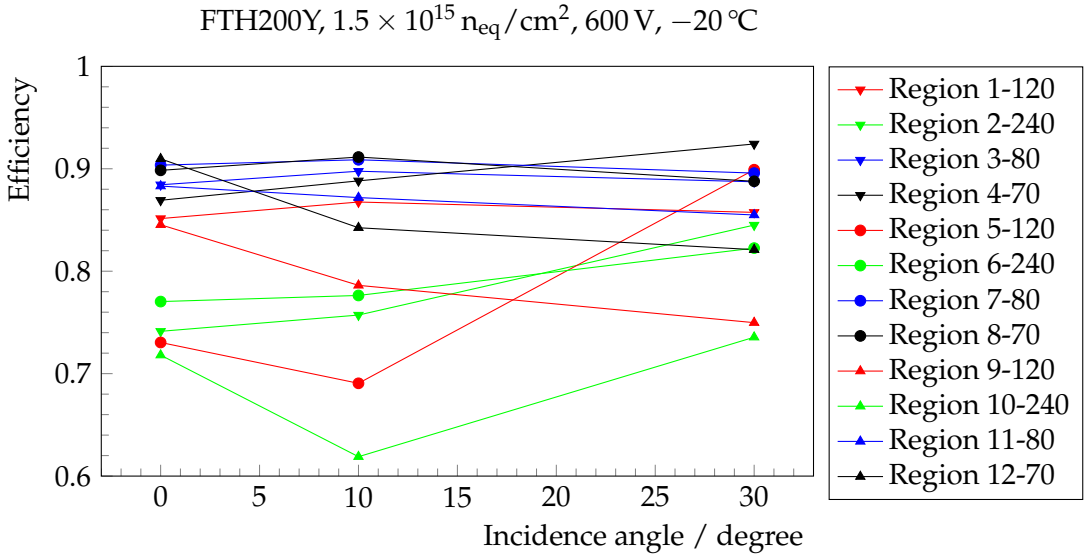

Figure 10.19.: Efficiency as a function of the track incidence angle as obtained on an irradiated FTH200Y sensor at 600 V bias voltage.

10.4.1 Angular dependence

The dependence of the signal and of the average cluster size from the track incidence angle has been studied. As seen before, the cluster signal increases with the track angle, whereas the seed signal is slightly reduced on the 80 µm pitch regions. This is reflected by the simulation, as shown in figure 10.20, for the most probable value of both cluster and seed signal. The simulation is represented by the colored bands, indicating the 1σ error of the most probable value of the Landau and Gaussian fit to the charge distribution in each angular bin. The rising trend of the cluster signal as well as the slightly falling trend of the seed signal is reproduced by the simulation model.

Figure 10.21 illustrates the average cluster size as a function of the track incidence angle. Due to the larger charge sharing at inclined incident, the average cluster size is increasing. The general trend is reproduced by the simulation model, although it slightly overestimates the increase of the average cluster size.

10.4.2 Sub-strip resolution

The cluster size as a function of the hit position in the strip unit cell of region 7-80 of the irradiated FTH200Y sensor is shown in figure 10.22. As already shown in figure 10.9b, the average cluster size increases due to the sharing of charge to neighboring strips towards the center of the pitch, where it reaches almost a value of 2. Directly on the strip, the average cluster size is smaller. This trend is reproduced by the simulation model, only directly in between the strips, the average cluster size is slightly larger than in the measured data.

A comparison of the measured cluster and seed signal to the simulation is given in figure 10.23. The simulated cluster signal distribution is relatively flat in the strip unit cell. This is expected, due to the fact that no real strip geometry is included in the model. The deposited charge is determined mostly by the path length of the particle in the sensor. The slight

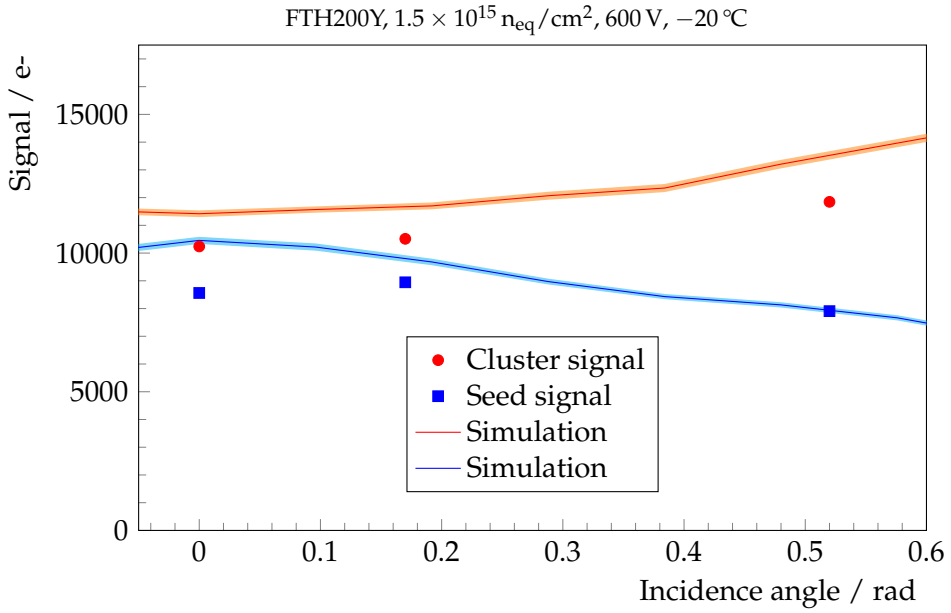

Figure 10.20.: Most probable value of the cluster and seed charge of the irradiated FTH200Y sensor at a bias voltage of 600 V as a function of the track incidence angle. The prediction of the simulation model is indicated by the colored bands, showing the 1σ error on the most probable value of the Landau and Gaussian fit to the simulated charge distribution.

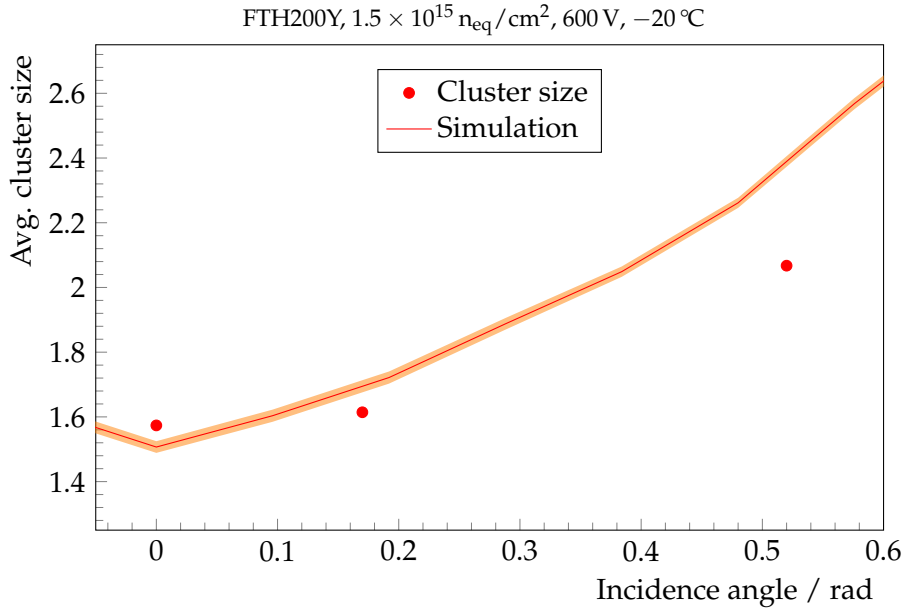

Figure 10.21.: Average cluster size as a function of the track incidence angle. Region 7-80 of an irradiated MSSD is compared to the predictions of the simulation model. Due to the larger lateral charge distribution at inclined incident, the average cluster size is increased. The general trend is reproduced by the simulation model, although it slightly overestimates the increase.

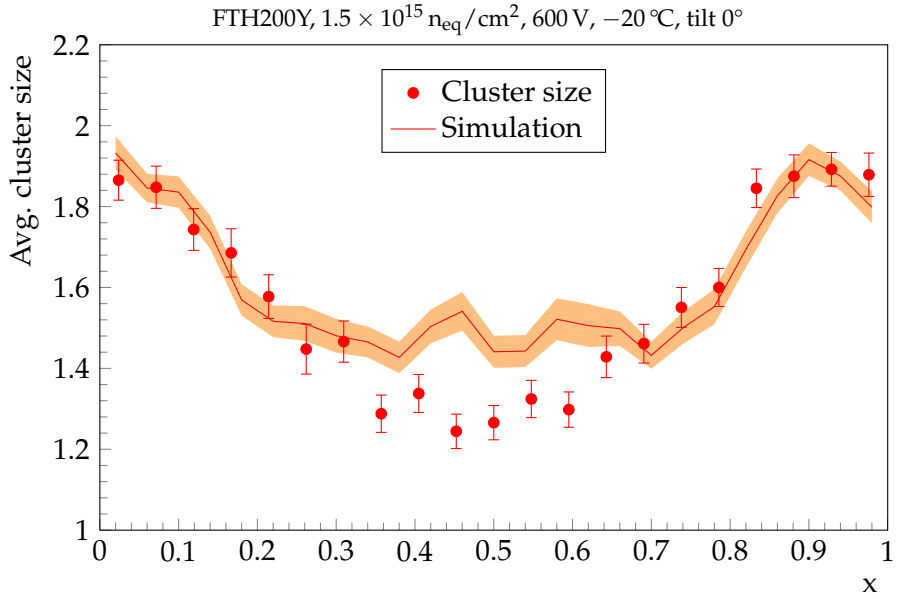

Figure 10.22.: Measured and simulated average cluster size as a function of the track hit point in the strip unit cell. Region 7-80 of a 200 µm thick sensor at 600 V bias is shown.

excess of charge near the strip is an indicator that the strip geometry directly influences the charge collection. Near the strips, the electric field is high which could lead to effects like impact ionization and charge multiplication. Considering the seed signal, the reduction due to charge sharing is reproduced by the simulation. Again, the signal directly on the strip is underestimated.

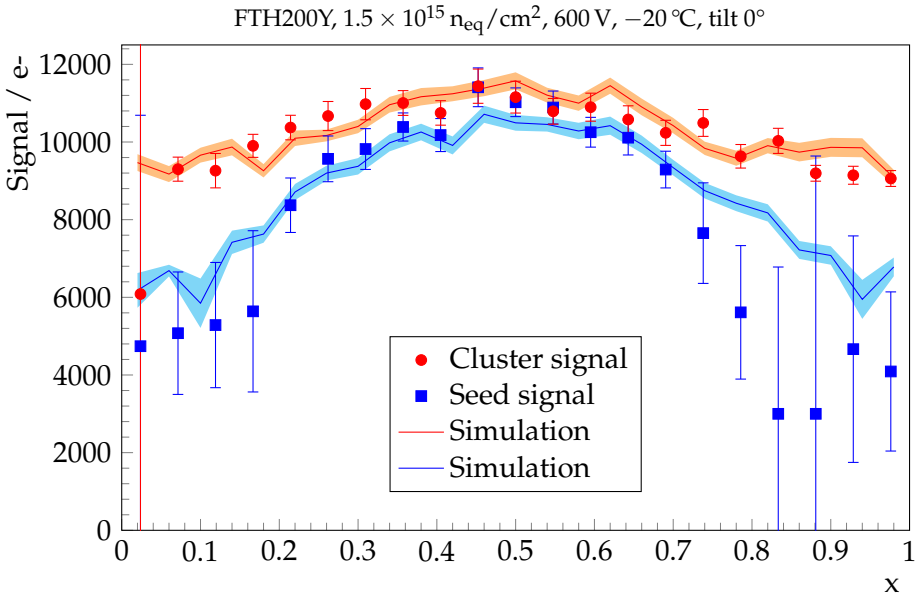

Figure 10.23.: Cluster and seed signal as a function of the track position in the strip unit cell. A comparison between measured and simulated data is shown. The reduction of the cluster signal been the strips has been implemented in the model. The falling trend of the seed signal towards the center of the pitch due to charge sharing is reproduced correctly.

11

Binary clustering

The next generation of readout chips used in the CMS Tracker, the CMS Binary Chip CBC, will be a binary readout chip. This means, the readout signal contains no information about the actual analogue pulse height of each individual strip as in the current tracker. In the future, the input signal given by the silicon sensor is compared to a programmable threshold already in the front-end chip. The information given to the DAQ chain contains only a binary one for a strip above threshold and a zero for any non hit strip. This resultss in a reduction of the data volume that has to be transmitted out of the tracker. A detailed description of the current prototype version of the chip, the CBC2, is given by Braga et al. [Bra+12].

In this chapter, data obtained using analogue readout systems has been reprocessed. A threshold is applied to the analogue data in a similar way as the new front-end chips will do. The resulting cluster properties are investigated as a function of the applied threshold and are compared to the output of the drift simulation model outlined in chapter 7.1.

11.1 ALiBaVa

Figure 11.1 shows a binary re-interpretation of data taken at the ALiBaVa setup on a 200 µm thick non-irradiated p-bulk sensor. Here, binary interpretation means, that the analogue strip data has been reanalyzed applying a binary threshold cut to the data. Every strip above the threshold is counted as cluster, every strip below the threshold is not. A threshold scan - as necessary on a binary chip to find the proper point of operation - can be performed by varying the applied threshold and studying the cluster parameters as a function of the threshold. Figure 11.1 shows a comparison between such a scan showing measured ALiBaVa data as well as simulated data. The average cluster size and the Cluster Identification Efficiency CIE are shown as a function of the applied cluster threshold in electrons. The Cluster Identification Efficiency is the efficiency of the binary clustering compared to the analogue readout with a 5σ-seed cut and a 2σ-neighbor cut. A CIE value of one means, that as many clusters are identified by the binary threshold clustering as with the analogue clustering.

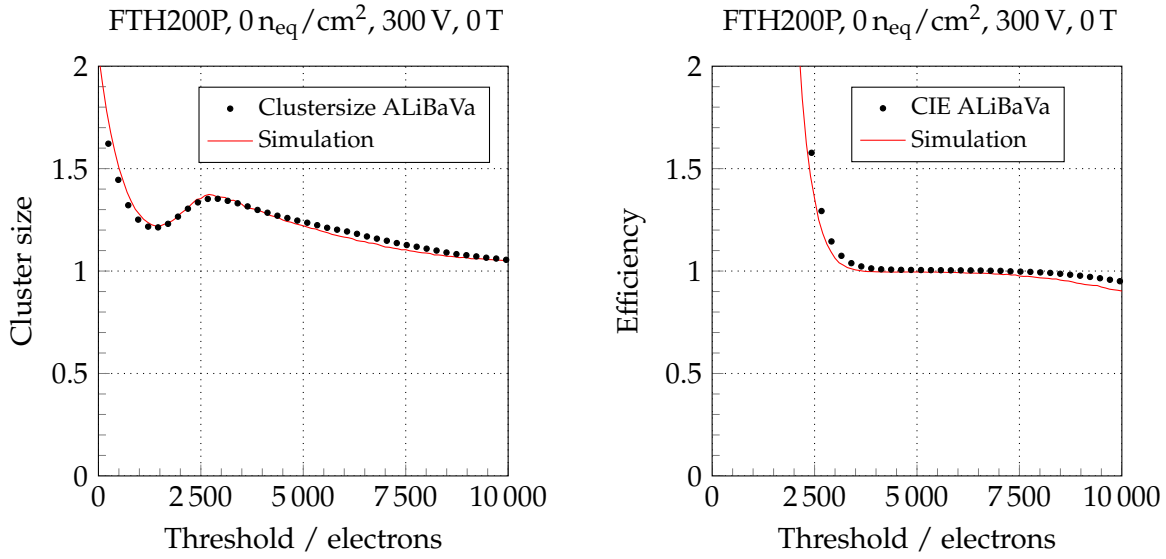

Figure 11.1.: Binary interpretation: comparison between a threshold scan on a measurement obtained at the ALiBaVa station and a simulation. The average cluster size and the Cluster Identification Efficiency are shown as a function of the applied cluster threshold in electrons.

At low thresholds, the distributions are dominated by noise clusters. In the region between 4000 and 8000 electrons, the Cluster Identification Efficiency is close to 1, meaning that all clusters are correctly identified. In that region, the average size drops with rising threshold, as the strips neighboring the seed strip are more likely to fall below the threshold cut if the cut is increased. Above a threshold of approximately 8000 electrons, the Cluster Identification Efficiency starts to decrease as more and more clusters fall below the threshold. The cluster size is close to 1.

The same analysis has been performed on simulated charge clusters. As for the measurement, 64 strips have been simulated and a similar noise of 950 electrons has been overlayed. The simulation reproduces the measured custer size and identification efficiency.

Figure 11.2 illustrates the same analysis performed on a 200 µm thick p-bulk sensor irradiated to a fluence of $1.5 \times 10^{15}\,n_{eq}/cm^2$ and an equivalent annealing of approximately eleven days at room temperature at a bias voltage of 600 V. Because of the radiation induced damage, the obtained signal from the sensor is reduced. This results in a reduced efficiency at high thresholds and the plateau with full efficiency close to 1 reaches only up to thresholds of 6000 electrons. The noise has not increased due to the irradiation and has been determined to be 900 ENC. If the reduced overall charge collection efficiency and the signal loss between the strips are taken into account, the simulation model describes the measurement of the cluster size and efficiency correctly.

After the comparison of the simulation output against the measured cluster parameters and the confirmation of the good agreement between the data points and the simulation model, the model can be used to interpolate cluster properties to other operation conditions. For example, the measurements in the ALiBaVa setup are performed without a magnetic field. Figure 11.3 shows an interpolation of the simulated threshold scan from 0 to 3.8 T. As expected, the average cluster size is increased due to the Lorentz shift of the drifting charge carriers, which enhances the sharing of charge to a neighboring strip (see also figures 6.3 and 6.4b).

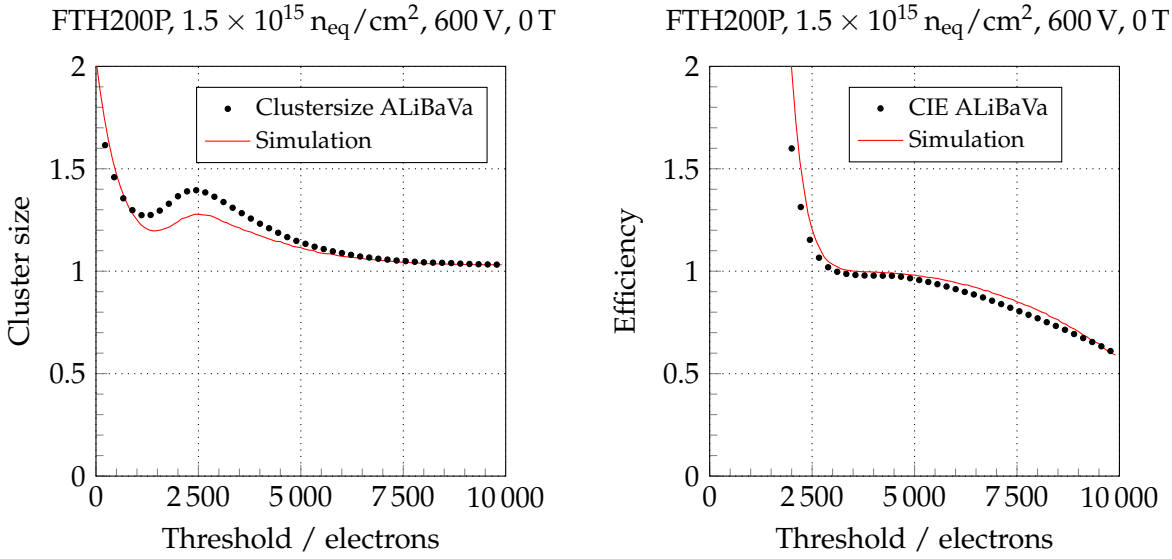

Figure 11.2.: Binary interpretation: comparison between a threshold scan on a measurement obtained at the ALiBaVa station on an irradiated sensor and a simulation. The average cluster size and the Cluster Identification Efficiency are shown as a function of the applied cluster threshold in electrons. The fluence is $1.5 \times 10^{15}\,n_{eq}/cm^2$, resulting in a most probable value of the cluster charge of 11 000 electrons. For the measurement and the simulation, 35 strips are considered, the width of the Gaussian noise distribution is 900 ENC in both cases.

This enhancement of the cluster size leads to a further reduction of the Cluster Identification Efficiency at high thresholds, as the leading strip in the cluster loses charge to its neighbor and thus is more likely to fall below the threshold cut.

Angular dependence

Figure 11.4 shows the result obtained from the binary cluster search with a threshold of 5000 electrons as a function of the track incidence angle. The simulated sensor is again a 200 µm thick n-bulk sensor at a bias voltage of 300 V. No magnetic field is applied. At perpendicular incident, the average cluster size is 1.2 strips. With rising track angle, the charge is distributed to neighboring strips and the average cluster size increases. The cluster identification efficiency is not affected by that, due to the still sufficiently large seed charge at large angles, as shown in figure 9.10.

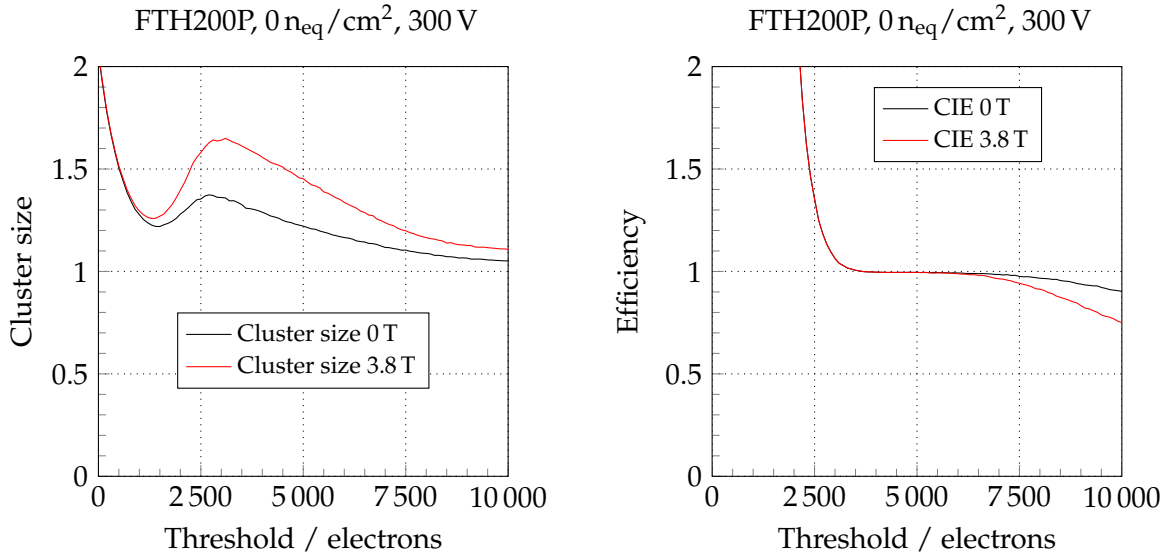

Figure 11.3.: Binary interpretation: extrapolation from 0T to 3.8T. The average cluster size is increased by the magnetic field due to a more pronounced charge sharing because of the Lorentz shift. The Cluster Identification Efficiency is reduced by that, because the leading strip in the cluster looses charge to its neighbor and is by that more likely below the threshold cut.

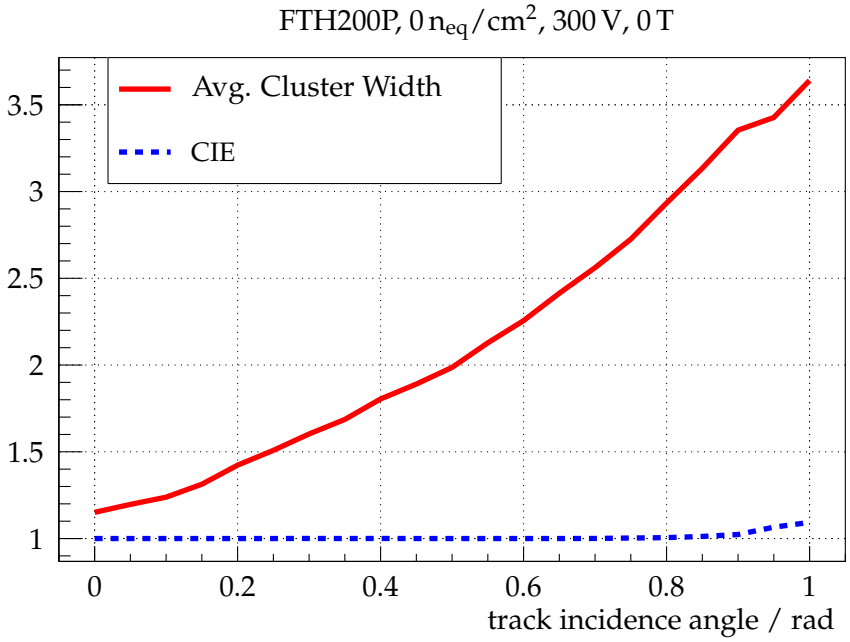

Figure 11.4.: Average cluster width and cluster identification efficiency with a binary clustering and a threshold of 5000 electrons as a function of the track incidence angle. The simulated sensor has a thickness of 200 µm and a strip pitch of 80 µm. No magnetic field is applied. The average cluster size increases due to the larger spread of the charge to neighboring strips. The identification efficiency stays constant.

11.2 Testbeam

The threshold is a parameter that has to be set in the front-end chip during data taking. Due to the on chip data reduction, no tuning of the threshold during the offline reconstruction is possible any more. For that, the threshold has to be tuned carefully. Obviously, the threshold has an impact on the resolution and efficiency. To estimate the the impact on the cluster parameters, the test beam data has been reanalyzed with binary clustering at different thresholds ranging from approximately 1000 to 15 000 electrons. Due to the modular software framework of the EUTelescope analysis package, only the clustering processor is modified.

Reasonable values for the clustering threshold are in the order of 4000 to 5000 electrons. An optimal value must compromise between efficiency, resolution and occupancy.

Using a binary readout, the cluster position can not be interpolated by e.g. the center of gravity of the analogue charge distribution, as given in equation 6.7. By taking the mean strip number of the charge cluster, the hit is placed either directly to the position of a strip, or in the center between two neighboring strips, by taking the center of gravity of the binary hit information:

$$x_{\text{hit}} = \frac{1}{N} \sum_{i=1}^{N} s_i \tag{11.1}$$

s_i denotes the strip number of strip i in the cluster. In contrast to the ALiBaVa setup, here only clusters that are assigned to a reference track have been taken into account. Only for the occupancy estimation, not assigned clusters have been counted, as well.

Here, only the irradiated FTH200Y sensor at perpendicual incident is shown. A comparison to the non-irradiated sensor and an inclined particle incident of 30° is shown in appendix B.

11.2.1 Cluster size

The average cluster size of the clusters that have been associated to a particle track as a function of the binary threshold is shown in figure 11.5. With increasing threshold, neighboring strips are more likely to fall below the threshold cut and the average cluster size is asymptotically falling to one strip. Towards low thresholds, the average cluster size is increasing due to the rising noise contribution to the clusters.

11.2.2 Efficiency & Occupancy

The reconstruction efficiency of a particle hit depends on the threshold. With rising threshold level, only large signals pass the cut. For that, the efficiency drops with the threshold, as illustrated in figure 11.6. At low thresholds, most tracks can be associated to a hit on the MSSD and the efficiency is close to 100 %. Besides the efficiency, also the occupancy of the detector is an important factor. Low thresholds give rise to high detector efficiency, but more and more noise clusters are also able to pass the threshold cut. This increases the occupancy of the detector, as shown in figure 11.7. Noise hits cannot be distinguished from real particle hits, for that, they complicate the track finding due to the larger combinatorics. Additionally, the probability of merging several distinct clusters increases. The lower limit for the threshold is therefore given by the noise of the detector. To estimate the occupancy, all clusters found on

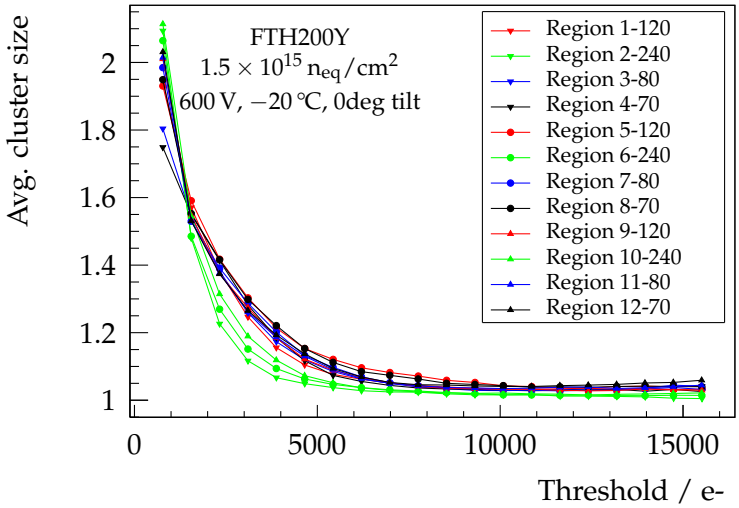

Figure 11.5.: Average cluster size as a function of the applied binary threshold at perpendicular particle incident. A comparison of the non irradiated MCz200P sensor to the irradiated FTH200Y sensor is shown. With rising threshold, neighboring strips are cut away and the average cluster size approaches a value of one strip at high thresholds.

the sensor have to be taken into account, not only clusters close to a particle track. Otherwise the large contribution of noise clusters to the occupancy at low threshold is lost.

11.2.3 Resolution

Figure 11.8 illustrates the width of the residual distribution as a function of the binary threshold. As with the analogue clustering, a clear hierarchy of the width of the residuals is given. Regions with large strip pitch have larger residuals than regions with small strip pitch, as expected from equation 10.1. The variations with the binary threshold originate from the variations of the cluster size and detector efficiency. As the seed signal depends on the track position in the strip unit cell, clusters induced by tracks passing between two strips are more likely to fall below the threshold than clusters originating from tracks hitting directly on a strip. As the remaining hits are located by definition directly on the strip and the track has also to pass nearby the strip in order to create a sufficiently large signal, the residuals are systematically reduced. This influence is clearly visible on the 240 µm regions after irradiation.

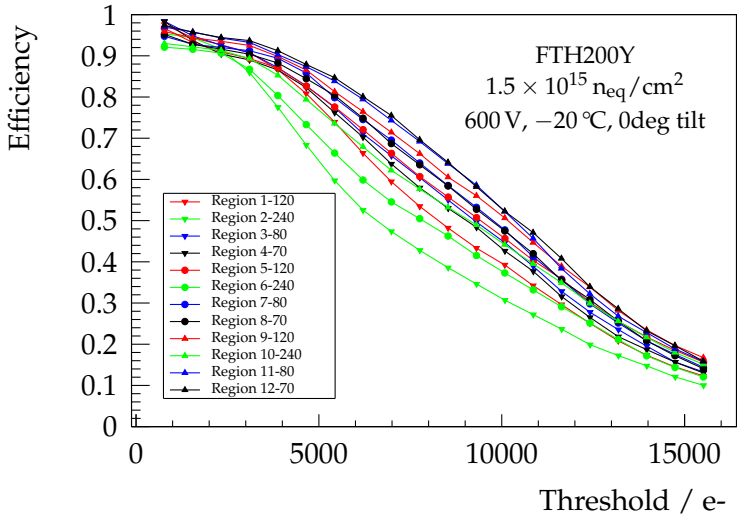

Figure 11.6.: Hit identification efficiency as a function of the binary threshold. With rising cut, more and more clusters fall below the threshold and the efficiency for identifying a hit after the traverse of a particle is reduced. At low thresholds, the efficiency is close to 100 %.

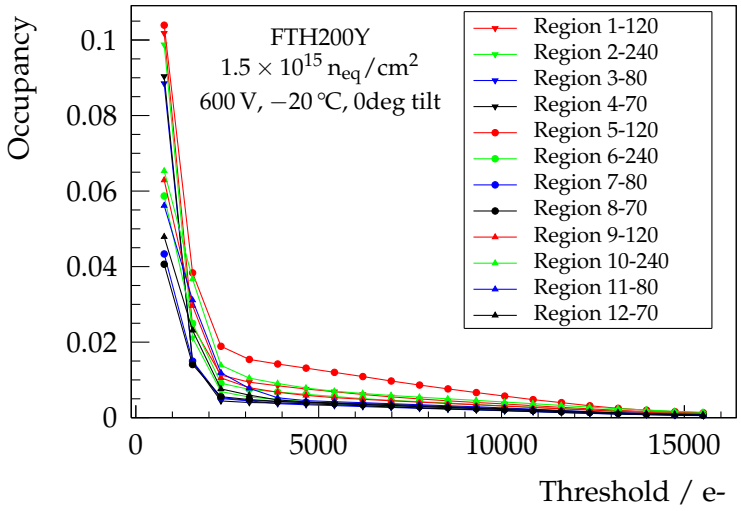

Figure 11.7.: Occupancy of the regions of the MSSD as a function of the binary threshold. Both, particle hits and noise clusters contribute to the occupancy. At low threshold, a strong increase of the occupancy due to noise clusters can be noted.

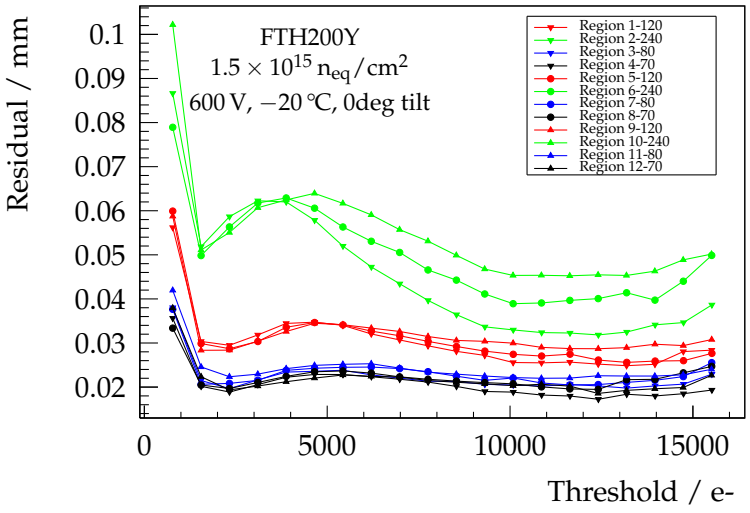

Figure 11.8.: Width of the residual distribution as a function of the binary threshold.

12

Trigger module

In this chapter, the obtained model for signal generation on silicon strip sensors is applied to the proposed trigger module concept foreseen to be operated in CMS Tracker after the phase 2 upgrade. As already mentioned briefly in chapter 2, the tracker shall contribute to the level 1 trigger decision. The readout bandwidth is limited, for that it is not possible to read out the entire tracker with the bunch crossing frequency of 40 MHz. To reduce the amount of data, the uninteresting low momentum tracks are filtered out at the module level and only hits from high momentum particles are read out and passed on to the trigger at the full bunch crossing frequency. For that, a module concept with integrated momentum discrimination has been developed by the CMS Tracker community. The target is to reject most low momentum particles below 1 GeV c^{-1} to a rate below <1% and to maximize the efficiency at a transverse momentum of 2 GeV c^{-1} [Abb13].

The hit information obtained by the Geant simulation presented in chapterr 7.2.3 is translated to charge clusters on the two sensors using the model outlined in chapter 7.1. In this way, the Lorentz shift of electrons and holes in the silicon due to the magnetic field is taken into account.

12.1 Analysis

To study the response of the module stack to the incident of a particle, charge clusters have to be identified. For that, a binary clustering algorithm using a signal threshold is applied to the sensor which is closer to the interaction point. For a strip that exceeds the threshold, a search window is applied on the second sensor, as outlined in figure 2.11a. Therefore, the offset correction as illustrated in figure 2.13 is applied by shifting the window following

$$\text{offset} = (\text{strip} - 512) \cdot \frac{\text{spacing}}{\text{radius}}. \tag{12.1}$$

By that, the search window is centered around the radial projection of the inner hit strip to the outer sensor. In the outer layers of the tracker, where 2S modules will be used, the offset

is at maximum ± 1 strip. The current prototype of the readout chip, the CBC2, allows the adjustment of the offset in the range of ± 3 strips for the whole readout chip [Bra+12]. If any strip inside the search window exceeds the threshold, the trigger bit is set for that event. By averaging over all events with a certain particle momentum, the trigger efficiency is obtained as a function of the particle momentum.

The trigger efficiency illustrated in the following plots is defined as the average fraction of particles that have been identified on both sensors and for which the hits pass the search window cut. To obtain the trigger efficiency as a function of the particle momentum, the efficiency is estimated in bins of 100 MeV c^{-1} size.

12.2 Results and optimization

In the following, the influence of the module geometry on the p_{T}-cut is investigated by varying geometrical parameters of the module design. Knowing the dependence of the momentum cut from the module geometry is important for choosing the optimal values to obtain a detector response as homogeneously as possible. Here, the tracker geometry as given by figure 2.7 with barrel layers at 20 cm, 35 cm, 50 cm, 70 cm, 90 cm and 110 cm radial distance has been used. Following the current design baseline, the simulated silicon sensors have a thickness of 200 µm, a strip pitch of 100 µm in the inner three layers for the PS module and 90 µm in the outer three layers for the 2S module. In all sensors, electrons are read out. During the charge transport in the sensors, the Lorentz deflection due to the 3.8 T magnetic field is considered. In the analysis step, binary clustering with a threshold of 5000 electrons has been applied. After optimization of the search window, the performance after irradiation is investigated.

12.2.1 Charge sign

Muons and antimuons are deflected in the opposite direction by the magnetic field and are more likely to hit the module stack at positive or negative angle. Due to the magnetic field in the detector the cluster generation is no longer symmetric around perpendicular incident. The trigger efficiency is for that not necessarily identical for positively and negatively charged particles. Figure 12.1 shows the simulated trigger efficiency as a function of the transverse momentum for muons and antimuons separately. The efficiency shows a steep increase in the range of 2 to 3 GeV c^{-1} and 100 % efficiency above 3 GeV c^{-1}, as desired.

No hit inefficiency has been observed for irradiated sensors with small strip pitch, for that the trigger efficiency shown in figure 12.1 is identical for muons and antimuons. For that reason, in the following examinations of non-irradiated trigger modules, the information obtained from muon and antimuon tracks is combined.

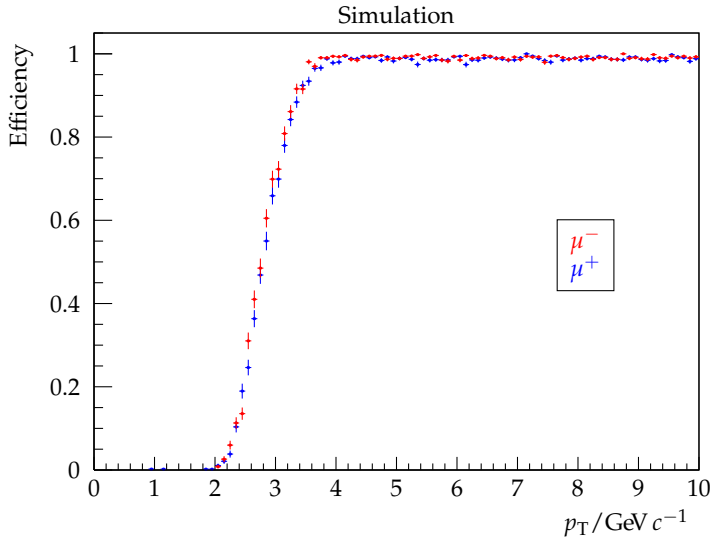

Figure 12.1.: Simulated trigger efficiency of a 2S module as a function of the particles transverse momentum. Here, the radial distance to the interaction point was 110 cm and the search window on the second sensor has been chosen to be nine strips. The spacing of the two sensors is 1.8 mm. During the digitization, the magnetic field of 3.8 T was considered. A steep turn on in the range of 2 to 3 GeV c^{-1} demonstrates the proper function of the concept. Despite the different curvature of the tracks of the two particle types, no difference in the efficiency is notable.

12.2.2 Sensor spacing

The sensor spacing is a geometrical parameter of the module that has to be fixed during the design phase of the new tracker. Due to mechanical and thermal constraints, the spacing can not be chosen completely free, but has to be in a certain range. For simplicity reasons during the module assembly, as less different spacings as possible are preferable in the tracker. Its influence on the trigger efficiency is shown in figure 12.2. The distance of the sensor stack to the interaction point has been chosen to be 110 cm, the search window is nine strips large. A smaller spacing in between the two sensors leads to a smaller lateral displacement of the second hit compared to the first one, as indicated by equation 2.4. For that, tracks with lower momentum are more likely to pass the selection window and by that are more likely to be passed on to the trigger logic. The threshold gets shifted towards lower particle momentum and the transition gets sharper.

12.2.3 Search window

Choosing the correct search window is important for the proper operation of the module concept. As smaller the search window, as stricter is the cut on the transverse momentum. As an example, figure 12.3 illustrates the trigger efficiency for a layer 6 module with 1.8 mm sensor spacing as a function of the search window size in the range of 1 strip to 9 strips. As expected, the trigger threshold is significantly lowered, by increasing the search window. In addition, the turn on is steeper and the threshold is sharper. In this example, a search window size of nine strips seems reasonable. To avoid ambiguities at high luminosities and high track

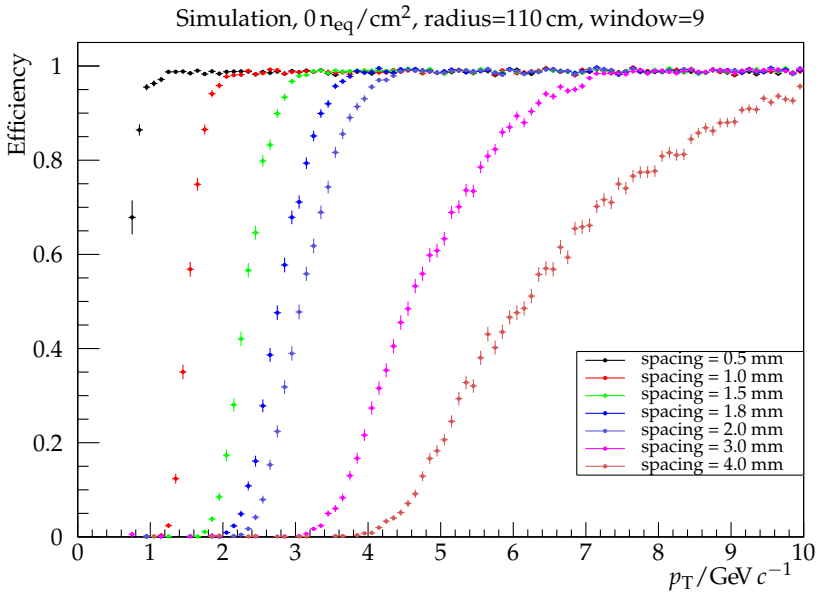

Figure 12.2.: Trigger efficiency as a function of the sensor spacing. The closer the two stacked sensors are placed together, the smaller the lateral displacement of the hit on the second sensor and the lower the momentum needed to fire the trigger. The layer radius is 110 cm, the size of the search window is 9 strips.

densities, the search window cannot be enlarged too far. For that, choosing a proper sensor spacing for tuning the momentum threshold is important.

12.2.4 Tracker layer

The effect of the radial dependence of the p_T-cut as illustrated in figure 2.11b is reproduced by the simulation. Figure 12.4 shows the trigger efficiency for three different radial distances from the interaction point. The sensor spacing is 1.8 mm in all three cases, the search window was chosen to be nine strips. As expected, the hits in the outer most sensor are wider separated for the same particle momentum and for that the trigger efficiency is reduced. Due to that, the turn on is shifted towards higher momenta.

12.2.5 Optimization of the search window

In order to optimize the search window in each tracker layer, equation 2.4 has been used with a target p_T-cut of 2 GeV c^{-1}. Table 12.1 and figure 12.5 illustrate the result. Over the considered tracker layers, a homogeneous momentum cut in the desired area is achieved. Above a transverse momentum of about 2 GeV c^{-1}, most layers show an efficiency close to 100 %, whereas tracks with a transverse momentum below 1 GeV c^{-1} are suppressed. Only in the innermost layer, the transition is softer.

Comparing the obtained results to a full simulation of the upgraded tracker e.g. shown by Boudoul [Bou13] or Pozzobon [Poz13], no qualitative difference can be observed. A steep turn on of the efficiency in the momentum range of 2 GeV c^{-1} can be achieved by adapting the search window to the module geometry.

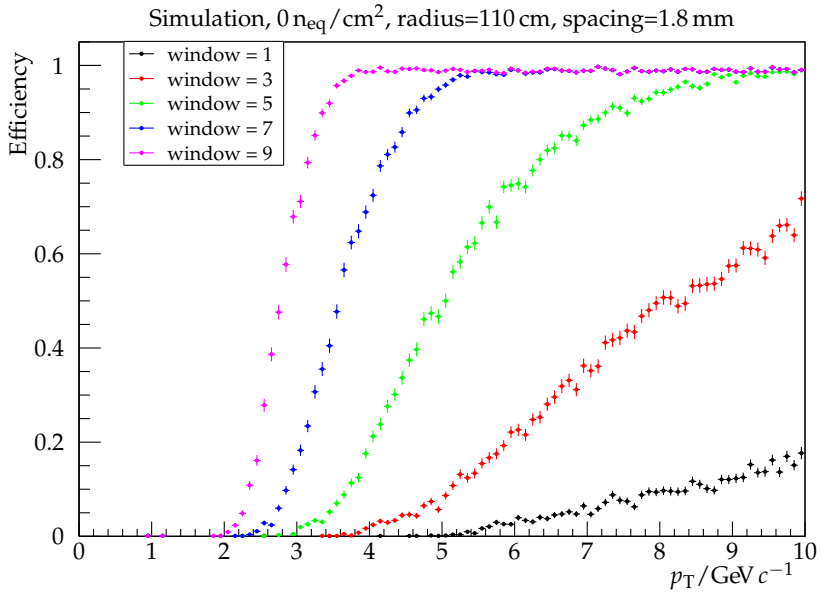

Figure 12.3.: Trigger efficiency as a function of the size of the search window. By varying the size of the search window, the threshold can be tuned in discrete steps over a wide range of momentum. In this example, the distance from the interaction point is 110 cm, the sensor spacing is 1.8 mm.

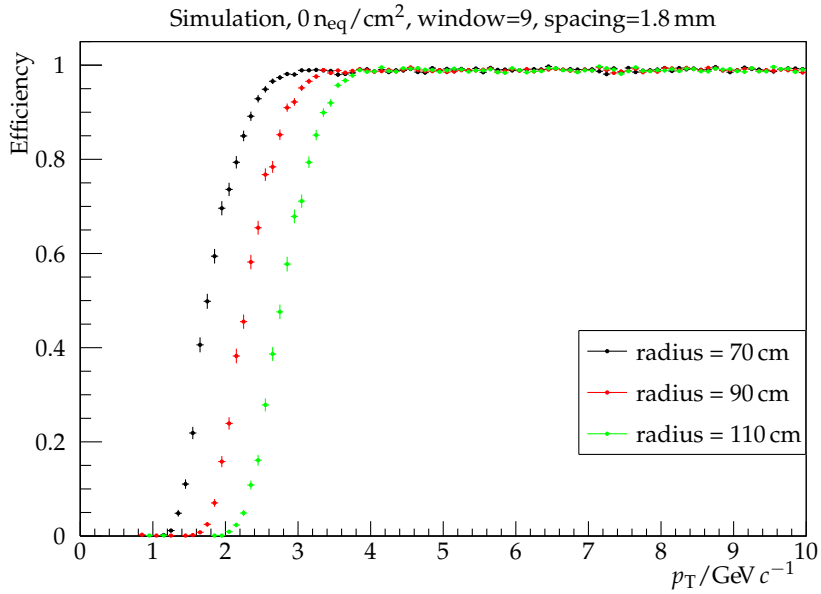

Figure 12.4.: Trigger efficiency as a function of the radial distance of the module from the interaction point. As expected, the efficiency is lower for higher radii. Sensor spacing is 1.8 mm in all three cases, the search window is 9 strips.

Table 12.1.: Tuned geometrical parameters of the trigger module geometry

tracker layer	strip pitch / µm	layer radius / cm	sensor spacing / mm	search window / strips
1	100	20	2.2	5
2	100	35	1.6	5
3	100	50	1.6	7
4	90	70	1.8	9
5	90	90	1.8	11
6	90	110	1.8	13

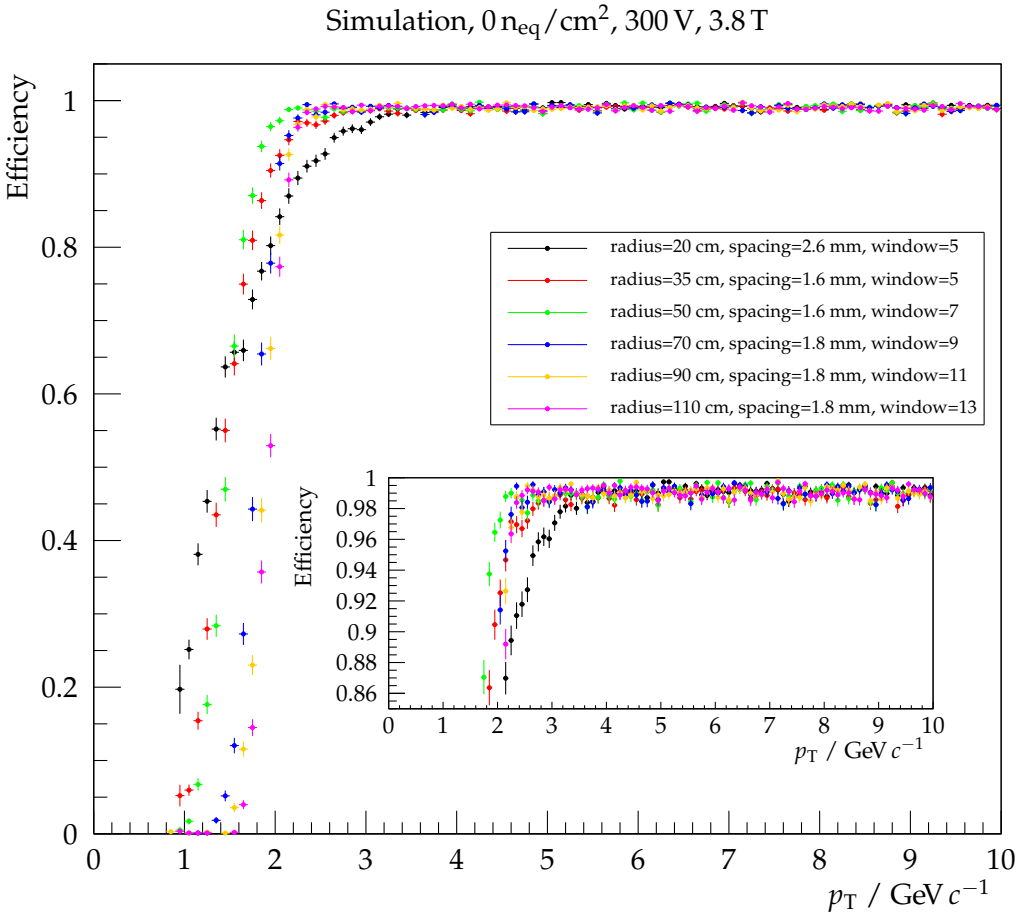

Figure 12.5.: Simulated trigger efficiency as a function of the transverse momentum after tuning the search window to a momentum cut of 2 GeV c^{-1}. The sensor spacing has been chosen according to the tracker layout. The noise is assumed to be gaussian distributed with a width of 1000 electrons, the applied threshold for the binary clustering is 5000 electrons. The small inlay depicts a detailed view of the efficiency above 85 %.

Table 12.2.: Simulation parameters used for the simulation after irradiation

tracker layer	expected fluence [BRIL2013] after 3000 fb^{-1} / (n_{eq}/cm^2)	collected signal / electrons	CCE / %
1	1.2×10^{15}	10 250	73.2
2	5.75×10^{14}	12 200	87.1
3	3.75×10^{14}	12 800	91.6
4	2.4×10^{14}	13 250	94.6
5	1.77×10^{14}	13 450	96.0
6	1.5×10^{14}	13 550	96.6

12.3 Irradiation

In the following, the impact of irradiation on the performance of the module concept is investigated. As before, the simulated sensors are 200 µm thick and have a strip pitch of 90 µm, the strength of the magnetic field is 3.8 T. Like for the non-irradiated case, the sensor spacing has been chosen following the layout for the new tracker. For including the radiation damage, the simulation model is parametrized for each layer with the options that have been obtained by adaption to the test beam results. The reduction of the collected signal is assumed to be linearly with irradiation fluence, which is an approximation to the results of Hoffmann [Hof13]. Summarized, the parameters are:

- a full depletion voltage of 450 V,
- Gaussian noise of 1000 ENC,
- an applied bias voltage of 600 V,
- a reduction of the charge collection efficiency in each layer following the expected irradiation fluence after 3000 fb^{-1} as given in table 12.2,
- additional charge loss of 20 % between the strips.

Figure 12.6 illustrates the obtained trigger efficiency as a function of the particle momentum using the geometric parameters given in table 12.1. No obvious difference in the turn-on can be observed compared to the non-irradiated case. This demonstrates that the concept in general still works with 200 µm thick sensors after an irradiation to 1.5×10^{15} n_{eq}/cm^2. However, the total trigger efficiency of the module stack for high momentum tracks which pass the window cut is reduced from 99 % in the non-irradiated case to 90 % in the innermost layer of the tracker because of the reduced charge collection efficiency.

As a worst-case scenario, the simulation has been performed with further reduced overall charge collection efficiency in the range of 50 to 100 % in the simulation. The resulting trigger efficiency for the innermost and outermost layer is illustrated in 12.7. As before, the binary threshold for the clustering is 5000 electrons, the simulated noise is 1000 ENC. The expected signal in a 200 µm thick sensor at 100 % CCE is 14 000 electrons.

The further reduced charge leads to inefficiencies in the hit identification in the individual sensors. As a result, the overall trigger efficiency is reduced, even for high momentum tracks.

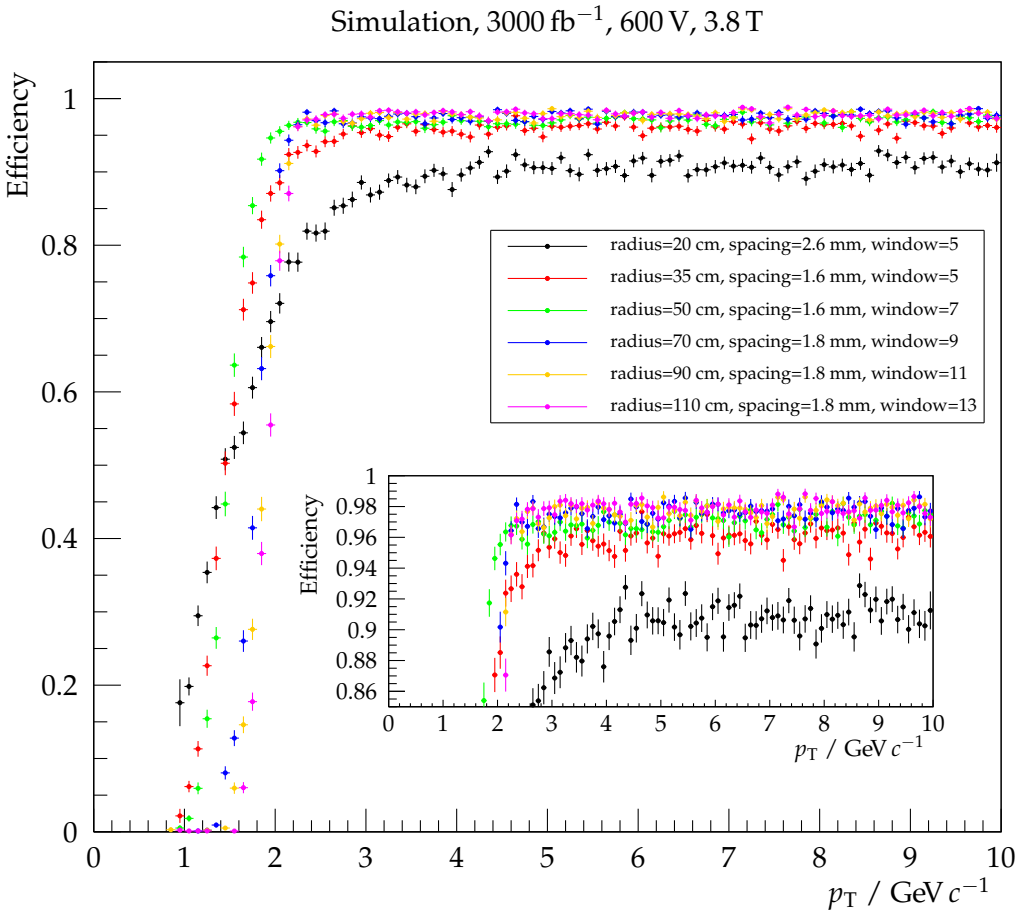

Figure 12.6.: Simulated trigger efficiency as a function of the transverse momentum. The noise is assumed to be gaussian distributed with a width of 1000 electrons, the applied threshold for the binary clustering is 5000 electrons. The small inlay depicts a detailed view of the efficiency above 85 %. The assumed charge collection efficiency in each layer is varied according to the expectation after 3000 fb^{-1} integrated luminosity at the HL-LHC.

For a correct positive trigger decision, a hit must be identified in both sensors simultaneously. The reduced charge collection has no impact on the turn-on behavior of the module, as the displacement of the hits on the two sensors is mainly defined by the geometry.

Figure 12.7 demonstrates, that already with slightly reduced charge collection, the efficiency of the trigger module is decreased. This emphasizes the need to obtain as much as possible signal from the sensor. In principle, two options to increase the signal exist. The first possibility is to increase the thickness of the sensors, as the ionization length is increased. However, after irradiation of $1 \times 10^{15}\,\mathrm{n_{eq}/cm^2}$ and higher, Hoffmann [Hof13] demonstrated that 200 µm thick sensors and 320 µm thick sensors collect at a bias voltage of 600 V the same amount of charge due to a faster increase of the depletion voltage of the thick sensors. This has already been illustrated in figure 8.8. Because of that, thicker sensors alone may not help in increasing the efficiency of the trigger module. The second option to increase the collected charge after irradiation is to increase the applied bias voltage. At 900 V and after $1.5 \times 10^{15}\,\mathrm{n_{eq}/cm^2}$, the collected charge is about 20 % higher. This is valid for both sensor thicknesses of 200 µm and 320 µm. During the beneficial annealing, a slight additional benefit from 320 µm thick sensors is to be expected from the measurements by Hoffmann [Hof13], as illustrated in figure 8.9b.

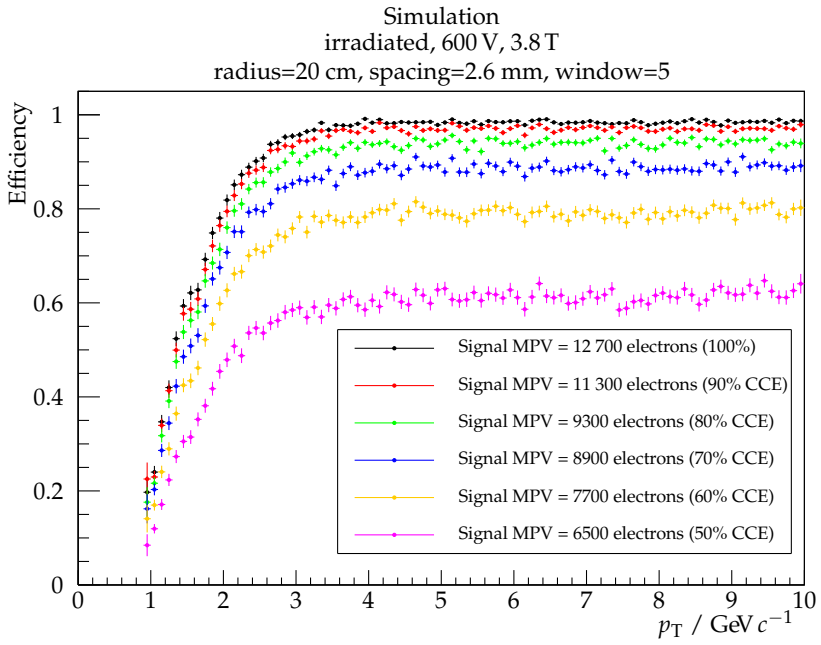

(a) Layer 1

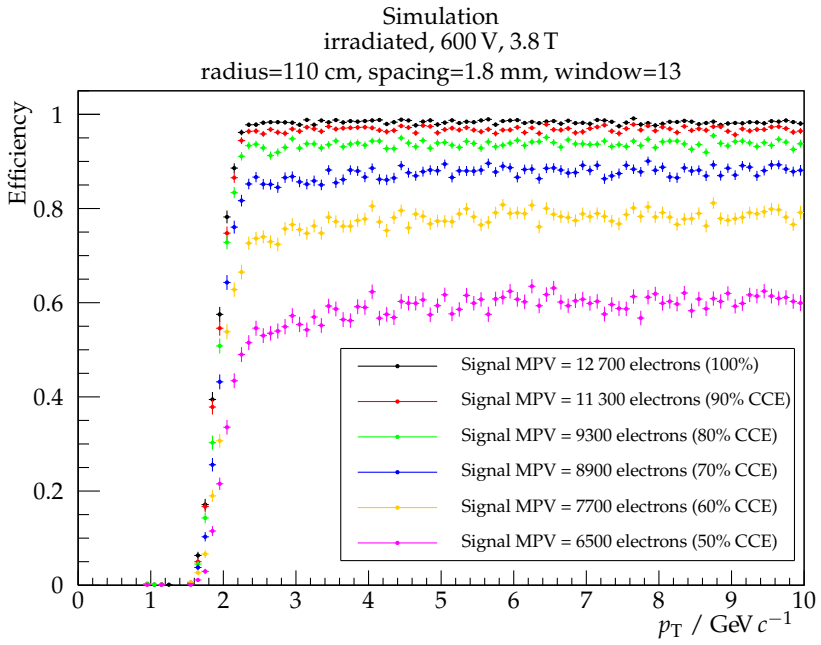

(b) Layer 6

Figure 12.7.: Simulated trigger efficiency as a function of the transverse momentum. The simulation parameters are set to match the measurements in the test beam after irradiation with a fluence of $1.5 \times 10^{15}\,\mathrm{n_{eq}/cm^2}$. The noise is assumed to be gaussian distributed with a width of 1000 electrons, the applied threshold for the binary clustering is 5000 electrons. Additionally, the charge collection efficiency is varied.

13

Summary and outlook

Extensive studies on the signal generation in irradiated silicon strip sensors have been performed with emphasis on the application as tracking detector in the CMS Tracker at the HL-LHC. Most of the work presented in the thesis at hand has been carried out in a large R&D campaign of the CMS Tracker Collaboration to find a suitable silicon base material and sensor layout for the future tracker. Based on the various studies performed in the HPK campaign, the collaboration recently decided to choose p-bulk material as base material for the tracker at HL-LHC [Die13a].

The new tracker has to meet several challenges. The higher track density requires a finer readout granularity with smaller strip pitch and hence more channels have to be read out. To handle the amount of data, a binary readout chip is being developed. Additionally, the tracker is required to provide information to the first trigger stage to handle the higher track rate. The third aspect is the increased radiation level. All three aspects have been studied in the scope of this thesis. The information from all measurements was used to develop a simulation model, in order to predict the properties of charge clusters after a particle incident.

Simulation model

A simulation model of the charge drift in the sensor under influence of a magnetic field has been implemented. By combining parameterizations of the involved processes, the Lorentz deflection of the drifting electrons and holes has been demonstrated to be modeled correctly. To reproduce the statistical properties of the ionization process after a particle incident, the model has been combined with a Geant4 simulation. A collimated radioactive source as used in the ALiBaVa setup as well as particles hitting the sensor at various angles have been implemented. The position and angle of the particle incident and the deposited energy are taken as input parameter for the drift simulation and charge carriers are placed in the sensor accordingly. The model has been validated with measurements on strip sensors using a fast readout system and a radioactive source. The focus is on the comparison using a binary re-interpretation of the data. Additionally, the model has been validated using test beam data. Here, the response to

perpendicular and inclined particle incidence and the cluster properties as a function of the track impact position in the strip unit cell has been compared to the test beam results. From that, slightly modified parameters have been determined to represent the influence of radiation damage.

The outlined simulation model is capable to describe the performed Lorentz angle measurements. Its relatively easy and fast calculations allow the investigation of the statistical ionization process on several thousand events. However, it relies on measurements of macroscopic properties of the sensor, especially the full depletion voltage. Also the electric field distribution in the sensor is a one-dimensional approximation. However, if modeled correctly, the simulation is able to predict properties of the charge clusters after the incident of an ionizing particle.

Using a proper microscopic defect model, T-CAD finite-element simulations of the sensors are able to predict the macroscopic properties of the silicon sensor like full depletion voltage and charge collection efficiency even after irradiation. Due to the longer calculation time, T-CAD simulations are not suitable for the investigation of a large amount of different conditions or statistical analyses. They nevertheless may serve as an input for the parametrization of macroscopic parameters which can be used by the simple one-dimensional model. The influence of process specific parameters like the doping concentration of the strip implants or a necessary p-stop or p-spray isolation on the sensor performance can only be studied using the full T-CAD simulation.

Both approaches have their specific advantages. If tuned correctly, the one-dimensional model gives the correct results and is for that sufficient to describe the response of irradiated silicon sensors after an incident particle.

Sensor geometry and binary readout

The investigation of the detector response of 200 µm thin sensors to the incidence of charged particles has been studied in a test beam campaign at the DESY accelerator using a 4.6 GeV electron beam. Irradiated multi-geometry strip sensors with various strip configurations have been read out. For that, the ARC read out system has been improved and optimized for the time structure of the beam at DESY.

The obtained results demonstrate that 200 µm thin p-bulk sensors can be operated properly after a proton irradiation to an equivalent fluence of $1.5 \times 10^{15}\,\mathrm{n_{eq}/cm^2}$ with an analogue readout. This fluence corresponds to a radial distance of 20 cm from the interaction point after $3000\,\mathrm{fb}^{-1}$ at the HL-LHC. As long as the bias voltage is large enough to deplete the sensor, here above 450 V after irradiation, the cluster signal, spatial resolution and efficiency of the sensor have been found to be mostly independent of the applied bias voltage. The obtained spatial resolution is in most cases better than the binary resolution of $\frac{p}{\sqrt{12}}$ and the efficiency is in the order of 90 % or higher. To be able to apply bias voltages of up to 900 V, a proper cooling of the sensor is essential to avoid thermal runaway.

Due to the good spatial resolution of the used reference telescope, the cluster properties have been investigated as a function of the position of the track hit in the strip unit cell. As expected, the cluster size is largest for tracks hitting directly between two neighboring strips, as the charge is distributed to both strips equally. The seed signal is reduced accordingly. However, also a reduction of the total cluster charge has been found for tracks passing the sensor between

two strips, compared to tracks directly hitting a strip. This charge loss is most pronounced on the 240 µm pitch regions, but is also present at smaller strip pitch. The loss of charge of about 20 % for particles hitting between two strips combined with the inevitable charge sharing leads to an additional reduction of the seed signal, which in turn leads to a detector inefficiency on some large strip pitch geometries. For the current sensor baseline with a strip pitch of 90 µm on 200 µm thick sensors, no inefficiency is expected from the measurements after an irradiation of $1.5 \times 10^{15}\,\mathrm{n_{eq}/cm^2}$, as the 80 µm pitch region has not been found to be inefficient between the strips. The charge loss is independent of the type of the silicon base material (float zone or magnetic czochralski) and the applied strip isolation technique (p-stop or p-spray). Small strip widths however enhance the charge loss effect.

For particles hitting the sensor at an angle relative to the surface, the total cluster signal is increasing with the incidence angle for all strip geometries. The total signal depends mostly on the path length of the particle in the sensor. Charge created by inclined tracks is shared among several strips more easily, compared to perpendicular incident. In general, an increase of the charge sharing and the cluster size with the track incidence angle is expected. Despite the quite complicated dependence of the seed signal and cluster size from the strip geometry, the spatial resolution and efficiency of the investigated sensors is in all regions independent of the incidence angle of the particle track in the range of 0° to 30°.

To estimate the performance of the sensors with the new binary readout chip, the obtained data has been reanalyzed using a binary clustering algorithm. By applying a variable threshold in the range of 1000 to 15 000 electrons, the cluster size, the efficiency, the occupancy and the spatial resolution have been studied. A threshold in the order of 5000 electrons resulted in a high detector efficiency of almost 90 % after irradiation to $1.5 \times 10^{15}\,\mathrm{n_{eq}/cm^2}$ and low noise occupancy. This is also valid for particle tracks that hit the sensor at an angle of 30° relative to the sensor plane.

Trigger module

The obtained simulation model has been used to study the new trigger module concept. Simulated muons and antimuons of different momentum in the range of 1 to 10 GeV c^{-1} hit the sensor stack in a magnetic field. The distance of the sensors from the particle origin has been chosen following the baseline layout for the new tracker. The spatial correlation of the hits in the two sensors was used to estimate the trigger performance of the module concept. The dependence of the trigger efficiency on the module layout and correlation search window has been studied. Optimized parameters for the search window resulting in a momentum cut of approximately 1 to 2 GeV c^{-1} have been determined. Depending on the radial position in the tracker, the search window has been chosen to be the central strip ± 2 strips in the inner layers up to the central strip ± 6 strips in the outer most layer.

If radiation damage as parametrized from the test beam studies is taken into account, the trigger efficiency of the module stack has been investigated as a function of the radial position of the individual sensor in the tracker. The expected equivalent particle fluence and from that the expected damage has been taken into account. This results in a reduction of the trigger efficiency for the innermost tracker layer from 99 % without irradiation to 90 % in the irradiated case. A further reduction of the signal will result in a further reduction of the efficiency.

This emphasizes the need for a large signal obtained from the sensor. At a bias voltage of 600 V, Hoffmann [Hof13] demonstrated that 320 µm thick sensors give no benefit after irradiation in terms of collected charge compared to 200 µm thick sensors. Because of that, an increase of the bias voltage above the present limit of 600 V may be necessary for the innermost layers of the new tracker to achieve a trigger efficiency as high as possible. At 900 V, an additional benefit in signal and efficiency can be achieved by 320 µm thick sensors, if necessary.

Radiation damage

Electrical characterization and charge collection

The results from the electrical characterization of the irradiated sensor prior to the assembly to modules is compatible with the expectations from literature. The increase of the normalized leakage current with fluence is linear, as expected from the Hamburg model given by Moll [Mol99]. The leakage current in some sensors is 10 to 50 % higher than the expectation, which is however based on measurements on diodes rather than strip sensors. The evolution of the full depletion voltage with irradiation and annealing follows qualitatively the prediction by the Hamburg model. Charge collection efficiency measurements using an infrared laser on 320 µm thick sensors showed a higher collected charge of p-bulk sensors with electron readout compared to n-bulk sensors with hole readout. In n-bulk sensors, no signal after irradiation higher than $2.1 \times 10^{15}\,\mathrm{n_{eq}/cm^2}$ could be measured, whereas in p-bulk sensors, the charge collection efficiency is still about 20 % after an irradiation to $5.8 \times 10^{15}\,\mathrm{n_{eq}/cm^2}$. This difference can be explained by the higher mobility and reduced trapping of electrons. In addition, the n-bulk sensors are degraded by an increased noise and a non-Gaussian contribution to the noise, which may fake particle hits. The use of this n-bulk sensors as tracking detectors is strongly disfavored.

Lorentz angle

The silicon sensors are affected by the 3.8 T strong magnetic field present in the CMS detector. Charges created by ionizing particles in the sensor are deflected by the Lorentz force during their drift towards the readout strips and the hit coordinate is shifted away from the real incidence point. This deflection has been measured on over 40 irradiated sensors in a superconducting magnet at KIT. The newly built setup allowed the investigation of up to six sensors in parallel. The hall mobility of holes has found to be $(194 \pm 35)\,\mathrm{cm\,V^{-1}\,s^{-1}}$ in 300 µm thick non-irradiated sensors at a bias voltage of 300 V and scaled to 0 °C. The used sensor type is similar to the sensors used in the inner layers of the current tracker. A direct measurement on the sensors of the current tracker using the cluster size methods with particle tracks resulted in a hall mobility value of $(208 \pm 6)\,\mathrm{cm\,V^{-1}\,s^{-1}}$, which is in good agreement with each other. The hall mobility of electrons is with $(760 \pm 50)\,\mathrm{cm\,V^{-1}\,s^{-1}}$ about a factor four larger than the hall mobility of holes.

Looking at irradiated sensors, the evolution of the Lorentz shift with the fluence is the most important parameter. The shift of electrons showed a falling trend with irradiation, in qualitative agreement with the predictions of the simulation model. During annealing, a correlation of the Lorentz shift to the annealing behavior of the full depletion voltage of the

sensor has been observed. Additionally, the temperature coefficient of the Lorentz shift of electrons changes its sign after an irradiation fluence of about $5 \times 10^{14}\,\mathrm{n_{eq}/cm^2}$.

For holes, the shift stays relatively constant with the irradiation fluence or shows a slightly rising trend, as long as the sensors can be fully depleted. After that point, the shift drops to zero. This is contradictory to the measurements by de Boer et al. [Boe10] on sensors produced by a different vendor, where an increased shift has been observed even after large irradiation fluence. However, the here investigated n-bulk sensors are heavily affected by an increased noise after irradiation and could not be operated after a fluence higher than $2.1 \times 10^{15}\,\mathrm{n_{eq}/cm^2}$. The negative shift of electrons after irradiation as observed by de Boer et al. [Boe10] has not been confirmed.

The influence of the magnetic field on the residual distribution and on the spatial resolution of the sensor has been demonstrated using the developed simulation model. For perpendicular particle incident, the reconstructed particle hit position is shifted due to the Lorentz deflection and the resulting residual distribution is no longer symmetrically centered around zero. For that, the Lorentz deflection has to be taken into account during event reconstruction in the CMS Tracker.

Outlook

Although simulations indicate the functionality of the new trigger module concept after irradiation corresponding to $3000\,\mathrm{fb^{-1}}$ at the HL-LHC, detailed studies on prototype modules will be inevitable. On the one hand to prove that the module concept still works after high irradiation, on the other hand to evaluate the performance of the new readout chip. Recently, a test beam run using first prototype modules with readout chips capable to correlate the hits in both sensors showed promising results [Die13b]. The response of the trigger during an angular scan was at least qualitatively comparable to the studies presented here. Quantitative analysis of the data is still to come.

Parts of the simulation model could be adopted to the main simulation of the future CMS Tracker. Especially, the correct description of the Lorentz shift and charge collection properties with irradiation are imperative for the optimization of the new layout and to maintain the excellent performance of the CMS Tracker in the future.

A

Technical drawings

Lorentz angle PCB

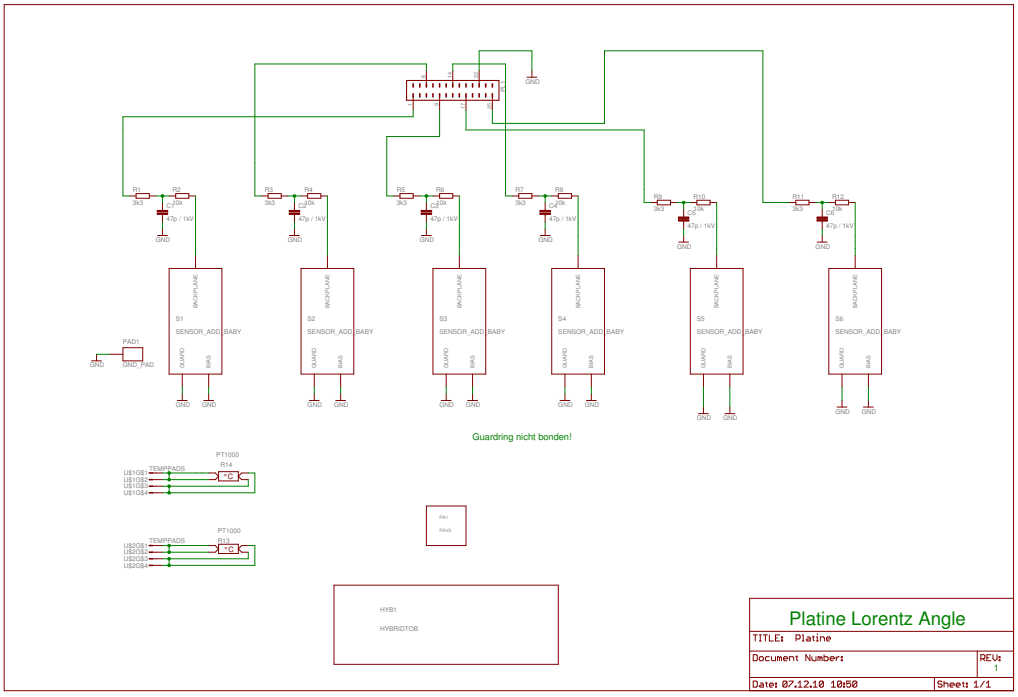

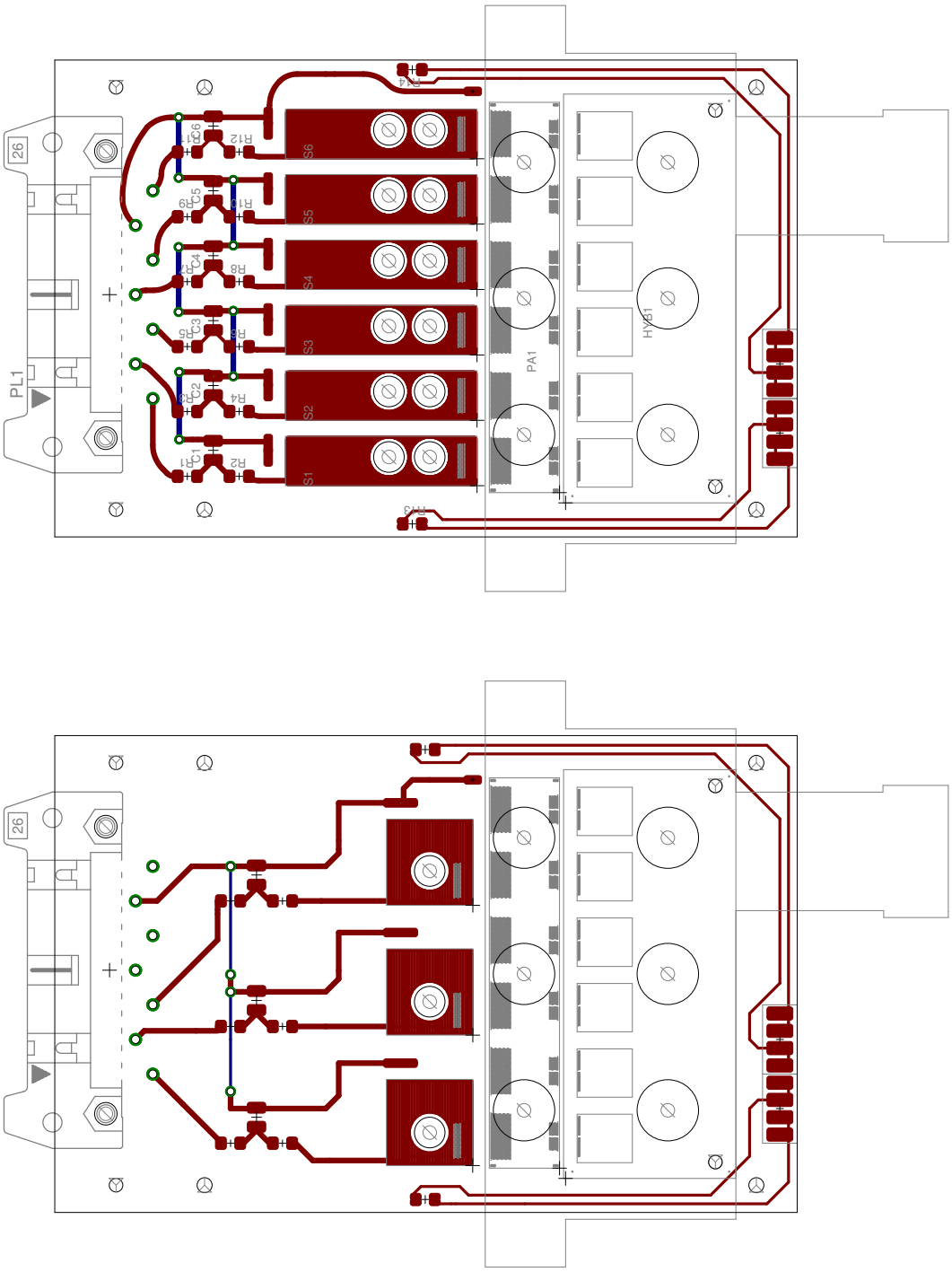

Lorentz angle setup

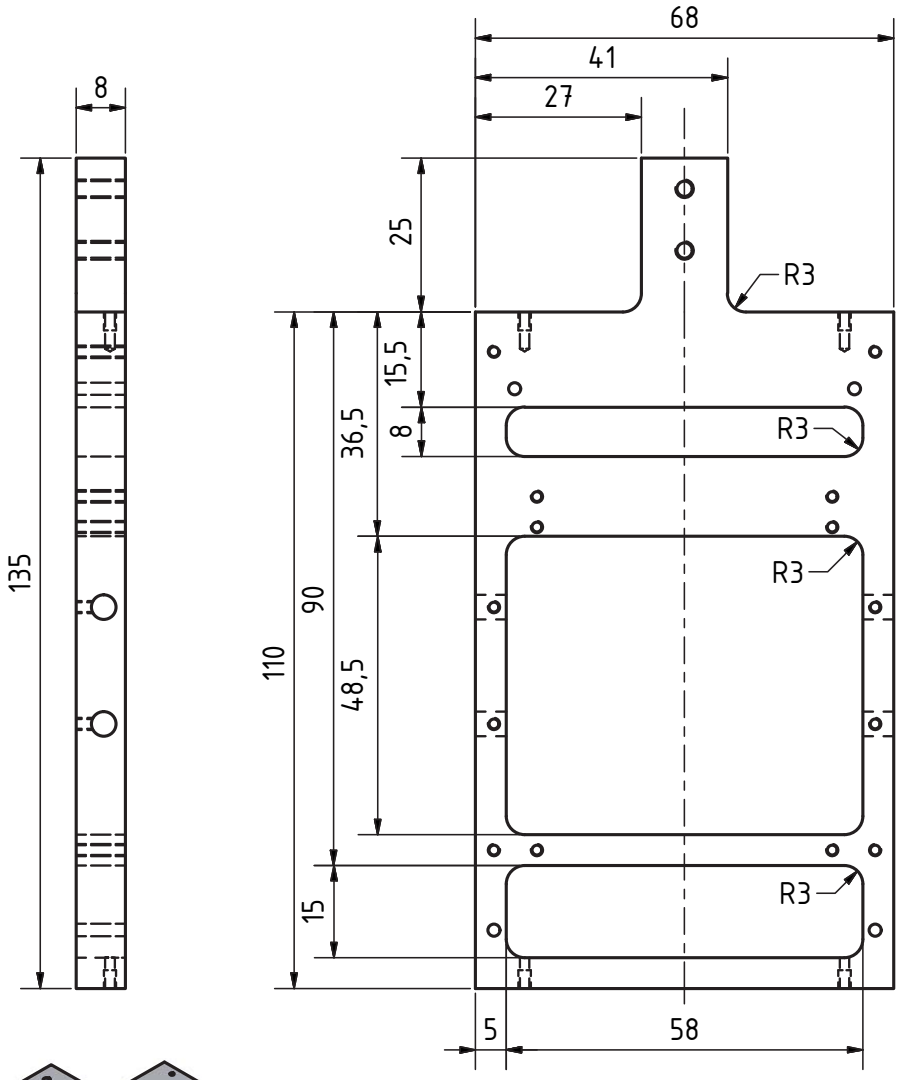

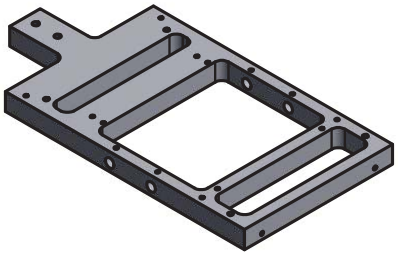

Blatt 1 von 3

					Material: Aluminium, geschliffen	
				Datum	Name	
				Gezeichnet 19.08.2010	Nürnberg	Stückzahl: 1
				Kontrolliert		
				Norm		
					Halteplatte	1
						A4
Status	Änderungen	Datum	Name			

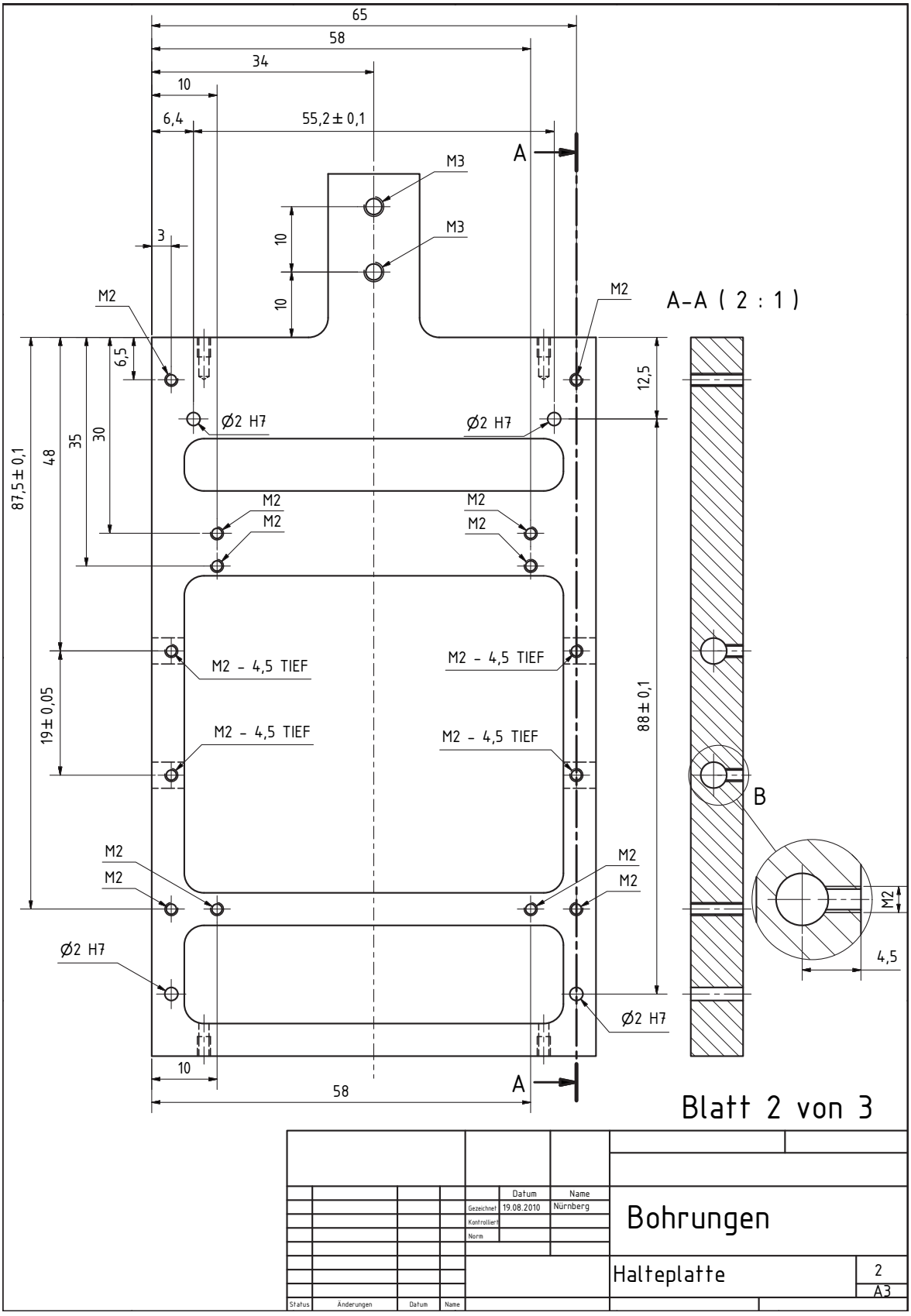
65
58
34
10
6,4
55,2 ± 0,1
A
M3
M3
3
10
10
M2
M2
A-A (2 : 1)
6,5
12,5
Ø2 H7
Ø2 H7
87,5 ± 0,1
4,8
35
30
M2
M2
M2
M2
M2 - 4,5 TIEF
M2 - 4,5 TIEF
M2 - 4,5 TIEF
M2 - 4,5 TIEF
19 ± 0,05
88 ± 0,1
B
M2
M2
M2
M2
M2
4,5
Ø2 H7
Ø2 H7
10
58
A
Blatt 2 von 3
Datum
Name
Gezeichnet
19.08.2010
Nürnberg
Konfrolliert
Norm
Bohrungen
Halteplatte
2
A3
Status
Änderungen
Datum
Name

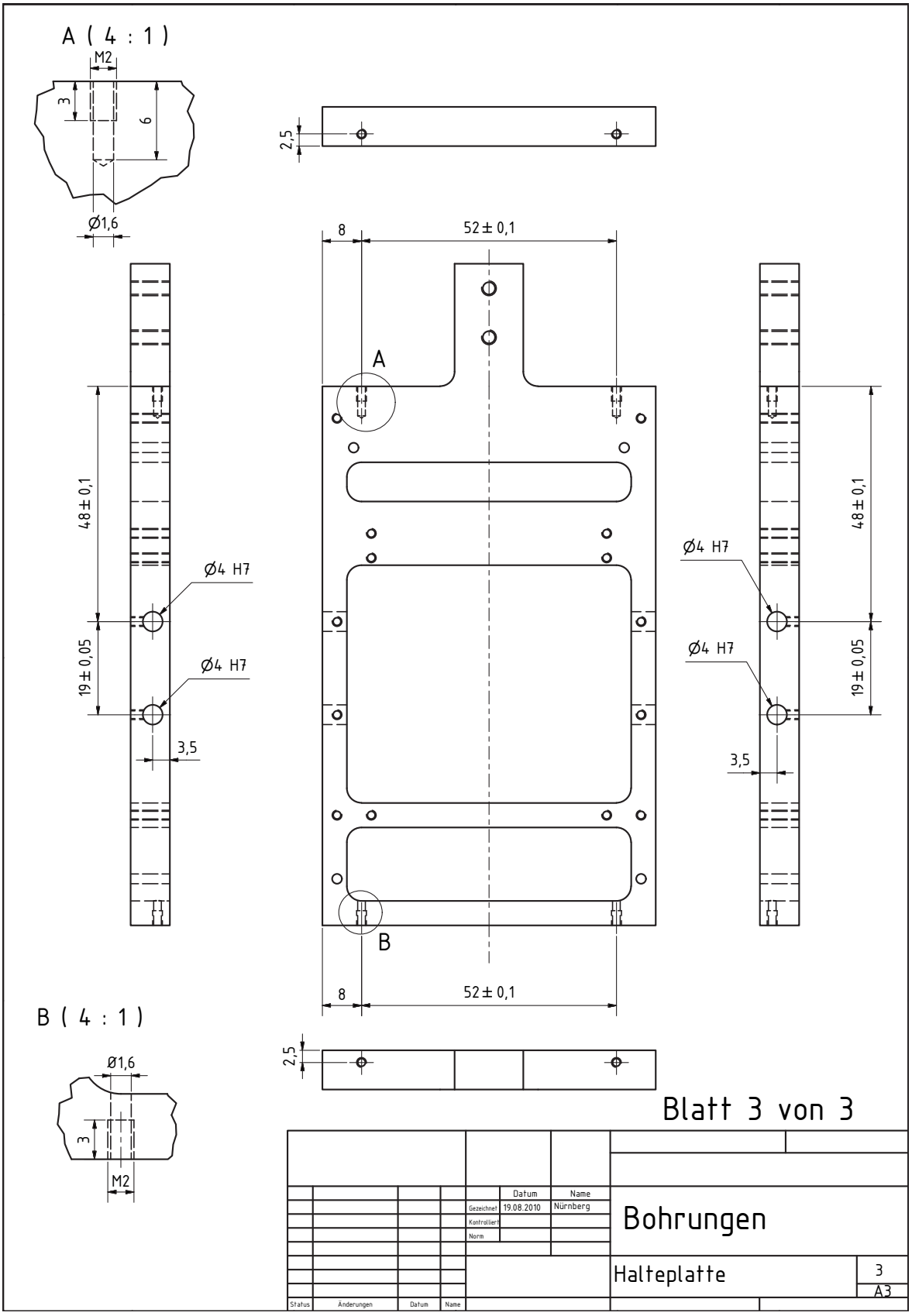
A (4 : 1)
M2
3
6
Ø1,6
2,5
8
52 ± 0,1
A
4,8 ± 0,1
Ø4 H7
19 ± 0,05
Ø4 H7
3,5
B
B (4 : 1)
Ø1,6
3
M2
Blatt 3 von 3
Datum
Name
Gezeichnet
19.08.2010
Nürnberg
Kontrolliert
Norm
Bohrungen
Halteplatte
3
A3
Status
Änderungen
Datum
Name

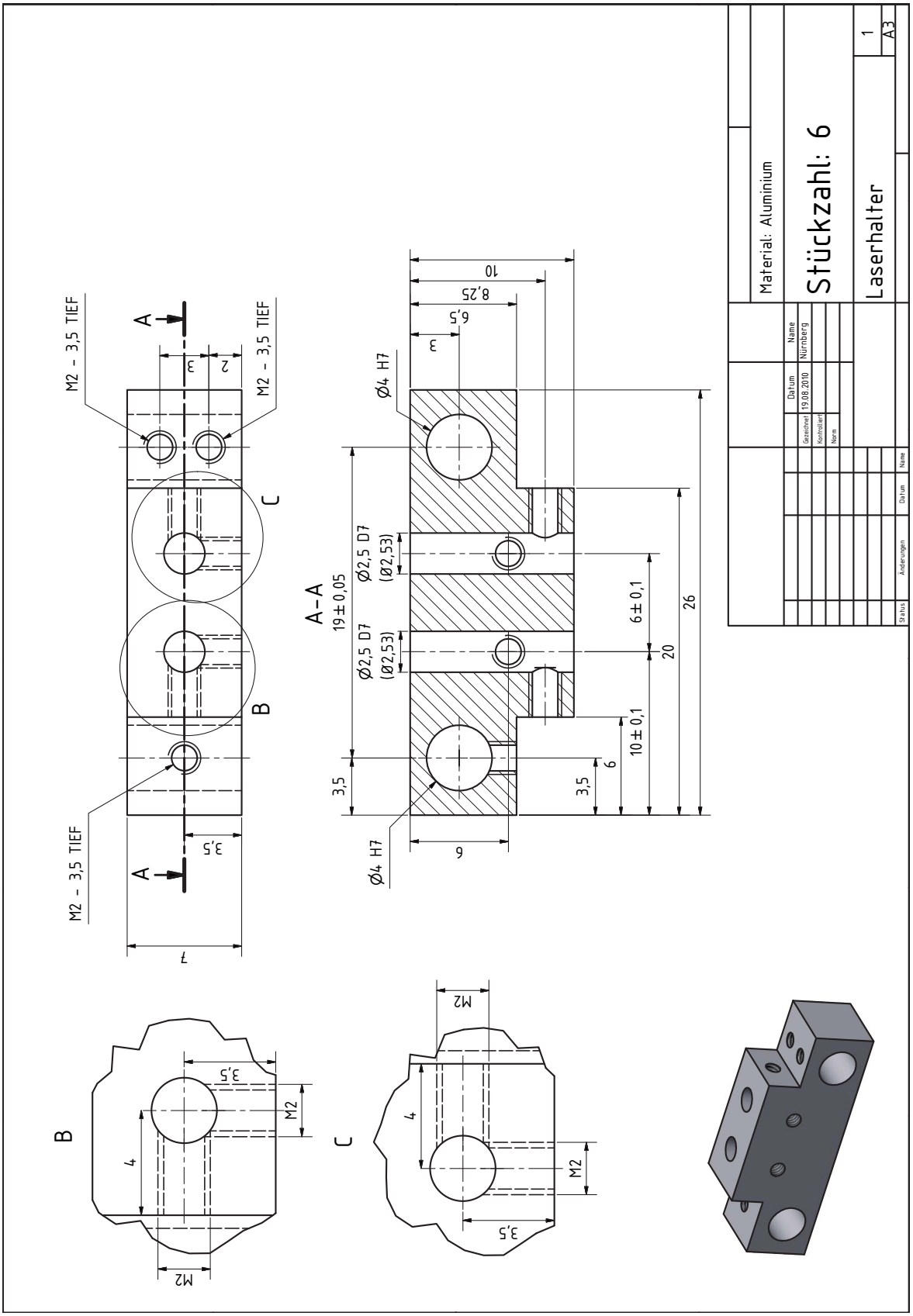
Material: Aluminium
Stückzahl: 6
Laserhalter
1
A3
Name
Datum
Nürnberg
19.08.2010
Gezeichnet
Kontrolliert
Norm
Änderungen
Datum
Name
Status
M2 - 3,5 TIEF
M2 - 3,5 TIEF
M2 - 3,5 TIEF
A
A
B
C
A–A
19 ± 0,05
Ø2,5 D7
(Ø2,53)
Ø2,5 D7
(Ø2,53)
Ø4 H7
Ø4 H7
6 ± 0,1
10 ± 0,1
26
20
3,5
6
3,5
10
8,25
6,5
3
6
3,5
M2
4
M2
4
M2
3,5
3,5

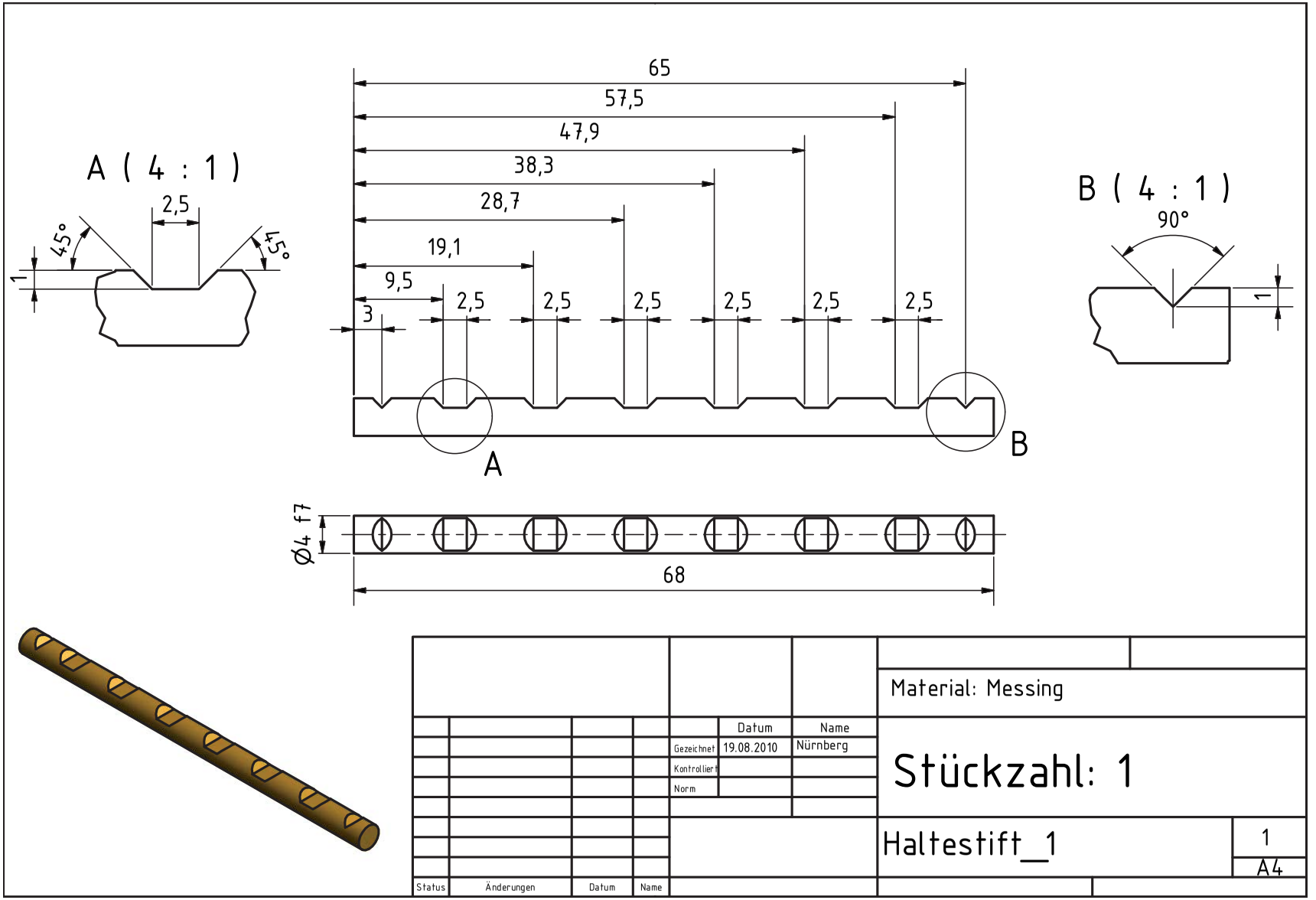
A (4 : 1)
2,5
45°
45°
1
65
57,5
47,9
38,3
28,7
19,1
9,5
3
2,5
2,5
2,5
2,5
2,5
2,5
A
B
B (4 : 1)
90°
1
Ø4 f7
68
Material: Messing
Datum
Name
Gezeichnet
19.08.2010
Nürnberg
Kontrolliert
Norm
Stückzahl: 1
Haltestift_1
1
A4
Status
Änderungen
Datum
Name

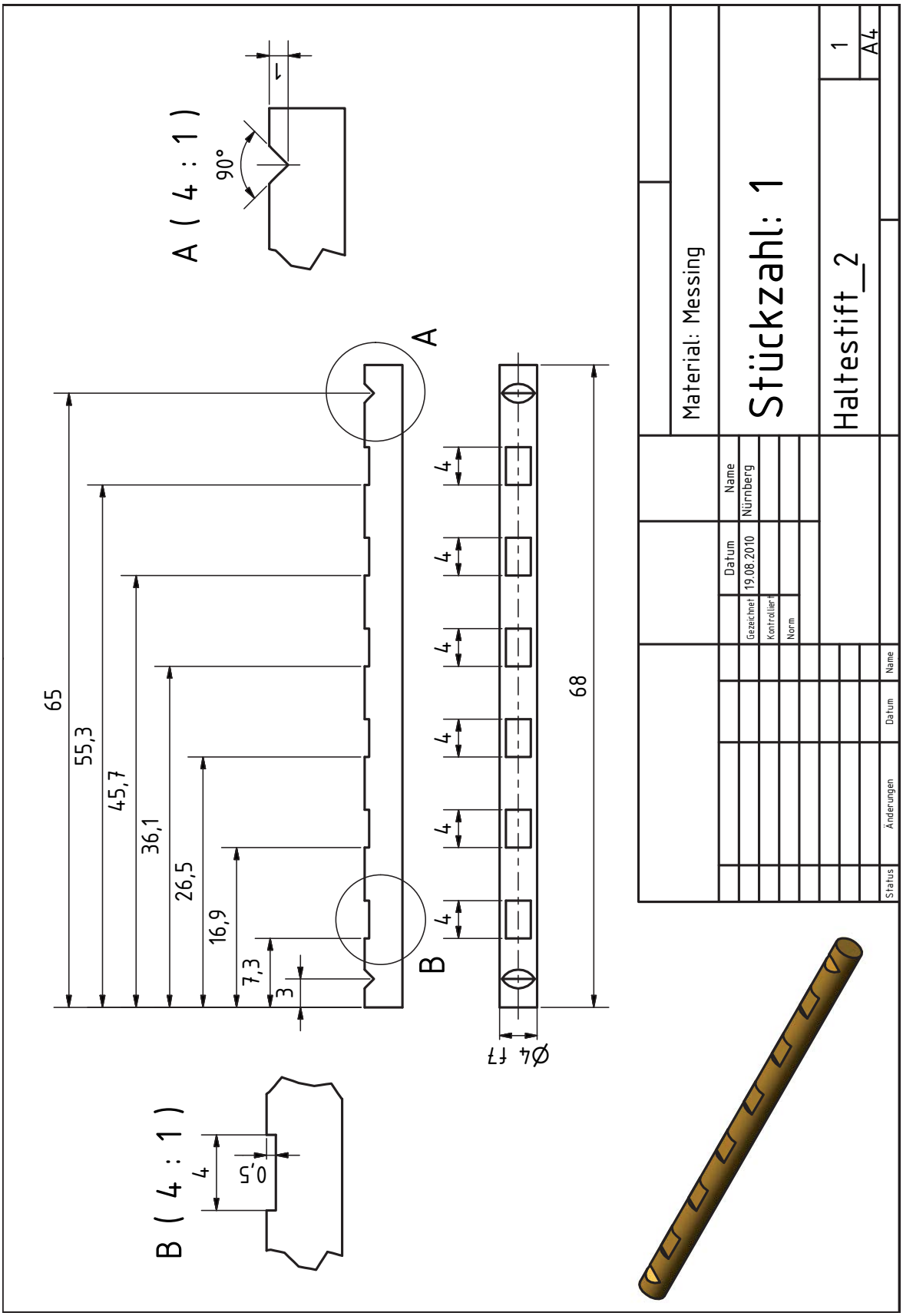
A (4 : 1)
90°
1
A
65
55,3
45,7
36,1
26,5
16,9
7,3
3
B
4
68
Ø4 f7
B (4 : 1)
4
0,5
Material: Messing
Stückzahl: 1
Haltestift_2
A4
1
Name
Datum
Gezeichnet
Nürnberg
19.08.2010
Kontrolliert
Norm
Status
Änderungen
Datum
Name

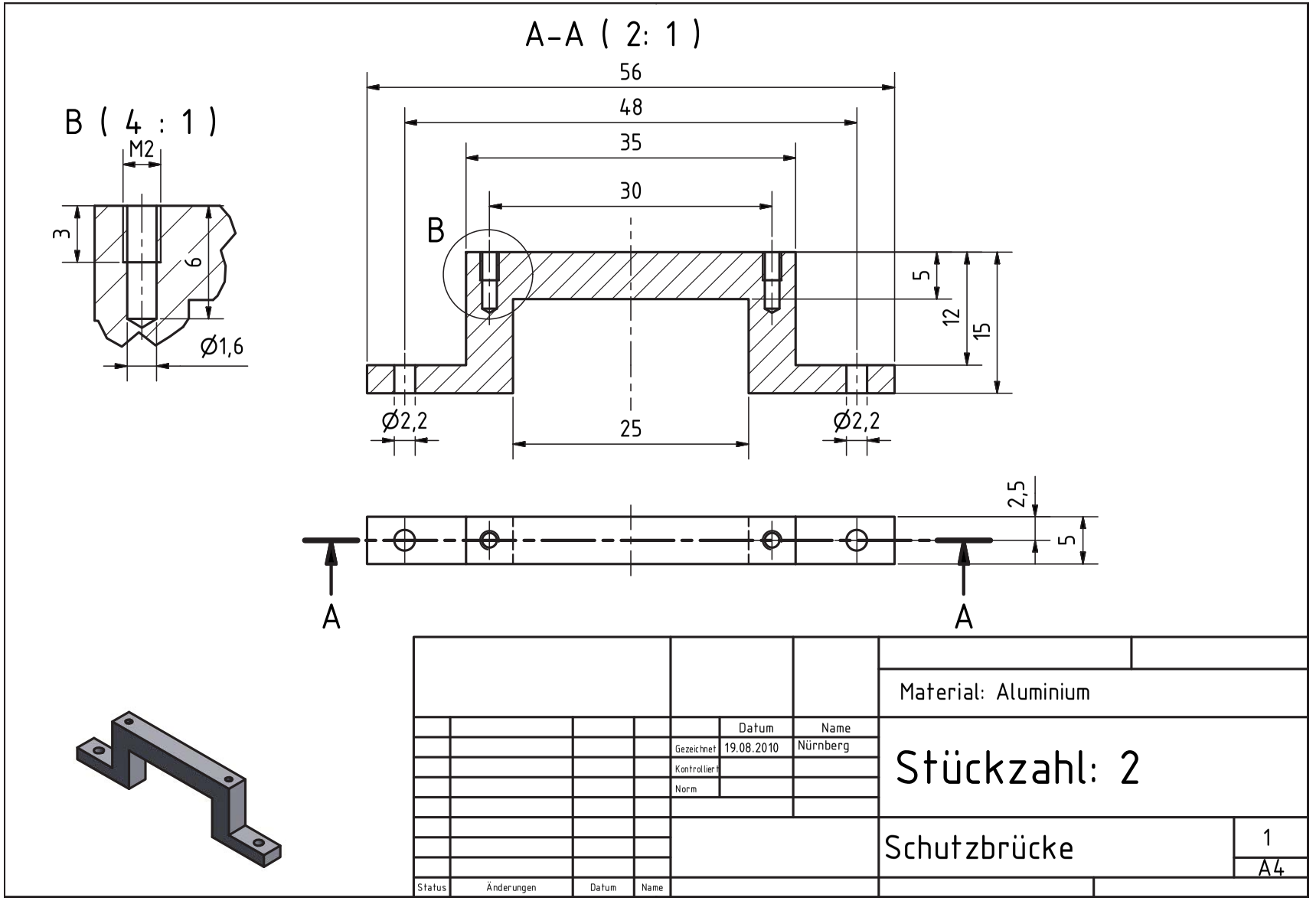
A-A (2: 1)
B (4 : 1)
M2
3
6
Ø1,6
56
48
35
30
B
5
12
15
Ø2,2
25
Ø2,2
2,5
5
A
A
Material: Aluminium
Datum
Name
Gezeichnet
19.08.2010
Nürnberg
Kontrolliert
Norm
Stückzahl: 2
Schutzbrücke
1
A4
Status
Änderungen
Datum
Name

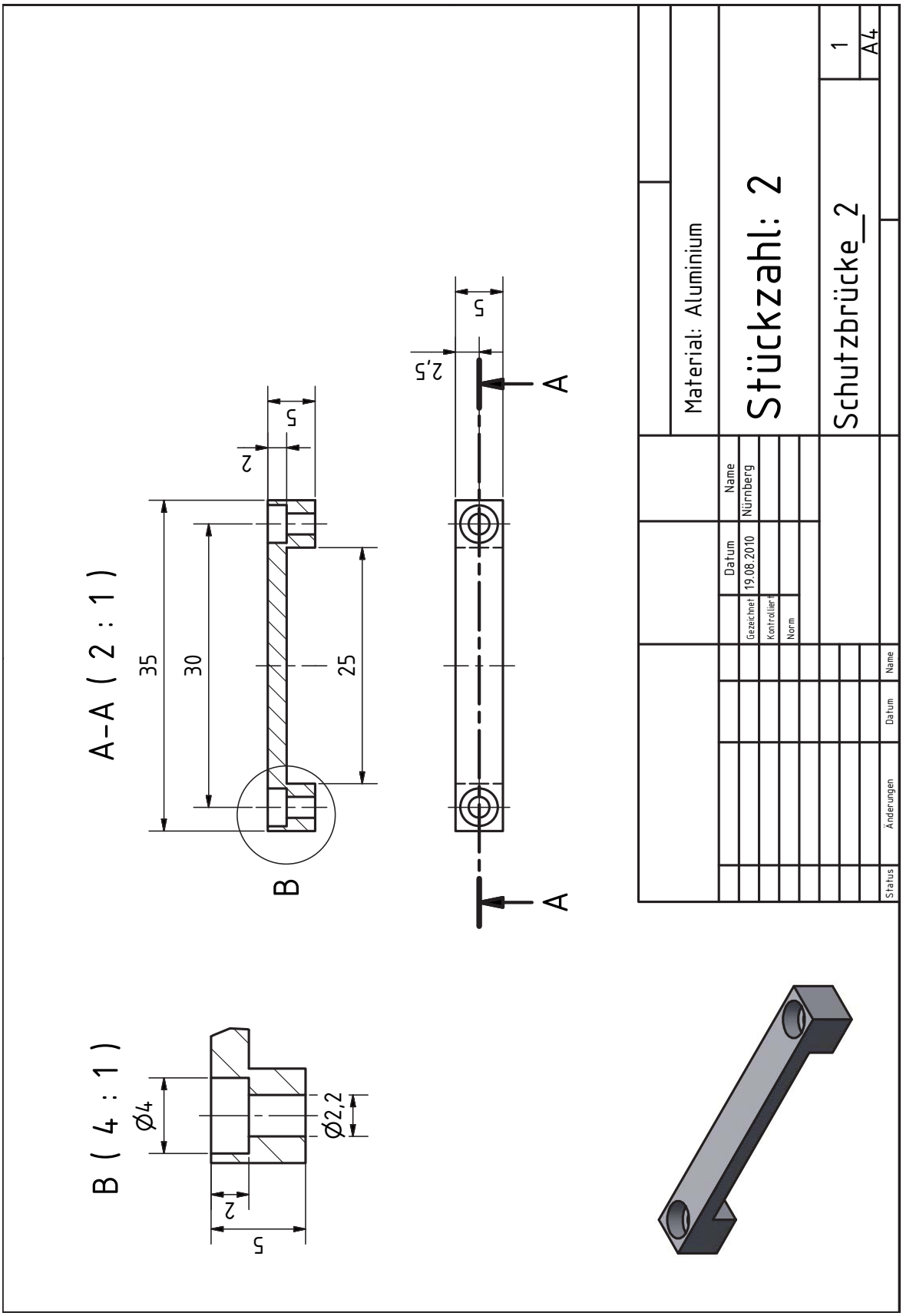
A–A (2 : 1)
35
30
25
5
2
B
A
2,5
5
A
B (4 : 1)
Ø4
Ø2,2
2
5
Material: Aluminium
Stückzahl: 2
Schutzbrücke_2
1
A4
Name
Datum
Gezeichnet
19.08.2010
Nürnberg
Kontrolliert
Norm
Status
Änderungen
Datum
Name

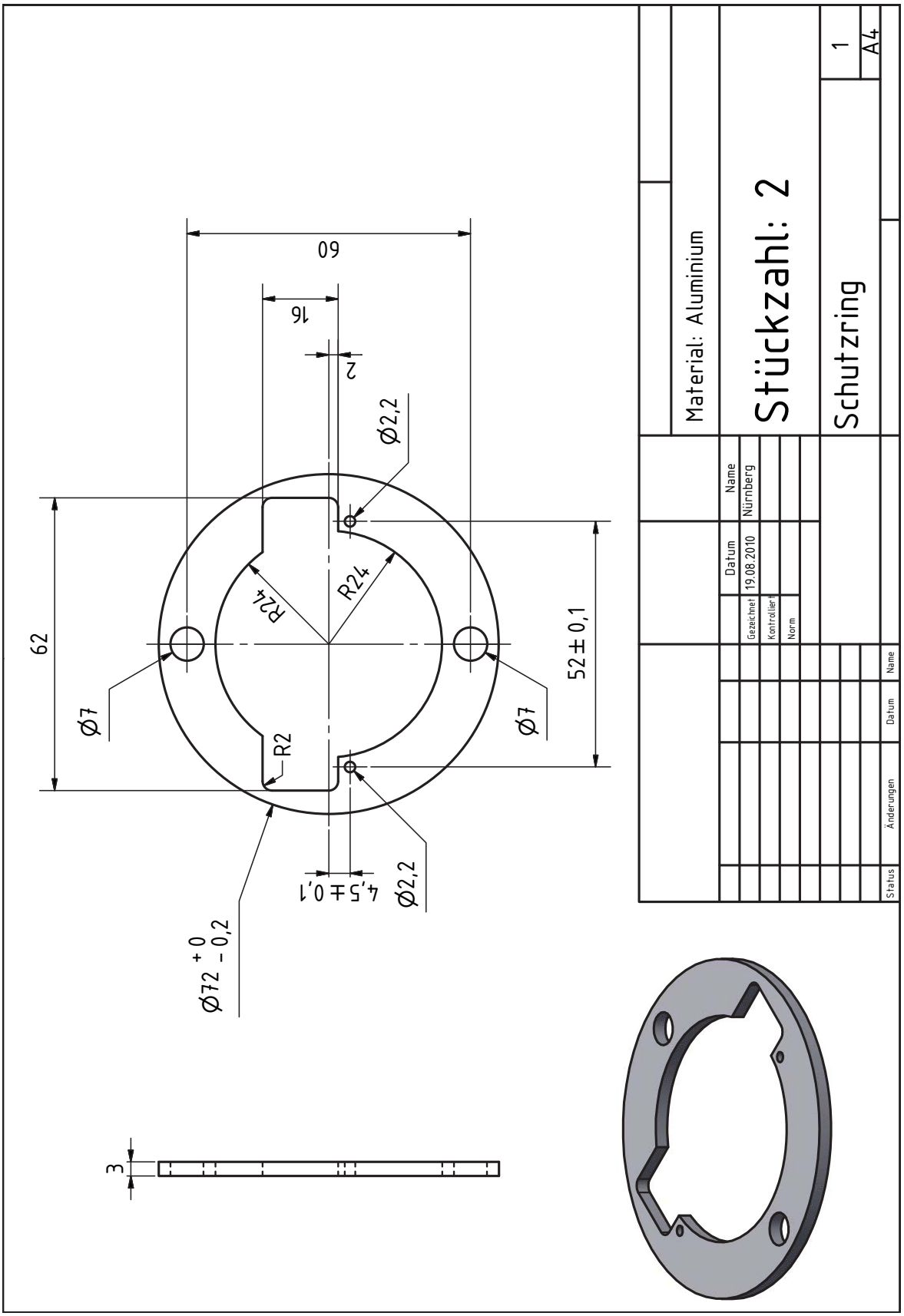
60
16
2
Ø2,2
62
Ø7
R24
R24
R2
52 ± 0,1
Ø7
4,5 ± 0,1
Ø2,2
Ø72 +0 -0,2
3
Material: Aluminium
Stückzahl: 2
Schutzring
1
A4
Name
Datum
Gezeichnet
19.08.2010
Nürnberg
Kontrolliert
Norm
Status
Änderungen
Datum
Name

Laserhalter montieren

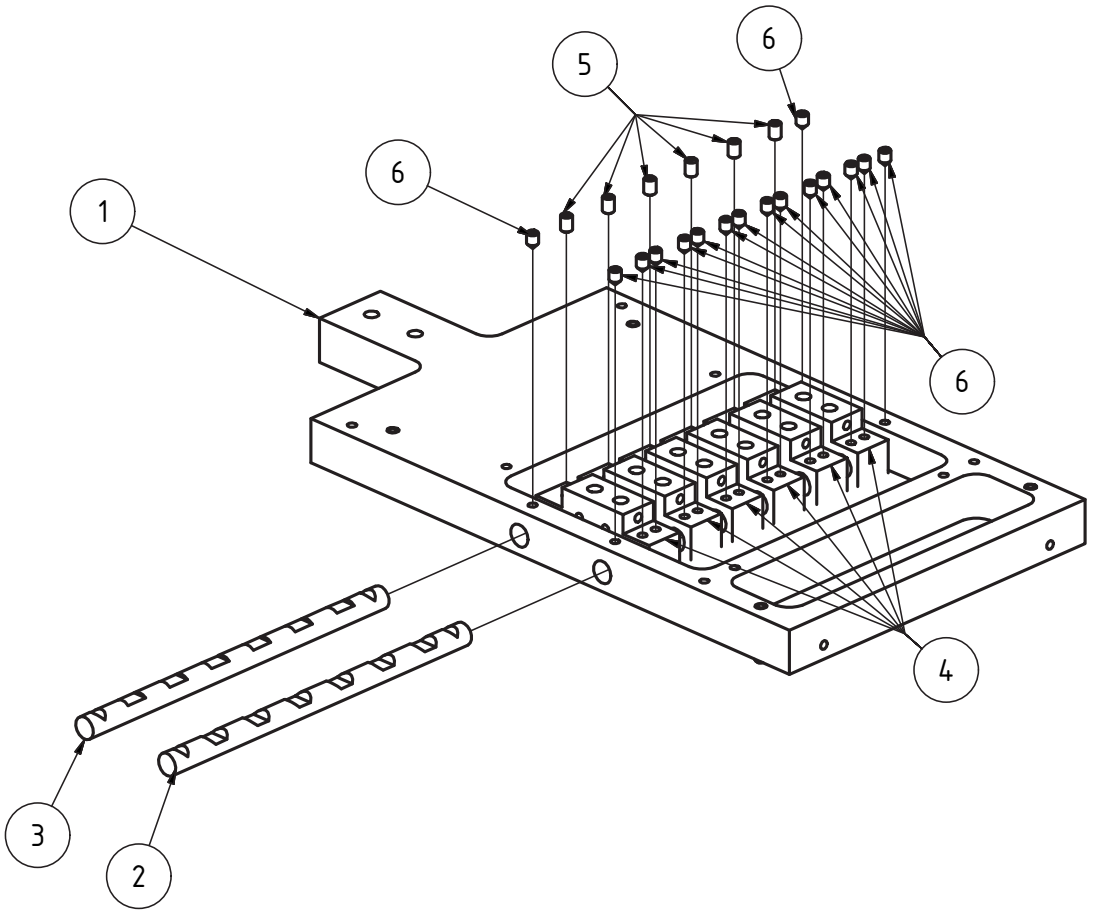

TEILELISTE			
OBJEKT	ANZAHL	BAUTEILNUMMER	BEZEICHNUNG
1	1	Halteplatte	
2	1	Haltestift_1	
3	1	Haltestift_2	
4	6	Laserhalter	
5	6	DIN 913 – M2 x 3	Gewindestift Kegelkuppe A2
6	16	DIN 914 – M2 x 3	Gewindestift Spitze 90° A2

	Datum	Name
Gezeichnet	19.08.2010	Nürnberg
Kontrolliert		
Norm		

Status	Änderungen	Datum	Name

1

A4

Passstifte einpressen

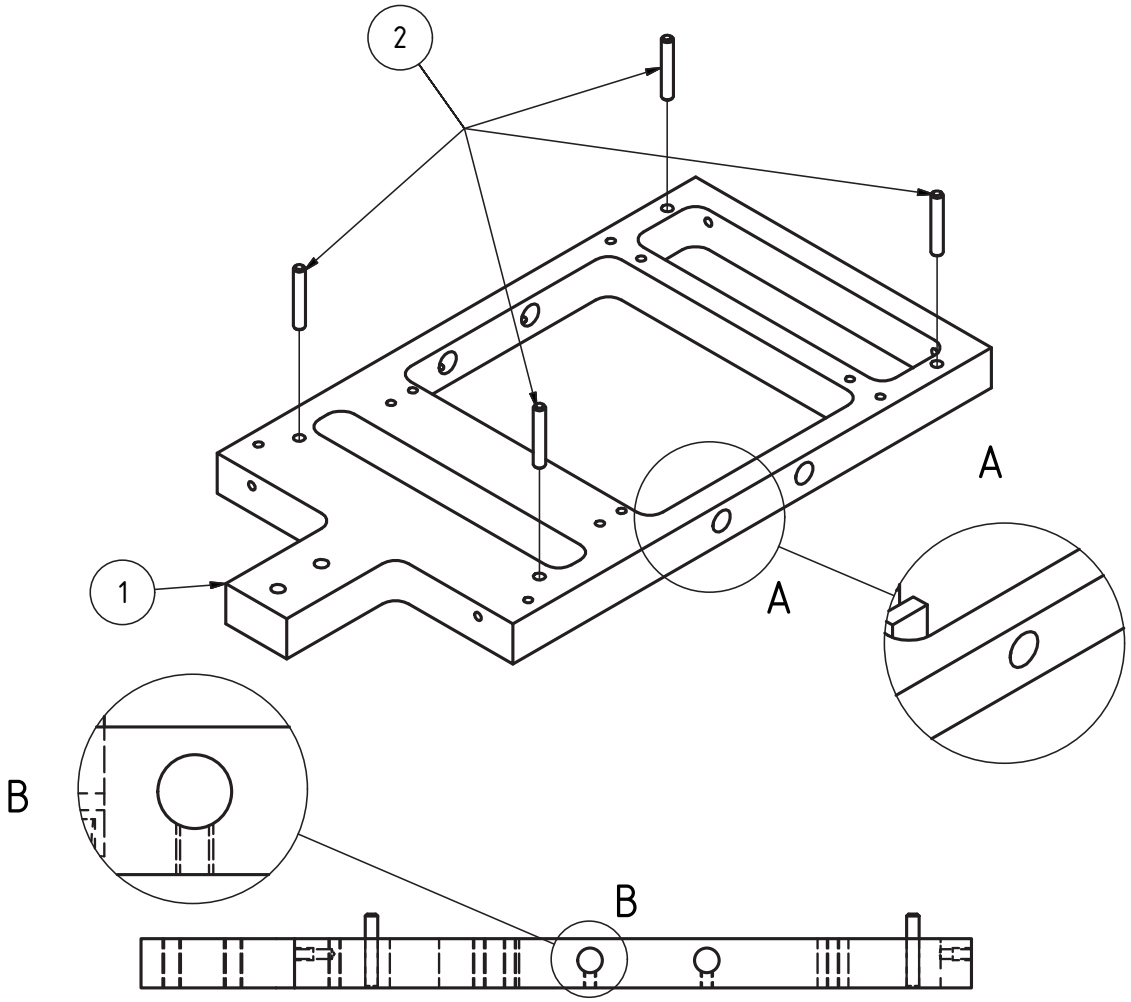

TEILELISTE

OBJEKT	ANZAHL	BAUTEILNUMMER	BEZEICHNUNG	KOMMENTAR
1	1	Halteplatte		
2	4	Passstift 2mm	Ø2 n6 12mm lang Edelstahl	Einpressen

	Datum	Name
Gezeichnet	19.08.2010	Nürnberg
Kontrolliert		
Norm		

1
A4

Status	Änderungen	Datum	Name

Schutzrbücken montieren

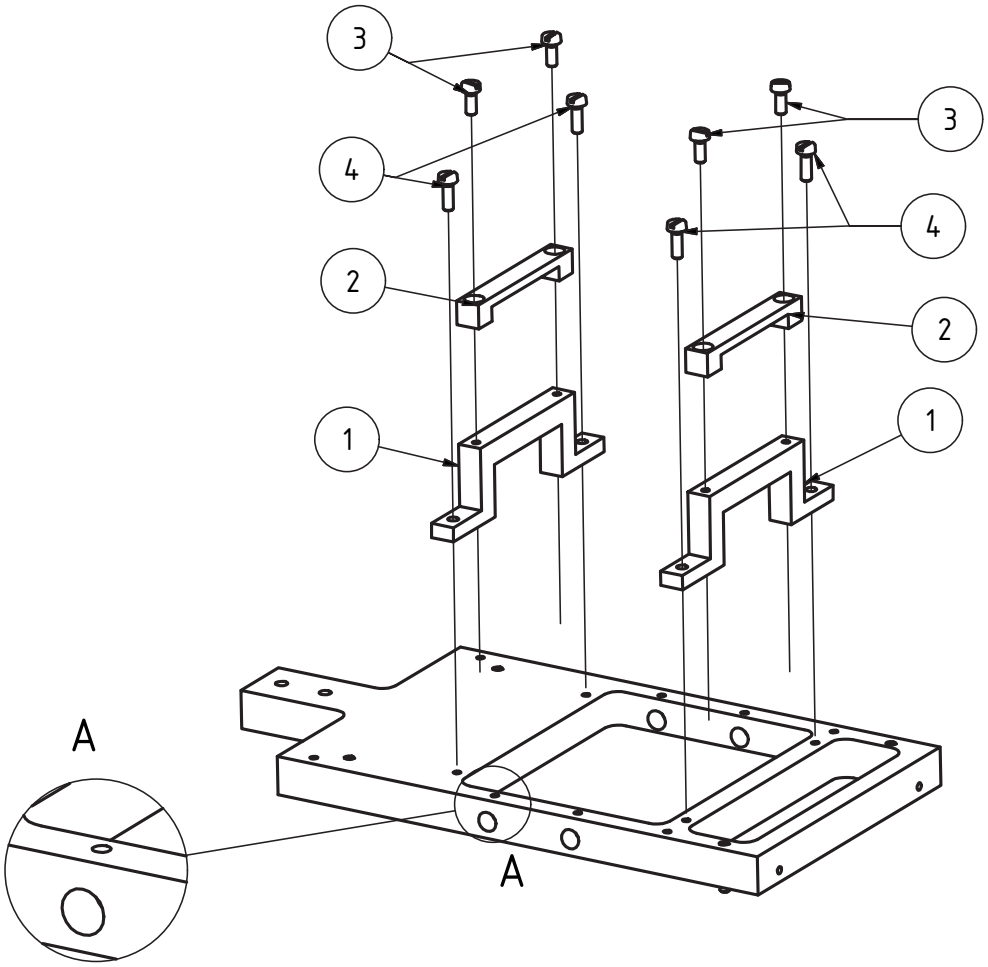

TEILELISTE

OBJEKT	ANZAHL	BAUTEILNUMMER	BEZEICHNUNG
1	2	Schutzbrücke	
2	2	Schutzbrücke_2	
3	4	M2 x 5	Zylinderschraube mit Schlitz A2
4	4	M2 x 6	Zylinderschraube mit Schlitz A2

	Datum	Name
Gezeichnet	19.08.2010	Nürnberg
Kontrolliert		
Norm		

Status	Änderungen	Datum	Name

1

A4

Schutzringe montieren

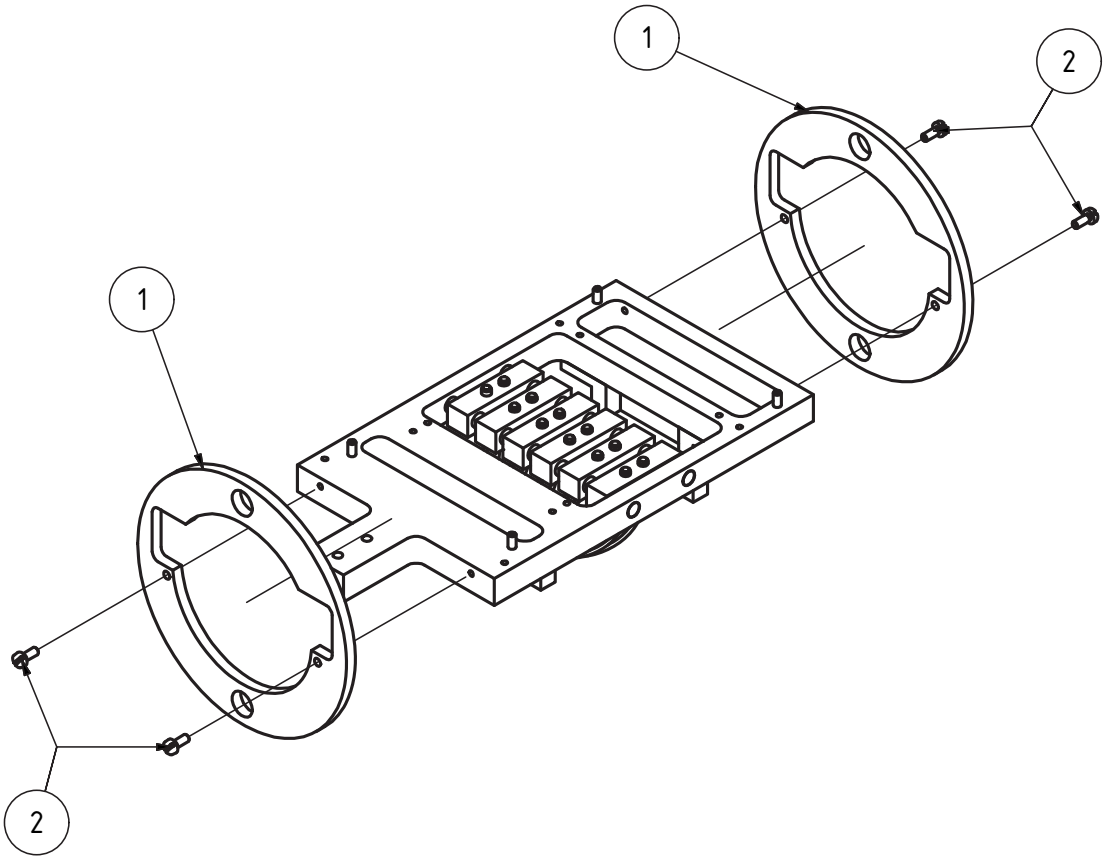

TEILELISTE

OBJEKT	ANZAHL	BAUTEILNUMMER	BEZEICHNUNG
1	2	Schutzring	
2	4	M2 x 5	Zylinderschraube mit Schlitz A2

	Datum	Name
Gezeichnet	19.08.2010	Nürnberg
Kontrolliert		
Norm		

1
A4

Status	Änderungen	Datum	Name

Zur Info

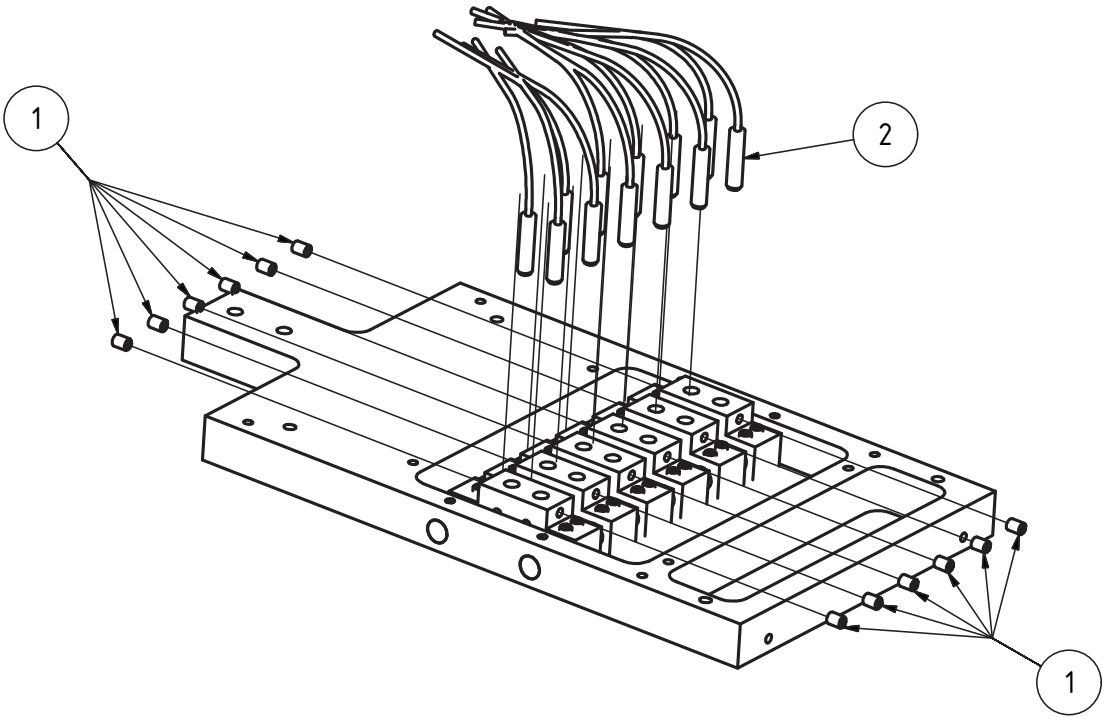

TEILELISTE			
OBJEKT	ANZAHL	BAUTEILNUMMER	BEZEICHNUNG
1	12	DIN 913 - M2 x 3	Gewindestift Kegelkuppe A2
2	12	Ferrule*	

* Ferrule: Siehe beigelegte Zeichnung

					Datum	Name
				Gezeichnet	19.08.2010	Nürnberg
				Kontrolliert		
				Norm		
Status	Änderungen	Datum	Name			

1
A4

Zur Info

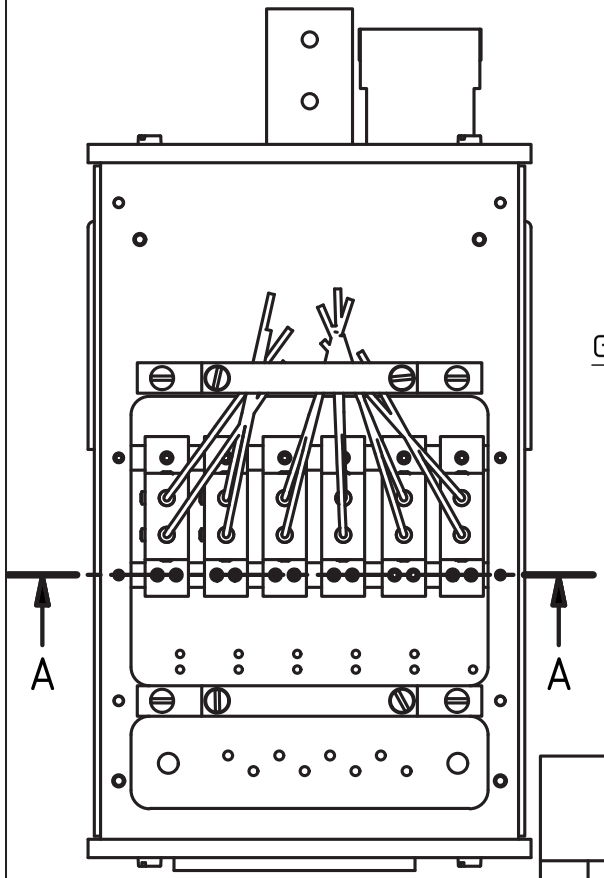

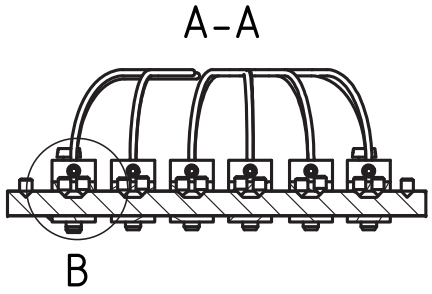

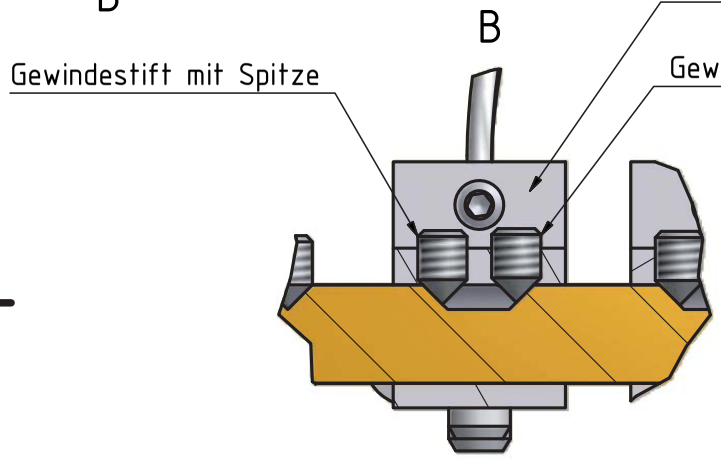

					Datum	Name
				Gezeichnet	19.08.2010	Nürnberg
				Kontrolliert		
				Norm		
Status	Änderungen	Datum	Name			

1
A4

B

Additional test beam plots

Binary clustering

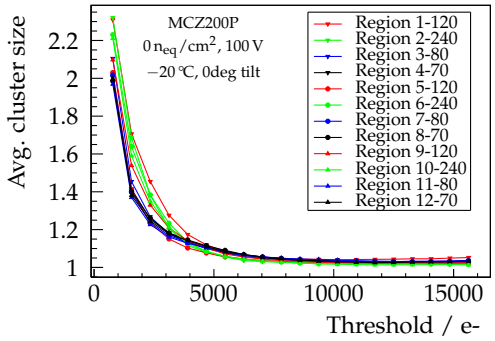

(a) 0 n_{eq}/cm^2, 0° incident

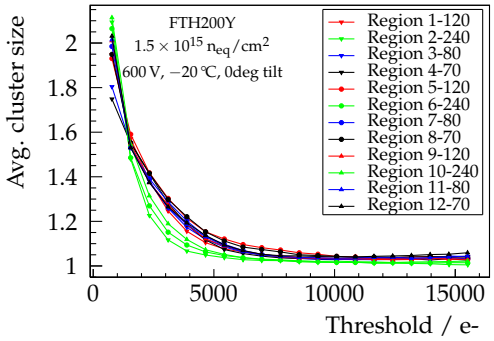

(b) 1.5×10^{15} n_{eq}/cm^2, 0° incident

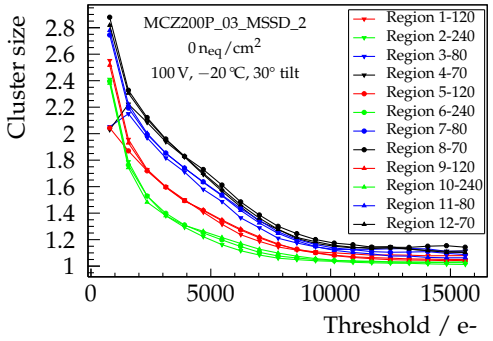

(c) 0 n_{eq}/cm^2, 30° incident

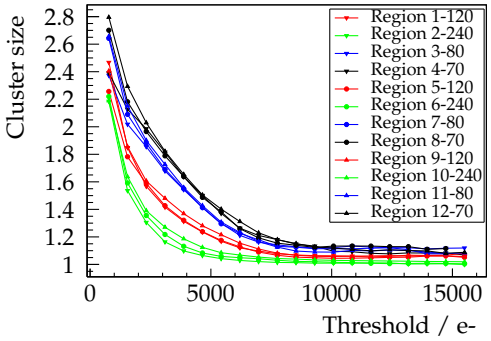

(d) 1.5×10^{15} n_{eq}/cm^2, 30° incident

Figure B.1.: Average cluster size as a function of the applied binary threshold at perpendicular particle incident. A comparison of the non irradiated MCz200P sensor to the irradiated FTH200Y sensor is shown. With rising threshold, neighboring strips are cut away and the average cluster size approaches a value of one strip at high thresholds.

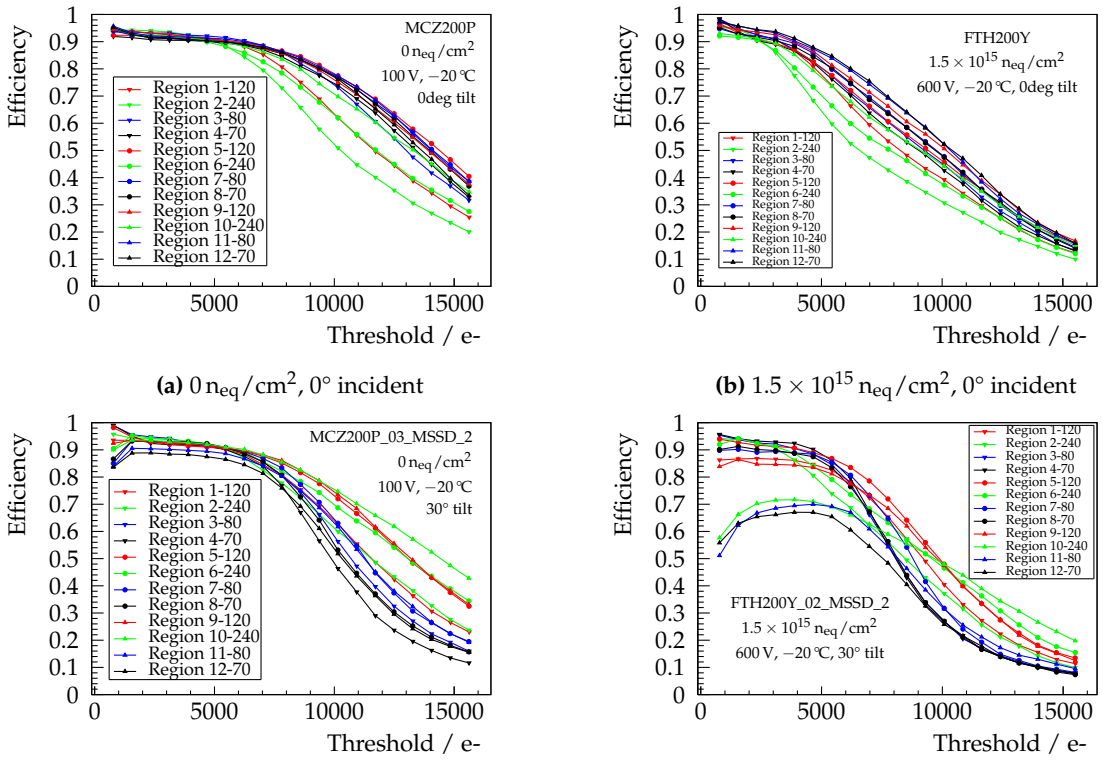

(a) $0\,n_{eq}/cm^2$, 0° incident

(b) $1.5 \times 10^{15}\,n_{eq}/cm^2$, 0° incident

(c) $0\,n_{eq}/cm^2$, 30° incident

(d) $1.5 \times 10^{15}\,n_{eq}/cm^2$, 30° incident

Figure B.2.: Hit identification efficiency as a function of the binary threshold. With rising cut, more and more clusters fall below the threshold and the efficiency for identifying a hit after the traverse of a particle is reduced. At low thresholds, the efficiency is close to 100 %.

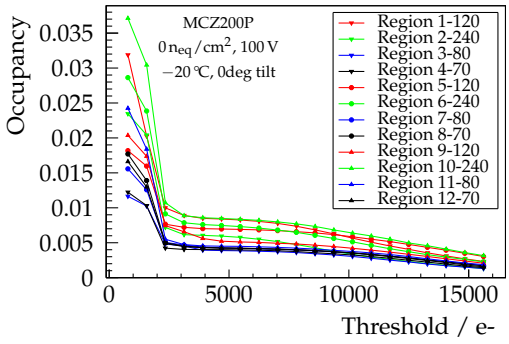

(a) $0\,n_{eq}/cm^2$, 0° incident

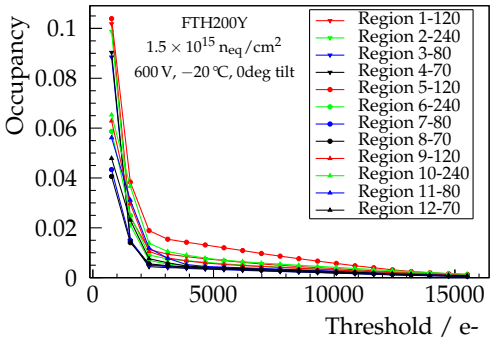

(b) $1.5 \times 10^{15}\,n_{eq}/cm^2$, 0° incident

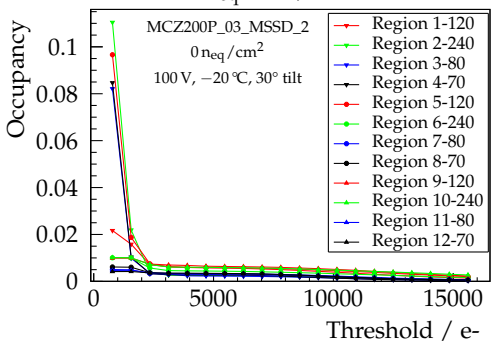

(c) $0\,n_{eq}/cm^2$, 30° incident

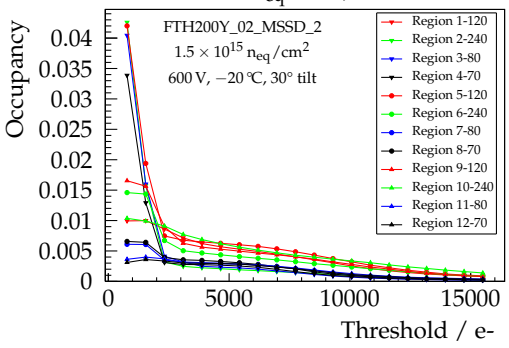

(d) $1.5 \times 10^{15}\,n_{eq}/cm^2$, 30° incident

Figure B.3.: Occupancy of the regions of the MSSD as a function of the binary threshold. Both, particle hits and noise clusters contribute to the occupancy. At low threshold, a strong increase of the occupancy due to noise clusters can be noted.

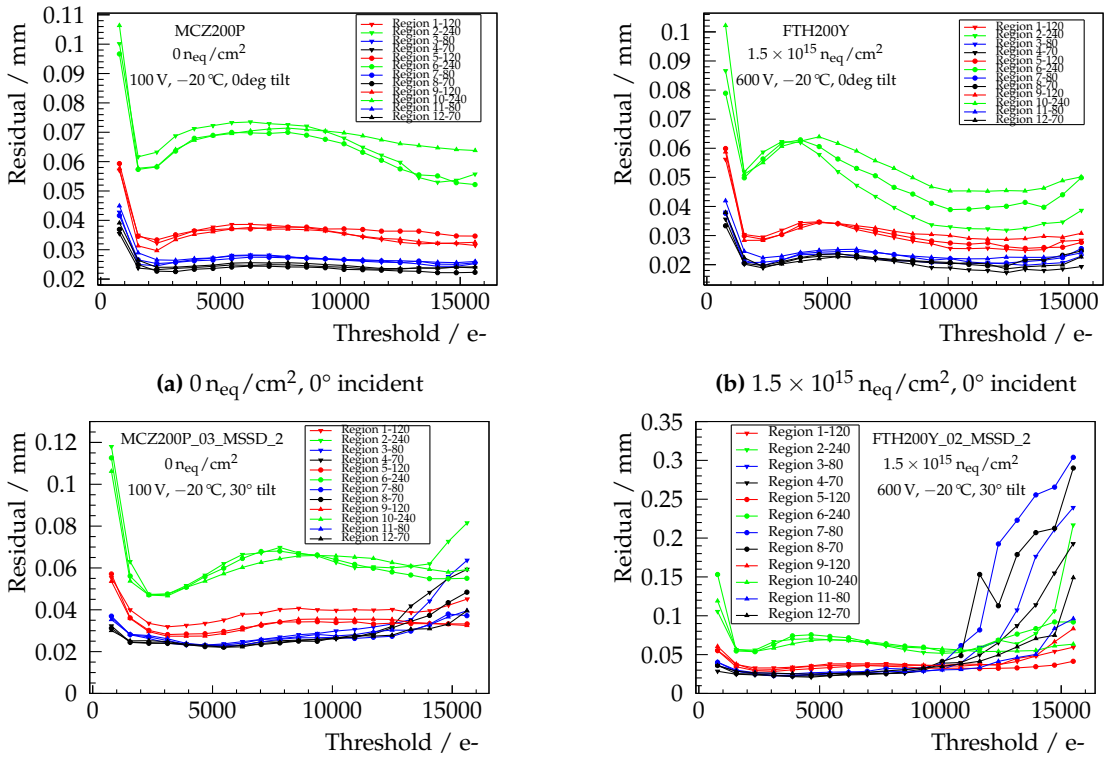

(a) $0\,n_{eq}/cm^2$, 0° incident

(b) $1.5 \times 10^{15}\,n_{eq}/cm^2$, 0° incident

(c) $0\,n_{eq}/cm^2$, 30° incident

(d) $1.5 \times 10^{15}\,n_{eq}/cm^2$, 30° incident

Figure B.4.: Width of the residual distribution as a function of the binary threshold.

Dependence of charge loss on seed cut

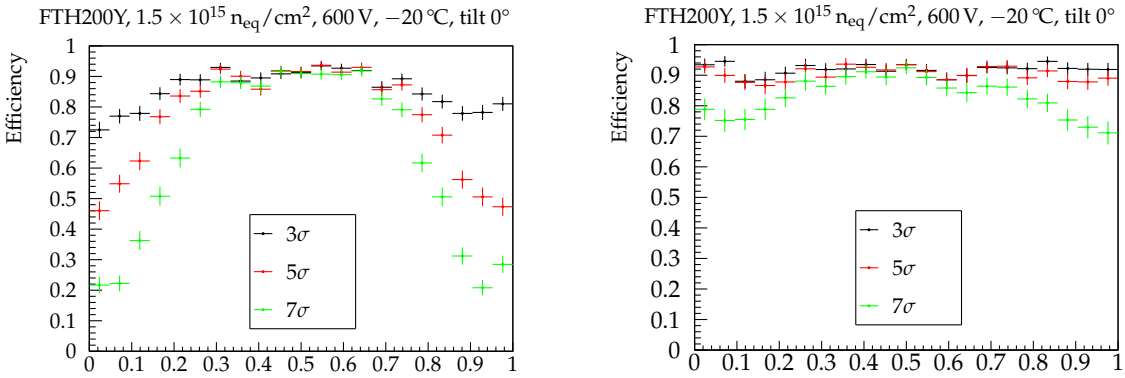

(a) Region 6-240 **(b)** Region 7-80

Figure B.5.: Efficiency as a function of the track position in the strip unit cell for different cluster cuts: The efficiency of regions 6 and 7 is shown for a cluster seed cut of 3σ, 5σ and 7σ above the noise level. The drop of efficiency on the 240 µm pitch region is enhanced with rising cluster cut. On the 80 µm region, only a slight reduction of the efficiency at a cluster cut of 7σ is observable.

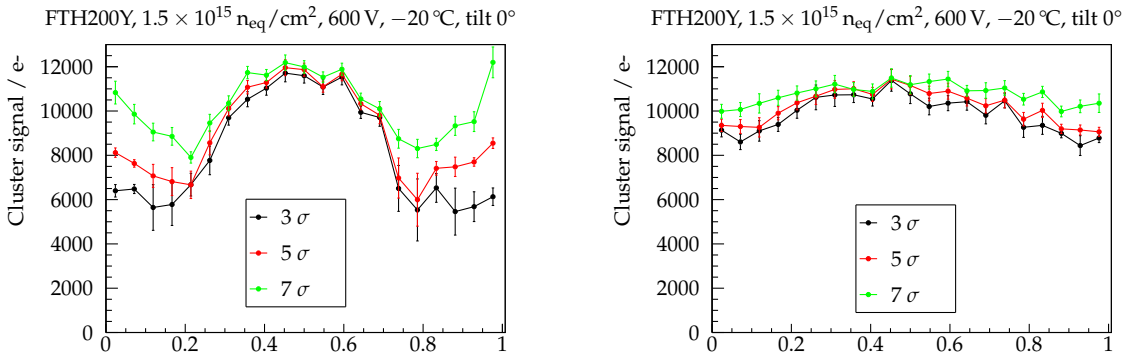

(a) Region 6-240 **(b)** Region 7-80

Figure B.6.: Cluster signal as a function of the track position in the strip unit cell for different cluster cuts: In the area between the strips, the reduction of the efficiency and the loss of low charge clusters leads to an increase in the cluster signal.

Dependence of charge loss on strip pitch

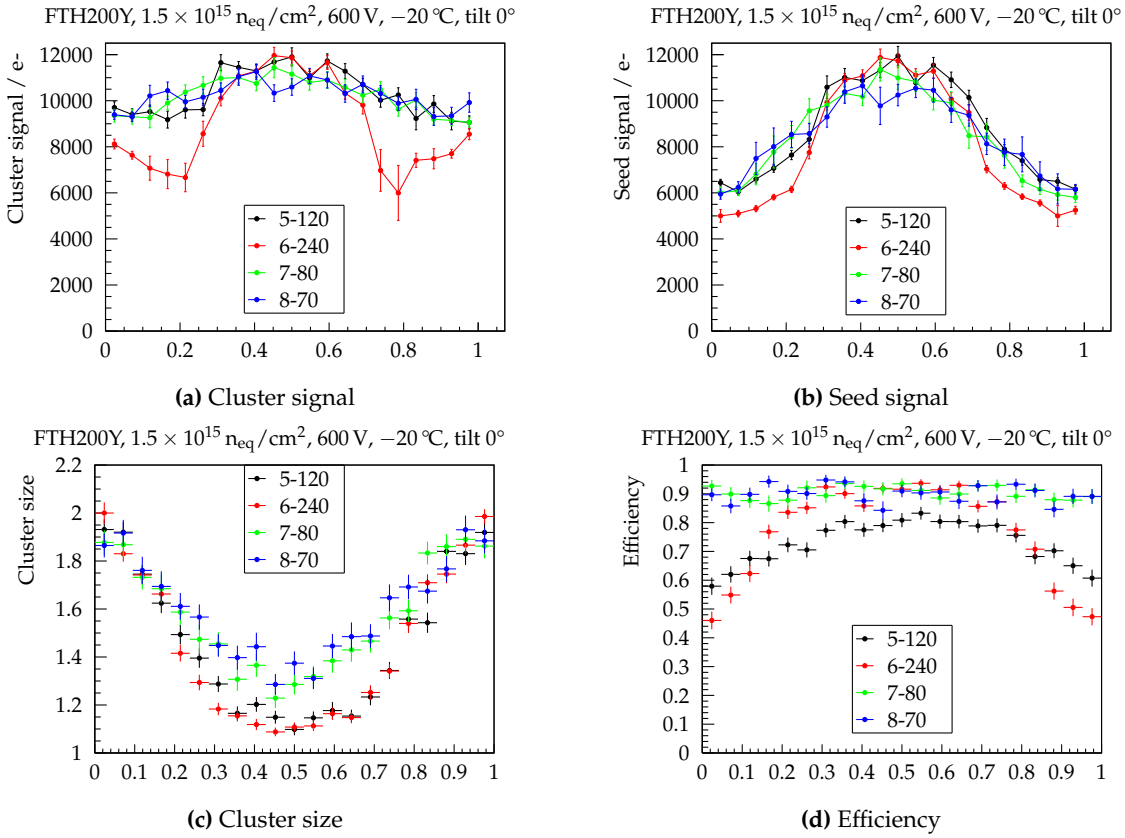

(a) Cluster signal

(b) Seed signal

(c) Cluster size

(d) Efficiency

Figure B.7.: Cluster signal, seed signal, cluster size and efficiency as a function of the position in the strip unit cell for the four different strip pitches.

Dependence of charge loss on silicon base material

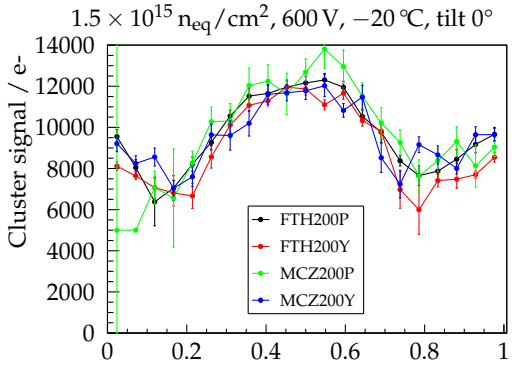

(a) Region 6-240

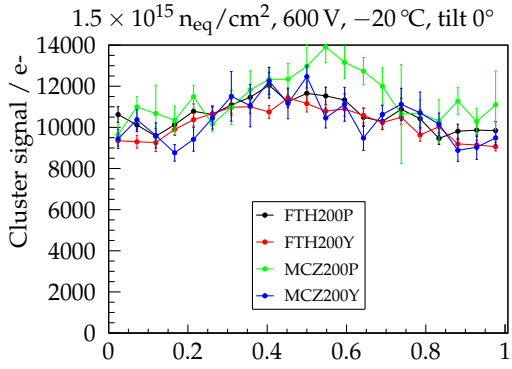

(b) Region 7-80

Figure B.8.: Cluster signal in the strip unit cell for all four irradiated p-bulk sensors. No obvious difference between the materials is visible. The reduced cluster signal in between the strips is common to all materials, independent of the strip isolation technique.

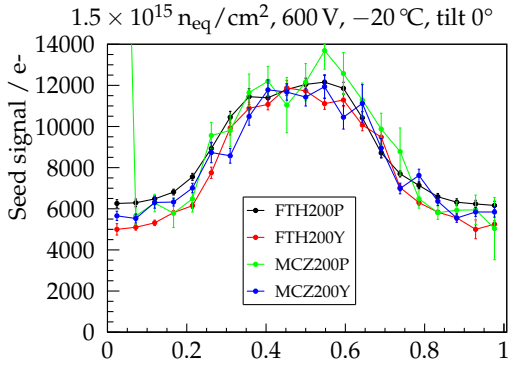

(a) Region 6-240

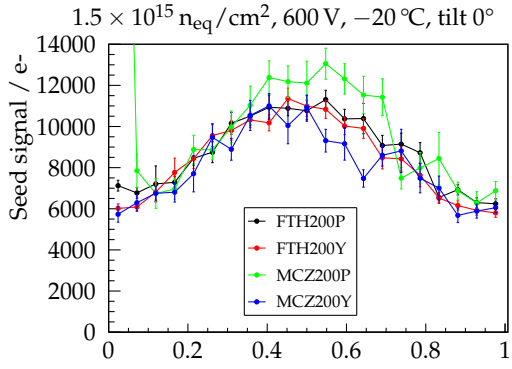

(b) Region 7-80

Figure B.9.: Seed signal in the strip unit cell for all four irradiated p-bulk sensors. The drop in the seed signal shows no difference among the different materials, indicating a similar charge sharing on all four sensors. Especially, no difference between the p-stop and p-spray isolation technique is observed.

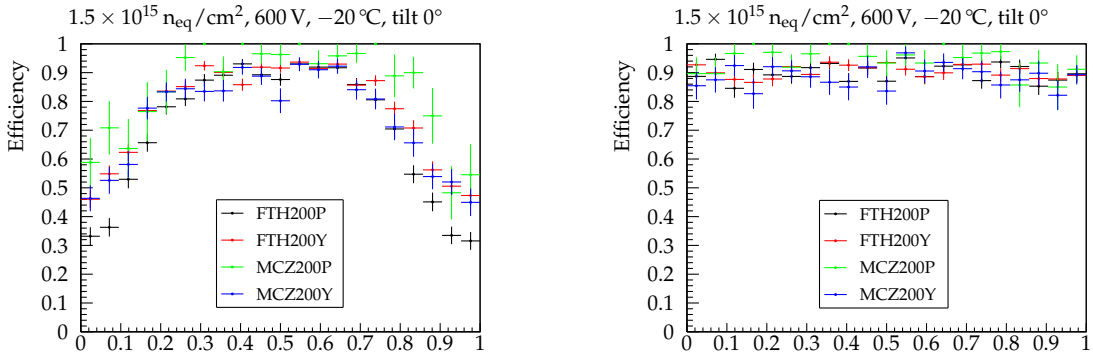

(a) Region 6-240

(b) Region 7-80

Figure B.10.: Efficiency in the strip unit cell for all four irradiated p-bulk sensors. A slight advantage of the MCZ200P sensor showing a higher efficiency is visible, especially on the 240 µm pitch region.

Dependence of charge loss on width to pitch ratio

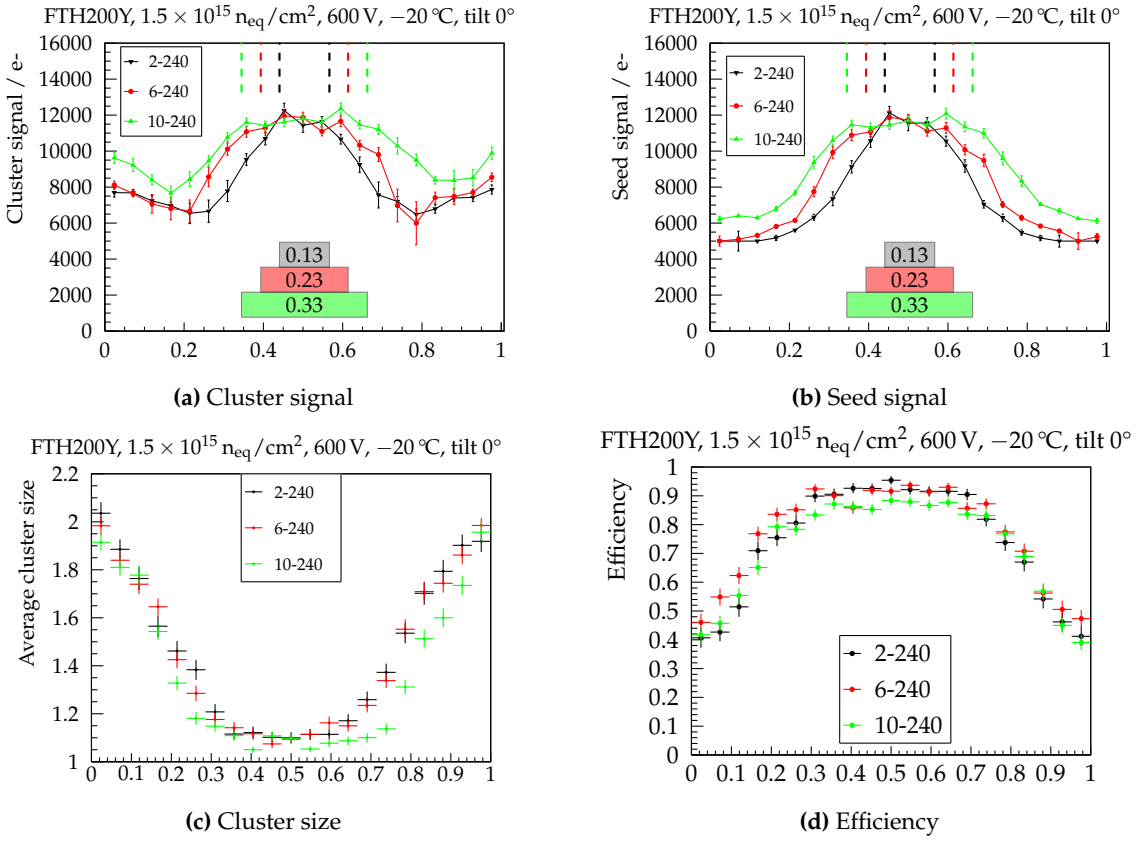

(a) Cluster signal

(b) Seed signal

(c) Cluster size

(d) Efficiency

Figure B.11.: Cluster signal, seed signal and cluster size in the 240 µm regions as a function of the position in the strip unit cell for three different width to pitch ratios. Directly under the strip implant, both the cluster and seed signal show their largest values. Outside the area covered by the implant, the signal is reduced. The colored bars in the bottom and the dashed lines in the top part illustrate the size of the strip implant.

C

Silvaco input file

The following listings are a set of sample input files as used for the strip sensor simulation using Silvaco Atlas 5.17.19.C.

Listing C.1: Parameter file (parameters.in)

```
##################################
##                              ##
##      PARAMETER FILE          ##
##                              ##
##################################

##################################
##                              ##
##      RUN OPTIONS             ##
##                              ##
##################################

# generate mesh? [boolean]
set geometry_on="true"

# run a ramp? [boolean]
set ramp_on="true"

# do a transient simulation? [boolean]
set trans_on="true"


##################################
##                              ##
##      PHYSICAL CONSTANTS      ##
##                              ##
##################################

# epsilon_0 [A s V^-1 m^-1]
set epsilon_0=8.854e-12
```

```
31
32 # epsilon_r_si [1]
33 set epsilon_r_si=11.68
34
35 # elementary charge [C]
36 set chargeconst=1.602e-19
37
38 # non-removable donor constant
39 set donorremove=7.5e-2
40
41 #BandGap
42 set Egap=1.12
43
44
45 ###################################
46 ##                               ##
47 ##      DEVICE SETTINGS ##
48 ##                               ##
49 ###################################
50
51 # n/p-type sensor: "n", "p"
52 set type="p"
53
54 # sensor thickness: [um]
55 set thick=320.0
56 set effthick=290.0
57
58 # Backplane type: "Gauss","HPK_120","HPK_200","HPK_320"
59 #set backplane="Gauss"
60 set backplane="HPK_320"
61
62 # number of strips [1]
63 set strips=5
64
65 # strip pitch: [um]
66 #set pitch=80.0
67 set pitch=80.0
68
69 # strip size: [um]
70 set stripsize=20.0
71
72 # eventual stopsize: [um]
73 set stopsize=5.0
74
75 # irradiation type: "p","n" or "pn"
76 set irrad="p"
77
78 # irradiation fluence: [n cm^-2]
79 set fluence=1e15
80
81 #Interface charge on silicon - SiO2 interface (Oxide charge)
82 set qf=1e12
83
84 # temperature: [K]
85 set T=253.0
86
```

```
# B-field: [T]
set B=4.0

# output directory for geometry: ""
set geo_out=geo

# depletion voltage: [V]
set depletionvoltage=220.0

# automatic bulk doping via depletion voltage: [cm^-3]
set bulkdop=2*$epsilon_0*$epsilon_r_si*$depletionvoltage*1e6/$effthick/
    $effthick/$chargeconst

# top implant doping: [cm^-3]
set topdop=1.0E17

# backside doping: [cm^-3]
set backdop=5.E18

# p-stop doping: [cm^-3]
set stopdop=1.0E17

# z-width multiplication: [um]
set geometrywidthmulti=27000


###################################
##                               ##
##      VOLTAGE RAMP SETTINGS    ##
##                               ##
###################################

# bias voltage: [V] (absolute integer)
set V_bias=600

# voltage step for ramping: [V]
set V_step=0.5

# step for saving until ramp: [V]
set V_savestep=50.0

# out directory for voltage ramp: ""
set ramp_out=ramp

# analysis mode: "ac", "dc"
set analysis="dc"

# AC analysis frequency: [Hz]
set acfreq=1000


###################################
##                               ##
##      BEAM TRANSIENT SETTINGS  ##
##                               ##
###################################
```

```
142
143 # step for transient after beam off: [s]
144 set t_step=1E-10
145
146 # step after which transient loop is stopped: [s]
147 set t_stopstep=5E-10
148
149 # step to save until transient: (multiples of t_stopstep) [1]
150 set t_savestep=2
151
152 # end time of signal transient: [s]
153 set t_end=25.0E-9
154
155 # end time of plot : [s]
156 set t_plot=5.0E-8
157
158 # wavelength: [nm]
159 set w_length=1055
160
161 # laser power: [W cm^-2]
162 set laserpower=1
163
164 # x position of laser [um]
165 set xlaser=110
166
167 # y position of laser [um]
168 set ylaser=322
169
170 # laser angle (set +90 for top) [deg]
171 set anglelaser=-90
172
173 # gaussian mean: [um]
174 set lasermean=0
175
176 # gaussian sigma: [um]
177 set lasersigma=45
178
179 # output directory for beam transient: ""
180 set trans_out=transient
181
182 # list of times where transient is saved
183 set timelist="2.0E-9,2.2E-9,2.4E-9,2.6E-9,2.8E-9,3.0E-9,3.2E-9,3.4E-9,3.6E
    -9,3.8E-9,4.0E-9,4.2E-9,4.4E-9"
184
185
186 ###################################
187 ##                               ##
188 ##      PLOT SIMULATED DATA      ##
189 ##                               ##
190 ###################################
191
192 # open tonyplot: [boolean]
193 set verbose="false"
194
195 # set location: ""
196 set setlocation=sets
```

Listing C.2: Definition of traps (p_traps.in)

```
trap e.level=0.525 acceptor density=3.0*$fluence degen=1 sign=1.0e-14 sigp=1.4e-14
trap e.level=0.45 acceptor density=4.0*$fluence degen=1 sign=8e-15 sigp=2.0e-14
trap e.level=0.4 acceptor density=4.0*$fluence degen=1 sign=8.0e-15 sigp=2.0e-14
trap e.level=0.5 donor density=0.6*$fluence degen=1 sign=4.0e-15 sigp=4.0e-15
trap e.level=0.45 donor density=2.0*$fluence degen=1 sign=4.0e-15 sigp=4.0e-15
```

Listing C.3: Mobility model (mob.lib)

```
#include <stdio.h>
#include <stdlib.h>
#include <math.h>
#include <ctype.h>
#include <malloc.h>
#include <string.h>
#include <template.h>
/*
 * ----------------------------------------------------------------------
 * ATLAS Parser Function Template
 * ATLAS Version 5.17.2.A
 * c 1993 - 2010 SILVACO International.
 * All rights reserved.
 * ----------------------------------------------------------------------
 */

int tofimun(double Eperp,double Na,double Nd,double nconc,double Eparl,double TL,double xcomp,double ycomp,double *mun,double *dmundep,double *dmundepar,double *dmundl,double *dmundn)
{
/* Example is Caughey-Thomas with Beta = 2.5 */
/*
double mu0 = 1000.0;double t1, t2, tmp;
double vsat=2.0e6;
double beta=2.5;

double f = Eperp + Eparl;

t1  = pow(mu0*f/vsat,beta);

t2  = 1.0/(1.0+t1);

tmp = pow(t2,1.0/beta);

*mun = mu0*tmp;

*dmundepar = -(*mun)*t1*t2/f;

*dmundep=0.0;
*dmundl =0.0;
*dmundn = 0.0;

return(0);
*/

```

```
44 //electrons
45 double mu0 = 1417.0 * pow(TL/300.0,-2.2);
46 double beta = 1.109 * pow(TL/300.0,0.66);
47 double vsat = 1.07e7 * pow(TL/300.0,0.87);
48
49 double t1, t2, tmp;
50 //double mu0=1000.;
51 //double vsat=2.0e6;
52 //double beta=2.5;
53
54 double f = Eperp + Eparl;
55
56 if (mu0<1) mu0=1417.0;
57 if (beta<0.01) beta=1.109;
58 if (vsat<1) vsat=1.07e7;
59 if (f<1e-3) f=1e-3;
60
61
62 t1  = pow(mu0*f/vsat,beta);
63
64 t2  = 1.0/(1.0+t1);
65
66 tmp = pow(t2,1.0/beta);
67
68 *mun = mu0*tmp*1.15;
69
70 *dmundepar = -(*mun)*t1*t2/f;
71
72 //*dmundep=0.0;
73 *dmundep=-(*mun)*t1*t2/f;
74 *dmundl =0.0;
75 *dmundn = 0.0;
76
77 return(0);
78
79 }
80
81
82 /*
83  * General field dependent mobility model for holes.
84  * TOtal FIeld Mobility (parallel and perpendicular field components)
85  * Statement: MATERIAL/MOBILITY
86  * Parameter: F.TOFIMUP
87  * Arguments:
88  * Eperp     [in] - perpendicular electric field (V/cm)
89  * Na        [in] - acceptor concentration  (/cm^3)
90  * Nd        [in] - donor concentration     (/cm^3)
91  * pconc     [in] - hole concentration      (/cm^3)
92  * Epar      [in] - parallel electric field (V/cm)
93  * TL        [in] - lattice temperature     (K)
94  * xcomp     [in] - x-species fraction      (0-1)
95  * ycomp     [in] - y-species fraction      (0-1)
96  *
97  * *mup      [return] - hole mobility (cm^2/Vs)
98  * *dmupdep [return] - derivative of *mup wrt Eperp
99  * *dmupdepar [return] - derivative of *mup wrt Epar
```

```
 * *dmupdl  [return] - derivative of *mup wrt TL
 * *dmupdp  [return] - derivative of *mup wrt pconc

*/


int tofimup(double Eperp,double Na,double Nd,double pconc,double Eparl,double
    TL,double xcomp,double ycomp,double *mup,double *dmupdep,double *dmupdepar,
    double *dmupdl,double *dmupdp)
{

/*mup = 500;

*dmupdepar = 0.0;
*dmupdep   = 0.0;
*dmupdl    = 0.0;
*dmupdp    = 0.0;

return(0);
*/

//holes
double mu0 = 470.5 * pow(TL/300.0,-2.5);
double beta = 1.213 * pow(TL/300.0,0.17);
double vsat = 8.37e6 * pow(TL/300.0,0.52);

double t1, t2, tmp;
//double mu0=1000.;
//double vsat=2.0e6;
//double beta=2.5;

double f = Eperp + Eparl;

if (mu0==0) mu0=470.5;
if (beta==0) beta=1.213;
if (vsat==0) vsat=8.37e6;
if (f==0) f=1e-3;

t1  = pow(mu0*f/vsat,beta);

t2  = 1.0/(1.0+t1);

tmp = pow(t2,1.0/beta);

*mup = mu0*tmp;

*dmupdepar = -(*mup)*t1*t2/f;

//*dmupdep=0.0;
*dmupdep = -(*mup)*t1*t2/f;
*dmupdl = 0.0;
*dmupdp = 0.0;

return(0);
}
```

Listing C.4: Run file (run.in)

```
1
2  ###################################
3  ##                                 ##
4  ##       INITIAL LOAD              ##
5  ##                                 ##
6  ###################################
7
8  # run atlas on X processors
9  go atlas simflags="-P␣14"
10
11 # load parameters
12 source parameters.in
13
14 # set bias polarity
15 set sig=1.0
16 if cond = (@type = "p")
17         set sig=-1.0
18 if.end
19
20 ###################################
21 ##                                 ##
22 ##       MESH BUILDING             ##
23 ##                                 ##
24 ###################################
25
26         # build mesh with periodic boundary conditions
27         mesh DIAG.FLIP=false periodic auto width=$geometrywidthmulti
28
29         # structure definition
30         set xsensor=$strips*$pitch
31         x.m l=0.0       s=.5
32         x.m l=$xsensor  s=.5
33         y.m l=-2.0 s=0.5
34         y.m l=-1.0 s=0.1
35         y.m l=-0.2 s=0.1
36         y.m l=0.0 s=0.1
37         y.m l=2. s=0.5
38         y.m l=30.0 s=6.
39         y.m l=272.0 s=3.
40         y.m l=$thick-1    s=0.5
41         y.m l=$thick+2.   s=0.5
42
43         set prejun=0
44         set prejun=$thick-30.0
45         set jun=0
46         set flat=0
47         if cond = (@backplane = "HPK_120")
48                 set prejun=$thick-230.0
49                 set jun=$thick-200.0
50                 set flat=$thick-50.0
51         if.end
52         if cond = (@backplane = "HPK_200")
53                 set prejun=$thick-150.0
54                 set jun=$thick-120.0
55                 set flat=$thick-40.0
```

```
56          if.end
57          if cond = (@backplane = "HPK_320")
58                  set prejun=$thick-70.0
59                  set jun=$thick-40.0
60                  set flat=$thick-28.0
61          if.end
62
63          # throw out columns in x-direction
64          set i=0
65          if cond = (@type = "p")
66                  loop steps = $strips
67                          set min=($pitch*$i)+$stopsize
68                          set max=($pitch*$i)+($pitch*0.5)-$stripsize+1
69                          ELIMINATE COLUMNS X.MIN=$min  X.MAX=$max  Y.MIN=-3.0 Y.
                                MAX=4.
70                          set i=$i+1
71                          set min=($pitch*$i)-($pitch*0.5)+$stripsize+1
72                          set max=($pitch*$i)-$stopsize
73                          ELIMINATE COLUMNS X.MIN=$min  X.MAX=$max  Y.MIN=-3.0 Y.
                                MAX=4.
74                  l.end
75          else
76                  loop steps = $strips
77                          set min=($pitch*$i)
78                          set max=($pitch*$i)+($pitch*0.5)-$stripsize+1
79                          ELIMINATE COLUMNS X.MIN=$min  X.MAX=$max  Y.MIN=-3.0 Y.
                                MAX=4.
80                          set i=$i+1
81                          set min=($pitch*$i)-($pitch*0.5)+$stripsize+1
82                          set max=($pitch*$i)
83                          ELIMINATE COLUMNS X.MIN=$min  X.MAX=$max  Y.MIN=-3.0 Y.
                                MAX=4.
84                  l.end
85          if.end
86
87          # throw out columns in y-direction
88          ELIMINATE COLUMNS X.MIN=0.  X.MAX=$xsensor Y.MIN=5.   Y.MAX=$thick+3.
89          ELIMINATE COLUMNS X.MIN=0.  X.MAX=$xsensor Y.MIN=10.0 Y.MAX=$thick+3.
90          ELIMINATE COLUMNS X.MIN=0.  X.MAX=$xsensor Y.MIN=20.0 Y.MAX=$thick+3.
91
92
93          # regions
94          region num=1 material=air     x.min=0.0 x.max=$xsensor  y.min=-2.0 y.
                max=$thick+2.
95          #region num=2 material=silicon x.min=0.0 x.max=$xsensor  y.min=0.0  y.
                max=$thick+1.
96          #region num=3 material=oxide   x.min=0.0 x.max=$xsensor  y.min=-1.  y.
                max=0.0
97          if cond = (@backplane = "Gauss")
98                  region num=2 material=silicon x.min=0.0 x.max=$xsensor  y.min
                        =0.0  y.max=$thick+1.0
99                  region num=3 material=oxide   x.min=0.0 x.max=$xsensor  y.min
                        =-1.  y.max=0.0
100                 #material material=silicon region=2 Eg300=1.12 TAUN0=1e-4 TAUP0
                        =1e-4
101                 set numreg=3
```

```
102         else
103                 region num=2 material=silicon x.min=0. x.max=$xsensor y.min=0.0
                        y.max=$flat
104                 region num=3 material=silicon x.min=0. x.max=$xsensor y.min=
                        $flat y.max=$thick+1.0
105                 region num=4 material=oxide   x.min=0.0 x.max=$xsensor  y.min
                        =-1.  y.max=0.0
106                 #material material=silicon region=2 Eg300=1.12 TAUN0=1e-4 TAUP0
                        =1e-4
107                 #material material=silicon region=3 Eg300=1.12 TAUN0=1e-4 TAUP0
                        =1e-4
108                 set numreg=4
109         if.end
110
111         # electrodes
112         set i=1
113         loop steps = $strips
114                 set min=($pitch*$i)-(0.5*$pitch)-0.5*$stripsize
115                 set max=($pitch*$i)-(0.5*$pitch)+0.5*$stripsize
116                 elec num=$i          name=dc$i  x.min=$min x.max=$max   y.min
                        =0.0 y.max=0.
117                 elec num=$i+$strips  name=ac$i  material=aluminum x.min=$min-5
                        x.max=$max+5 y.min=-2. y.max=-1.
118                 set i=$i+1
119         l.end
120         set i=1
121         loop steps = $strips
122                 set min=($pitch*$i)-(0.5*$pitch)-0.5*$stripsize
123                 set max=($pitch*$i)-(0.5*$pitch)+0.5*$stripsize
124                 elec  name=ac$i  material=aluminum x.min=$min   x.max=$max   y.
                        min=-1. y.max=-0.2
125                 set i=$i+1
126         l.end
127
128         elec material=aluminum name=vgg x.min=0. x.max=$xsensor y.min=$thick+1.
                y.max=$thick+2.
129
130
131         # contact
132
133         set i=1
134         loop steps=$strips
135                 contact name=dc$i resistance=1.5E6 OHMS
136                 set i=$i+1
137         l.end
138
139
140         # bulk doping
141         # donor removal for irradiated n-type FZ:
142         if cond = (@type = "n")
143                 set bulkdop=$bulkdop-$donorremove*$fluence
144                 if cond = (@bulkdop < 1e11)
145                         set bulkdop=1e11
146                 if.end
147         if.end
148
```

```
149         if cond = (@type = "p")
150                 dop region=2 unif p.type conc=$bulkdop outfile=$geo_out/doping.
                        dop
151         else
152                 dop region=2 unif n.type conc=$bulkdop outfile=$geo_out/doping.
                        dop
153         if.end
154
155         # strip doping
156         set i=1
157         loop steps = $strips
158                 set min=($pitch*$i)-(0.5*$pitch)-0.5*$stripsize
159                 set max=($pitch*$i)-(0.5*$pitch)+0.5*$stripsize
160                 if cond = (@type = "p")
161                         dop region=2 gaus n.type conc=$topdop x.min=$min  x.max
                                =$max  junc=1. ratio.lat=1. erfc.lat
162                 else
163                         dop region=2 gaus p.type conc=$topdop x.min=$min  x.max
                                =$max  junc=1. ratio.lat=1. erfc.lat
164                 if.end
165                 set i=$i+1
166         l.end
167
168         # p-stop doping, via junction or gaussian peak
169         if cond = (@type = "p")
170
171                 dop region=2 gaus p.type conc=$stopdop x.min=0.  x.max=(0.5*
                        $stopsize) junc=1. ratio.lat=1. erfc.lat
172                 #dop region=2 gaus p.type conc=1e16 peak=0.3 char=0.3 x.min=0 x
                        .max=(0.5*$stopsize)  ratio.lat=1. erfc.lat
173                 set i=1
174                 loop steps = $strips-1
175                         set min=($pitch*$i)-0.5*$stopsize
176                         set max=($pitch*$i)+0.5*$stopsize
177                         dop region=2 gaus p.type conc=$stopdop x.min=$min  x.
                                max=$max  junc=1. ratio.lat=1. erfc.lat
178                         #dop region=2 gaus p.type conc=1e16 peak=0.3 char=0.3 x
                                .min=$min x.max=$max  ratio.lat=1. erfc.lat
179                         set i=$i+1
180                 l.end
181                 dop region=2 gaus p.type conc=$stopdop x.min=$xsensor-(0.5*
                        $stopsize) x.max=$xsensor junc=1. ratio.lat=1. erfc.lat
182                 #dop region=2 gaus p.type conc=1e16 peak=0.3 char=0.3 x.min=
                        $xsensor-(0.5*$stopsize) x.max=$xsensor  ratio.lat=1. erfc.
                        lat
183         if.end
184
185         # backplane doping
186         if cond = (@type = "p")
187                 if cond = (@backplane = "Gauss")
188                         dop region=2 gaus p.type conc=$backdop peak=$thick+0.7
                                char=0.3 ratio.lat=1.0 erfc.lat
189                 else
190                         dop region=2 erfc p.type peak=$flat junction=$jun conc=
                                $backdop ratio.lat=0.3 erfc.lat
191                         dop region=3 unif p.type conc=$backdop iregion=2
```

```
192                 if.end
193         else
194                 if cond = (@backplane = "Gauss")
195                         dop region=2 gaus n.type conc=$backdop peak=$thick+0.7
                                char=0.3 ratio.lat=1.0 erfc.lat
196                 else
197                         dop region=2 erfc n.type peak=$flat junction=$jun conc=
                                $backdop ratio.lat=0.3 erfc.lat
198                         dop region=3 unif n.type conc=$backdop iregion=2
199                 if.end
200         if.end
201
202         #if cond = (@type = "p")
203         #       dop region=2 gaus p.type conc=1e16 peak=$thick+0.7 char=0.3 x.
                min=0.  x.max=$xsensor  ratio.lat=1. erfc.lat
204         #else
205         #       dop region=2 gaus n.type conc=1e16 peak=$thick+0.7 char=0.3 x.
                min=0.  x.max=$xsensor  ratio.lat=1. erfc.lat
206         #if.end
207
208         #Interface charges on silicon-oxide interface
209         INTERFACE QF=@qf
210
211         # regrid to get fine mesh at doping gradients
212         #regrid logarithm doping ratio=4 smooth.key=4 dopfile=$geo_out/doping.
                dop
213
214         #plot
215         save outf=$geo_out/geometry.str
216         if cond = (@verbose="true")
217                 tonyplot $geo_out/geometry.str -set $setlocation/geometry.set
218         if.end
219
220 ################################
221 ##                            #
222 ##      VOLTAGE RAMP          #
223 ##                            #
224 ################################
225
226 # define loop number
227 set loops=0
228
229 # run ramp?
230 if cond = (@ramp_on = "true")
231
232         MATERIAL F.TOFIMUN="mob.lib" F.TOFIMUP="mob.lib"
233         material material=silicon region=2 Eg300=1.12 TAUN0=1e-4 TAUP0=1e-4
234
235         output E.VELOCITY EX.VELOCITY EY.VELOCITY E.MOBILITY H.VELOCITY HX.
                VELOCITY HY.VELOCITY H.MOBILITY BAND.PARAM BAND.TEMP IMPACT J.
                CONDUCT J.DISPLACEMENT PHOTOGEN TRAPS TRAPS.FT
236         # physical models
237         #models consrh conmob fldmob  auger boltzmann bgn bz=$B print
                temperature=$T
238         model bipolar print bz=$B temp=$T
239         #cvt
```

```
240
241         #mobility n.canali p.canali
242         #mobility NEWCVT.N NEWCVT.P bn.cvt=3e6 bp.cvt=3e6
243
244
245
246         # set avalanche
247         impact SELB
248
249         if cond = (@type = "p")
250                 source p_traps.in
251         else
252                 source n_traps.in
253         if.end
254
255         # specify method for solving, carriers=2 for impact ionization, gummel
                newton for floation junctions (p-stop), but without periodic
                boundary
256         method GUMMEL NEWTON GUM.INIT=5 carriers=2 trap atrap=0.25 maxtrap=10
257         #method NEWTON carriers=2
258
259         # compute initial solutions
260         solve init
261         set i=1
262         set j=$strips+1
263         loop steps = $strips
264                 solve v$i=0. v$j=0.
265                 set i=$i+1
266                 set j=$j+1
267         l.end
268
269         # apply bias voltage (save binary .str for further simulations)
270         # select AC or DC ramp
271         if cond=(@analysis="dc")
272
273                 log outf=$ramp_out/sweep_iv.log
274                 solve name=vgg vvgg=0. vstep=$sig*0.1 vfinal=$sig*2.
275                 solve name=vgg vvgg=$sig*2. vstep=$sig*0.1 vfinal=$sig*5.
276                 solve name=vgg vvgg=$sig*5. vstep=$sig*0.2 vfinal=$sig*10.
277                 save outf=$ramp_out/solve_dc_10V.str
278
279                 set start=10
280                 set stop=$V_savestep
281                 set loops=floor(($V_bias-$start)/$V_savestep)
282                 loop steps=$loops
283                         solve name=vgg vvgg=$sig*($start+$V_step) vstep=$sig*
                            $V_step vfinal=$sig*$stop
284                         save outf=$ramp_out/solve_dc_$"stop"V.str
285                         set start=$stop
286                         set stop=$stop+$V_savestep
287                 l.end
288
289                 solve name=vgg vvgg=$sig*($start+$V_step) vstep=$sig*$V_step
                    vfinal=$sig*$V_bias
290                 save outf=$ramp_out/solve_dc.str
291                 log outf=$ramp_out/dummy
```

```
292                 solve name=vgg vvgg=$sig*$V_bias outf=$ramp_out/
                        solve_dc_bin_Vbias.str
293
294
295                 # plot
296                 if cond = (@verbose="true")
297                         tonyplot $ramp_out/solve_dc.str -set $setlocation/
                            solve_dc.set
298                         tonyplot $ramp_out/sweep_iv.log -set $setlocation/
                            sweep_iv.set
299                 else
300                 if.end
301
302         else
303
304                 log outf=$ramp_out/sweep_cv.log
305                 solve name=vgg vvgg=0. vstep=$sig*0.1 vfinal=$sig*2. AC freq=
                        $acfreq
306                 solve name=vgg vvgg=$sig*2. vstep=$sig*0.2 vfinal=$sig*5. AC
                        freq=$acfreq
307                 solve name=vgg vvgg=$sig*5. vstep=$sig*0.5 vfinal=$sig*10. AC
                        freq=$acfreq
308                 save outf=$ramp_out/solve_ac_10V.str
309
310                 set start=10
311                 set stop=$V_savestep
312                 set loops=floor(($V_bias-$start)/$V_savestep)
313                 loop steps=$loops
314                         solve name=vgg vvgg=$sig*($start+$V_step) vstep=$sig*
                            $V_step vfinal=$sig*$stop AC freq=$acfreq
315                         save outf=$ramp_out/solve_ac_$"stop"V.str
316                         set start=$stop
317                         set stop=$stop+$V_savestep
318                 l.end
319
320                 solve name=vgg vvgg=$sig*($start+$V_step) vstep=$sig*$V_step
                        vfinal=$sig*$V_bias AC freq=$acfreq
321                 save outf=$ramp_out/solve_ac.str
322                 log outf=$ramp_out/dummy
323                 solve name=vgg vvgg=$sig*$V_bias outf=$ramp_out/
                        solve_dc_bin_Vbias.str
324
325
326                 # plot
327                 if cond = (@verbose="true")
328                         tonyplot $ramp_out/solve_ac.str -set $setlocation/
                            solve_ac.set
329                         tonyplot $ramp_out/sweep_cv.log -set $setlocation/
                            sweep_cv.set
330                 else
331                 if.end
332
333         if.end
334
335 else
336
```

```
337         solve init
338         load infile=$ramp_out/solve_dc_bin_Vbias.str
339
340 if.end
341
342
343 ##################################
344 ##                              #
345 ##      BEAM TRANSIENT          #
346 ##                              #
347 ##################################
348
349 # define time-dependant naming of save files
350 set savename=0
351
352 # run transient?
353 if cond = (@trans_on = "true")
354         # define beam
355         beam num=1 x.origin=$xlaser y.origin=$ylaser angle=$anglelaser
                wavelength=$w_length/1000 \
356                 xmin=$lasermean-2.0*$lasersigma xmax=$lasermean+2.0*$lasersigma
                        GAUSSIAN MEAN=$lasermean SIGMA=$lasersigma RAYS=200
357
358         # solve method (cf. ramp)
359         method GUMMEL NEWTON GUM.INIT=5 carriers=2
360         #method NEWTON  carriers=2
361
362         # output logfile.
363         log outf=$trans_out/transient.log
364
365         # run transient first 0.5 ns
366         solve b1=0.   beam=1 lambda=$w_length/1000 ramptime=1e-15 tstop=2.E-9
                dt=1E-12
367         save outf=$trans_out/transient_0ns.str
368         solve b1=$laserpower  beam=1 lambda=$w_length/1000 ramptime=1E-10 tstop
                =2.2E-9 dt=2E-13
369         save outf=$trans_out/transient_0.2ns.str
370         solve b1=0.   beam=1 lambda=$w_length/1000 ramptime=1E-10 tstop=2.3E-9
                dt=2E-12
371         save outf=$trans_out/transient_0.3ns.str
372         solve b1=0.   beam=1 lambda=$w_length/1000 ramptime=0 tstop=2.5E-9 dt=2
                E-11
373         save outf=$trans_out/transient_0.5ns.str
374
375         # run transient remaining time
376         set i=1
377         set loops= floor(($t_end-2.5E-9)/$t_stopstep)
378         loop steps = $loops
379                 solve b1=0.   beam=1 lambda=$w_length/1000 ramptime=0 tstop=2.5
                        E-9+$i*$t_stopstep dt=$t_step
380                 if cond=(fmod(($i),$t_savestep)=0)
381                         set savename=($i*$t_stopstep*1e9)+0.5
382                         save outf=$trans_out/transient_$"savename"ns.str
383                 if.end
384                 set i=$i+1
385         l.end
```

```
386         solve b1=0.   beam=1 lambda=$w_length/1000 ramptime=0 tstop=$t_plot dt
                =1E-10
387         set savename=$t_plot*1e9
388         save outf=$trans_out/transient_$"savename"ns.str
389
390         # plot transient, show first 4 edensity and hdensity plots
391         if cond = (@verbose="true")
392                 tonyplot $trans_out/transient_0ns.str $trans_out/transient_0.2
                    ns.str $trans_out/transient_0.3ns.str $trans_out/
                    transient_0.5ns.str -set $setlocation/edensity.set
393                 tonyplot $trans_out/transient_0ns.str $trans_out/transient_0.2
                    ns.str $trans_out/transient_0.3ns.str $trans_out/
                    transient_0.5ns.str -set $setlocation/hdensity.set
394                 tonyplot $trans_out/transient.log -set $setlocation/transient.
                    set
395         else
396         if.end
397
398 else
399 if.end
```

Acknowledgement/Danksagung

The work presented in this thesis would not have been possible to carry out without the support of many colleagues. I would like to thank all of them.

Diese Arbeit wäre nicht möglich ohne die Hilfe und Unterstützung vieler Kollegen. Allen sei an dieser Stelle gedankt.

Herrn Prof. Wim de Boer danke ich für die Möglichkeit, meine Doktorarbeit am Institut für Experimentelle Kernphysik anzufertigen. Für das Vertrauen in meine Fähigkeiten und die Freiheiten die er mir eingeräumt hat, bin ich ihm sehr dankbar. Prof. Thomas Müller danke ich für die Übernahme des Korreferats.

Alexander Dierlamm danke ich für die Unterstützung während meiner gesamten Zeit am EKP und für die vielen Anregungen und guten Ideen die diese Arbeit bereichert haben.

Theo Schneider und seinem Team vom Institut für Technische Physik danke ich für den unkomplizierten Zugang zum Jumbo und für ihre Unterstützung während der Messwochen.

Weiterer Dank gebührt

- Frank Hartmann,
- Hans-Jürgen Simonis,
- Pia Steck für ihre Unterstützung beim Bau der Module für Lorentzwinkel- und Teststrahlmessungen,
- Tobias Barvich für seine Unterstützung in allen mechanischen Fragen beim Aufbau des Lorentzwinkel-Setups,
- Felix Bögelspacher für die zuverlässige Durchführung der Bestrahlung der Sensoren,
- Diana Fellner, Brigitte Gering und Bärbel Bräunling für die Bewältigung der bürokratischen Angelegenheiten,
- den langjährigen Doktorandenkollegen: Robert Eber, Karl-Heinz Hoffmann, Martin Printz, Stefan Heindl und Moritz Guthoff für die gegenseitige Unterstützung,
- meinen Bachelorstudenten Max Schmenger und Julius Krause für die Unterstützung während der Lorentzwinkel Messungen am Jumbo,
- allen Studenten und Mitarbeitern der CMS Gruppe am Campus Nord für die schöne Zeit, die unterhaltsamen Kaffeepausen und sonstigen Aktivitäten innerhalb und außerhalb der Arbeit,

- Martin Printz, Volker Heine, Angelika Schulz, Alexandra Junkes[1], Matteo Centis Vignali[1], Thomas Eichhorn[2] und Hanno Perrey[2] für die Unterstützung und die Übernahme der (Nacht)schichten während des Testbeams am DESY,
- Catherine Vander Velde[3], Thierry Caebergs[4] and Gregory Hammad[3] for the fruitful cooperation on the Lorentz angle task in the CMS Tracker Detector Performance Group,
- meinen Eltern Barbara und Hans Georg und meinem Bruder Thomas für die Unterstützung.

This work is supported by the Initiative and Networking Fund of the Helmholtz Association, contract HA-101 ("Physics at the Terascale").

The research leading to the results of this thesis has received funding from the European Commision under the FP7 Research Infrastructures project AIDA, grant agreement no 262025.

[1]Uni Hamburg
[2]DESY Hamburg
[3]Université libre de Bruxelles
[4]Université de Mons

List of Figures

List of Tables

Bibliography

[AAC10] Anthony Affolder, Phil Allport, and Gianluigi Casse. Collected charge of planar silicon detectors after pion and proton irradiations up to $2.2 \times 10^{16} n_{eq} cm^{-2}$. Nuclear Instruments and Methods in Physics Research Section A: Accelerators, Spectrometers, Detectors and Associated Equipment (623)1: (2010), 177–179, 1st International Conference on Technology and Instrumentation in Particle Physics. DOI: 10.1016/j.nima.2010.02.187.

[Abb11] Duccio Abbaneo. Upgrade of the CMS Tracker with tracking trigger. Journal of Instrumentation (6)12: (2011), C12065. DOI: 10.1088/1748-0221/6/12/C12065.

[Abb13] Duccio Abbaneo. Summary of the Phase II days and plans for the TP. Dec. 2013. URL: https://indico.cern.ch/contributionDisplay.py?contribId=11&sessionId=1&confId=278409.

[Acc99] CERN PhotoLab / Accelerators. The four main LHC experiments. June 1999. URL: http://cds.cern.ch/record/40525.

[Ago+03] S. Agostinelli et al. Geant4 - a simulation toolkit. Nuclear Instruments and Methods in Physics Research Section A: Accelerators, Spectrometers, Detectors and Associated Equipment (506)3: (July 2003), 250 –303. DOI: 10.1016/S0168-9002(03)01368-8.

[All+06] J. Allison et al. Geant4 developments and applications. IEEE Transactions on Nuclear Science (53)1: (2006), 270–278. DOI: 10.1109/TNS.2006.869826.

[Auz13] Georg Auzinger. Silicon Sensor Development for the CMS Tracker Upgrade. PhD thesis. TU Vienna, Oct. 2013.

[Axe+01] Markus Axer et al. A Test Setup for Quality Assurance of Front End Hybrids. Geneva: CERN, Oct. 2001.

[BC10] David Barney and Sergio Cittolin. CMS 3D image. July 2010. URL: https://cms-docdb.cern.ch/cgi-bin/PublicDocDB/ShowDocument?docid=2715.

[BG09] Burton Betchart and Yuri Gotra. Presentations in CMS Tracker Detector Performance Group meetings. 2009.

[BRIL2013] CMS collaboration. FLUKA particle flux maps for CMS Detector. CMS DP-2013/028. Oct. 2013.

[Bar+03] Valeria Bartsch et al. An algorithm for calculating the Lorentz angle in silicon detectors. Nuclear Instruments and Methods in Physics Research Section A: Accelerators, Spectrometers, Detectors and Associated Equipment (497)2003: (2003), 389–396. DOI: 10.1016/S0168-9002(02)01801-6.

[Bar11a] David Barney. CMS slice. Sept. 2011. URL: https://cms-docdb.cern.ch/cgi-bin/PublicDocDB/ShowDocument?docid=5581.

[Bar11b] Christian Barth. Evolution of silicon sensors characteristics of the current CMS tracker. Nuclear Instruments and Methods in Physics Research Section A: Accelerators, Spectrometers, Detectors and Associated Equipment (658)2011: (2011), 6 –10, RESMDD 2010. DOI: 10.1016/j.nima.2011.05.045.

[Bel+83] E. Belau et al. Charge collection in silicon strip detectors. Nuclear Instruments and Methods in Physics Research (214)2-3: (1983), 253–260. DOI: 10.1016/0167-5087(83)90591-4.

[Ber+12] J. Beringer et al. Review of Particle Physics. Physical Review D (86) (1 July 2012), 010001. DOI: 10.1103/PhysRevD.86.010001.

[Blo07] Volker Blobel. Millepede II - Linear Least Squares Fits with a Large Number of Parameters. Institut für Experimentalphysik, Universität Hamburg. 2007.

[Boe10] Wim de Boer et al. Lorentz shift measurements in heavily irradiated silicon detectors in high magnetic fields. Proceedings of Science (RD09) (2010), 022, arXiv:1005.3629 [physics.ins-det].

[Bou13] Gaelle Boudoul. A Level-1 Tracking Trigger for the CMS upgrade using stacked silicon strip detectors and advanced pattern technologies. Journal of Instrumentation (8)01: (2013), C01024. DOI: 10.1088/1748-0221/8/01/C01024.

[Bra+12] D. Braga et al. CBC2: a microstrip readout ASIC with coincidence logic for trigger primitives at HL-LHC. Journal of Instrumentation (7)10: (2012), C10003. DOI: 10.1088/1748-0221/7/10/C10003.

[Bul+07] A. Bulgheroni, T. Klimkovich, P. Roloff, and A.F. Zarnecki. EUTelescope: tracking software. 2007. EUDET-Memo-2007-20

[CMS02] The CMS Collaboration. The TriDAS Project Technical Design Report, Volume 2: Data Acquisition and High-Level Trigger. CERN/LHCC 2002-26 CMS TDR 6. Dec. 2002.

[CMS07] The CMS Collaboration. CMS Expression of Interest in the SLHC. CERN/LHCC 2007-014. Mar. 2007.

[CMS08] The CMS Collaboration. The CMS experiment at the CERN LHC. Journal of Instrumentation (3)08: (2008), S08004. DOI: 10.1088/1748-0221/3/08/S08004.

[CMS] CMS public website - Silicon Strip Tracker. URL: http://cms.web.cern.ch/news/silicon-strips.

[CMS12] The CMS Collaboration. New world record - first pp collisions at 8 TeV. URL: http://cms.web.cern.ch/news/new-world-record-first-pp-collisions-8-tev.

[Can+75] C. Canali, G. Majni, R. Minder, and G. Ottaviani. Electron and hole drift velocity measurements in silicon and their empirical relation to electric field and temperature. IEEE Transactions on Electron Devices (22)11: (1975), 1045–1047. DOI: 10.1109/T-ED.1975.18267.

[Cha+12] S. Chatrchyan et al. Observation of a new boson at a mass of 125 GeV with the CMS experiment at the LHC. Physics Letters B (716)1: (2012), 30–61. DOI: 10.1016/j.physletb.2012.08.021.

[Chi13] A. Chilingarov. Temperature dependence of the current generated in Si bulk. Journal of Instrumentation (8)10: (2013), P10003. DOI: 10.1088/1748-0221/8/10/P10003.

[Ciu+07] Vitaliano Ciulli, Raffaello D'Alessandro, Simone Frosali, and Chiara Genta. Determination of the Lorentz Angle in Microstrip Silicon Detectors with Cosmic Muons. Geneva: CERN, Sept. 2007.

[Cre03] L. Cremaldi. CMS pixel detector – overview. Nuclear Instruments and Methods in Physics Research Section A: Accelerators, Spectrometers, Detectors and Associated Equipment (511)1–2: (2003), 64 –67, Proceedings of the 11th International Workshop on Vertex Detectors. DOI: 10.1016/S0168-9002(03)01752-2.

[Cus09] David Cussans. Description of the JRA1 Trigger Logic Unit (TLU), v0.2c. 2009.

[Dal+13] Ranjeet Dalal et al. Simulations for Hadron Irradiated n+p- Si Strip Sensors Incorporating Bulk and Surface Damage. Presented at 23rd RD50 Workshop, CERN. Nov. 2013.

[Dal13] Ranjeet Dalal. Private communication. 2013.

[Desy] Test Beams at DESY. URL: http://testbeam.desy.de.

[Die12] Alexander Dierlamm. Silicon sensor developments for the CMS Tracker upgrade. Journal of Instrumentation (7)01: (2012), C01110, Proceedings of the 9th International Conference on Position Sensitive Detectors (PSD9). DOI: 10.1088/1748-0221/7/01/C01110.

[Die13a] Alexander Dierlamm. Planar sensors for future vertex and tracking detectors. Geneva: CERN, Dec. 2013. Proceedings of the 22nd International Workshop on Vertex Detectors

[Die13b] Alexander Dierlamm. The CMS Outer Tracker Upgrade. 7th Annual Workshop of the Helmholtz Alliance "Physics at the Terascale". Dec. 2013. URL: https://indico.desy.de/getFile.py/access?contribId=18&sessionId=8&resId=0&materialId=slides&confId=8029.

[Dom07] Aaron Dominguez. The CMS pixel detector. Nuclear Instruments and Methods in Physics Research Section A: Accelerators, Spectrometers, Detectors and Associated Equipment (581)1-2: (2007), 343–346, Proceedings of the 11th International Vienna Conference on Instrumentation. DOI: 10.1016/j.nima.2007.07.156.

[Ebe13] Robert Eber. Investigations of new Sensor Designs and Development of an effective Radiation Damage Model for the Simulation of highly irradiated Silicon Particle Detectors. IEKP-KA 2013/27. PhD thesis. Karlsruher Institut für Technologie, Institut für Experimentelle Kernphysik, 2013.

[Eck14] Doris Eckstein. CMS outer tracker detector upgrade plans. Geneva: CERN, Jan. 2014. CMS-CR-2014-008

[Erf09] Joachim Erfle. Entwicklungen für neue Siliziumstreifensensoren und deren Qualitätskontrolle. IEKP-KA/2009-27. Diploma Thesis. Institut für Experimentelle Kernphysik, Karlsruher Institut für Technologie, 2009.

[Erf14] Joachim Erfle. Irradiation study of different silicon materials for the CMS tracker upgrade. In preparation. PhD thesis. Universität Hamburg, 2014.

[Eut] EUTelescope - A Generic Pixel Telescope Data Analysis Framework. URL: http://eutelescope.web.cern.ch/.

[Fre12] Sabine Frech. Einfluss von Strahlenschäden auf Siliziumstreifensensoren aus unterschiedlichen Grundmaterialien. IEKP-KA/2012-21. Diploma thesis. Karlsruhe Institute of Technology, 2012.

[GM12] Rudolf Gross and Achim Marx. Festkörperphysik. Oldenbourg Wissenschaftsverlag, 2012.

[GS12] D. Giordano and G. Sguazzoni. CMS reconstruction improvements for the tracking in large pile-up events. Journal of Physics: Conference Series (396)2: (2012), 022044. DOI: 10.1088/1742-6596/396/2/022044.

[HJ01] Louis-Andre Hamel and Manuel Julien. Comments on Ramo's theorem. Proc. SPIE 4507, Hard X-Ray and Gamma-Ray Detector Physics III (4507) (Dec. 2001), 255–263. DOI: 10.1117/12.450766.

[HL-LHC] HL-LHC: High Luminosity Large Hadron Collider. URL: http://hilumilhc.web.cern.ch/HiLumiLHC/about/.

[Hal11] Geoff Hall. Conceptual study of a trigger module for the CMS Tracker at SLHC. Nuclear Instruments and Methods in Physics Research Section A: Accelerators, Spectrometers, Detectors and Associated Equipment (636)1, Supplement: (2011), S201–S207, 7th International Hiroshima Symposium on the Development and Application of Semiconductor Tracking Detectors. DOI: 10.1016/j.nima.2010.04.110.

[Har09] Frank Hartmann. Evolution of Silicon Sensor Technology in Particle Physics. Springer Tracts in Modern Physics. Springer, 2009.

[Hau00] Florian Hauler. Lorentzwinkelmessungen an bestrahlten Siliziumstreifendetektoren im Temperaturbereich T=77-300 K. IEKP-KA/2000-12. Diploma Thesis. 2000.

[Hoc07] Michael Hoch. Placing the Tracker inside CMS. CMS Collection. Dec. 2007. URL: http://cds.cern.ch/record/1275108.

[Hof11] Karl-Heinz Hoffmann. Campaign to identify the future CMS tracker baseline. Nuclear Instruments and Methods in Physics Research Section A: Accelerators, Spectrometers, Detectors and Associated Equipment (658)1: (2011), 30–35, RESMDD 2010. DOI: 10.1016/j.nima.2011.05.028.

[Hof13] Karl-Heinz Hoffmann. Development of new Sensor Designs and Investigations on Radiation Hard Silicon Strip Sensors for the CMS Tracker Upgrade at the High Luminosity Large Hadron Collider. IEKP-KA/2013-1. PhD thesis. Karlsruhe Institute of Technology, 2013.

[Huh02] Mika Huhtinen. Simulation of non-ionising energy loss and defect formation in silicon. Nuclear Instruments and Methods in Physics Research Section A: Accelerators, Spectrometers, Detectors and Associated Equipment (491)1-2: (2002), 194–215. DOI: 10.1016/S0168-9002(02)01227-5.

[Hun12] Siegfried Hunklinger. Festkörperphysik. 3rd ed. Oldenbourg, 2012.

[IL09] Harald Ibach and Hans Lüth. Solid-State Physics - An Introduction to Principles of Materials Science. 4th ed. Springer Berlin Heidelberg, 2009. DOI: 10.1007/978-3-540-93804-0.

[Irr] Irradiation Center - proton irradiation. URL: http://www.ekp.kit.edu/english/264.php.

[Jac+77] C. Jacoboni, C. Canali, G. Ottaviani, and A. Alberigi Quaranta. A review of some charge transport properties of silicon. Solid-State Electronics (20)2: (1977), 77–89. DOI: 10.1016/0038-1101(77)90054-5.

[Jun11] Alexandra Junkes. Influence of radiation induced defect clusters on silicon particle detectors. DESY-THESIS-2011-031. PhD thesis. Universität Hamburg, 2011.

[Klä11] Marion Kläser. Institute for Technical Physics, KIT. Private communication. Sept. 2011.

[Lut99] Gerhard Lutz. Semiconductor Radiation Detectors: Device Physics. Accelerator Physics Series. Springer-Verlag, 1999.

[MH09] R. Marco-Hernandez. A Portable Readout System for Microstrip Silicon Sensors (ALIBAVA). Nuclear Science, IEEE Transactions on (56)3: (2009), 1642–1649. DOI: 10.1109/TNS.2009.2017261.

[Mer+12] Stefano Mersi, Duccio Abbaneo, Nicoletta De Maio, and Geoff Hall. CMS Tracker Layout Studies for HL-LHC. Physics Procedia (37)0: (2012), 1070–1078, Proceedings of the 2nd International Conference on Technology and Instrumentation in Particle Physics (TIPP 2011). DOI: 10.1016/j.phpro.2012.03.729.

[Mol99] Michael Moll. Radiation Damage in Silicon Particle Detectors. DESY-THESIS-1990-040. PhD thesis. Universität Hamburg, 1999.

[Mäe13] Teppo Mäenpää. Performance of different silicon materials for the upgraded CMS tracker. Geneva: CERN, Aug. 2013. Proceedings of RD13 - 11th International Conference on Large Scale Applications and Radiation Hardness of Semiconductor Detectors

[NS13] Andreas Nürnberg and Theo Schneider. Lorentz angle measurements as part of the sensor R&D for the CMS Tracker upgrade. Journal of Instrumentation (8)01: (2013), C01001, Proceedings of the 14th International Workshop on Radiation Imaging Detectors (iWoRID2012). DOI: 10.1088/1748-0221/8/01/C01001.

[OMP] The OpenMP® API specification for parallel programming. URL: http://openmp.org/wp/.

[Pil] PiLAS - Picosecond gain switched laser diode module for OEM and R&D applications. URL: http://www.alsgmbh.com/ds/PiLas.pdf.

[Poz13] Nicola Pozzobon. Development of a Level 1 Track Trigger for the CMS experiment at the high-luminosity LHC. Nuclear Instruments and Methods in Physics Research Section A: Accelerators, Spectrometers, Detectors and Associated Equipment (2013). DOI: 10.1016/j.nima.2013.06.010.

[RHS00] A. Rimikis, F. Hornung, and T. Schneider. High field magnet facilities and projects at the Forschungszentrum Karlsruhe. IEEE Transactions on Applied Superconductivity (10)1: (2000), 1542–1545.

[RIC] Reactor Infrastructure Centre (RIC) "Jožef Stefan" Institute. URL: http://www.rcp.ijs.si/ric.

[RSS79] K. Rajkanan, R. Singh, and J. Shewchun. Absorption coefficient of silicon for solar cell calculations. Solid-State Electronics (22)9: (1979), 793–795. DOI: 10.1016/0038-1101(79)90128-X.

[Ram39] Simon Ramo. Currents Induced by Electron Motion. Proceedings of the IRE (27)9: (1939), 584–585. DOI: 10.1109/JRPROC.1939.228757.

[Ran13] Reinhard Randoll. Modellierung der Rekonstruktion von Teilchendurchgängen im neuen CMS-Spurdetektor am HL-LHC. IEKP-KA/2013-4. Diploma thesis. Karlsruher Institut für Technologie, Institut für Experimentelle Kernphysik, Apr. 2013.

[Ray+00] Mark Raymond et al. The APV25 0.25 µm CMOS readout chip for the CMS tracker. In: Nuclear Science Symposium Conference Record, 2000 IEEE. (2) 2000, 9/113–9/118. DOI: 10.1109/NSSMIC.2000.949881.

[Rub10] Igor Rubinskiy. EUTelescope. Offline track reconstruction and DUT analysis software. 2010.

[Rub12] Igor Rubinskiy. An EUDET/AIDA Pixel Beam Telescope for Detector Development. Physics Procedia (37)0: (2012), 923 –931, Proceedings of the 2nd International Conference on Technology and Instrumentation in Particle Physics (TIPP 2011). DOI: 10.1016/j.phpro.2012.02.434.

[SZT12] Luka Snoj, Gašper Žerovnik, and Andrej Trkov. Computational analysis of irradiation facilities at the JSI TRIGA reactor. Applied Radiation and Isotopes (70)3: (2012), 483–488. DOI: 10.1016/j.apradiso.2011.11.042.

[Sau09] Rolf Sauer. Halbleiterphysik: Lehrbuch für Physiker und Ingenieure. Oldenbourg Wissensch.Vlg, 2009.

[Sch+10] Theo Schneider et al. Superconducting High Field Magnet Engineering at KIT. IEEE Transactions on Applied Superconductivity (20)3: (2010), 624–627.

[Sch03] Stefan Schael. The CMS silicon strip detector - mechanical structure and alignment system. Nuclear Instruments and Methods in Physics Research Section A: Accelerators, Spectrometers, Detectors and Associated Equipment (511)1-2: (2003), 52–57, Proceedings of the 11th International Workshop on Vertex Detectors. DOI: 10.1016/S0168-9002(03)01750-9.

[Sch11] Max Schmenger. Messung des Lorentzwinkels an bestrahlten Silizium-Streifendetektoren. IEKP-Bachelor-KA/2011-16. Bachelor thesis. Karlsruher Institut für Technologie, Institut für Experimentelle Kernphysik, 2011.

[See91] Karlheinz Seeger. Semiconductor physics: an introduction. Springer series in solid-state sciences. Springer-Verlag, 1991.

[Sho38] William Shockley. Currents to Conductors Induced by a Moving Point Charge. Journal of Applied Physics (9)10: (1938), 635–636. DOI: 10.1063/1.1710367.

[Sil] Atlas User's Manual. Silvaco, Inc. Aug. 2013.

[Sin08] Ajay Kumar Singh. Electronic Devices And Integrated Circuits. Prentice-Hall Of India Pvt. Limited, 2008.

[Spi05] Helmuth Spieler. Semiconductor Detector Systems. Oxford scholarship online. OUP Oxford, 2005.

[Str12] Martin Printz (geb. Strelzyk). Design studies of n-in-p silicon strip sensors for the CMS tracker. IEKP-KA/2012-22. Diploma Thesis. Karlsruher Institut für Technologie, Institut für Experimentelle Kernphysik, 2012.

[Swa+04] Morris Swartz et al. Type inversion in irradiated silicon: a half truth. Sept. 2004.

[Swa13] Morris Swartz. Private communication. 2013.

[Syn] Sentaurus Device – An advanced multidimensional (1D/2D/3D) device simulator. URL: http://www.synopsys.com/Tools/TCAD/DeviceSimulation/Pages/SentaurusDevice.aspx.

[Sze69] Simon M. Sze. Physics of Semiconductor Devices. John Wiley & Sons, 1969.

[Tro12] Georg Troska. Development and operation of a testbeam setup for qualification studies of ATLAS Pixel Sensors. PhD thesis. Technische Universität Dortmund, 2012.

[Vai+13] Juozas Vaitkus, A. Mekys, V.Rumbauskas, and J. Storasta. Peculiarities of Dark Conductivity in Irradiated Silicon. Presented at 23rd RD50 Workshop, CERN. Nov. 2013.

[Var67] Yatendra Varshni. Temperature dependence of the energy gap in semiconductors. Physica (34)1: (1967), 149–154. DOI: 10.1016/0031-8914(67)90062-6.

[Wun92] Renate Wunstorf. Systematische Untersuchungen zur Strahlenresistenz von Silizium-Detektoren für die Verwendung in Hochenergiephysik-Experimenten. DESY-FH-1-K-92-01. PhD thesis. Hamburg: Universität Hamburg, Oct. 1992.

[ZAG] Zyklotron AG. URL: http://www.zyklotron-ag.de.

[ZN07] A.F. Zarnecki and P. Niezurawski. EUDET Telescope Geometry and Resolution Studies. Feb. 2007. EUDET-Report-2007-01